UNIVERSITY OF SOUTHAMPTON

FACULTY OF PHYSICAL SCIENCE AND ENGINEERING

Optoelectronics Research Centre

Characterisation of Imperfections in Hollow Core Photonic Bandgap Fibres

by

Seyed Reza Sandoghchi

Supervisors:

Prof. David J. Richardson

Prof. Francesco Poletti

Dr. Marco N. Petrovich

Thesis for the degree of Doctor of Philosophy

December 2016

UNIVERSITY OF SOUTHAMPTON

ABSTRACT

FACULTY OF PHYSICAL SCIENCE AND ENGINEERING

Optoelectronics Research Centre

Thesis for the degree of Doctor of Philosophy

CHARACTERISATION OF IMPERFECTIONS IN HOLLOW CORE PHOTONIC BANDGAP FIBRES

Seyed Reza Sandoghchi

Over the past decades, the performance of standard single-mode fibre (SSMF) has improved to the point that limited scope now exists for significant further reductions in loss and nonlinearity, which determine the fibre's transmission capacity. Given the current 40% per annum growth in data traffic, and the fact that state-of-the-art data transmission experiments are operating close to the fundamental information-carrying limit of SSMF, there is strong interest in developing radically new fibres capable of much higher data carrying capacity. Recently, a potentially disruptive new type of fibre, the hollow-core (HC) photonic bandgap fibre (PBGF), has emerged as a credible candidate. It guides light predominantly (i.e. ~99%) in air, providing a unique set of optical properties such as ultralow nonlinearity, ultimate low signal latency, and the potential for lower loss compared to SSMF. However, to enable the application of HC-PBGFs for data transmission, the fabrication of long lengths of uniform, low-loss HC-PBGFs is essential, which had not been possible until recently. Despite empirical observations of high loss section along HC-PBGFs and of more frequent fibre breaks than in conventional fibres were known, very little was known about the root cause of these issues at the start of this PhD project.

The investigation of the problems preventing the fabrication of long length of uniform, defect free HC-PBGF is the topic of this thesis. I developed and/or applied a suite of characterisation methods, such as IR side-scatter imaging, X-ray tomographic analysis and optical side scattering radiometry, aimed at identifying defects and imperfections that arise in HC-PBGFs. Through these techniques, I studied the morphology and longitudinal evolution (e.g. formation, stabilisation and decay) of such defects, the first systematic study of this kind for HC-PBGFs. Furthermore I could backtrack their origin to well defined stages in the fabrication (e.g. preforms and canes). My observations suggest that all or at least most defects arise due to contamination or stacking errors, which are unintentionally introduced when the HC-PBGF preforms are assembled from

arrays of glass capillaries. Ultimately, the methods I have developed and the findings described in this PhD Thesis helped develop ways to greatly reduce (and hopefully, in future, completely eliminate) these defects, which resulted in several breakthroughs including the achievement of the current record length of low loss HC-PBGF, i.e., a 11km long fibre with a uniform 5.2dB/km loss and more than 200nm transmission bandwidth, a factor of 10 longer length than what had been reported before the start of this project.

Table of Contents

List of Tables

List of Figures

DECLARATION OF AUTHORSHIP

I, Seyed Reza Sandoghchi,

declare that this thesis and the work presented in it are my own and has been generated by me as the result of my own original research.

Characterisation Of Imperfections In Hollow Core Photonic Bandgap Fibres

I confirm that:

1. This work was done wholly or mainly while in candidature for a research degree at this University;
2. Where any part of this thesis has previously been submitted for a degree or any other qualification at this University or any other institution, this has been clearly stated;
3. Where I have consulted the published work of others, this is always clearly attributed;
4. Where I have quoted from the work of others, the source is always given. With the exception of such quotations, this thesis is entirely my own work;
5. I have acknowledged all main sources of help;
6. Where the thesis is based on work done by myself jointly with others, I have made clear exactly what was done by others and what I have contributed myself;
7. Parts of this work have been published as: [please see Appendix B]:

Signed: .....

Date: .....

Acknowledgements

I would like to express my gratitude to the people who helped me in this research, without whom it would not have been possible to produce this work. I am thankful to Prof. David J. Richardson, Prof. Francesco Poletti, and Dr. Marco N. Petrovich for their kind and continuous help and support through the entire length of my PhD, not only in my academic life, but also in my hard and difficult times during the past four years. I would like to say another thanks to Dr. Petrovich, whose help and support have gone beyond my description. Special thanks to Dr. Yong Chen, Dr. Greg Jasion, Dr. David Gray, Dr. Natalie Wheeler, Dr. John Hayes, Dr. Eric Numkam Fokoua, Dr. Tom Bradley, Seyed Mohammad Abokhamis Mousavi, Dr. John Wooler, Marcelo Alonso Gouveia, and Naveen K. Baddela for their kind help and supportive assistance, simply, without them I would have not reached this stage. Also, I would like to thank, Dr. Yongmin Jung, Dr. Zhixin Liu, Dr. Shaif-ul Alam, Dr. Radan Slavik, Dr. Hans Christian Mulvad, Glenn Topley, Dr. Zhihong Li, Dr. James Gates, Dr. Peter Cooper, Nicholas White, Dr. Francesca Parmigiani, Dr. Saurabh Jain, Dr. Ali Masoudi, Dr. Lewis Carpenter, Dr. Armen Aghajani, Neil Sessions, Dr. Andrew Webb, Dr. Senthil Ganapathy, Professor Peter Lanchester, Professor James Wilkinson, Professor Gilberto Brambilla, Professor Periklis Petropoulos, Professor Peter Smith, Paul Allwood, Oliver Matthews, Paula Smith, Mike Bartlett, Richard Kean, Mark Lessey, Robert Standish, Dr. Mohammad Belal, Asiri Obeysekara, and other people at the ORC who have both encouraged me through the difficult times during this PhD and supported me in carrying out my experiments e.g. through useful discussion, lending equipment, providing training and making parts for the measurements setups I designed and used. I am truly thankful to all of them.

My hearty thanks goes to my family, they have given me their love and non-stop support throughout my whole life. Finally, my utmost gratitude goes to God, the one who has never left me on my own even for a moment.

Definitions and Abbreviations

µm	Micro-Meter
ADU	Analog to Digital Unit
AFM	Atomic Force Microscope
ASE	Amplified Spontaneous Emission
BD	Beam Dump
BSD	Back Scattered Electron Detector
BSE	Back Scattered Electron
CAD	Computer-Aided Design
CCD	Charge-Coupled Device
CL	Confinement Loss
cm	Centimetre
CP	Cumulative out-scattered Power
CT	Computed Tomography
CW	Continuous Wave
dB	Decibel
DR	Dynamic Range
DWDM	Dense Wavelength Division Multiplexing
ECOC	European Conference on Optical Communication
EDFA	Erbium Doped Fibre Amplifier
EDX	Energy-Dispersive X-Ray Spectroscopy
EU	European
FFT	Fast Fourier Transform
FM	Fundamental Mode
FORJ	Fiber Optic Rotary Joint

FUT	Fibre Under Test
fW	femto-Watt
FWHM	Full-Width Half-Maximum
GUI	Graphical User Interface
HCF	Hollow-Core Fibre
HC-PBGF	Hollow-Core Photonic Band-Gap Fibre
HgCdTe	Mercury Cadmium Telluride
HV	High Vacuum
Hz	Hertz
ID	Internal Diameter
InGaAs	Indium Gallium Arsenide
IR	Infrared
IS	Integrating Sphere
km	Kilometre
kVp	kilo Volt peak
LIA	Lock-in Amplifier
LMA	Large Mode Area
LO	Local Oscillator
LP	Linearly Polarised
m	meter
MCF	Multi-Core Fibre
MCT	Mercury Cadmium Telluride
MCVD	Modified Chemical Vapour Deposition
MEF	Multi-Element Fibre
MIF	Metal-Incorporated Fibre

mm	millimetre
MMF	Multimode Fibre
MOF	Microstructured Optical Fibre
mW	Milli-Watt
NA	Numerical Aperture
NEP	Noise Equivalent Power
nW	Nano-Watt
OD	Outer Diameter
OFC	Optical Fiber Communication Conference
OLCR	Optical Low Coherence Reflectometry
OM	Optical Microscope
ORC	Optoelectronics Research Centre
OSA	Optical Spectrum Analyser
OSSR	Optical Side-Scattering Radiometry
OTDR	Optical Time Domain Reflectometry
OVD	Outer Vapour Deposition
PBG	Photonic Band-Gap
PBGF	Photonic-Band-Gap Fibre
PC	Polarisation Controller
PCF	Photonic Crystal Fibre
PM	Polarisation Maintaining
pW	pico Watt
RMS	Root Mean Square
ROV	Remotely Operated Vehicle
s	second

SCW	Surface Capillary Wave
SDM	Spatial Division Multiplexing
SE	Secondary Electron
SEM	Scanning Electron Microscopy
SM	Surface Mode
SMF	Single-Mode Fibre
SNR	Signal to Noise Ratio
SSMF	Standard Single-Mode Fibre
TDFA	Thulium Doped Fibre Amplifier
TLH	Triangular Lattice of Holes
TLS	Tuneable Laser Source
USB	Universal Serial Bus
UV	Ultra Violet
VAD	Vapour Axial Deposition
WD	Working Distance
WDM	Wavelength Division Multiplexing
XCT	X-ray Computed Tomography

Chapter 1: Introduction

The focus of the past few decades of communications research has been on developing innovative ways to exploit the enormous potential transmission bandwidth of silica based optical fibres through the generation, coding, amplification, (de-)multiplexing and detection of optical signals [1]. Kao and Hockham in the mid-1960s [2] identified silica glass as the most suitable material for optical fibres. Their insight initiated intensive research around the world aiming to realize low-loss silica based guiding structures, and silica became the unquestionable material of choice following the demonstration of silica fibres with less than 20dB/km loss by researchers at Corning laboratories in 1970 [3]. An order of magnitude reduction in optical loss was achieved within less than a decade [4], and since then the construction of long-haul networks using single-mode silica fibres became firmly established.

While the performance of standard single-mode fibre (SSMF) has undergone significant further improvements since then (e.g. the reduction of water induced losses), its basic design has remained almost unchanged for many years - in fact, it is believed that there is only very limited scope for further optimization [5]. Given the 40% per annum growth in data traffic, and that the latest transmission experiments are within a factor of two or so of the fundamental information carrying limit of SSMF, there is renewed interest in developing radically new fibres capable of much higher data carrying capacities and much research is now going on around the world looking at solutions to this problem.

Recently [6], a radically new class of silica-based fibre, the hollow-core photonic bandgap fibre (HC-PBGF), has been put forward that has attracted a great deal of attention. The light transmitted by a HC-PBGF travels predominantly (i.e. ~99%) in air, inside its 'hollow core', providing a unique set of intriguing optical properties. In particular, this structure offers ultralow nonlinearity [7], ultimate low latency [8], and the potential for lower attenuation than the SSMF [9]. Because of this unique set of features, HC-PBGFs may provide wider application opportunities relative to conventional solid optical fibres, both in terms of conventional uses of fibre optics (e.g., in telecoms/datacomms and high power laser light delivery), and in new application areas besides (e.g., gas-sensing , and particle guidance). In time sensitive applications in particular, such as intra- and inter- connections in data centres, the 1.54μs/km latency reduction offered by HC-PBGFs is very attractive.

Reducing optical loss and manufacturing increased fibre lengths represent major challenges for HC-PBGFs. Until recently, as evident from the literature, the longest reported HC-PBGF was ~ 1km [10, 11]. On the other hand, although the predicted minimum loss in HC-PBGFs is of the order 0.1

to 0.2dB/km[9], the measured loss values are still an order of magnitude higher, with a properly documented record lowest loss of 1.7dB/km around 1550nm for an 800m long HC-PBGF [11].

The intrinsic loss of these fibres is associated with the roughness of the air-glass interfaces within the fibre structure, more specifically those surrounding the core [12]. However, the estimated loss associated with the fibre design and observed levels of surface roughness, do not always agree with direct fibre measurements. For example, in our labs we have produced fibres with almost identical structure, but with very different optical losses – one fibre guiding in the dB/km regime and the other showing a ~100dB/km loss. Routinely, such problems have simply been attributed to "fibre fabrication errors" and the corresponding high loss fibres scrapped.

In addition, the fabrication of these fibres with anomalously high loss, often coincide with the occurrence of several fibre breaks during the draw. This is a known fact among fibre fabricators, and again is often simply attributed to "a poor quality fibre preform" and/or "fabrication errors". Although such occurrences have been around since the very earliest days of HC-PBGFs, (they are thankfully relatively rare nowadays after many years of fibre development), the reason for such problems has not been systematically studied, leaving a significant gap in the literature.

SSMF owes its nearly ideal performance (down to its intrinsic limitations) to the enormous amount of efforts put into understanding fabrication difficulties and the developments/improvements that such studies have aroused. It is hard to deny that the development of HC-PBGFs would benefit from such detailed and systematic studies and this formed the motivation for my PhD Thesis.

In order to produce low loss, uniform, long lengths of HC-PBGFs, three key challenges can be identified and need to be resolved:

- Fibre breaks during the fibre draw process;
- Inconsistencies/defects along the fibre length, which may cause a local increase in loss;
- Distortions in the fibre structure because of the fibre draw dynamics of large diameter preforms.

The latter topic is the research focus of an immediate ORC colleague who is modelling the dynamics of the fibre draw process in order to scale up the fabrication process of HC-PBGFs to lengths of the order of 100km. Increasing the size of fibre preforms is necessary to achieve this goal which consequently involves a huge dimensional change at the transition region between the preform and fibre. In particular, it is important to understand the dynamics of the draw within the transition region, during which almost all of the structural changes occur. I have done measurements of such transition regions in our current HC-PBGF preforms to aid this work.

On the other hand, arguably, at the scale of current fibre production rate (<15km per preform per draw), the maximum length of fabricated fibre is limited by fibre breakages during the fabrication process and inconsistencies/defects along the fibre length. Any sudden variation in control parameters during the fibre draw process on one hand, and structural and material imperfections on the other hand, may cause fibre breakages and/or additional losses, which in some cases render the whole fabrication effort useless. The extensive manual process of HC-PBGF preform assembly is prone to the inclusion of particles and contaminations that are barely visible to the naked eye. Such imperfections, although small relative to the dimensions of fibre preforms, are often large enough relative to the dimension of the drawn fibres to cause structural failures, such as fibre breakages or structural deformations.

A detailed and systematic study of the first two challenges, as briefly introduced above, is the main goal of my PhD, which has focussed on the detection and identification of imperfections in HC-PBGFs and their preforms. The optical loss in HC-PBGFs proved to be a very challenging parameter to study via conventional methods like the cutback technique and optical time domain reflectometry (OTDR). Moreover, commercially available tools and techniques used to check fibre integrity and the longitudinal uniformity of fibres have proved too coarse and insufficient to test HC-PBGFs in their current state of development. Through careful design, fabrication and characterisation of fibres, I developed new perspectives and techniques to study the loss and integrity of HC fibres.

As well as implementing several existing and applicable fibre examination methods, I developed other novel characterisation systems and techniques to facilitate the identification and quantification of uncommon but highly impactful fabrication imperfections in these fibres, providing much deeper insight into the loss and integrity aspect of HC-PBGFs. Largely as a result of my work many breakthroughs and achievements have been made in producing record-breaking fibres in terms of length and loss.

At the beginning of my PhD, I started measuring scattered light from HC-PBGFs and identified that in some fibres at least light was being scattered from discrete scattering points as well in the expected distributed sense along the fibre length. Following these observations, I developed a fibre inspection method and a high precision fibre cleaver that allowed me to identify accurately the position of the scattering points along the fibre and then to investigate the underlying mechanism of the excessive scattering through precise cleaving the fibre at the respective position (**Chapter 3**). These findings then led to the requirement for a non-destructive 3D imaging technique with high longitudinal resolution along the fibre axis, which was not possible through successive fibre cleaves. I developed a novel method based on X-ray computational tomography

(CT) to capture unprecedented details about the imperfections in HC-PBGFs, as well as their preforms. This work was highlighted as a prestigious “Spotlight in Optics” article in the Optics Express journal (see **Chapter 4**). Alongside the X-ray CT method, I developed a technique to measure the longitudinally resolved side scattered light from HC-PBGFs – which I have called optical side scattering radiometry (OSSR). This tool provides a combination of high sensitivity, high resolution and wide dynamic range. The measurement capability is far better than that available from any commercially available instrument on the market. This work was awarded the best student paper prize at ECOC 2015, and it also generated another “Spotlight in Optics” article in Optics Express (see **Chapter 5**). The combination of the above tools and methods enabled me to find and study fibre imperfections in HC-PBGFs, which in turn resulted in the fabrication of a record-breaking 11km length of low-loss HC-PBGFs [13]. The methods and systems I developed within my PhD are now being routinely used by my colleagues not only in HC-PBGF research, but also in other optical fibre related studies.

Next, I will discuss the outline of this thesis.

1.1 Structure of thesis

Following the introduction, in Chapter 2, a generic picture of a HC-PBGF is provided and its main structural parameters are introduced, these are required to understand the following discussions in this thesis and in the associated literature. This is followed by a discussion on the state-of-the-art achievements in HC-PBGF technology. Next, the guidance mechanism of HC-PBGFs, i.e. photonic bandgap (PBG) guidance, is introduced and thoroughly discussed, in order to provide the background needed to capture the importance of structural parameters in the formation of the PBG and consequently to understand the guiding properties of HC-PBGFs. The fabrication process of HC-PBGFs is discussed in detail at this point in order to visualise the challenges faced in the realisation of such exotic fibres. The details provided in this section highlight the potential pitfalls that may lead to compromised performance of HC-PBGFs. Characterisation methods that are conventionally used to measure the fibre performance are then discussed, with particular attention paid to methods that measure optical loss and fibre integrity. These methods and their results are referred to throughout this thesis and many have shortcomings when it comes to the measurement of HC-PBGFs. At the end of Chapter 2, the characteristics and performance of HC-PBGFs are discussed, with particular emphasis on the mechanisms underpinning the optical loss in these fibres. The background information provided in this chapter should set the scene for the activities that I report in the rest of thesis, the aim of all of which has been to identify and characterise possible difficulties that limit the optical loss and fabricated length of HC-PBGFs.

In Chapter 3, I present a method based on use of a sensitive IR camera to identify and study the imperfections in HC-PBGFs with a better local resolution and sensitivity in finding defects than conventional methods. In addition, I introduce two fibre-cleaving setups that I made for capturing the internal structural deformation happening within the fibre at and around the scattering points identified by the IR camera. In this chapter, I explain my early attempts to identify the origin of structural deformations by studying the evolution of defects. From these studies, two further investigation techniques emerged and that are discussed in Chapters 4 and 5: one technique to improve the study of defect evolution, and the another technique to automatize the process of finding the location of scattering points, in particular for long fibre samples.

Chapter 4 shows the first demonstration of the potential of X-ray Computed Tomography (in short, XCT) for the structural analysis of both preforms and fibres, which enables non-destructive measurements that have not previously been achievable by other means (particularly for preforms). In this chapter, I describe the use of XCT to achieve detailed and accurate high-resolution analysis of the internal structure of preforms and fibres, thus characterising the full fabrication flow of HC-PBGFs. I begin with a discussion of the conventional methods used to inspect fibres and preforms, and then briefly explain the concepts and operating principles of X-ray CT. This is followed by a description of the experimental setups and equipment I used. Next, I discuss the X-ray CT analysis of two particular examples of specialty fibres (non HC-MOFs), which have been selected to show the versatility and usefulness of X-ray CT for the analysis of fibres and preforms. In particular, I apply XCT to study the structural uniformity and consistency in a metal incorporated soft-glass fibre, and the internal arrangement of fibre elements in a multi-element fibre. I then discuss the main topic of this chapter, i.e. the use of XCT to preform non-destructive structural analysis of HC-PBGFs and their preforms. In this section, I show X-ray CT to be a valuable tool for inspection of first stage preforms and canes, providing unparalleled details about their consistency and uniformity. I highlight the advantages of this method to the study of fibre defects, examples of which have been discussed in Chapter 3. I then report other exemplar applications of the technique in other areas of HC-PBGF study. More in detail, I use the technique to understand the internal deformations caused during the splicing process of HC-PBGFs, and to study the end facet damage induced by coupling light from a high peak-power pulsed laser source in to Kagome fibres.

In Chapter 5, I present the method I have developed to measure the longitudinally resolved optical out-scattered fibre power with high spatial resolution (~cm scale) and large dynamic range (>50dB). I will discuss how this measurement can then be used to infer information on the locally propagating signal and to obtain information on both local and distributed forms of loss. The method is validated through measurements on a standard telecoms fibre (Corning SMF28e) and

subsequently used to examine an 11km HC-PBGF, which would not have been possible with any standard high-resolution reflectometry technique. I then use the technique to examine another HC-PBGF with unusually high loss, and finally I demonstrate the flexibility of the method by measuring a HC-PBGF operating at a wavelength of 2μm, a wavelength at which no commercial OTDR is currently available.

I provide a summary of the activities, findings and achievements that I have discussed throughout this thesis in Chapter 6. Here I also discuss some possible paths for further investigation and additional future work.

Chapter 2: Principles of HC-PBGFs – Guidance, fabrication, characterisation and properties

2.1 Overview

HC-PBGFs are interesting because they guide light in a fundamentally different way to conventional all solid fibres. A HC-PBGF, as seen in Figure 2.1 a, is able to confine light in its air-core by means of a complex microstructure in its cladding. Since Light is effectively guided in air rather than solid glass, HC-PBGFs have a number of attractive optical properties including **ultra-low optical nonlinearity** [7]and **low latency** [8] over potentially a **wide bandwidth** [8, 14]. According to current best models, the ultimate optical **attenuation (Loss)** of HC-PBGFs is predicted to be at least as low as current telecom SMFs (~0.2dB/km), however loss in practical fibres is much higher than this in the ≈few dB per km range [9] and thus loss reduction is one of the major outstanding challenges for this fibre technology. Another recognised challenge that does require suitable solutions in order to allow a more widespread adoption of these fibres in experiments (and demonstrators) of realistic scales is the achievement of sufficiently long fibre lengths. Most studies to date have used fibre samples with relatively modest lengths (typically less than 1km). The last two properties, i.e. loss and length, are being actively investigated by several groups worldwide, in particular trying to identify the reason for the relatively high loss and to establish improved fabrication, qualification and characterisation methods to increase the lengths of low loss fibre that can be produced.

In this chapter, I lay the groundwork for the remainder of the Thesis, providing the basic concepts and properties about HC-PBGFs, their fabrication and characterisation, and also helping the reader to place this work in the wider context of the development of this relatively novel type of optical fibres. First, a generic picture of a HC-PBGF is provided and its main structural parameters are introduced. The section includes a discussion on the state of the art achievements in this technology. Next, the guidance mechanism of HC-PBGFs, i.e. photonic bandgap (PBG), is introduced and discussed in detail (section 2.3). This provides the necessary information to understand the importance of structural parameters in the formation of PBG and, consequently, on the guidance and optical properties of HC-PBGFs. In section 2.4, the fabrication process of HC-PBGFs is detailed, in order to visualise what are the challenges involved in realising a PBG in a real optical fibre. This section also introduces the potential fabrication related pitfalls and shortcomings that may lead to compromised performance of HC-PBGFs. Characterisation methods that are used to measure the performance of conventional fibres are discussed in

section 2.5, where the important differences and caveats required when measuring HC-PBGFs are also highlighted, with particular attention to the methods that measure optical loss and the fibre integrity. There are of course a number of other shortcomings that require the development of characterisation techniques tailored for HC-PBGFs and these will be discussed throughout this Thesis. Finally, the characteristics and performance of HC-PBGFs are discussed in section 2.6, with particular emphasis on the modal properties of the guided light and the mechanisms underpinning the optical loss in these fibres. The chapter ends with a conclusion section that summarises all above. The background information provided here should set the necessary ground for my research and activities that I report in this thesis, the aim of all of which has been to identify, and characterise possible difficulties that limit the optical loss and fabricated length of HC-PBGFs.

2.2 Hollow core photonic bandgap fibres

2.2.1 Introduction

A detailed description of a generic HC-PBGF provides the basic information needed for a reader to understand the whole background section. In this section, I introduce HC-PBGFs in detail and provide some description of the terms and parameters used in their study.

Hollow core photonic bandgap fibres belong to the family of microstructured optical fibres (also, referred to as Photonic Crystal Fibres or PCFs) [15]. Figure 2.1 **a** shows a cross section image of a typical HC-PBGF obtained by an electron microscope. The HC-PBGF's structure can be divided in three sections, as shown in the figure, including a jacketing layer, a microstructured cladding and a hollow core. Typically, a HC-PBGF is a mono-material structure made of a very high purity glass. Ideally, this cross-section view does not vary and is uniform along the fibre length in terms of material properties and structure, as shown by Figure 2.1 **b**. The microstructure cladding is a honeycomb structure with a few hundreds of hexagonal cells, as shown by Figure 2.1 **c**, in which a number of cells in the middle have been removed to create a central defect within the honeycomb known as the hollow core, where the light is guided. The number of removed cells, e.g. 7 (shaded as green), 19 (green + red) or 37 (green +red+ orange) is used to name the structure, such as 7-cell HC-PBGF, 19-cell HC-PBGF or 37-cell HC-PBGF. The fibre in Figure 2.1 **a** and **b** shows an example of a 19-cell HC-PBGF. HC-PBGFs are by far one of the most complex optical fibres made to date. To illustrate their complexity, the cross-section design of a standard telecoms single mode fibre is shown in Figure 2.1 **d**.

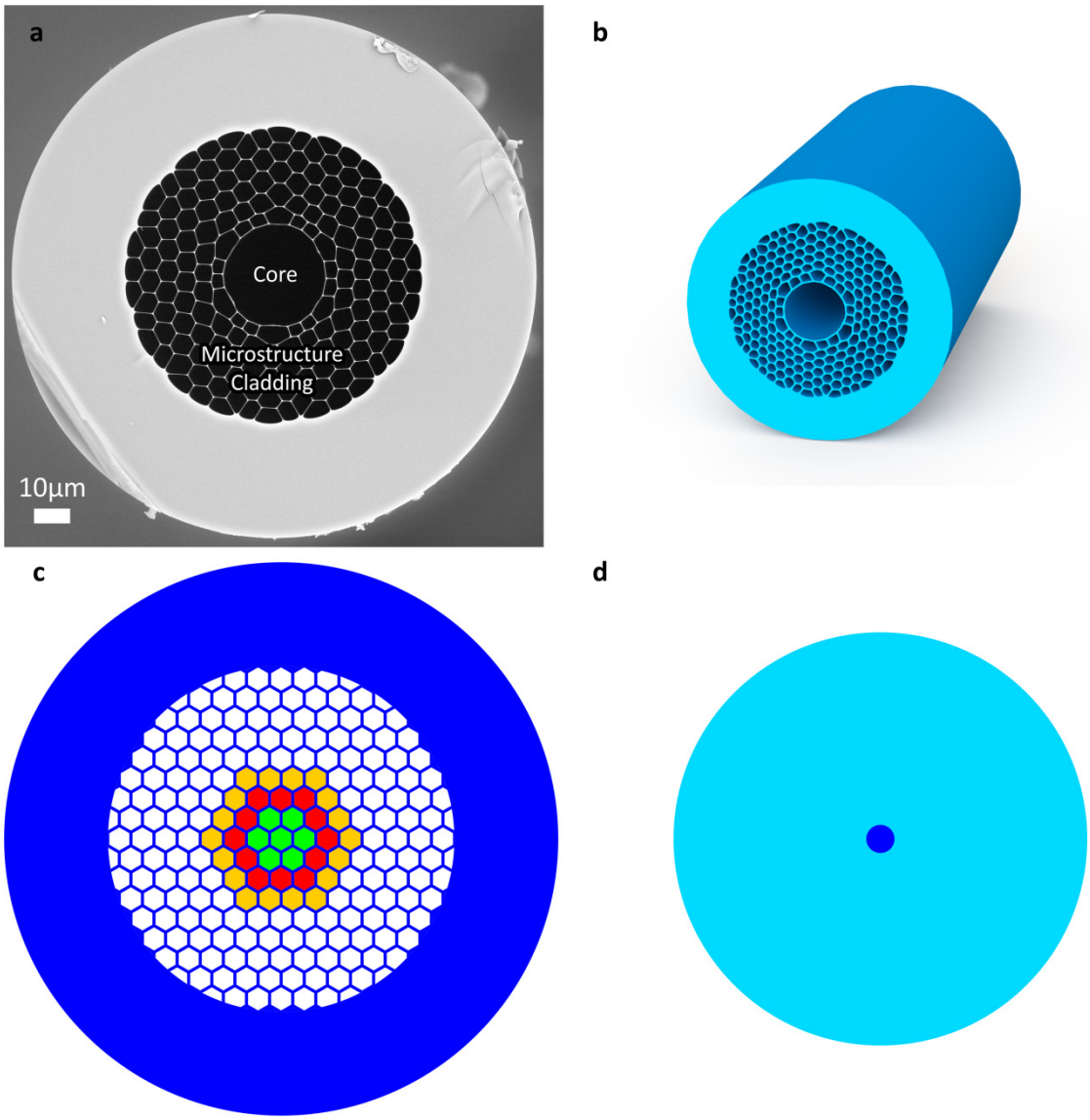

Figure 2.1: Hollow core photonic bandgap fibres. **a**, A SEM image of the cross-section of an HC-PBGF. **b**, A 3D representation of a piece of an HC-PBGF. **c**, A schematic of the honeycomb microstructure. **d**, The cross-section view of a typical standard telecom single mode fibre.

In the following, the attenuation of optical signal power (guided by an optical fibre) per unit length is defined as loss, which often varies with wavelength. The continuous wavelength range within which the optical loss is no larger than twice the minimum loss is defined as spectral 3dB-bandwidth, or in short bandwidth. These parameters are used to evaluate the performance of optical fibres.

2.2.2 Main structural parameters of HC-PBGFs

The optical performance of HC-PBGFs can be accurately described using the geometry of their cross-sections. One can assess the impact of geometry changes on the fibre performance such as

loss and bandwidth via suitable theoretical models by using these parameters as an input [16-18]. Figure 2.2 **b** shows a quarter of the cross section image of a typical 19-cell HC-PBGF with the structural parameters frequently used to describe its geometry. The cladding is a triangular lattice of holes (TLH) with air holes spacing Λ (also known as pitch). The air holes can be described as hexagons of side-to-side (diameter) d, the corners of which are rounded. The glass membranes that make the sides of the hexagons are called 'struts' and have a thickness, $\mathbf{t}$. At each corner of the hexagons, there is a 'node' (whose size is shown by a fitted circle of diameter $\mathbf{d_n}$) that joins three struts together. The struts' thickness is therefore obtained by $\mathrm{t} = (1 - \mathrm{d}/\Lambda)$. In addition, the fibre outer diameter (OD) and the microstructure diameter are also shown in Figure 2.2 **a**.

The holes in the first ring surrounding the core are divided into two groups based on the number of their sidewalls. Those with six sidewalls are given a specific name, known as 'corner holes'. The other holes in the first ring only have five sidewalls. The core's size is estimated by a circle with nominal radius $\mathbf{R_c}$. The core boundary has its own characteristic thickness $\mathbf{t_c}$, which is not necessarily equal to t. In fact, in ideal case, $\mathrm{t_c} \sim \mathrm{t}/2$ if no core tube has been used in the design of the preform. Another important parameter (not shown in the figure) is the number $\mathbf{N}$ of rings of air holes in the microstructure cladding, which largely determines the leakage loss of the fibre.

An air-filling fraction ($\boldsymbol{f}$) is often used to describe the structure of a HC-PBGF, and as its name indicates, is a measure of the percentage of air with respect to the area of a unit cell (or equivalently the photonic crystal lattice). In general, it depends both on the thickness of the struts and on the shape/size of the nodes in the cladding. For a given d/Λ, it determines the size of nodes.

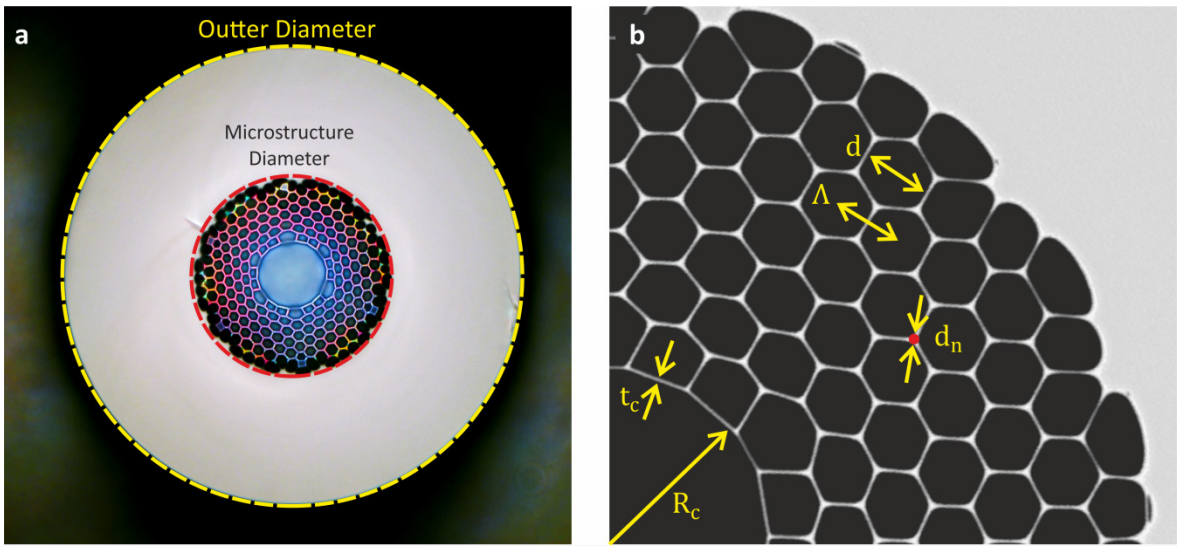

Figure 2.2: Various features of HC-PBGFs. **a**, A typical HC-PBGF. **b**, A part of the microstructure cladding.

Ideally, the complex cladding/core structure described here needs to be maintained along the entire length of fibre in order to maintain the optical properties, such as loss and transmission bandwidth, uniform from end to end. Any local structural change would constitute a structure with different bandwidth and supported modes, and the transition from one structure to another would generally involve loss and coupling to other modes and overall limitation in supported bandwidth (unless the transition is by chance adiabatic). The importance of each of these parameters on the fibre performance is explained in more detail in section 2.3.

2.2.3 State-of-the-art in HC-PBGF technology

Three important areas of active research that are trying to improve the performance of HC-PBGFs in term of loss, bandwidth and length are discussed below.

Since the first demonstration of HC-PBGFs in 1999 [6], several milestones in **loss reduction** have been reported [19-21]. The ~dB/m fibre losses at the early days of this technology reduced to a record loss of 1.2dB/m at 1600nm [12] in the course of only a few years by impressive improvements in the design and fabrication techniques. The loss reduction was both due to the optimisation of fibre design based on the advances in the understanding of the guidance mechanism in these fibres, and also due to the breakthroughs in the fibre fabrication techniques. Although this result is impressive in itself, this loss level is about an order of magnitude higher than the loss of the SSMF. Today, certain forms of HC-PBGFs are currently commercially available "off-the-shelf" from an EU manufacturer, NKT Photonics, which produces small-core fibres centred at a range of wavelengths (0.8, 1, 1.55 and 2µm) with losses from 10 to 300dB/km, and a larger core version at 1.55µm only [22]. However, these loss levels are not suitable for applications in telecom or datacomms.

Another area of research focuses on **maximizing the width** of the low loss transmission window ("transmission/spectral bandwidth"). The spectral bandwidth is important for applications such as WDM/DWDM transmission where information is sent through a number of different wavelength channels. Increased bandwidth in this context is equivalent to more data carrying capacity. The design approach that was exploited for the 1.2dB/km PBGF unfortunately also has the disadvantage of a reduced bandwidth (~20nm centred at 1565nm) [23]. This will be discussed further in section 2.6.1.2. Further studies indicate that a much wider bandwidth (in excess of 200nm) is achievable, though at a cost of a slightly higher loss [14]. Further modelling work from our group at the ORC indicates that in principle, both wide bandwidth (580nm) and ultra-low loss (0.2dB/km) HC-PBGFs should be possible [24].

Fabricating a long length HC-PBGF that has a relatively large bandwidth and a reasonable low loss is an important technological advancement. Until recently, based on the literature, the longest HC-PBGFs were only about or shorter than 1km [10, 11]. Fibre breakages during the fibre drawing process and high-loss scattering points along the fibre length are two main limiting factors ahead of increasing the fabrication yield. At the start of this Thesis, little was known about the origin of such potential contamination and defects. Through the findings of my work, I have shown that these issues originate due to both contamination and structural inconsistencies/defects within the starting preform. By reducing/eliminating these defects and contamination, we demonstrated HC-PBGFs with reasonable loss and much longer length, e.g., the record-length 11km HC-PBGF with 5.2dB/km loss [25].

2.3 Photonic bandgap guidance

The interesting properties of HC-PBGFs are because of their ability to guide light in their air core. In this section, I discuss the fundamental mechanisms behind the optical guidance in HC-PBGFs, which helps us to understand the origin and impact of fibre parameters in the transmission properties and performance of the fibre. It also provides a better understanding of the structural consistency and uniformity challenges that one need to take into account when fabricating these fibres.

2.3.1 What is a photonic bandgap?

HC-PBGFs confine light in their hollow core by means of a photonic bandgap (PBG) formed by their 2D periodic microstructured cladding [9, 26, 27]. The microstructured cladding can be seen as a photonic crystal (that similar to the atomic crystals in solid-state physics) generates a photonic bandgap (similar to the concept of electronic bandgap) that stops light from propagating into the cladding. The parameters of the photonic crystal determine the wavelength and the incident angle of the light that is banned to penetrate through the structure [26, 27].

The idea of photonic crystals, originates from the works in the field of strong localisation of light back in 1987 [28] and in the inhibition of spontaneous emission [29]. Later, it was shown that light propagation could be suppressed at certain wavelengths for periodic arrangement of dielectrics, regardless of propagation direction and polarisation. Figure 2.3 shows examples of 1D, 2D and 3D photonic crystal [27].

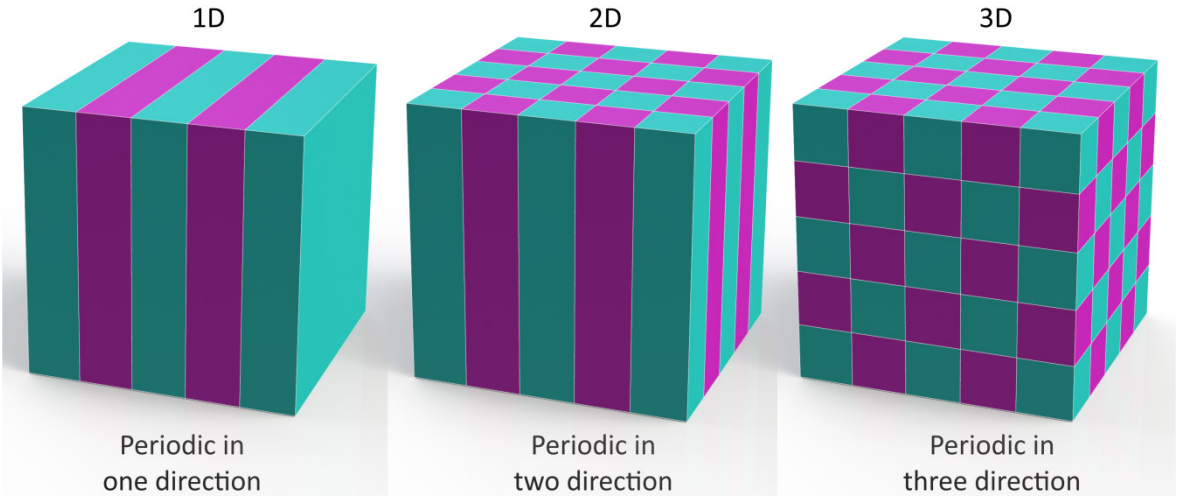

Figure 2.3: Examples of 1D, 2D and 3D photonic crystals. Each block (separated by different colour) within these structures represents a material with a particular refractive index. The periodicity is the essential characteristic of a photonic crystal. Idea from [27].

A multilayer reflector, or Bragg mirror, is the simplest device that uses the concept of a photonic bandgap. This device is a periodic stack of two dielectric layers, as illustrated in Figure 2.4. Light that is propagating in the z direction (i.e. normal to the layers/x-y plane) experiences successive reflections and transmissions at the interfaces between all layers. For a certain thickness and refractive index of layers, this device can reflect the incident light. In fact, this condition happens if all the reflections from the interfaces add up constructively (in phase) and all transmissions interfere destructively. In such a device, the incident light with an almost normal angle can be totally reflected for a certain wavelength range. In the case of a stack with infinite alternating layers, Bloch theorem is used conventionally (in solid-state physics) to find the solutions of the propagation equation. Since, such a structure possesses translational symmetry (with respect to x-y plane), the Bloch theorem suggests that the solutions can be expressed in the form of Bloch waves. Therefore, any two wave-vectors, which are different by a (multiple of) vector of the reciprocal lattice ($\frac{2\pi}{a}\hat{\mathbf{z}}$) are physically the same. Therefor it would be enough to study the dispersion diagram only in the first Brillouin zone, i.e. $-\pi/a < k_z \leq \pi/a$. At the edges of the Brillouin zone (i.e., π/a and $-\pi/a$ for any given a) two solutions exist, which have the same wave-vector but different frequencies (a vertical line that crosses the blue curves in Figure 2.4 in 2 frequency points). Importantly, in between those two frequencies no other solutions for propagating waves exist at all, which makes the so called 'bandgap' [27].

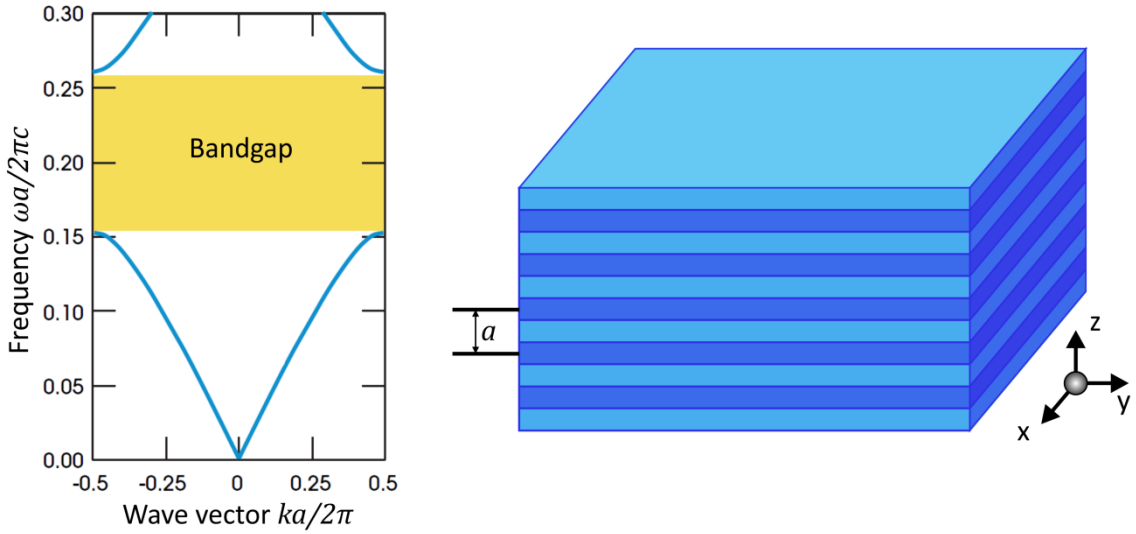

Figure 2.4: The Bragg mirror, a 1D photonic crystal. The index variation is only in z direction. Right side: Band diagram for a Bragg mirror with refractive indices 3.6 and 1. Adapted from reference [27].

The concept of 1D photonic crystal can be generalised to the case of 2D and 3D photonic crystals, by extending the directions at which the bandgap occurs to within the plane or the space of periodicity, respectively. In other words, in the Bragg mirror, the light propagating in the z-direction (the direction of periodicity) was experiencing the bandgap. For a 2D photonic crystal, like the middle structure in Figure 2.3, assuming x-y plane as the plane of periodicity, the light propagating at any direction in the plane of periodicity (i.e. the light wave-vectors in x-y plane) will face the bandgap.

Imagine the case where a part of the infinite photonic crystal is removed, i.e., a hole or defect surrounded by infinite photonic crystal. If a suitable light is injected inside the hole, it will trap inside the hole and cannot escape. In other words, some localised defect states for isolated frequencies emerge within the frequency range of the bandgap. As those frequencies are forbidden by the bandgap in the photonic crystal, they are bounded within the defect. Therefore, one can think of creating a longitudinal hole in a 3D photonic crystal to trap and guide light. Originating from this idea, it was shown that even a longitudinal hole stretched along the periodic structure and normal to the plane of periodicity of a 2D photonic crystal, could also be used to trap light [30]. This fibre was named photonic crystal fibre, after its initial structure. It is also known as the photonic bandgap fibre, to appreciate its guidance mechanism.

2.3.2 Guiding in an air-core by PBGF

One remarkable feature of a photonic bandgap fibre is that, the frequency band at which the light is trapped in the defect does not vary with the refractive index of the defect material. As such

light can be guided in a lower refractive index material, such as air or other liquid and gasses that have lower refractive index than the photonic crystal structure.

There are two ways to create the cladding periodicity around a longitudinally stretched central defect. The first structure is a 1D radial periodicity, which has been utilised by the Bragg fibres [31, 32], which requires large index contrast to form an omnidirectional reflector around the central defect [33, 34]. The other structure uses a 2D periodic arrangement (usually of air holes in silica glass) such as the structure in Figure 2.1 **a,** which is the fibre I study in this thesis.

The light that is propagating down the central defect of a photonic bandgap fibre, experience a different bandgap properties as compared to the light that is traveling in the plane of the periodicity of the photonic crystal [35, 36]. The former case is commonly referred to as out-of-plane bandgap guidance [37]. However, in the latter case, the component of the wave-vector normal to the plane of periodicity is equal to zero, such as in-plane propagation in a 2D photonic crystal or a fibre Bragg grating. In the both in-plane propagation examples, the period of the lattice Λ must be of the order of half the wavelength, requiring sub-micrometre features for operation in the visible or near-IR.

However, for the out-of-plane propagation, the sub-micrometre lattice periodicity is relaxed. To explain this let us decompose the wave-vector (nk_0) into its longitudinal component (propagation constant β) and transverse component (transverse wave number $k_\perp = \sqrt{n^2k_0^2 - \beta^2}$). $k_0 = \frac{2\pi}{\lambda}$ is the vacuum wavenumber and n is the refractive index of the defect material. In order to form a suitable bandgap, the lattice period is now determined by the transverse component, and the transverse component is usually much smaller than the wave-vector, in particular in the case of the common photonic crystal lattice shown in Figure 2.5. This allows the period of lattice Λ of several μm to be used to form a suitable bandgap, or allows the bandgap to work at much shorter wavelength.

Also, a lower refractive index contrast can be used to open a bandgap. For a silica matrix with a triangular lattice of circular holes (Figure 2.5), there is no complete photonic bandgap in the transverse propagation plane, due to an insufficient index contrast [38]. However, for out of plane propagation ($\beta \neq 0$), achieving a suitable index contrast in transverse (rather than in the direction of absolute wave-vector) is possible, and this can be made arbitrarily large for a wave-vector, even if the contrast between the refractive indices itself is small [39]. By use of this condition demonstration of air-guiding in hollow core PBGFs made of pure silica became possible[6]. In the following section, I explain the out of plane guidance in detail.

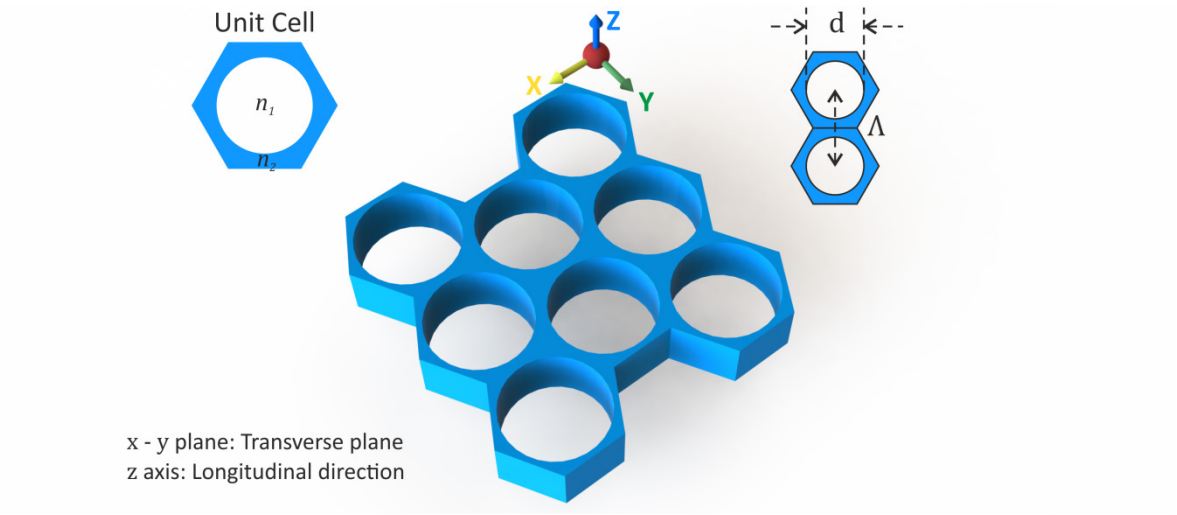

Figure 2.5: A commonly used photonic crystal structure.

2.3.3 Out of plane PBG guidance

The ratio between the wave-vector components in the plane of periodicity (transverse plane) for the two dielectrics, $k_{\perp 1}/k_{\perp 2}$, must exceed a certain critical value, in order to create PBGs that are suitable for guiding light in the low refractive index medium. This value depends on the structural properties of the lattice [38]. For light propagating in the plane of periodicity, typically a large refractive index difference between the two dielectrics is needed. For a triangular arrangement of circular holes $\Delta n > 2.2$ [40]. This considerably limits the choice of dielectric pairs that can be used, to only high refractive index glasses or semiconductors for guiding in an air core. Back in 1990s, Russell suggested that, for light propagating out-of-plane, it should be possible to achieve any desired $k_{\perp 1}/k_{\perp 2}$ ratio in a structure with the periodic dielectric arrangement that is infinitely elongated in the third dimension. Therefore, it is possible to open up a PBG, for any choice of dielectric pairs [40], if the propagation direction is making a sufficiently small angle with the normal vector of the plane of periodicity [30, 39]. This radical insight, combined with a few years of developing the required fibre fabrication technology, resulted in the first demonstration of an air-silica HC-PBGF [6]. This fibre could guide light in air, albeit with relatively high losses in the first instance, despite the refractive index difference of only 0.44 silica and air. The range of frequencies at which this condition is satisfied determines the width of bandgap.

The above perspective to the guidance mechanism of HC-PBGFs (i.e. trapping light in a photonic crystal structure by means of its photonic bandgap) provides a useful understanding of the optical properties of perfectly symmetric and infinitely extended lattices, however it hardly captures the behaviour of guided modes in the central defect (core) of HC-PBGFs. In addition, this picture does not provide a useful insight into how structural perturbations of the cladding periodicity and/or distortions at the defect termination (core boundary) affect the optical properties of the fibre.

2.3.4 Another view to the formation of PBG

More recently, a different yet simple model have been put forward (more familiar to the fibre optic community) to explain the formation of PBG because of anti-resonant interactions in arrays of closely spaced resonators in the microstructured cladding [41, 42]. In a HC-PBGF, these resonators are the 'nodes' (see section 2.2.2). Figure 2.6 explains the origin of bandgaps in HC-PBGFs using this resonator model as described below.

The model is built upon the well-known dispersion relations for a silica rod surrounded by air. Each curve in Figure 2.6 **a** shows the dispersion of a vector mode guided in the rod as a function of its v parameter ($v = \frac{2\pi r}{\lambda}\sqrt{n^2 - 1}$, where n is the glass index, r is the rod radius and λ is the wavelength of operation). Below the air-line (highlighted by red line at $w^2 = r^2(\beta^2 - k_0^2) = 0$) a continuum of plane-wave-like air modes exists (grey area). The white space above the air-line, may be interpreted as (v, β) combinations for which modes cannot propagate in the cladding (air), and cannot be sustained in the rods, i.e., modes are in 'antiresonance' with cladding and rod.

The dispersion relations of modes are substantially different once a number of identical rods are put close together (Figure 2.6 **b**). Close to the cut-off condition ($w^2 \sim 0$ or $\beta \sim k_0$) the curves broadens showing a continuum of allowed guided states instead of a single state associated with a rod. This can be explained by the expansion of the modes (of each rod) in to the cladding (in particular for smaller values of v), to an extent that they significantly overlap with the other rods. Therefore, a band of 'supermodes' with its own range of allowed effective indices is formed by the coherent spatial superposition of the modes [41]. The most important effect though, is the formation of multiple forbidden guidance regions (PBGs) below the air-line (white regions in Figure 2.6 **b**). By making a defect in this structure, e.g., by removing a rod, light can be confined in the defect for frequencies/propagation constant values inside the PBG regions.

Decreasing the rod separation (Figure 2.6 **c**), increases the strength of interaction between the modes, which widens the supermode bands and tightens the frequency width of the air band gaps. In addition, decreasing the separation, increases the average refractive index of the structure (as the low index area (air) in between rods is reduced), which result in deeper PBGs and hence more air-guided modes for the same defect size.

Another point to note is the effect of index contrast between the rods and the low index surrounding. For example, in all-solid PBGFs (with typical $\Delta n \sim 1 - 3\%$), formed by an array of high index rods in a low-index silica background [42], the vector effects become less prominent, which, for example, tightens the separation between the dispersion curves of vector modes belonging to the same "LP" group (see Figure 2.6 **a**).

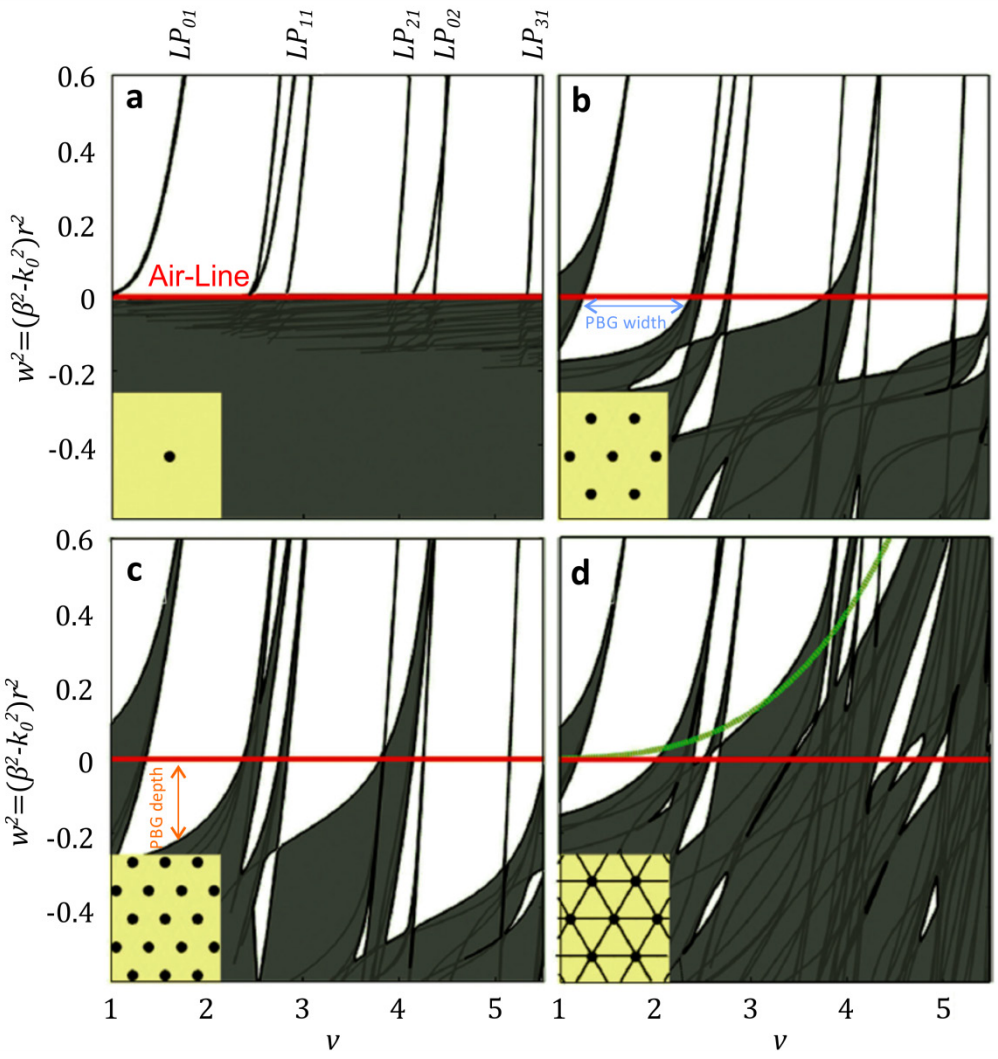

Figure 2.6: Photonic-band gap formation by resonator model: **a**, Dispersion diagram of the guided vector modes for a thin glass rod surrounded by air. **b**, Dispersion diagram for a number of identical thin glass rods that are close to each other. **c**, The dispersion diagram shows deeper band-gaps as the rod are brought closer. **d**, A more practical situation with glass rod connected to each other through a web of thin glass membranes. Adapted from reference [9].

In practice, the rods in the structure in Figure 2.6 **c** need to be physically interconnected, if for example this structure is supposed to be used as the cladding of an optical fibre. Figure 2.6 **d** shows the result of adding a thin network of interconnecting struts (made of the same material as the rods). As a result, as can be seen, PBG regions are severely modified, in particular the depth of PBGs. This can be explained by the dispersion relation of the medium surrounding the rods including the thin struts. Unlike the previous dispersion-less air medium, the new surrounding medium is strongly wavelength dependent. At higher v values, the effective index of the

surrounding medium (or more precisely, of its fundamental space filling mode[1] [15, 43]) increases because of stronger light confinement in the glass struts. The dispersion characteristics of the fundamental space filing mode is shown by the green line in Figure 2.6 **d**. The PBGs at larger v (higher order PBGs) suffer more and may be shifted above the air-line, even in the case of the thinnest practically feasible struts. As such, HC-PBGFs typically have only the first PBG region and consequently guide light over frequency range supported by the first PBG that usually happens in the interval $1 \leq v \leq 2$. In all-solid PBGFs [42], however, the multiple PBGs in Figure 2.6 **c** are observed. This allowed frequency range of the PBG, set a maximum cap to the **bandwidth** of the fibre, which can be modified and reduced by other fibre characteristics that I will discuss in section 2.6.1.

It is possible to define a structural 'scaling law' for HC-PBGFs [39], which suggests: the operating wavelength range of HC-PBGFs can be controlled by scaling the resonator size so that r/λ remains constant. In practice, this is done by a rigid scaling of the entire microstructure.

It is worth noting, it is possible to generalise the qualitative conclusions drawn here to structure other than the periodic triangular arrangement of circular rods discussed in Figure 2.6. Furthermore, it is clear that: the rod size is primary responsible parameter in the formation and characteristics of PBGs. If the rod sizes are not changed, any small variation in their optimum position within the structure may have only a very small effect on the PBG characteristics. This is often observed in the fabrication of large core (19-cell or 37-cell) HC-PBGFs with compressed or expanded claddings in the radial direction, which also may have irregular distribution of rods (nodes) at the core-surround.

2.4 Fibre fabrication

The fabrication process of HC-PBGFs has experienced remarkable improvements over the years [9], however the development of these fibres have hit problems that are hard to solve. Understanding the fabrication process of HC-PBGFs provides an insight to the possible vulnerabilities therein and as well as a better understanding of some of the possible sources of optical loss. Additionally, it is crucial to understanding the origin of fabrication imperfections, i.e. how they can arise, what may cause them, and, more importantly, how to avoid them through improved processes and fabrication methods, and thus to obtaining high performance HC-PBGFs. In this section, I explain the fabrication processes of HC-PBGFs in detail.

[1] The fundamental space-filling mode is the mode with the maximum effective index allowed in the infinite photonic crystal cladding without the core defect.

In general, an optical fibre with km-scale length and outer diameter of a few 100 microns are made from a macroscopic structure called a **preform**, which is typically about 1m to 2m long and has an OD of a few centimetres (development preforms and special fibres) to a few tens of centimetres (in the case of single mode fibres, typically produced in very large volumes). The fabrication of a fibre from a preform usually takes place in a fibre draw tower through a process called fibre drawing. The preform structure is either a macroscopic copy of the fibre structure that is scaled down directly to fibre geometry in the fibre draw process (e.g. in the case of standard all solid SMFs/MMFs), or is the closest structure to the final fibre, where it is too difficult to obtain the fibre geometry at macroscopic level. In the latter case, the preform can be drawn into structured rods or 'canes' which are typically ~10x smaller in diameter (e.g. a few millimetres). As will be explained in the following, this step provides the opportunity to make some of the structural changes that are required to transform the preform structure to the final fibre design. The same fibre draw tower is used to draw canes (however with some little modification) – this step is often called cane draw process. The cane draw process is very similar to a fibre draw process, however with some appropriate adjustments (e.g. slower drawing speed). The cane can then be drawn in a further step. A secondary preform is made by inserting a cane into a suitable jacketing glass tube. This secondary preform is then drawn to fibre by the draw tower in a fibre draw process. This procedure is termed a "dual stage" or "two-stage" fibre drawing process, and is used for some solid fibres but more typically for microstructured fibres.

Next, I introduce a typical fibre draw tower and a generic fibre draw process. The description focusses on the points that are mainly relevant to the fabrication process of HC-PBGFs. In the following section 2.4.2, I will discuss the stack-and-draw technique (the preferred manufacturing process of HC-PBGFs), through which I will emphasize on the multi-step processes therein.

2.4.1 Standard optical fibre fabrication

The manufacturing process of conventional SMFs has gone through a tremendous amount of improvement during the past several decades, to an almost perfect condition right now with more than 200 million kilometre fibre fabricated annually [44]. These fibres are fabricated in two steps: preform deposition and fibre drawing. First, a fibre preform is made using a chemical vapour deposition method (see below). The preform is a glass rod with a specific radial index profile (e.g. a step index single/multi- mode, graded index profile, or more complex) that is uniform along the preform length. The second process involves drawing a fibre from the preform. The preform, is held at one end and fed at a constant speed (~mm/min) into a cylindrical furnace, where it is heated up to its softening temperature. From the other end of the furnace, a fibre thread is pulled out at a constant speed. During this transition, the geometry i.e. the index profile

is preserved, aside from the scale reduction. The fibre diameter is set by controlling the ratio between the two speeds (as the glass mass is conserved). The simplified fabrication process introduced here, in practice, involves sophisticated advance technologies to ensure the uniformity of the index profile along the entire length of the fibre [44-46]. In the following, I provide some more details.

Preform fabrication: Typically, preforms are manufactured through well-established chemical vapour deposition techniques, such as Modified Chemical Vapour Deposition (MCVD), Vapour Phase Axial Deposition (VAD), or Outside Vapour Deposition (OVD). Figure 2.7 shows a schematic diagram of the MCVD process and the glass-working lathe used in this technique. A silica glass tube is installed on the glass-working lathe. Vapours of $SiCl_4$ mixed with O_2 are passed through inside the tube while an oxygen-hydrogen flame heats the tube from the outside to a temperature around 1800-2000˚C [47]. At the position of the burner, the $SiCl_4$ reacts with O_2 and forms a silica (SiO_2) layer, either in the form of a soot, or a fully sintered glass (depending on the temperature). The burner moves along the length of tube back and forth and on each path a new silica layer is deposited. A few layers of silica are deposited on the inner wall of the tube to form the fibre cladding. Then, to form the fibre core, a small flow of $GeCl_4$ is added to the mixture to raise the refractive index. Once the required core to cladding thickness ratio is achieved, the flame temperature is raised and the tube collapse to form a rod, which is the fibre preform.

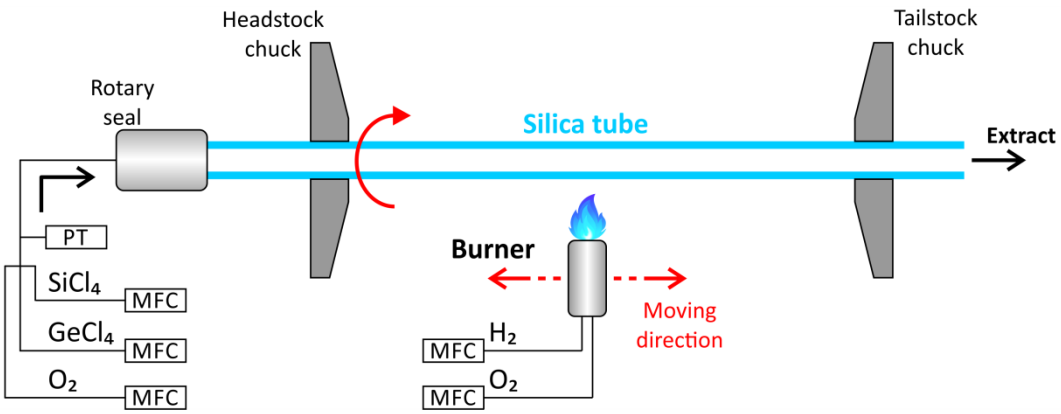

Figure 2.7: Detailed schematic diagram of the MCVD process and essential parts of the deposition lathe used for the fabrication of fibre preforms.

Fibre drawing: The preform is then drawn to fibre using the fibre draw tower. Figure 2.8 shows a generic schematic diagram of a fibre draw tower and its essential features. These include from top to down: a **chuck** attached to a **feed mechanism** to hold the preform assembly and lower it into the furnace at a precisely controlled speed; a **graphite furnace** which is constantly purged with argon (in order to avoid oxidation), a **laser diameter gauge** to do continuous non-contact measurements of the fibre diameter; a **cane puller** that is used to provide the motive force in the

fabrication of non-bendable products e.g. capillaries, rods, and canes (it is not used in the fabrication of fibres); a **coating applicator** (die) to apply a polymer coating to the fibre; a **UV oven** to cure the polymer; a **tension meter** to measure the fibre draw tension; a **capstan** to pull the fibre; and a **drum winder** to collect the fibre. The cane puller consists of two halves, which can be opened during the fibre draw and is closed for cane fabrication. The coating applicator, UV oven and tension meter can be moved out of the way to provide enough room for cane fabrication. The temperature of the furnace is measured by a pyrometer within 1°C precision, and a control loop maintains the temperature of the furnace. Another control loop adjusts the capstan speed based on the fibre diameter readings from the diameter gauge and the desired value.

During the fibre draw, the preform is lowered into the furnace. The furnace is heated to and kept at a temperature at which the glass is sufficiently soft to allow a fibre to be drawn from its tip. The diameter transition from the preform to the fibre geometry happens at the furnace hot zone, which is by design only a few centimetres wide. The transition region itself is often called **neck-down** region. Beyond the hot zone, glass is rapidly cooled down and at a particular temperature (the **glass transition temperature** T_g) it solidifies. Before being collected, the fibre is coated with a UV curable polymer in the coating applicator, which is cured in a UV oven. The polymer coating acts as a protection layer for the fibre against surface scratches and cracks that can greatly reduce the fibre strength [44, 46]. The polymer coating can also be engineered to alleviate the effect of micro-bend induced loss in fibres [48, 49]. Below the UV oven, the fibre is passed through the capstan, which provides the force required to pull the fibre from the preform tip and through the coating applicator. The fibre is then collected on a drum by a motor winder. The pulling force exerted by the capstan is an important process parameter and is measured by a tension meter (typically located below the UV oven and just above the capstan). The pulling force gives an indication of the viscosity of the glass in the hot zone and thus of the actual drawing temperature of the preform [44].

In a steady state draw condition, for a solid glass preform (made up of an incompressible material and structure) the cross sectional areas of the preform and fibre (A_p and A_f respectively), the fibre draw speed v_f , and preform feed rate v_p are linked together through conservation of glass mass:

$$A_p \times v_p = A_f \times v_f \tag{2.1}$$

which for a cylindrical geometry can be rewritten as:

$$d_p{}^2 \times v_p = d_f{}^2 \times v_f \tag{2.2}$$

where d_p and d_f are the preform and fibre diameters respectively. Therefore, for a given preform diameter and preform feed rate, the diameter of the fibre is controlled directly by the square root of the fibre draw speed. This can be used to adjust the fibre diameter in the draw process. The fibre diameter can be controlled automatically by the tower control system, which uses the fibre diameter readings from the laser gauge to adjust the capstan speed.

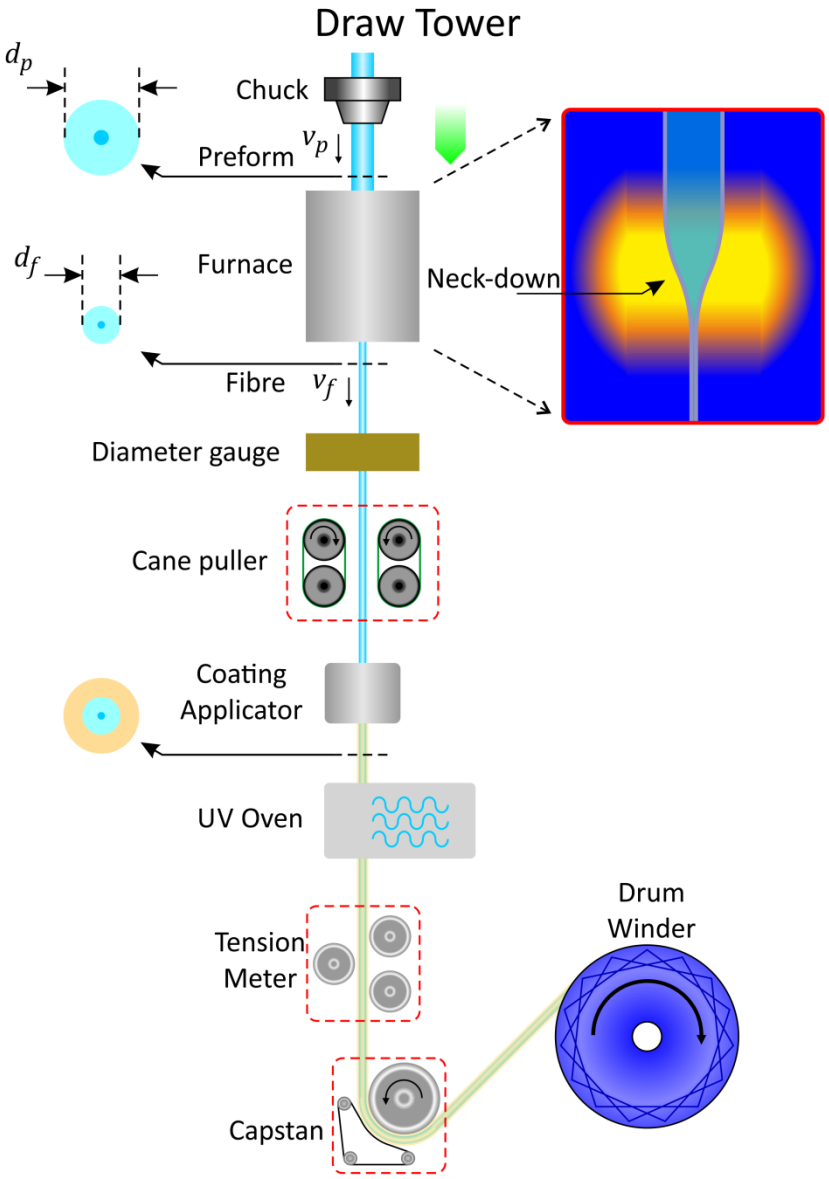

Figure 2.8: Schematic of a draw tower for making optical fibres and its functioning.

The draw tower pictured above is used not only in manufacturing conventional fibres but also (with suitable additions and modifications) in fabrication of MOFs and other speciality fibres. By slight adjustment of various parts of the tower, it can be used to accommodate materials with diverse properties, such as polymers, chalcogenides and borosilicate glasses.

2.4.2 HC-PBGF fabrication

A variety of techniques have been demonstrated for the fabrication of MOFs including drilling [50, 51], extrusion [52], sol-gel casting [53], additive manufacturing (3D printing) [54], or stack-and-draw [55]. Often a method tends to suit a particular type of MOFs better than the others do. When it comes to the fabrication of silica HC-PBGFs, the stack-and-draw [56] is the most commonly used fabrication method. In particular, this technique has used for the fabrication of all record-breaking HC-PBGFs in terms of loss[12], length[25], and bandwidth[14].

2.4.2.1 Stack-and-draw

The HC-PBGF fabrication through the stack-and-draw is a two-stage process. Briefly, as shown in Figure 2.9, it involves two draw processes. In the first stage, hundreds of ~mm-OD, ~meter-long glass capillaries of equal size, and a number of solid rods with different diameters are made according to the stack design (**Step 1**); the capillaries are then stacked with an hexagonal arrangement, and then the stack is inserted into a jacketing tube and is fixed inside the tube using some extra capillaries and packing rods (**Step 2**). At the end of Step 2 the first-stage preform is obtained, which is then drawn to canes in **Step 3**. Next, the second stage begins with making a preform assembly from a cane inserted into a suitable jacketing tube (**Step 4**). The second-stage preform is then drawn to a fibre in final step (**Step 5**).

A main advantage of the two-draw technique is in the fabrication of the structures with large air-filling fraction or small (e.g. sub-wavelength) feature sizes, as it provides much wider flexibility to modify the initial structure as compared to a single-stage draw because, as will be seen in the following, one can modify and tailor the structure (e.g. by applying pressure differential to the holes and gaps in the structure, which is widely used in the fabrication of HC-PBGFs).

Here I explain each step, in more detail. This will give us a clear understanding of the fabrication that I will discuss in the rest of this chapter and of the problems that may intervene, which constitute the focus of this thesis.

Step 1 – Fabricating capillaries and packing rods

Hundreds of capillaries, with OD of $\sim$1mm and a specific aspect ratio, are required for making the first-stage preform. The exact size of capillaries is determined based on the initial fibre design along with practical considerations with regard to handling and device constraints. For example, within our draw tower, we are limited to a preform diameter $\leq 28\mathrm{mm}$ (because of the furnace bore size), fibre draw speed of $\leq 30\mathrm{m/minute}$ and capillary/rod/cane draw speed of $0.5\text{-}3\mathrm{m/minute}$ (in order to obtain samples during the draw process without interruption to the

draw), and capillary aspect ratio ≤ 0.96 (because capillaries with higher aspect ratio are often crushed by the cane puller).

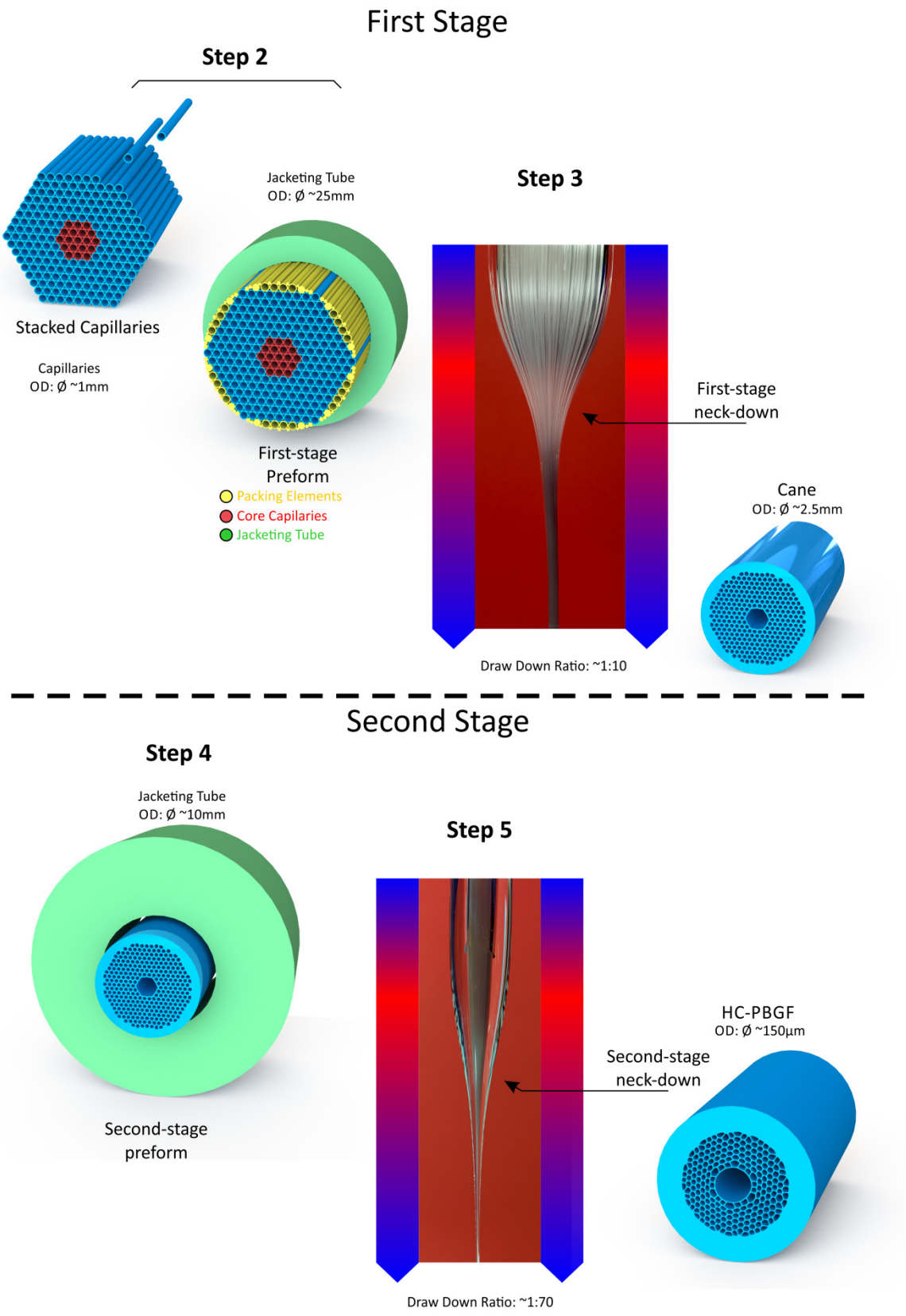

Figure 2.9: The fabrication of an HC-PBGF via a two-stage stack and draw process.

The capillaries are made from commercial Suprasil F300 synthetic silica glass tubes using the draw tower. Typically, these tubes are ~1m long and have an OD and ID of ~28mm and 24mm respectively. These tubes go through some preparation before they are drawn, to ensure a best quality for the capillaries is achieved, in particular, the capillaries that are making the core surround in the fibre geometry. The tubes are supplied in sealed plastic and are packed under cleanroom conditions. In some cases, a tube needs to be cut to the right length using a water lubricated diamond saw. After cutting, the tube is cleaned thoroughly to remove any debris and/or contamination by foreign particles. This is done using a specific detergent solution, deionised water and acetone. The tube is then blown dry using filtered, dry nitrogen.

Next, the glass tube is fitted on a glass-working lathe, for additional process. The **lathe process**, in first place, is to ensure that the tube surface, which is used for capillary draw, is pristine. Secondly, it is used to attach a short glass rod to one end of the tube, which will be used to start the draw process. The lathe is similar to the one used in MCVD process (see Figure 2.7). On the lathe, the tube is heated (locally, by the burner) to temperatures sufficient for glass working (typically 1600°C to 2000°C). An intense light is generated in this process and a part of it is trapped inside the glass. Any minute scratches, defects or residual contaminants on the surfaces are highlighted as they scatter some of the trapped light. These visible defects are removed by multiple passes of the burner while oxygen is passed through the tube. The temperature of the hot zone is gradually increased in this process; otherwise, some defects and localised contamination remain (one possible explanation is they are buried in the glass before they oxidise). In the case of persistent defects or contamination, or, when the most demanding preparation is required, the inner wall of the tube is etched by sulphur hexafluoride (SF_6). At the end, a glass rod is joined to the end of the tube, which will be used to start the capillary draw.

Capillaries are then drawn from the processed tube using the same draw tower. In the capillary draw, cane puller provides the drive force to pull the capillary. The capillaries are cut to ~1m length below the cane puller. During the draw, capillaries do not pass through the coating applicator and UV oven. The capillaries' bore may collapse (partially or completely) due to surface tension or a negative pressure difference. It may also expand (relative to the aspect ratio) if a positive internal pressure exists. Therefore, capillaries' OD and their aspect ratio (ID/OD) for a given tube size and feed speed become a function of the furnace temperature, draw speed and any pressures difference applied to the tube's hole. Controlling the **pressure differential** is fundamental in the fabrication of capillaries. In principle, this can be done by two methods. One can directly connect the hole to a source of pressure, where the differential pressure is controlled externally. This is referred to as 'direct pressurization'. In another method, the hole is sealed and 'self-pressurization' enables the hole to stay open. Direct pressurization is preferred for the

greater flexibility in controlling the final structure; however, this comes at the expense of designing a suitable pressure interface. Finally, a few hundred meter-long millimetre-diameter glass capillaries are drawn, which are usually obtained within a single draw process.

Fabrication of the packing rods is done similarly to the fabrication of a standard fibre from a solid preform discussed in section 2.4.1. Again, in the rod draw, the cane puller is used due to the large diameter (up to 1mm) of packing rods, similar to the capillaries. Various packing rod diameters are needed which all can be obtained within one draw as only a few tens of meter long pieces are required. As the packing rods do not have any particular role in the optical properties of the fibre, it is sufficient to have a relatively clean initial solid preform without needs for any special treatment.

Step 2 – Capillary stacking and first-stage preform assembling

The capillaries are manually arranged (stacked) into a predetermined shape on an assembly rig. The rig ensures that capillaries are held in the right place during the stacking. This process takes place in a cleanroom environment, where dust and particles are limited. Each capillary is held by hand from its either side and is visually checked before being placed in the stack. A drawing of the stacked capillaries (or in short, stack) is shown in the top left corner of Figure 2.9 **a**. The actual stack and the assembly rig is seen in Figure 2.10 **a**. The stack is then fixed inside a jacketing tube, by use of additional capillaries and packing rods, to form the first stage (primary) preform (as illustrated next to the stack in Figure 2.9 **a**). Figure 2.10 **b** shows the end face of a 19-cell HC-PBG first stage preform. Fixing the stack inside the jacketing tube is a very delicate job, as one need to be careful not to break the capillaries when inserting (and pushing in) the packing capillaries and rods (highlighted in the figure). The capillaries that determine the six sides of the stack are highlighted by the yellow dashed line. The rods and capillaries beyond this line are packing elements. The jacketing tube has a typical outer diameter of 20 to 30mm, made of the same material and quality as the capillaries (e.g. Suprasil F300). In order to form the core, a number of capillaries are removed from the centre of the stack and replaced with either one larger tube across the entire length of the preform or with a short stack of capillaries at both ends of the preform (as shown by the red capillaries in Figure 2.9 **a**).

The preform is then treated by an **oxidation** process, to remove any residual contamination that may have been built up during the capillary stacking process.

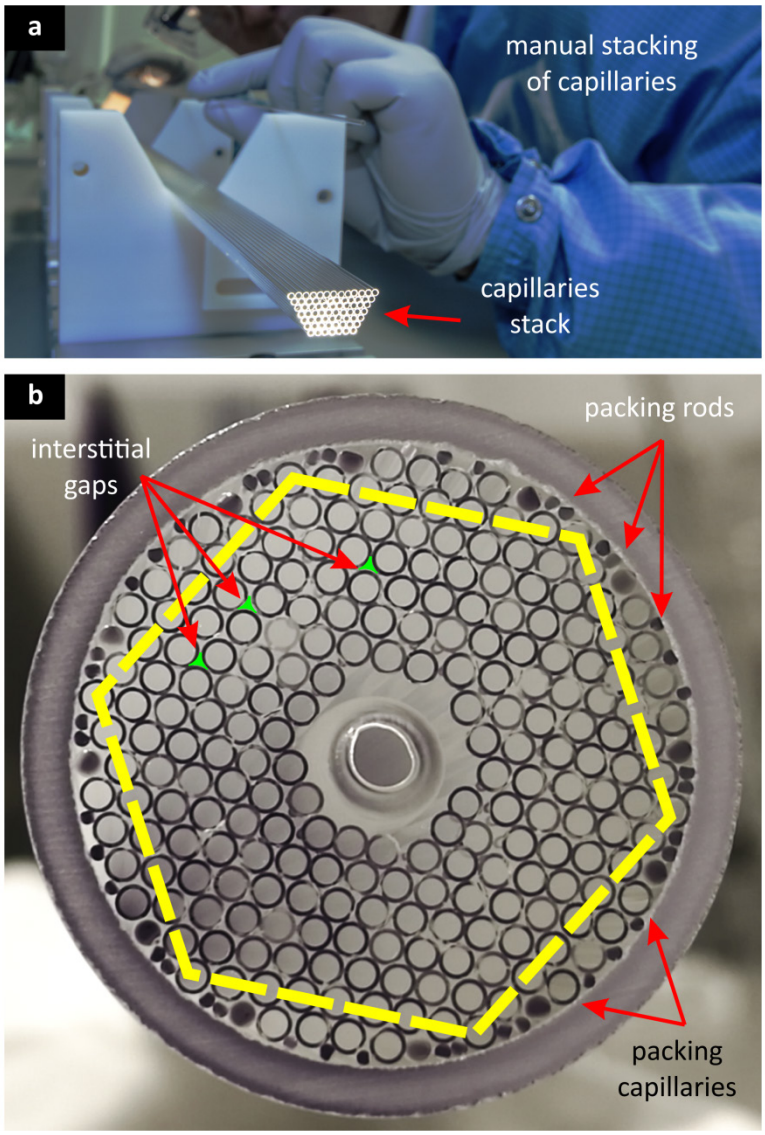

Figure 2.10: Capillaries stacking and preform assembling. **a**, Shows the manual process of stacking a few hundreds of capillaries. **b**, An image of one end of the first stage preform. One can see the packing rods and capillaries around the inner edge of the jacketing tube.

Step 3 – Cane drawing

The first stage preform is then drawn to canes using the same draw tower, with a draw down ratio of about 1:10. The draw process is similar to the capillary fabrication. The canes are made to have a typical outer diameter of ~3mm and they are cut to about a meter long. At this stage, the interstitial gaps between capillaries are reduced or totally eliminated by use of suitable pressure differentials. As mentioned before, this is an important advantage of a two-stage draw, which allows applying a part of modifications to the preform structure (to obtain the final fibre design) during the first draw.

An image of the transition region of the first stage preform to a cane (first stage neck-down), and a CAD illustration of a cane (based on an actual sample) are shown in Figure 2.9. The interstitial

gaps between capillaries in the stack are highlighted in Figure 2.10 **b**, which have been greatly reduced in the canes, as the microscope cross-section image of the cane in Figure 2.11 **a** shows. The scale of modifications to the preform structure in order to obtain the cane can be observed by comparing these images. At this point, the first stage of fabrication is completed, with several canes produced from a single first-stage preform.

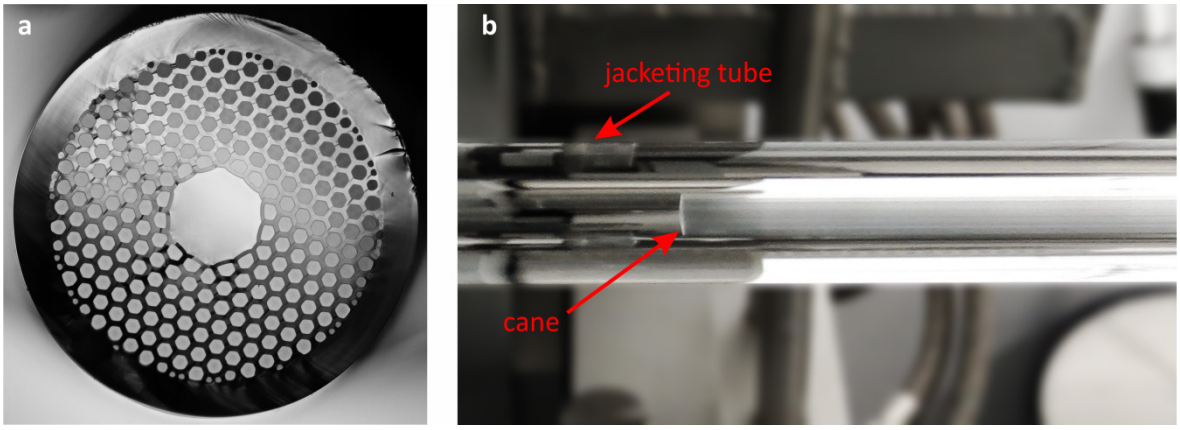

Figure 2.11: **a**, An optical micrograph of a 19-cell HC-PBG cane; and **b**, A photo of a second-stage preform.

Step 4 – Second-stage preform assembling

In the second stage of the fabrication, one of the canes is fixed inside a jacketing tube with a typical outer diameter of about 10mm, to form a second stage preform (also known as secondary/fibre preform). The jacketing tube undergoes heat treatments similar to the tube preparation for the fabrication of capillaries, in order to remove residual contamination and possible micro cracks. At the end of the process, the second stage preform is immediately taken to the draw tower for fibre fabricating. Figure 2.11 **b** shows the cane inside the jacketing tube in a second stage preform.

Step 5 – Fibre drawing

HC-PBGF drawing at this point is very similar to the fabrication of conventional fibres, i.e. using the same draw tower with similar draw tower devices, however with the main difference being the pressurization of the preform. The secondary-stage preform may be pressurised for two main reasons: firstly, to collapse the coaxial gap between the cane and jacketing tube; and secondly, to modify the cane structure in order to achieve the final fibre design. The latter is done by a proprietary pressurization setup that allows controlling the pressure of different regions of the microstructure, e.g. the core, and cladding. The pressurization allows achieving air-filling fractions and small feature sizes (in the final fibre) that would in fact be impossible to achieve from practically accessible preforms [8, 41, 57]. Figure 2.9 **b** shows the transition region of a second

stage preform, and the CAD drawing of a HC-PBGF. Thanks to the developments I present in this thesis, recently we demonstrated the fabrication of a record-length of low loss HC-PBGF with a length in excess of 11km [13, 25]. Increasing the fibre yield to beyond 10s of kilometres is critical for practical applications of this fibre technology, particularly for telecommunications.

On another front, it is important to understand the dynamic of the fibre fabrication to improve the fabrication yield and fibre performance. This has been extensively done for conventional telecom SMFs. However, as shown above the production of HC-PBGFs is different from solid fibres in several ways. The split of the draw process in two stages in one hand and the need to apply pressure during the second stage draw are the two main differences. In fact, the pressurization and its associated draw dynamics makes the HC-PBGF's upscaling a more challenging task than for all solid fibres.

Recently, an ORC colleague (Dr Greg Jasion) has developed a very powerful fluid dynamics model that can be used to virtually draw HC-PBGFs from preforms [58]. In particular, fibre draw simulations were used to investigate how to increase the yield of HC-PBGFs to much longer lengths beyond 100km, required for mass-producing such fibres. Given realistic parameters, strategies were suggested which could lead to fibre yields more >200km per preform. In this work, interesting theoretical findings about the draw dynamics of hollow core MOFs have been put forward. The draw tension was shown to be the driving parameter controlling the microstructure, rather than peak temperature, furnace profile or preform feed rate. In addition, some variations in the ratio between surface tension and gas pressure at different points during the neck-down were identified, which could result in an initial contraction and then expansion of the core along the neck-down. If real, this potential contraction presents a limit to the minimum achievable core size. I have carried out X-ray CT analysis of the neck-down region in HC-PBGFs (presented in Chapter 4), which agrees with findings of this model and was thus crucial in providing experimental validation of the model.

2.4.3 Defect and fabrication problems (their origin and ways to eliminate them)

Defects and fabrication problems (including material and structural Imperfections) can greatly reduce the fibre yield and degrade the fibre performance either by: causing fibre breaks during the fibre draw; and/or by creating bad sections along the fibre (e.g. with high loss) which need to be identified and removed after fabrication before the remaining good sections can be used. Better still, understanding their origin and the ways to eliminate them is essential.

A number of possible causes have been discussed in the following section and section 2.6.2.5 including: geometrical defects/contamination (e.g. stack errors, organic/inorganic particles) in the

original preform, impurities or contaminants introduced during the fabrication process (also including contamination produced by chemical reaction between the glass constituents and ambient atmosphere), and noise or fluctuations in fibre drawing parameters such as the furnace temperature, preform feed and draw speed, and fluctuations in the values of pressure and/or vacuum applied to the various volumes within the preform. All have potential to introduce inhomogeneity.

These problems have been addressed in the case of conventional fibres and suitable solutions identified over the past ~40 years, a particular example of which is the standard low loss telecoms single mode fibre [59] (see section 2.6.2.5 for detailed discussion). While it is known that defects and structural imperfections and inhomogeneities can occur, very little has been presented and discussed in the literature.

2.4.4 Caveats associated with the HC-PBGF fabrication

The manual, labour-intensive fabrication process of HC-PBGFs in general is prone to fabrication errors and inclusion of foreign particles and contamination, which may adversely affect the performance of the fibres and the overall yield of the fabrication. Therefore, this process needs additional considerations and requires a controlled environment, to minimise fabrication errors. In the following, our latest developments in this regard are described and discussed in detail.

The cleanliness of glass capillaries used in the stack is of paramount importance. Any foreign particles and contamination at this stage can have a severe impact on the final fabrication stage (e.g. fibre breaks during the draw process which considerably reduce the useful yield) and on the produced fibre (e.g. structural deformations and defect that cause excessive loss and poor transmission properties, removal of which, again reduces the effective fibre length).

One should in particular pay attention to the cleanliness of the outer surface of these capillaries, three outcomes are possible for such contamination as the preform undergoes the diameter transition at the neck-down point: a variation in the strut thickness corresponding to the contaminated surface, a variation in the node size and position, and in a more severe scenario, a complete deformation of microstructure e.g. due to the contaminant boiling off and locally affecting the pressure within the holes. The latter case will be discussed in detail in Chapter 3.

In some HC-PBGF designs, the inner wall of the fibre core is in fact formed from the outer surface of the capillaries in the stack. The core surround has the highest interaction with the guided optical field and any non-uniformity, discontinuity and inconsistencies can severely affect the

fibre performance in many ways (e.g. by increasing the scattering loss, or by locally creating coupling to undesirable, high loss modes such as Surface modes and cladding modes).

As discussed earlier, the heat treatment and oxidation process of preforms and tubes may help to reduce residual contamination and stress, micro bubbles, and/or micro cracks. Such issues, in the initial glass tubes for example, can cause the capillaries to fail during the fabrication process. However, the assessment of the glass quality after these processes is down to visual inspections by expert fabricators, which may be insufficient as some of these problems may be obscure – some evidences of which I will discuss in Chapter 3, and 4. In fact, apart from the techniques available to the conventional fibre fabrication process, there is no standard routine to examine HC-PBGFs' with this regard. The conventional techniques also, are hardly produce meaningful results in the case of HC-PBGFs.

Some of the contamination sources that are hard to be picked up by visual inspections include: sub-hundred micron contaminants (including organic (e.g. from the people in the lab, and or consumables) or inorganic (e.g. ceramic particles from the cleaver and metals from burner and various tools). Some of these are not removed or are partly removed by the glass processing discussed earlier.

These can be introduced during various stages of the fabrication, manual handling and storage. For instance, particular attention is required with electrostatically induced particles, specifically in the stacking process, where glass capillaries may be electrostatically charged by manual handling. Also the repelling force between charged capillaries in the stack can lead to problems in the arrangement of capillaries which in turn may lead to broken photonic crystal structure in the final fibre that adversely affect fibre performance.

Finally yet importantly, fixing the stacked capillaries in the jacketing tube is a very delicate task. Any excessive force during the insertion of packing rods and capillaries can damage the stack and break the capillaries, which in most cases cannot be rectified, rendering the stack useless. In particular, cracks in the stacked capillaries can cause pressure leakages and consequently structural deformations.

In addition to above, another type of inhomogeneity in fibres may originate from noise or fluctuations in the fibre drawing parameters (e.g. the furnace temperature, preform feed rate, fibre draw speed, and/or the differential pressure). In fact, the fluctuation will affect the whole section of the preform that is within the hot zone and is softened. Depending on the length of hot zone, preform feed rate and the draw speed, one can estimate the length of affected preform and fibre to be, respectively:

$$L_{pa} = L_{hz} + v_p \cdot \Delta t \tag{2.3}$$

$$L_{fa} = \frac{L_{pa}}{v_p} \times v_f \tag{2.4}$$

where $L_{pa}$is the affected length of preform, $L_{fa}$is the affected length of fibre, L_{hz} is the length of hot zone and Δt is the duration of the fluctuation. As an example, a 1s spike in the furnace temperature, for the preform feed rate of 5mm/minute, hot zone length of 20mm and draw speed of 15m/minute, result in the affected preform length of ~20.1mm and the affected fibre length of 60.25m. As it can be seen, the length scale of these defects is different from the point inclusions in the preform.

In my PhD, I developed methods to identify and characterise these problems in various stage of the fibre fabrication form the first-stage preform to the final fibre and tried to explain the origin of these issues based on the knowledge of fabrication I have provided here.

2.5 HC-PBGF characterisation

The next main step following the fabrication of a fibre is measuring its optical and transmission properties such as: attenuation or loss, transmission bandwidth, modal properties, chromatic dispersion etc. As all these quantities are typically measured over medium to long sample lengths, it is also crucial to ascertain the integrity and uniformity of the fibre itself. This is particularly important for PBGFs and Hollow core fibres more in general, since, as mentioned before, their properties depend strongly on the structure. Thus, methods and techniques to ascertain the uniformity of the fibre geometry along its length are of great importance.

To be able to perform characterisation, a number of preparatory steps are generally employed. Often, in a single fibre draw, several bands of fibres with different characteristics are produced. The immediate step following the fabrication is re-spooling each fibre band neatly on another drum (usually with smaller diameter for storage/shipping efficiency). Once re-spooled, conventionally, each band is tested using an OTDR (to check its integrity and to identify if there is any significant defect), and its transmission measured using a broadband source (and its loss via the cutback technique). The applicability of both methods to the case of HC-BGFs is discussed in more detail in the following sections. However, for any measurement to be done, an essential requirement is the ability to prepare a good quality termination to be able to efficiently couple light in/out of the fibre itself. HC-PBGFs require a special attention, as often, standard fibre cleavers designed for solid fibres (such as SSMF) fail to produce good quality and/or repeatable results. In particular, preparing a flat cleave with high precision and accuracy, requires speciality

fibre cleavers, which can be fine-tuned for a particular fibre. Fibre cleavers usually do not have any control on the position of cleave along the fibre length and they (in particular, speciality fibre cleavers) tend to have a long waste length (several tens of millimetres). This is a limitation in the study of defects, which I will discuss in Chapter 3. Angle cleaving HC-PBGFs is even more challenging. Inspection of the end face (to ensure the cleave quality) is either done by splicing machines that can produce automated angle measurement, or using an optical microscope. However, if the cross section image is also needed, optical microscopy (OM) is the most time efficient solution. OM can be used either with reflected illumination (the reflected light from the surface of specimen is collected by the microscope objective lens), which is used for structural measurements (such as, fibre OD, microstructure OD, core diameter, and pitch size), or transmitted illumination (the light is coupled to the sample and then is captured by the objective lens). The latter approach can produce aesthetically striking images (see Figure 2.1 **a**) which can however provide some information about the transmission characteristics of the fibre. Often, the resolution of optical microscope is not high enough to produce accurate measurements of the size of nodes and thickness of struts, as they both are typically sub-wavelength. In this case, use of a scanning electron microscope (or similar technique) is required. I have carried out many SEM measurements, as in our group, we use SEM extensively to estimate the fibre characteristics and they are also used as inputs for modelling tools developed by my colleagues in the fibre design team. Through collecting more than 1000 SEM images, I have perfected a method that allows achieving a high contrast, yet sharp fibre images that can provide very accurate measurements of their structural features. I will discuss my SEM measurement procedure in more detail in Appendix A. Finally, yet importantly, coupling light into HC-PBGFs can present significant challenges, as excellent mode and NA matching needs to be achieved in order to obtain efficient light coupling as required for precise measurements.

Once the required preparation is achieved, a suitable characterisation approach is required to study HC-PBGFs. Many measurement techniques have been developed and standardised during the course of the development of conventional fibres, such as the cutback loss measurement and OTDR for fibre integrity testing. Although these methods have been standardised for use with conventional fibres, including telecoms single mode and multimode fibres, they are also used to investigate the characteristics of unconventional and new fibres. In the following, some of the most frequently used characterisation methods are discussed.

2.5.1 Spectral loss measurements

The cutback technique is commonly used to measure the loss of an optical fibre thorough a simple intuitive procedure [60]. The schematic of a cutback setup is shown in Figure 2.12. Light from a

source is coupled into the fibre under test (FUT) via a coupling fibre (or free space optics). The spectral bandwidth of the source can be either narrow (e.g. for a laser diode or tunable laser source) or, more commonly, wide (e.g. for an incandescent white light source, ASE source, or supercontinuum laser). Depending on the modality of the FUT at the operating wavelength (whether it is multimode or single mode), some mode conditioning may be required immediately after the input coupling point to selectively launch light in a specific mode (if the fibre can support multiple modes) or to enable an equilibrium modal distribution to be achieved [60]. For example, mode scramblers can be used to equalise power in all the modes, and/or mode filters can be used to reduce the power in higher order modes; additionally, cladding mode strippers can be used to strip out the radiation modes. Next, P_2, which is the power at the output end of the FUT after the fibre's full length, is measured using a power metre. An optical spectrum analyser is typically used when the source is broadband. Then, a length L_2 of the fibre is cut, measured from the output end, the position of which is marked with the red arrow in the figure. Afterwards, P_1, the output power after length L_1, is measured. The length L_1 should be long enough to allow the equilibrium modal distribution to be achieved. In addition, the length L_2 should be long enough to cause a meaningful difference between P_2 and P_1 measured by the power meter (i.e. $\Delta P \gg$ power meter precision). Moreover, the stability of the source and coupling conditions are of paramount importance during the course of the measurement.

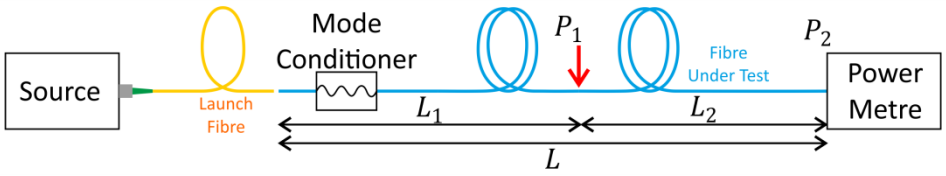

Figure 2.12: The schematic of a cutback measurement setup.

The loss of the fibre over length L_2 $(= L - L_1)$ is then obtained by:

$$\alpha_{avg} = -\frac{P_2 - P_1}{L_2 - L_1} \tag{2.5}$$

where, P_2 and P_1 are in dBm and consequently α_{avg} is in dB per unit length. From this discussion it is clear that the loss measured via the cutback method is the **average** loss (α_{avg}) over the measured length L, and the method implicitly assumes that the loss is uniformly distributed along such length which, as we will see in the following and in Chapter 3 in particular, is not always necessarily the case for HC-PBGFs. If a wideband source such as white light source or supercontinuum laser is used, one can also estimate the operating spectral **bandwidth** of the fibre using the cutback result.

The cutback method is intrinsically destructive. In addition, it is poorly applicable to field deployed optical fibres, as it requires access to both ends of a fibre length (while, for instance, OTDR only requires access to one end). Moreover, its results do not provide information about the uniformity of loss across the length of the FUT. For these scenarios, methods based on reflectometry such as optical time domain reflectometry are used.

2.5.2 Reflectometry for identification of defects

Scattering is a major contributor to the attenuation of optical fibres. Backscattered light is a fraction of the total scattered light (of different type e.g. Rayleigh or Mie from the bulk glass, or from interfaces and boundaries of the waveguide/structure), which is re-captured by the fibre, and propagates in the opposite direction of the incident light, backwards to the source.

Rayleigh scattering is an important linear effect in solid optical fibres, as it typically sets the fundamental limit for the transmission loss. It accounts for most of the loss in the conventional SMFs in the centre of silica's transmission window, as other sources of loss have been already minimized [4, 59, 61]. Backscattering in HC-PBGFs is caused by surface scattering which (incidentally) also set the minimum achievable loss in these type of fibres [12].

Backscattered light is used in optical reflectometry techniques (such as OTDR [62], optical low coherence frequency domain reflectometry (OLCR) [63] and coherent optical frequency domain reflectometry (OFDR) [64]) to analyse the longitudinal distribution of fibre attenuation, (i.e. to measure a fibre's attenuation or backscatter coefficients, or to detect and locate local reflections or fibre breaks) [60].

Each method has a different capability in terms of range (the length of fibre sample), spatial resolution, speed, sensitivity (lowest measurable reflection) and accuracy (absolute length/position measurement). The low coherence technique is typically used for sub-millimetre resolution measurements with very high sensitivity (-160dB) but only on short samples (< 5m) [65]. OTDR is used to measure much longer samples with typical range (100s of meter to several 10s of kilometres) and low sub-meter resolution. OFDR fills the gap between OTDR and OLCR with its range capabilities on the order of 10s to 100s of meters and millimetre resolution [66, 67].

In the following, I will discuss OTDR and OFDR techniques, as they are relevant to the characterisation of HC-PBGF samples that I have studied and measured in Chapter 3 and Chapter 5.

2.5.2.1 OTDR

OTDRs are nowadays standard tools for fibre characterization and have gone through years of improvement [68] since the first demonstration by Barnoski back in 1977 [62]. Several types of OTDR have emerged, however their operating principle is still the same. They all have similar signal generation techniques, but utilize different detection methods of the (weak) backscattered signal, mainly to improve the dynamic range and/or signal to noise ratio.

In optical time domain reflectometry (OTDR), a train of optical pulses is launched into the fibre under test and the time resolved trace of the backscattered power from the fibre (as a function of the light's delay in the fibre) is detected. Pulse width can vary from ~ns to several 10s or even 100s of μs. The (power vs time) trace provides the detailed local and distributed loss information along the fibre – by resolving spatial position based on the group velocity of the pulses. OTDR only needs access to one end of the fibre because the back scattered signal is picked from the same end, which is an important advantage of this technique. It is also a non-destructive technique – which is another important advantage. Rayleigh backscattering is a linear process, i.e. the magnitude of the backscattered power is linearly proportional to the optical power at that location. As such, the backscattered power gradually decreases with the same rate as the fibre attenuation coefficient.

Figure 2.13 shows a schematic diagram of a basic OTDR instrument in a measurement setup. The pulse train is generated by the source and is coupled to the fibre under test via a circulator (directional coupler). The back scattered power from the FUT is directed to a time-gated detector (photodiode). The equivalent electrical signal from the detector is sent to an oscilloscope. The time axis of the oscilloscope is synchronised by a trigger signal from the source. Typically, the trigger signal indicates the rising edge of an optical pulse. The oscilloscope waveform shows the magnitude of the backscattered power as a function of the propagation delay.

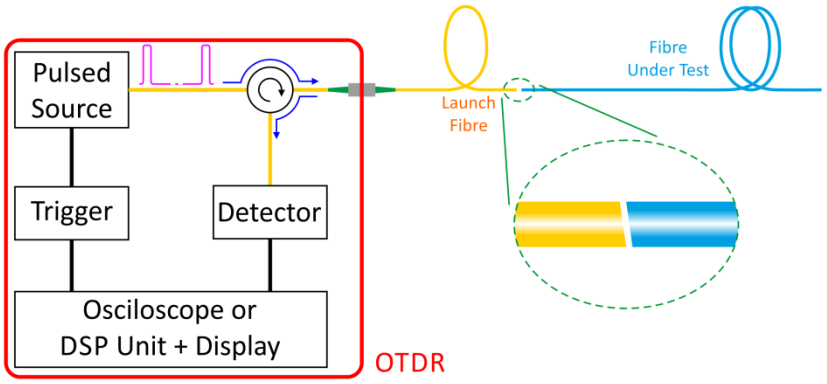

Figure 2.13: Schematic of the OTDR measurement technique.

Principle of operation of OTDR

The total attenuation coefficient of an optical fibre α (commonly expressed in dB/km) comprises two terms, the scattering loss α_s and absorption loss α_a (i.e. $\alpha=\alpha_s+\alpha_a$) [60]. The transmitted optical power I_t along the fibre can be described by:

$$I_t(z) = I_0 e^{-\alpha z} \tag{2.6}$$

with distance z from the input port and I_0 incident optical power.

The backscattered power from a forward-propagating optical pulse depends on the pulse length Δp in the fibre. The pulse length determines the fibre section that gives rise to the scattering and for the optical pulse duration τ_p, it is given by:

$$\Delta p = \frac{c_0}{n_{gr}}\,\tau_p \tag{2.7}$$

where c_0 is the vacuum speed of light and n_{gr} is the effective group refractive index of the fibre. The n_{gr} (also referred to as 'group index' or 'group velocity refractive index') is determined by the fibre properties using:

$$n_{gr} = n_{eff} - \lambda\,\frac{dn_{eff}}{d\lambda} \tag{2.8}$$

where n_{eff} is the effective index of the fibre (experienced by a given mode(s)) and λ is the vacuum wavelength. For example, this is ~1.468 for SSMF and ~1.003 for a typical 19-cell HC-PBGFs. For a narrow linewidth optical source, the pulse propagates with a constant group velocity $v_{gr} = c_0/n_{gr}$, therefore the position z of an event in the fibre that produce a backscattered power can be calculated from the total temporal delay Δt that the pulse experiences when propagating in forward and backward direction:

$$z = v_{gr} \cdot \frac{\Delta t}{2} = \frac{1}{2}\frac{c_0}{n_{gr}}\,\Delta t \tag{2.9}$$

The Rayleigh scattered power from a short section of fibre dz is:

$$dI_s = I_t(z)\,.\,\alpha_s\,.\,dz \tag{2.10}$$

The backscattered portion of this scattered power is then obtained by:

$$dI_{bs} = I_t(z)\,.\,\alpha_s\,.\,S\,.\,dz \tag{2.11}$$

where S is the recapture coefficient of the fibre, which determines the amount of scattered power captured by the fibre in backward direction. This is an important fibre characteristic, which in solid fibres depends on fibre parameters such as the numerical aperture (NA), the refractive index of the core and the wavelength [69].

The backscattered power in Equation (2.11) is attenuated in its way back to the OTDR input port. The power received at the input port is then obtained by:

$$dI_{bs} = I_t(z) \,.\, \alpha_s \,.\, S \,.\, dz \,.\, e^{-\alpha z} \tag{2.12}$$

As suggested by the following expression, the backscattered power from a pulse with pulse length Δp received at a given time at the input port corresponds to a fibre section ($\Delta z = z_2 - z_1$) equal to half of the pulse length:

$$\begin{cases} 2z_1 = v_{gr}t \\ 2z_2 = v_{gr}t + \Delta p \end{cases} \xrightarrow{yields} \Delta z = z_2 - z_1 = \frac{\Delta p}{2} \tag{2.13}$$

Therefore, the backscattered power $I_{bs}(z)$ collected at the input port generated by the optical pulse with duration τ_p can be obtained by (assuming a rectangular optical pulse):

$$I_{bs} = S\ \alpha_s\ \frac{\Delta p}{2}(\ I_0\ e^{-2\alpha z}) = \frac{1}{2} S\ \alpha_s\ \frac{c_0}{n_{gr}}\ \tau_p\ I_0\ e^{-2\alpha z} \tag{2.14}$$

The fibre loss can be estimated from the rate of change of $I_{bs}(z)$ with distance:

$$\frac{dI_{bs}(z)}{dz} = -2\alpha \cdot I_{bs}(z) \tag{2.15}$$

The total backscattered power I_{RB}, can be calculated from Equation (2.14) as follows:

$$I_{RB}(L) = \int_0^L I_{bs}(z)\frac{1}{\Delta p}dz = \frac{1}{4\alpha}\ S\ \alpha_s\ \ I_0\ (1 - e^{-2\alpha L}) \tag{2.16}$$

where L is the fibre length. This is similar to condition when fibre is filled with a continuous wave (CW) signal. For a long fibre ($\alpha L > 2$ and $\alpha \approx \alpha_s$), the total Rayleigh backscattered power is mainly determined by the capture coefficient S.

OTDR measurement parameters:

Commonly used OTDR measurement parameters are, spatial resolution, dynamic range and sensitivity, which are discussed in the following.

Spatial resolution

The spatial resolution R of an OTDR (also known as the two-point resolution), is defined as the minimum distance between two separable reflective events of equal power in a fibre, which is equal to the full-width half-maximum (FWHM) of a single reflection on a reflectometry trace. On the other hand, this is obtained theoretically by [60, 70]:

$$R = \frac{v_{gr}\,\tau_p}{2} = \frac{1}{2}\frac{c_0}{n_{gr}}\tau_p \tag{2.17}$$

This parameter is linearly reduced with further decreasing the pulse width.

Dynamic range

The total fibre length that can be analysed with an OTDR depends on the dynamic range D. In order to measure a fibre with length L and attenuation coefficient α_{dB}, the required dynamic range for OTDR measurement is determined by the roundtrip fibre attenuation over the total length, which is $\Delta P_{dB} = 2\,\alpha_{dB}\,L$. Therefore, for practical reason, the dynamic range is estimated by the difference between the initial backscatter level and the noise signal at SNR= 1.

In another definition, dynamic range is defined as the difference between the initial backscatter level and the 98% noise level [71]. This dynamic range is $\sim 1.8\mathrm{dB}$ smaller than the $\mathrm{SNR}=1$ dynamic range [60]. It is a common practice to report the dynamic range after 3 minutes of averaging and for the longest pulse length. The highest dynamic range in the best OTDRs in the market is ~50dB (for 20µs pulse width).

Sensitivity

The OTDR sensitivity is defined as the lowest detectable backscatter power (noise level) for a certain measurement time (typically three minutes or average on equivalent number of pulses) and pulse duration. For example, a receiver with a low noise-equivalent power of $\mathrm{NEP}=0.5\,pW/\sqrt{\mathrm{Hz}}$, and bandwidth of $1\mathrm{MHz}$, achieves $\mathrm{SNR}=1$ at signal optical power of $\mathrm{P_{BS}}=0.5\mathrm{nW}=$-$63\mathrm{dBm}$. One can improve the SNR by a factor of $\sqrt{\mathrm{N}}$ through averaging, where N is the number of averaged pulses [60].

Dynamic range vs resolution

The dynamic range and spatial resolution are interlinked in OTDR measurements. A short pulse for high spatial resolution measurement results in reduced backscattered power level and consequently lower dynamic range. In addition, detection of short pulses needs wide receiver bandwidth, which further degrades the SNR and therefore the dynamic range. Increasing the optical pulse power can be used to increase the initial backscatter level; however, this should be kept lower than the level at which nonlinear scatter phenomena in the fibre begin.

Other considerations

Another important quality parameter in OTDR is the “dead-zone”, which is a distance (equivalent to a time) over which the receiver recovers from a saturating event [60]. For example, the Fresnel

reflection at the fibre input terminal for a flat end facet of a conventional fibre (assuming an air ($n = 1$) silica ($n = 1.47$) interface) is approximately 3.6%, or –14.4dB. This level is several orders of magnitude above the Rayleigh backscatter level of the fibre. After the saturation, the receiver recovers its sensitivity in an exponential manner, during which the backscatter signal from fibre is superimposed by the receiver's overload behaviour. With proper time gating of the receiver, this effect is reduced [72]. Nevertheless, OTDR is one of the most popular equipment for fibre characterisation; in particular, it is extensively used to do attenuation measurement, fibre length measurement, and troubleshooting in fibre-optical systems [60].

2.5.2.2 OFDR

OFDR is based on the coherent detection of the backscattered light from a fibre under test (FUT) when the source wavelength is swept [73-75]. Figure 2.14 shows a basic OFDR setup. Briefly, in OFDRs, the beat signal generated by the interference between the backscattered light from the FUT and a fixed reference reflection (known as local oscillator reflection) is analysed, when the frequency of the light source is swept [66]. The interferometry setup is built based on a Michelson interferometer, for which the reflection at the end of one arm provides the local oscillator (LO), and the other arm is connected to the FUT. The light from a narrowband laser source enters the input arm of the Michelson interferometer, and its frequency is linearly swept. For any given scattering point in the FUT, the distance between the LO and the point is proportional to the beat frequency, the accuracy of which is largely dependent on the linearity of the sweep. The intensity of the reflection is determined by the squared amplitude of the beat signal, which in this configuration, corresponds to the electric field of the reflected light. This greatly improves the sensitivity of the measurement as compared to direct detection methods [75]. In order to match the polarization state of the reflected fields in test and reference arms (a fundamental challenge in coherent detection methods), a polarization controller is used in the reference arm. A fast Fourier transform (FFT) spectrum analyser is used to analyse the beat signal, which visualise the backscattered trace of the FUT similar to an OTDR.

Resolution

The spatial resolution, Δz, the minimum spatial separation necessary to resolve two reflective events, in an OFDR measurement, is proportional to the delay resolution $\Delta\tau$ in time domain (after the Fourier transform). It is therefore, determined by the spectral bandwidth of the scan Δf according to [64, 75]:

$$\Delta z = \frac{c_0}{2\, n_{gr}} \Delta\tau \cong \frac{c_0}{2\, n_{gr}\, \Delta f} \tag{2.18}$$

This equation determine the theoretical resolution of an OFDR measurement, however in practice, the linearity of the frequency sweep plays the most important limiting role in the resolution of the measurement[66].

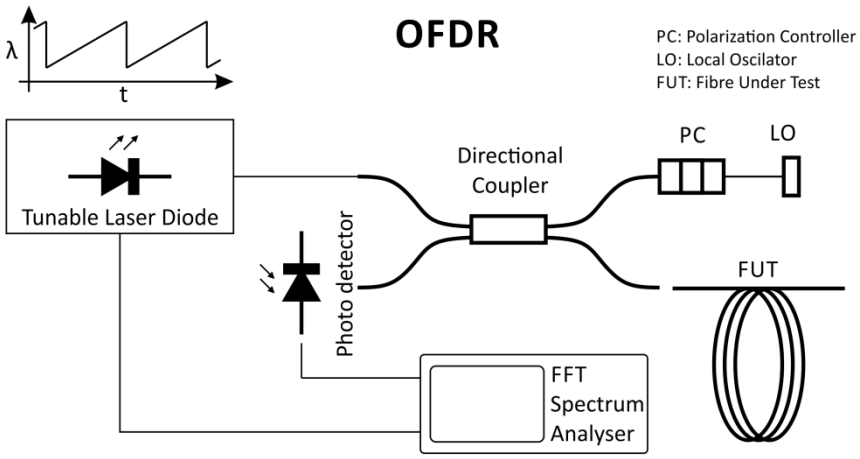

Figure 2.14: A fibre based experimental setup for OFDR measurements. Adapted from [66].

Sensitivity

Although sensitivity in OFDR should be limited by quantum noise only (since it is a coherent detection method) [66, 75], however, in practice the noise floor varies by the measurement bandwidth, so that by reducing the bandwidth the sensitivity will improve and vice versa [66]. However, for specific measurement condition (suitable scan parameters), sensitivities close to the fundamental limit has been shown [66, 76].

Several other parameters such as the intensity noise of the laser source, and the sampling jitter (linearity of the sweep) also limit the sensitivity [75-77].

Dynamic range

Dynamic range in OFDR measurements, in general is not a limiting factor for the typical measurement range it is used. The lengths of samples that are measured are usually below 100m with few examples of mm-resolution, km-length measurement demonstrated [78]. The round trip losses of these samples are therefore small and only needs dynamic range of only several dBs. For instance, the round trip loss for a 2km SSMF at 1550nm is less than 1dB. Based on the dynamic range definition that is used for OTDRs, OFDRs' dynamic range are typically in similar range as to OTDRs. Based on the dependence of dynamic range to $\mathrm{SNR}=1$ level, one expect a better dynamic range for higher sensitivities and therefore, dynamic range is also a function of scan bandwidth [66].

Other notes

As discussed earlier, typically, OFDR systems are designed for applications requiring intermediate length ranges (tens to hundreds of meters), where the spatial resolution required is not met by OTDRs. In coherent reflectometry, the length range is limited by the coherence length of the laser, which is determined by its linewidth [76]. As such, the maximum fibre length that can be measured using a coherent detection method is determined by:

$$L_{max} = \frac{L_{coh}}{2} = \frac{c_0\,\tau_{coh}}{2} = \frac{c_0}{2\,\Delta\upsilon} \tag{2.19}$$

where τ_{coh} is the coherent time and $\Delta\upsilon$ is the linewidth of a laser with rectangular spectral density.

In practice, the length range in the OFDR system discussed above, is determined by the sampling frequency (F_s) of the FFT analyser (or equivalently, the differential delay in sample acquisition τ_s) [64]:

$$L_{max} = \frac{1}{2}\cdot\frac{1}{2}\cdot\frac{c_0}{n_{gr}}\cdot\frac{1}{F_s} = \frac{c_0\,\tau_s}{4\,n_{gr}} \tag{2.20}$$

where the first and second one-over-two factors are due to the sampling theorem and the double-pass nature of the measurement interferometer.

Finally yet importantly, the choice of the scan bandwidth depends on the actual length of the FUT. For long lengths samples the bandwidth must be smaller, in order to cover all the beat frequencies under the maximum range of the FFT spectrum analyser.

2.6 HC-PBGF characteristics

So far, HC-PBGFs and their parameters have been introduced, their guidance mechanism has been discussed, their fabrication process has been explained in detail and the operation principle of some measurement techniques to characterise HC-PBGFs has been presented. In this section, the behaviour and characteristics of HC-PBGFs with respect to the light that is propagating in the core are discussed.

As introduced earlier in section 2.2.1, the core of a HC-PBGF is a defect formed by removing 7, 19 or 37 unit cells from a TLH photonic crystal. The light that is coupled into the core is confined and guided if its wavelength (frequency) and angle of incident lies within the PBG of the cladding. Otherwise, light is not confined in the structure and scatters out. In the following, the modal

characteristics and loss mechanisms of the guided light in this type of fibres are presented in detail.

2.6.1 Modality in HC-PBGFs

The modes supported by HC-PBGFs are divided into two categories, i.e. air-guided modes (or core modes) and surface modes. Most of the optical power in air-guided modes is in the core, whereas the optical power of surface modes is mainly located in the struts at the core boundary or in its close proximity.

2.6.1.1 Air-guided modes – multimode HC-PBGFs

As I will discuss in the following, the type and number of air-guided modes supported by a PBGF depends on the size and shape of the core and that of its glass boundary. Based on a modification of a method frequently employed in quantum electrodynamics to estimate the density of modes in a confined space [79], Cregan et al. [6], suggested the following expression to determine the number of guided modes in PBGFs:

$$N_{PBGF} = \frac{{R_c}^2(\beta_H^2 - \beta_L^2)}{4} \tag{2.21}$$

where β_H and β_L are the upper and lower edges of the PBG at a given λ and R_c is the core radius [6]. This has been verified by other theoretical [80, 81] and experimental studies[19]. This equation implies, the number of modes in a HC-PBGF is strongly dependent on the core radius, i.e. it scales linearly with the area of the core (${R_c}^2$). Also, it can be shown that a single cell (i.e. $R_c \sim 0.5\ \Lambda$) is insufficiently large to guide a mode in a typical HC-PBGF structure [6], whereas a typical 7-cell HC-PBGF with $R_c \sim 1.5\ \Lambda$ and a 19-cell HC-PBGF, with $R_c \sim 2.5\ \Lambda$, are expected to supports 10 to 14 and 35 to 45 modes respectively [57].

The maximum core radius supporting only a single mode however, is slightly larger than the hole-to-hole spacing (i.e., $R_c \sim 0.6\ \Lambda$) [57]. To achieve single mode operation in HC-PBGFs, core size reduction strategies have been proposed and numerically studied in [82, 83]. Single mode operation in 3-cell HC-PBGFs was experimentally reported in in [57, 83]. It is worth noting that a 4-cell HC-PBGF has been also demonstrated for high birefringence operation [84].

Although 7-cell and 19-cell HCPBGFs are multimode, this has not been a significant issue in most of their applications reported so far [6, 19]. By controlling the launch condition, their fundamental mode can be selectively excited. Also, an effective single mode operation can be obtained by exploiting the differential loss among the modes.

Figure 2.15, adapted from [57], shows the air-guided modes and their characteristics for three HC-PBGFs with different core size, i.e. 3-cell, 7-cell and 19-cell HC-PBGFs, in left, middle and right columns respectively. In particular, dispersion curves (effective index vs wavelength), confinement loss and normalised F factor vs wavelength for each air-guided mode have been plotted, in top, middle and bottom rows respectively. The microstructured cladding parameters are the same for all these structures and therefore the PBG (as shown by the black curve in the top row) is the same for all three structures. However, as discussed above, the 3-cell HC-PBGF is single-mode, the 7-cell supports 12 modes and the 19-cell core can accommodate more than 35 modes. In these plots, the curves associated with fundamental mode and the highest order mode are coloured as dark blue and dark red respectively.

Each mode crosses the PBG edges at different frequency, which indicates that the range of frequency at which a particular mode is supported is slightly different to the other modes. As such, each mode has its own bandwidth and cut-off wavelength.

In the middle row, the confinement loss (CL) for each of these modes is shown. Confinement loss will be discussed later in section 2.6.2; however, as the relative position of the curves indicates, the fundamental mode experiences the lowest CL. CL gradually increase as the order of modes raises.

The last row shows the normalised F factor, which (as I will discuss later in section 2.6.2) is used to quantifies the contribution of surface roughness in the loss of HC-PBGFs (the most significant loss factor in a uniform HC-PBGF). The F factor has a direct relationship with loss and lower F values indicate lower loss. As highlighted by the curves, the fundamental mode suffers the least from this loss and the loss gradually increases for higher order modes.

The combined effect of CL and Fshows an important characteristic of HC-PBGFs, i.e. the **differential attenuation** among the guided modes, which can be beneficial to produce effectively single mode output after certain length of light propagation in these multimode fibres. This will explain some of the observations in future chapters (in particular Chapter 5).

Unlike most conventional fibres, the output modal content of HC-PBGFs, (the presence of higher order modes and the distribution of power among the modes) cannot be easily estimated by mode quality factor (M^2) measurements, mainly due to the non-Gaussian profile of the air-guided modes [85] (see the mode profile of the fundamental mode for a 7-cell HC-PBGF in Figure 2.16 **a** and **b**). Instead, spatial and spectral (S^2) imaging technique may be used to decompose modal content in terms of their relative power, intensity distribution, and relative group delay [86], even real-time [87].

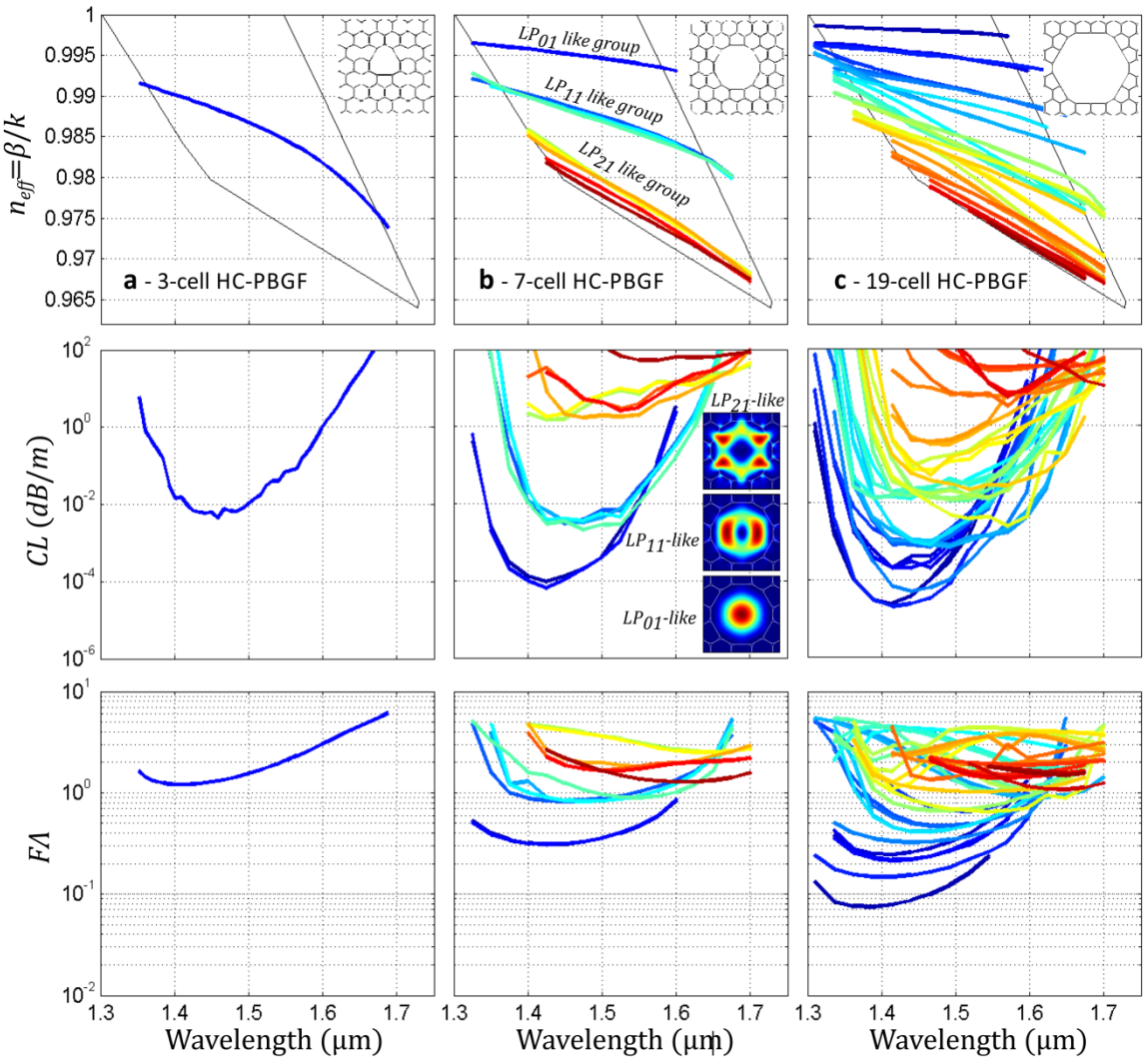

Figure 2.15: Modal properties of HC-PBGFs. Column **a**, **b** and **c** show the modal properties for a 3-cell, 7-cell and 19-cell HC-PBGFs respectively. Top, middle and bottom rows show the dispersion diagram, confinement loss and normalised F factor for the modes of each fibre, respectively. Adapted from [57].

One should also note that, the difference in effective index between the modes can be predicted to scale approximately as $\lambda^2/{R_c}^2$– in analogy to what happens in circular core hollow waveguides [88, 89]. This implies, for the larger cores, as the number of core modes increases, the difference in propagation constant of the modes decreases and the fibre becomes less resilient to perturbation-induced modal coupling (e.g. intermodal coupling due to local structural variations along the fibre); nevertheless, within the PBG, the longer wavelengths are more resilient to the same effect. In a 7-cell PBGF, under optimized launch conditions, the fraction of power being transferred from the fundamental to higher order modes has been quantified to be only a few percent after propagation through a 50m length of fibre [90].

Phase velocity and group velocity of modes

Group velocity is an important parameter in different characterisation techniques and measurements, such as OTDR, S^2 and time of flight among others.

Air-guided modes supported by the PBG have effective indices below air-line (i.e. <1). This indicates that the phase velocity of these modes is faster than the speed of light in vacuum! However, this should not be confused with the group velocity which determines the rate at which the energy of light travels (which determines the speed at which information is carried by modes). The group velocity of these modes is determined using the group index according to equations 2.22 and 2.23. The group index is slightly higher than 1, which suggests a group velocity very close to the speed of light in vacuum, i.e., $v_g \sim 0.995\ c$.

$$n_g = c\left(\frac{\partial \beta}{\partial \omega}\right) = n_{eff} + \omega \frac{\partial n_{eff}}{\partial \omega} \tag{2.22}$$

$$v_g = \frac{c}{n_g} \tag{2.23}$$

This is one of the intriguing properties of HC-PBGFs, which allows data transmission at very low latencies. This feature is in particular very advantageous for demanding high-speed data transmission in datacentres and critical telecommunications.

2.6.1.2 Surface modes

As discussed earlier, the creation of the HC-PBGF core requires a defect in the photonic crystal lattice that terminates the periodic structure. Such sudden termination at the core surround can cause spurious guided modes, similar to surface states at the semiconductor edge. These spurious guided modes, commonly referred to as surface modes (SMs, in analogy to the surface states), are localised at the interfaces between core and cladding, and often appears at wavelengths within the bandgap [27]. Another familiar example of such waves bounded between two semi-infinite systems in nature is the water surface ripples that are surface waves guided by the interface between air and water. In fact, in HC- PBGFs, SMs are confined within the core boundary struts, and decay exponentially in any direction away from the surface. Examples of SM are shown in Figure 2.16 **c** and **d** for a 7-cell HC-PBGF.

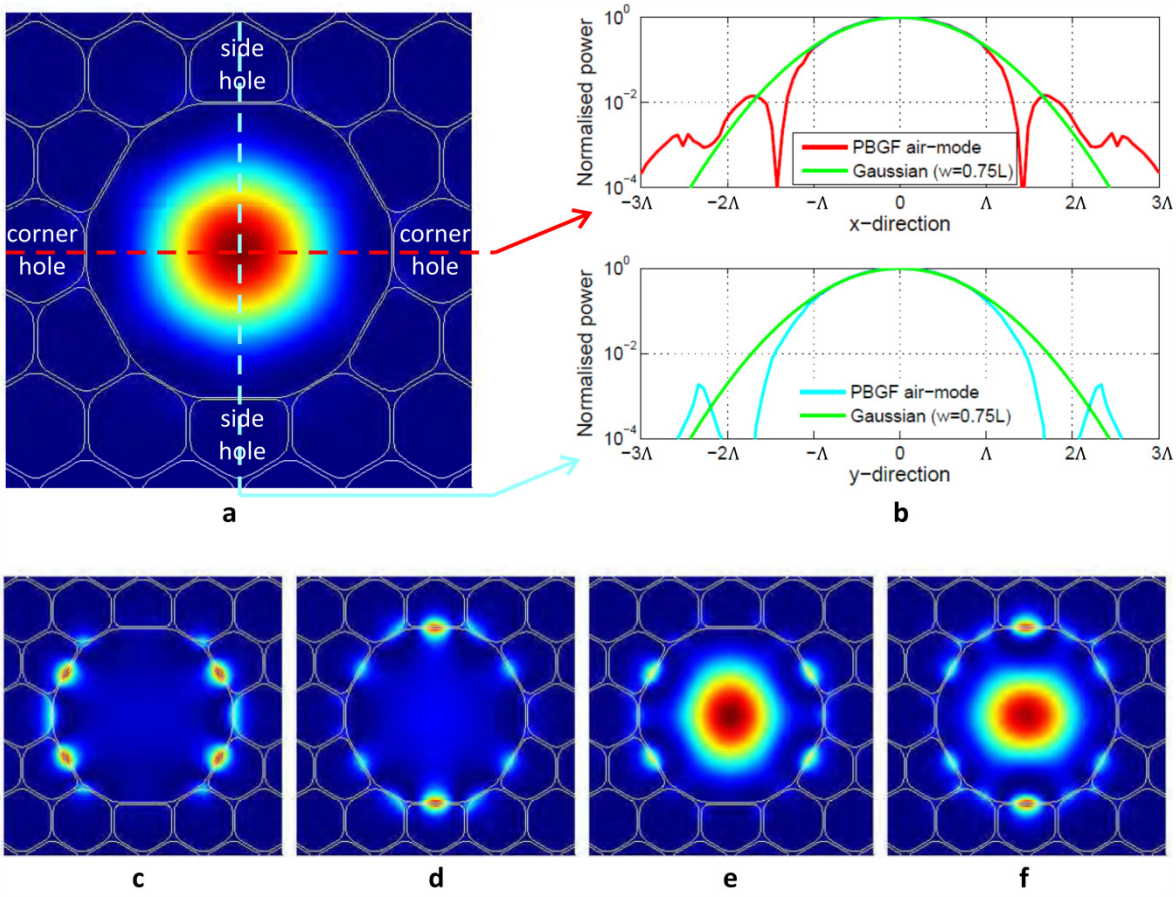

Figure 2.16: Examples of guided modes' profiles in a 7-cell HC-PBGF. **a**, Fundamental air-guided mode. **c** and **d,** Surface modes. **e** and **f**, Hybrid 'supermodes' close to the anti-crossing region between **a**-**c** and **a**-**d** respectively. **b,** A comparison between the normalised power of the FM and a Gaussian function with $1/e = 0.75\ \Lambda$. Adapted from [91].

The interaction between the SMs and air-guided modes introduces an important loss mechanism and can effectively reduce the **bandwidth**. The dispersion curve of SMs is very steep relative to the air-guided modes, which is due to the tight light confinement in the very narrow width of the silica struts. At the wavelengths where the dispersion curves (one very steep and the other nearly flat) of these two different class of modes approach together (i.e., when the SMs and air-guided modes have similar propagation constants), these modes often undergo hybridisation and form avoided crossings [92]. In other words, the system forms `supermodes' from these eigenmodes by linear combinations of the individual air-guided and surface modes, two examples of which are shown in Figure 2.16 **d** and **e**. Because of the energy transfer between air-guided modes, SMs and lossy cladding modes in the close proximity of these avoided crossings, air-guided modes suffer from additional loss [92-95]. As a result of these modal interactions, Lorentzian-like peaks in the fibre transmission spectrum appear that can severely limit the fibre's transmission **bandwidth** [11, 96]. Additionally, numerical and experimental studies revealed other detrimental consequences

of these SM anti-crossings such as increased sensitivity to external perturbations as a result of high polarisation dependent loss [17] and strong polarisation mode coupling [90].

Because of the potential severe effects of the SMs on HC-PBGFs performance, a number of studies have been explored strategies to minimise the impact of SMs through appropriate terminations of the photonic crystal at the core surround [82, 97, 98]. Fibre designs that could potentially eliminate surface modes were proposed [82, 94], which for example require challenging-to-fabricate protrusions into the core.

In other studies [18, 99, 100], the number of SMs and their wavelength position relative to the centre of the bandgap have been shown to be largely determined by the thickness of the silica ring, which defines the core boundary. It was reported that a surface mode free regime can be achieved for core wall thickness between 0.45 and 0.65 times the thickness of the cladding struts [18]. A core wall thickness of ~0.5 times the thickness of the cladding struts is an achievable fabrication target. This criterion was used in [99] and led to the fabrication of a surface mode free HC-PBGF. Moreover, control of surface mode position within the PBG has been demonstrated by reducing the core wall of the fibre using hydrofluoric acid etching post fabrication [101]. Yet, this technique is currently only suitable for short fibre samples and therefore is not applicable for treating the long length HC-PBGFs.

2.6.2 Loss mechanisms in HC-PBGFs

The total attenuation of a HC-PBGF can be described by the expression:

$$\alpha = \eta\left(\frac{A(\lambda)}{\lambda^4} + C_1 e^{\frac{C_2}{\lambda}} + D_1 e^{\frac{-D_2}{\lambda}} + E(\lambda)\right) + F\left(\frac{H(\lambda)}{\lambda^3} + E\acute{(}\lambda)\right) + B(\lambda) + G(\lambda) + Z(\lambda). \quad (2.24)$$

In this expression, η describes the fraction of the core-guided mode, which propagates in the silica regions of the photonic crystal cladding [102]. This fraction, typically 1-3% depending on fibre design, defines the magnitude of the contribution of bulk-glass attenuation-effects to the overall fibre loss. The first term in the left hand side bracket describes the Rayleigh scattering loss, followed by terms describing the "electronic" and IR absorption edges respectively, while the final term represents the total (scattering plus absorption) loss due to impurities within the glass. The F factor is a relative measure of the overlap of the optical field intensity of a particular mode with the silica/air interfaces within the fibre [12]. This factor quantifies the contribution of surface roughness and surface impurity absorption and scattering to the total fibre loss, which are the first and second terms in the second bracket respectively. $B(\lambda)$ describes waveguide imperfection loss and the penultimate term on the right hand side represents the confinement

loss. The final term, $Z(\lambda)$, represent the contribution of micro-bend induced loss. Amongst these terms, the middle bracket is the most important contribution to the loss.

It is to be noted that the Equation (2.24) assumes the HC-PBGF core/holes filled with a lossless medium, while real fibres are filled with air or other gas. For the purpose of this discussion I will assume the HC-PBGF is filled with a non-absorbing gas species (nitrogen is a good example at near-IR wavelengths). Every gas species also has a Rayleigh scattering component, which however is found to be typically very small (e.g. the Rayleigh scattering coefficient of air is $4.8\times10^{-3}\mathrm{dB/km/\mu m^4}$ which compares with $0.6\mathrm{dB/km/\mu m^4}$ for pure silica glass) and thus is neglected from the following discussion.

In the following sections, after first discussing in more detail the mode overlap η and the F factors, the "conventional" loss mechanisms are discussed, some of which are also common to all-solid fibres. Subsequently, loss mechanisms, such as the confinement loss and surface scattering are discussed, which are more specific to photonic bandgap fibres.

2.6.2.1 F factor and η

As mentioned above, reduction of both the F factor and mode overlap factor (η) will reduce the overall fibre attenuation. For a HC-PBGF with a TLH cladding (as shown in Figure 2.17), a range of values for the mode overlap η have been reported, spanning from 0.12 [103] to 0.8% [95]. It is noteworthy that broadband guiding hollow core Kagome fibres have a much lower modal overlap with the microstructure of 0.01% [104], implying that a large reduction in this parameter is possible.

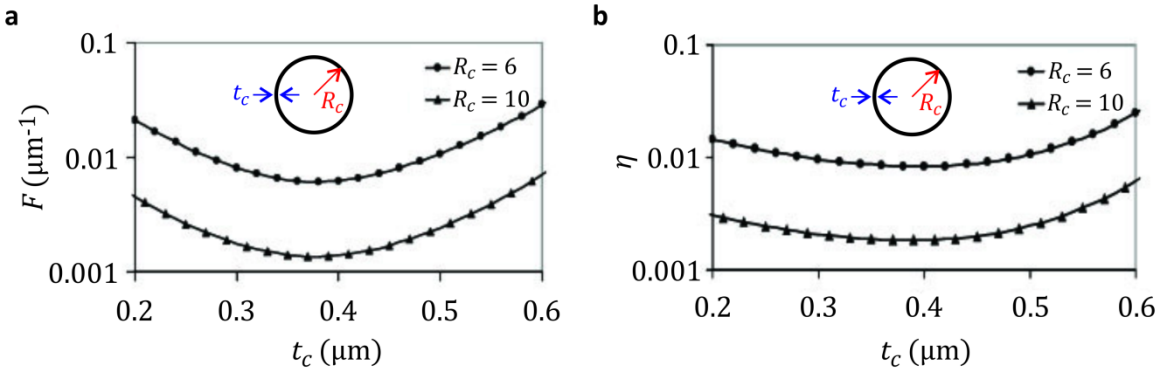

Figure 2.17: F factor and mode overlap factor, η, as a function of core wall thickness, t_c. The calculation is for a theoretical structure consisting of the core wall surround only. The signature of anti-resonance is the minimum in both these parameters for a wall thickness of ~ 0.4μm. Adapted from reference [103].

The key difference between the reported values for the TLH cladding structure is that the lowest mode overlap has been reported for a HC-PBGF designed with an anti-resonant core surround. This fibre design expels the optical field from the glass core wall, and it was used by Roberts et al. [12] to fabricate the lowest loss HC-PBGF reported so far. Using this design, the same authors, aiming at low loss at 1550nm, fabricated a fibre with a core wall surround with a thickness of ~0.4μm [103]. This thickness, t, was calculated by considering the transverse anti-resonance condition [23],

$$t_c = \frac{\lambda}{4 \times \sqrt{{n_g}^2 - 1}}(2n - 1) \tag{2.25}$$

where λ is the operating wavelength, n_g is the refractive index of silica and n is an integer. The reduction in both the F factor and η achieved using an anti-resonant core wall surround are highlighted by the results shown in Figure 2.17 [103], where these parameters are plotted as a function of core wall thickness. Note that these results are calculated for a theoretical structure consisting of the core wall surround only. The attenuation spectrum for the anti-resonant core surround fibre is shown in Figure 2.18 [23] and indicates the record minimum attenuation of 1.2dB/km. However, an important feature to note with this spectrum is the limited **bandwidth** of the low loss transmission window (~20nm centred at 1565nm); this is a result of surface modes being supported by the anti-resonant core surround design within the spectral **bandwidth** of the PBG. It is preferable to seek alternative methods to reduce both the F factor and η, as surface modes' interaction with core-guided modes can be inhibited by both reduced F and η. In [23], interesting designs are suggested which lead to reduced F factor and η. In [105], Mangan et al. report fabrication of one such design with anti-resonant elliptical nodes on six of the twelve struts which form the core wall. Through this approach, they achieve a record low loss for a 7-cell HC-PBGF of 9.3dB/km at 1585nm. Although there is still spectral evidence of surface modes in the fibre transmission, the useable bandwidth is increased to over 100nm.

A simple alternative to an anti-resonant core surround is to increase the core radius. The effect of core radius increase on the F factor and η is also shown in Figure 2.17.

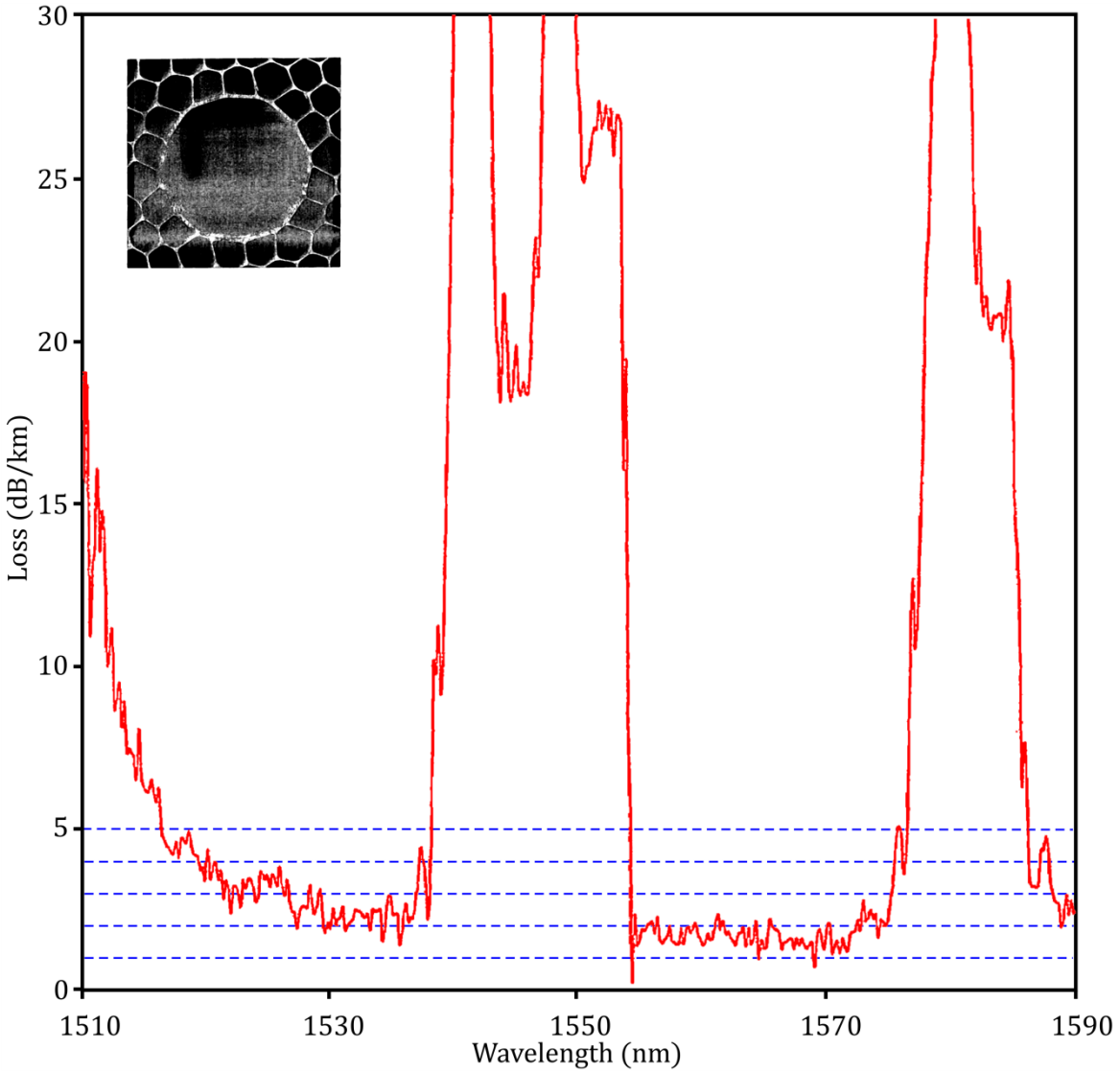

Figure 2.18: Attenuation spectrum of the record low loss 19-cell HC-PBGF (inset: SEM image of the core surround). Transmission bandwidth of the fibre is effectively reduced because of the interaction of core guided modes with surface modes. Adapted from [23].

2.6.2.2 Rayleigh scattering

As mentioned above, the contribution from bulk glass loss mechanisms to the total loss of a HC-PBGF is defined by the mode overlap factor with the microstructured region, η. Rayleigh scattering is one such mechanism and arises from local density (and thus, refractive index) fluctuations in pure silica glass which are frozen in as the glass cools below the glass transition temperature, T_g. This form of scattering is the dominant source of loss in conventional, all-solid fibres and therefore a wealth of literature exists which describes this loss mechanism and possible means to reduce it. The Rayleigh scattering coefficient, A, can be described by the expression [106]

$$A = (5 \times 10^{-18})\, n_0\, p^2\, K_T(T_f)\, T_f \tag{2.26}$$

where n_0 is the linear refractive index, p is the angularly averaged photoelastic constant and $K_T(T_f)$ is the isothermal compressibility. T_f, denotes the fictive temperature, which is defined as the temperature at which the glass structure is frozen in when the glass is cooled through the glass transition [107].

2.6.2.3 Bulk glass absorption: UV and IR

At telecommunications wavelengths the main absorption loss of silica glass is due to the IR absorption edge. This absorption is a contribution of multi-phonon absorption and the vibrational modes of the glass network. The presence of hydroxyl groups in different bonding sites can also act to increase the absorption coefficient of some of these phonon modes. Doping silica with different compounds can modify the energy/strength of the main phononic absorption bands, thus shifting the IR absorption edge to shorter or longer wavelengths. Particular dopants to avoid, which increase absorption at telecommunications wavelengths, are B_2O_3, BeO, Li_2O and P_2O_5 [106]. Fluoride glasses have been investigated as these have a longer wavelength IR absorption edge than pure silica, which in principle opens up the possibility of wider transmission windows leading to lower minimum loss. However, crystallisation issues in fluoride glass fibres have limited their practical loss and furthermore their lower environmental stability as compared to silica glass, which inhibits their use for long-distance transmission fibres [108].

At the short wavelength end the transmission window of silica is limited by electronic absorption, which gives rise to the UV absorption edge, also known as the Urbach edge [109]. In pure silica electronic absorption is the dominant loss mechanism for wavelengths below 400nm but it decreases exponentially with increasing wavelength and becomes almost completely negligible at telecommunications wavelengths, although a measurable effect is reported in detail by Pederson et al. in [110]. The position of the UV edge can be shifted to shorter wavelengths by fluorine doping due to reduction in structural disorder [111]. However, the minimal effects of this absorption edge at telecommunications wavelengths, combined with the fact that in HC-PBGF, the majority of core-guided modes propagate in air, renders this contribution to the loss of HC-PBGF negligible.

2.6.2.4 Imperfection loss

Imperfection loss generally arises from inhomogeneities in the fibre structure, which can cause local scattering and can favour coupling from a low loss core guided mode to a lossier mode, e.g. a cladding mode or a surface mode. According to couple mode theory, if the surface micro-deformations/roughness, satisfy the phase matching condition ($L_{Bragg} = 2\pi/\Delta\beta$), and the mode

field overlap integral $\iint \psi_{lm}\phi_{l'm'} \cdot ds$ is nonzero, then a strong wavelength dependent power transfer between modes happen. The source of these inhomogeneities could be:

- geometrical defects in the original preform;
- impurities or contaminants introduced during the fabrication process;
- noise or fluctuations in fibre drawing parameters such as the furnace temperature, preform feed and draw speed. Additionally, in the HC-PBGF fabrication process, fluctuations in the values of pressure and/or vacuum applied to the various volumes within the preform has also potential to introduce inhomogeneities.

In my PhD, I have tried to identify, detect and study these issues – for example by detecting their scattering signature (as will be discussed in chapter 3 and 5) or through other visualizing techniques like X-ray computed tomography (as will be shown in chapter 4).

In HC-PBGF fabrication, the stacking process can introduce contamination, scratches and defects, which weaken the glass capillaries and can also increase surface roughness.

In order to reduce the roughness, polishing and etching techniques can be applied [112]. These techniques were used, along with dehydration processes, in the fabrication of the lowest loss index guiding microstructured fibre reported so far (0.18dB/km [113]).

In solid core fibres, imperfection loss is also referred to as 'anomalous' loss. In [61], Ohashi et al., attribute this loss to residual stress in the fibre core. In [114], the same authors reduce this loss by viscosity-matching the core and cladding components; two different dopants are used which have different effects on the host material viscosity. These authors also report that at higher tension, residual stress on the core is reduced and imperfection loss is reduced. These strategies, in particular the latter, are applicable to HC-PBGFs.

In [115], reduction of imperfection loss in solid core photonic crystal fibres is achieved using chlorine-doped silica capillaries in the stack. This reduces the viscosity of the core and microstructured cladding regions compared to that of the outer cladding and thus reduces residual stress on the core and the associated imperfection loss. This technique should be transferrable to HC-PBGF. However, the use of chlorine again may be detrimental due to reports of outgassing and also its effect on surface tension (see section 2.6.2.6).

Impurities

In HC-PBGFs, the presence of impurities in the final fibre product can be attributed to:

- impurities, which were present e.g. in the initial glass tube used to form the capillary elements then used in the stacking process and/or
- contaminants, which absorb into and adsorb on the glass during the various stages of the fibre fabrication process.

The large silica/air surface area in HC-PBGFs, combined with the multistage fabrication process, which is partly reliant on manual handling, increases the opportunity for the introduction of impurities through adsorption to the silica surface. Furthermore, cleaning processes during the fabrication process may be difficult or inhibited due to the geometry of the capillaries, canes and the final fibre product. These impurities increase the final fibre attenuation through both scattering and absorption from the silica surface and, arguably to a smaller extent, from the bulk glass. Again, the specific contaminants to avoid depend on the operating wavelength but the hydroxyl is always an issue due to the multitude of fundamental and overtone hydroxyl (OH) absorption bands distributed throughout the visible and near IR spectral regions [116]. At an operating wavelength of 2µm, specific contaminants, which may cause excess absorption, are also absorbing gas species such as carbon mono- and dioxide, hydrogen fluoride and chlorine [117].

Contamination can be avoided to a certain extent by minimising glass handling and processing time. Gris-Sánchez et al. [118] designed and carried out a study on the effect of processing time on the various absorption features of pure silica fibre using a simple solid core PCF (Figure 2.19 inset). Figure 2.19 [118] compares the attenuation of three fibres, drawn 3 hours, 18 hours and 7 days after cane fabrication. From this data, it is clear that even reasonably short delays in processing from cane to fibre lead to increased loss in several spectral regions. The absorption bands at 630nm and 900nm were first analysed by Kaiser [119] and attributed to larger OH content and fibre drawing conditions. The absorption bands centred at 1240nm and 1385nm have been previously identified as due to an OH overtone combination band with a fundamental silica absorption and the first OH stretching overtone respectively [116]. The increase in attenuation in all these regions is indicative of OH contamination due to processing delay. In [118], the authors identify the source of the broad attenuation around 900nm to be damage to the silica matrix induced by a processing delay. This work highlights the necessity for either fast processing and/or suitable storage during processing delays in an OH free atmosphere when fabricating PCF.

Reduction of absorption loss in optical fibres due to OH ions has been reported extensively in the literature. Most recently, record low attenuation in solid core photonic crystal fibre (0.18dB/km [113]) was reported and partially attributed to reduction of OH through a combination of contamination avoidance and careful cleaning [113, 120]. Figure 2.20 [112] compares a standard solid core PCF attenuation spectrum ($d/\Lambda = 0.5$) with a fibre with exactly the same physical

structure that had been fabricated using the OH reduction procedure. The reduction of OH starts from the initial choice of glass, which in this case was high purity silica made using the vapour axial deposition (VAD) technique. The authors report that the choice of VAD glass limits the peak OH absorption to a very low value of less than 0.2dB/km in the final fibre [112]. Additional dehydration is then carried out on the capillary elements used in the stack and the stack is also assembled in an OH free environment. At the end, the final fibre is drawn in a dry atmosphere by purging with an inert gas during the fabrication process. Through this thorough process the OH peak absorption was reduced substantially, from 15dB/km to 0.4dB/km at 1380nm.

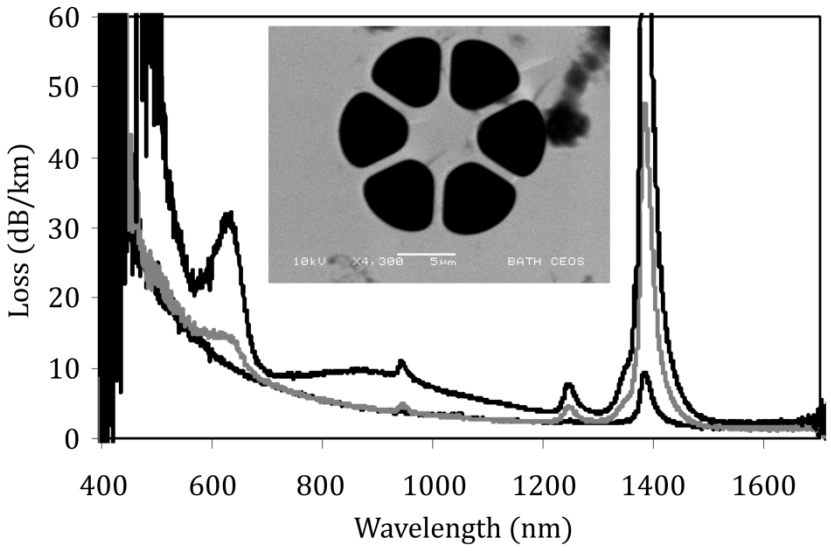

Figure 2.19: Attenuation spectra of 3 fibres with same physical structure (shown inset) but drawn from cane after different time delays: 3 hours, 18 hours and 7 days (from bottom to top). Adapted from [118].

This work is highly relevant to the reduction of loss in HC-PBGF, not only in order to reduce absorption and scattering from the bulk glass but also, very importantly, due to the effect of surface hydroxyl (in the form of silanol groups) on the **surface tension** of silica. This is discussed in more detail in the following section.

A final note, specifically on OH absorption in fibres, is that there is an extensive body of work which describes methods and results of deuteration of silica (e.g. [121] for a review). Through this technique OH are substituted by deuteroxyl groups, which have absorption features shifted to longer wavelengths compared to the same modes of OH. For example, in deuterated fibre, the first overtone OH stretch at 1380nm is significantly repressed and instead there is a signature of the deuteroxyl first overtone stretch at ~1860nm. Although, the deuteration process opens up an almost OH absorption free absorption region between 1300 and 1600nm, for low loss HC-PBGF

where the aforementioned effect of hydroxyl on surface tension is also important, the effect of the deuteroxyl groups on surface tension would have to be considered.

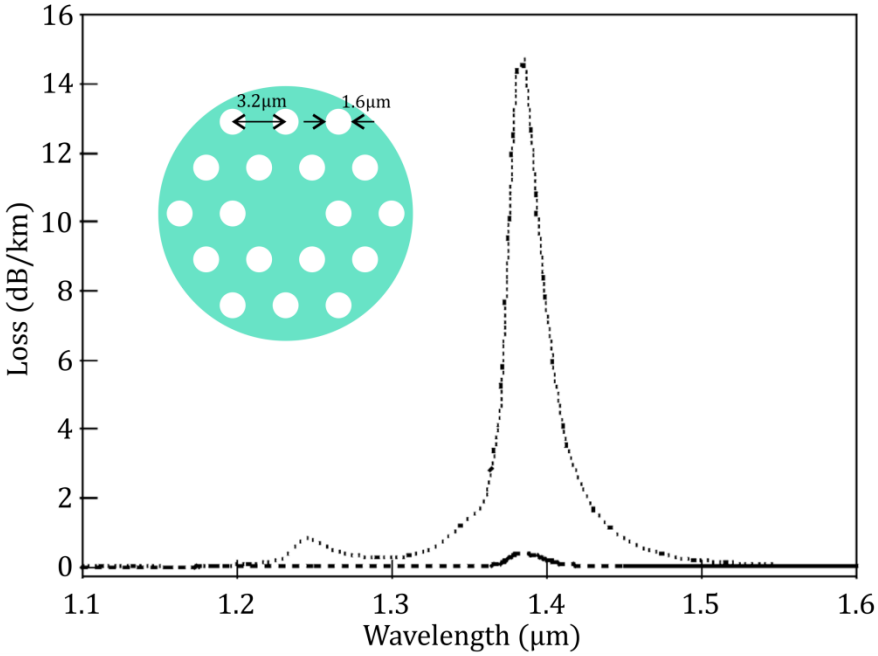

Figure 2.20: Attenuation spectra of two solid core PCFs: without dehydration processes (dotted line) and with dehydration process (dashed line). Adapted from reference [112].

2.6.2.5 Confinement loss

Confinement loss (also known as leakage loss) of HC-PBGF describes the loss due to light escaping from the core-guided modes through the cladding structure via tunnelling[122]. Addition of more rings to the cladding structure increases confinement and therefore reduces this form of loss [123]. However, as the guided core mode decays exponentially into the cladding structure, addition of each subsequent ring has a much-reduced effect relative to the previous ring. The lowest loss HC-PCF reported so far, had seven complete cladding rings [12], and structures with eight rings have also been fabricated [19]. A structure with more rings increases the complexity and processing time of the fabrication process and the potential for defects and problems in the draw. It may be informative to point out that in a suitably designed HC-PBGF with six ring structure and high air-filling factor (>96%) the confinement loss can be significantly lower than other contributions to loss [24].

2.6.2.6 Surface Roughness Scattering

As mentioned above, one unique feature of a PCF, as compared to a conventional all-solid fibre, is the large amount of silica surface area present due to the microstructure of the fibre. In [12],

Roberts *et al*. report that the ultimate loss limit of HC-PBGF is associated with the roughness of these surfaces. This roughness is defined by thermal surface capillary waves (SCWs) [124] which are frozen into the glass surface as it is cooled below the glass transition temperature.

Evidence for the SCW loss mechanism

In [12] the authors introduce a statistical spectral density, $S_z(\kappa)$, which describes the mean square amplitude of the roughness components ascribed to SCWs, with spatial frequencies between κ and $\kappa + d\kappa$ along the fibre. This is quantised by considering the finite perimeter, W, of a given hole, and then expressed as,

$$S_z(\kappa) = \frac{k_B\, T_g}{4\pi\, \gamma\, \kappa} \coth\left(\frac{\kappa\, W}{2}\right) \tag{2.27}$$

where k_B is the Boltzmann constant and γ is the surface tension.

Roberts *et al*. [12] present three experiments which support the SCW hypothesis. Firstly, measurements of the loss of state-of-the-art HC-PBGF show that the minimum loss of HC-PBGFs designed for operation at different operating wavelengths scales with $1/\lambda^3$ where λ is the operating wavelength. This differs with the $1/\lambda^4$ loss dependence observed in conventional all-solid fibres, which is due to Rayleigh scattering. In HC-PBGFs, **surface roughness provides an additional loss mechanism by weakly coupling guided core modes to lossy cladding modes at wavelengths within the bandgap**. By considering such mode coupling-induced loss, it is found that the $1/\lambda^3$ scaling of the minimum loss is consistent with the hypothesis of roughness due to SCWs being the dominant loss source [12].

Secondly, atomic force microscope (AFM) measurements of the inner surface profile of holes from the microstructured fibre revealed height profiles from which $S_z(\kappa)$ was calculated. By fitting Equation (2.27) to this data, a value of $1\ \mathrm{J/m^2}$ for the surface tension was derived. This is in reasonable agreement with the published value of $0.3\ \mathrm{J/m^2}$ [125], especially considering the dehydration steps in the fibre fabrication process which reduce the silanol groups on the glass surface and therefore act to increase the surface tension [126]. In fact, the theoretical value for a silanol-free silica surface is $5.2\ \mathrm{J/m^2}$ [125], which highlights a means for further increase in the surface tension if improved dehydration is employed in the fabrication process. Here it is noteworthy that, in [127], AFM measurements of cladding holes of a solid core PCF are reported and compared to the surface roughness of the exterior surface of the fibre. Their surface analysis does not agree with roughness from the intrinsic thermodynamic limit and they suggest that a new and undefined phenomenon is occurring within cladding holes that is not necessarily related to the draw conditions because the external surface of the fibre was found to be much smoother.

We recently managed to perform non-destructive measurement of the surface roughness of the core surround in a 37-cell HC-PBGF [128]. Our findings agree with the suggested spectral densities at high spatial frequencies ($>10^{-2}\mu m^{-1}$), however, below $5\times10^{-2}\mu m^{-1}$, our measurements suggest a much steeper change in spectral density, which may account for an important part of the optical loss in HC-PBGFs .

A third experiment in support of SCW induced loss and reported in [12, 129] is the integration of angular scattering measurements from a small uncoated section of the low loss HC-PBGF. These implied a scattering loss, which was in good agreement with the total fibre attenuation, indicating that indeed the main source of fibre loss is from a scattering and not an absorption mechanism. Furthermore, the bandgap signature is observed as expected at an effective index of 1, indicating negligible tunnelling loss directly from the fundamental mode. This further supports a scattering loss mechanism through which light from the fundamental mode is coupled into core and cladding modes that have higher loss. Finally, away from the bandgap, the authors in [12] find an excellent fit proportional to $F/|n-n_0|$, which is also in agreement with the SCW loss mechanism.

2.6.3 Best window of operation

The wavelength dependence of the SCW induced scattering loss mentioned above provides a means to reduce the effect of SCW scattering without actually reducing the magnitude of the roughness; it is favourable to shift the central transmission wavelength of the PBG to longer wavelengths. This is limited as far as $\sim2\mu m$ due to the trade off with the IR absorption edge. However, by shifting the central wavelength from $1.55\mu m$ to $2\mu m$ the fibre attenuation is reduced by a factor of ~2.1.

2.7 Conclusion

In this chapter, I have presented a selection of background material concerning the properties of HC-PBGFs and relevant to the main body of my experimental activity, which will be described in the following chapters. In particular, I provided a description of HC-PBGFs and of their basic properties, defined their main structural parameters, which was followed by a discussion on the latest achievements in this research area. I reviewed the principles of guidance in these fibres, which is based on a PBG formed by the glass nodes and struts present in their microstructured cladding. Two views to the formation of PBG was discussed, photonic crystal and resonator models, which both are useful in understanding the importance of structural parameters in the formation of PBG and consequently guiding properties of HC-PBGFs. Then, described the

fabrication process of HC-PBGFs in detail, in order to illustrate the challenges characterising the practical realisation of the complex microstructure providing the PBG in an HC-PBGFs. This section also highlights the potential pitfalls that may lead to a compromised performance of HC-PBGFs. Some of these fabrication problems (e.g. origin of “point” defects along the fibre), their detection and identification of suitable routes for their removal constitute one of the main topic of this thesis. Conventional characterisation methods that are used to measure the fibre performance (e.g., cutback loss and OTDR measurements) were also discussed. These techniques are of particular interest here as they characterise optical loss and the fibre integrity, which are closely related to the focus of this thesis i.e. the effect of defects in the fibre performance. These methods and their result are often discussed throughout this thesis and have shortcomings when it comes to the measurement of HC-PBGFs, which will be discussed in their relevant chapters. At the end, the characteristics and performance of HC-PBGFs were discussed in, with particular emphasis on the fibre modality and the mechanisms underpinning the optical loss in these fibres. In specific, I discussed the loss due to imperfections and surface scattering near the end as these discussions are immediately relevant to the ideas and discussion in the coming chapters. This chapter should have provided the necessary information for my research and activities that I will discuss in the following chapters. Once again, the objective of all of these discussions is to identify, and characterise possible difficulties that limit the optical loss and fabricated length of HC-PBGFs.

Chapter 3: Defect analysis

3.1 Overview

Imperfections and structural deformations, which I broadly refer to as 'defects', in optical fibres in general, affect the fibre performance by inducing additional loss and modal coupling. The additional loss limits the reach of the fibre and in the case of multimode fibres, the modal coupling causes interference and increased noise levels at the detector. Moreover, defects can be structurally weak points with increased chance of fibre breaks and cuts. Finding the position and the scale of these features along the fibre is important, as it allows identification of uniform defect-free lengths and accurate measurement of the fibre characteristics. Additionally, it allows investigating the origin of problems and ways to eliminate them. Conventional methods and systems for the detection of these events in the fibre, such as OTDRs and OFDRs, have limitations that make them rather ineffective, especially when it comes to unconventional hollow core fibres like HC-PBGFs. In this chapter, I present a method to identify and study the imperfections in HC-PBGFs that has better local resolution and sensitivity in finding the defects, and that allows one to obtain unparalleled information about their properties. Preliminary findings reported in this chapter have been presented at the Optical Fiber Communication Conference (OFC) 2014.

3.2 Background

Defects and unwanted structural variations in HC-PBGFs are not a frequent subject of discussion in the literature. This might be partly due to the immaturity of HC-PBGFs' technology as well as the very few reports of the fabrication of km-scale low loss fibre lengths to date. As discussed in Section 2.4, HC-PBGFs are fabricated via a two-stage fabrication technique, in which accurate control of pressure and other draw parameters is paramount to obtain a long length of a consistent fibre. Benabid *et al* in [130] briefly discussed some of the challenges in preserving structural integrity that may lead to distortions in the cladding structure of HC-PBGFs (with some pictorial examples). Such challenges have been also observed in other microstructured fibre types [131]. Such distortions are usually due to undesired variation of some draw parameter such as draw speed, core and cladding pressure and temperature of the furnace, some of which can be addressed by careful modifications of the fabrication methods and adjustment of the control parameters.

In contrast, occasionally, I observed local defects in HC-PBGFs, which unlike the former type, happen suddenly within the regular structure of the fibre and disappear quickly after a short

length. Such sudden longitudinal changes of this type in principle may arise due to (i) the presence of some inhomogeneity in the original cane, and/or (ii) the existence of contamination in the cane, such as dust, organic or non-organic particles and impurities. These two broad categories are expected to have widely different length scales in the fabrication and consequently different signature in the final fibre. The former category may induce changes that affect the fibre over long lengths and in many cases extends end to end. The latter is characterized by potentially very short length scales.

The short length scale defects, to the best of my knowledge, have not been a subject of discussion or studies in the HC-PBGF literature prior to this work. Here I present the first systematic study of defects in HC-PBGFs aimed at identifying their origin and possible ways to eliminate them. I examined a large number and variety of defects in HC-PBGFs using both OTDR and direct imaging techniques to study their morphology and longitudinal characteristics.

3.3 Methods and results

Any sudden, non-adiabatic change in the structure of a fibre will in general cause some local light scattering, which can be detected by backscattered light in an OTDR measurements or by direct detection of side scattered intensity e.g. using an infrared (IR) camera. As discussed in Chapter 2, Optical time domain reflectometry (OTDR) is commonly used to study longitudinal variations and defects in conventional fibres. It has also been used to characterize HC-PBGFs [132]. The OTDR trace in Figure 3.1 **a** is an example of a good quality, low loss HC-PBGF. Figure 3.1 **b** shows, for illustration purposes, an example of a particularly 'bad' fibre, where several spikes due to back scattering from structural defects can be seen. Clearly, such defects have the potential to introduce undesirable loss and intermodal power coupling, so a detailed investigation of their origin and characteristics is extremely important.

While in principle both OTDR and/or IR camera can be used to locate the coarse position of a defect, in practice OTDR measurements have a minimum spatial resolution that is poorly suited for short-scale variations or for accurately pinpointing the onset of a defect. This is illustrated in Figure 3.1 **c**, which shows the OTDR trace of a 280m long, 19-cell HC-PBGF operating at the wavelength of ~1.5µm. The trace includes a single reflection peak at L=125m. On the other hand, I developed a camera inspection method that works according to the diagram in Figure 3.2 **a**. The fibre is wound on a (white) polystyrene bobbin in a single layer, and light at the operating wavelength of the fibre (~1.5µm in this case) is coupled into one end. The inset of Figure 3.1 **c** shows an image of the same fibre acquired with an InGaAs IR camera.

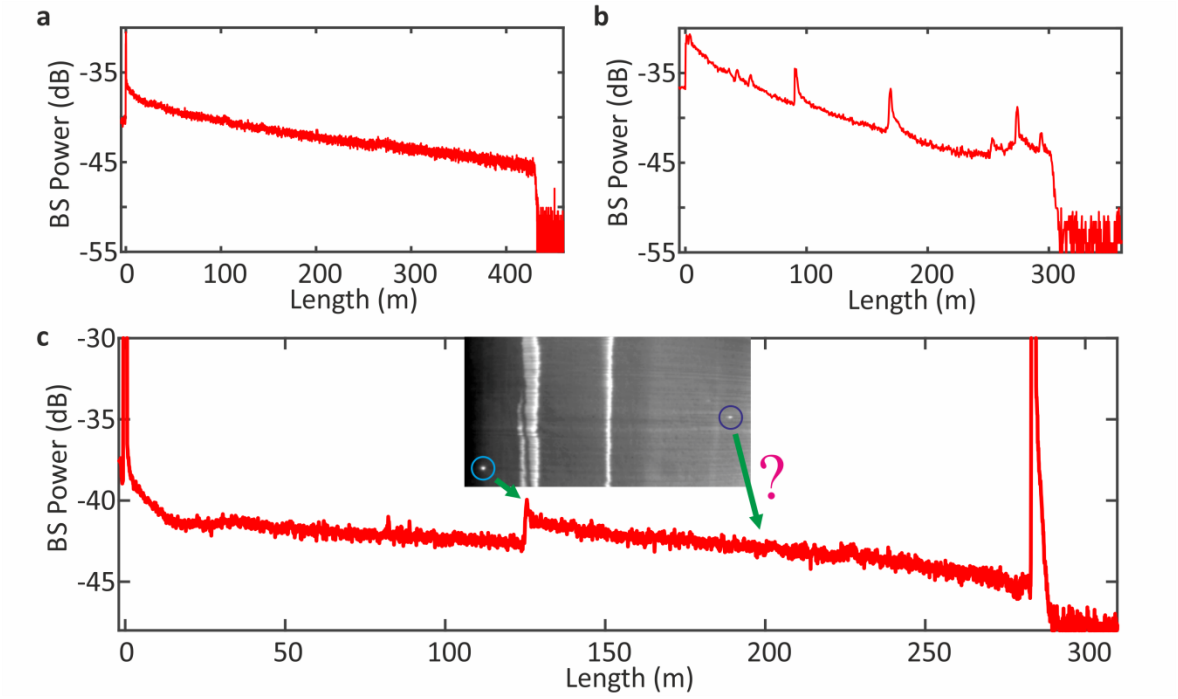

Figure 3.1: Conventional inspection of the integrity of optical fibres. **a** and **b**, Examples of OTDR traces of a good and a defective fibre, respectively. **c**, The OTDR trace of a fibre with two defects. The inset shows an image of the fibre spool captured by an IR camera while light is coupled to the fibre. It shows two discrete scattering points, the position of one of which corresponds to an event in the OTDR trace. However, the other scattering point has no visible signature in the OTDR trace.

Besides the vertical reflection lines (caused by stray light from room lights) two white spots corresponding to local scattering points are clearly detectable along the fibre. The stray light is useful to highlight the fibre on the bobbin; otherwise, the fibre is hardly detectable (See Figure 3.2 **b** for a fibre on the bobbin with stray light reflection that is caused by ambient illumination and without it). Out of the two detectable spots, only one correlates with the position of the OTDR peak in the trace. No detectable OTDR event corresponds to the second scattering point, which indicates that the defect occurs over length scales much shorter than the OTDR resolution and/or produces a much lower backscattered power than the minimum detection level of the OTDR. In contrast, the IR camera can locate the position of the scattering points with millimetre precision.

It is good to note that the backscattered light is only a small portion of the total light scattered by an event in a fibre, and it needs to travel back the length of the fibre to reach the OTDR detector, experiencing additional loss due to fibre attenuation and coupling points. Therefore, local detection of the out-scattered light, if accessible, is a much more efficient way to detect scattering events. Although access to the out-scattered light is not always possible, for example due to cabling or field deployment of the fibre, such an integrity check can be done immediately

after fibre fabrication when no further process has taken place, which in addition helps in cost and time management.

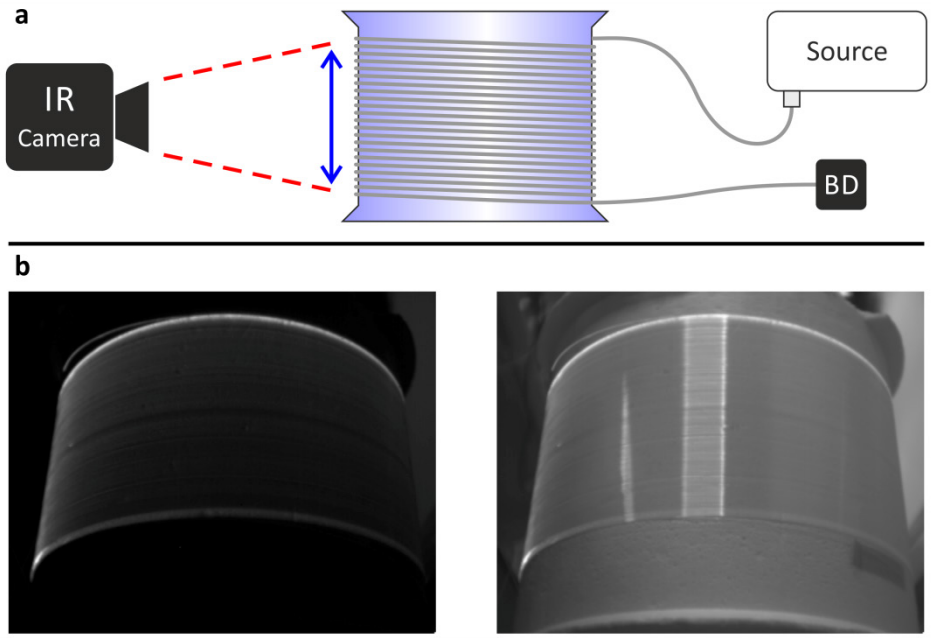

Figure 3.2: IR camera inspection method. **a**, IR camera inspection setup. **b**, Stray reflection.

In addition to the above example, in many other occasions, I have observed that a single OTDR peak could correspond to a few closely spaced scattering points (a few cm apart). Figure 3.3 shows such an example with closely spaced scattering points. The length of the examined fibre is 25m and includes two groups of scattering points, one is near the beginning and the other close to the end of the fibre. In this case, the OTDR (red trace) could only detect two events corresponding to the two groups of scattering points, despite the fact that the first and the second group consist of four and two discrete scattering points, respectively. After cutting the fibre somewhere between group defect 1 and group defect 2, I measured another OTDR trace (the curve in the inset) while coupling light from the opposite direction. The trace shows only a single peak that corresponds to the four discrete scattering points of the second group, which clearly shows the inaccuracy of the OTDR in handling these situations, due to its limited spatial resolution.

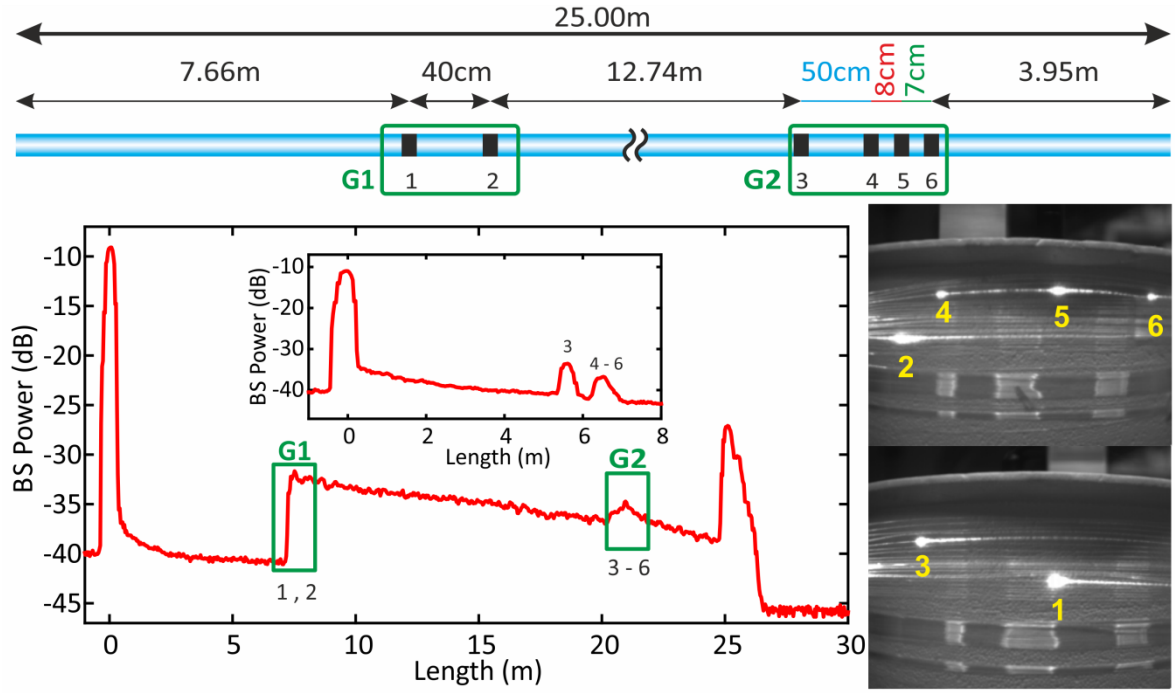

Figure 3.3: Example of a fibre with closely spaced scattering points examined with OTDR and IR Camera.

The ability to precisely locate the accurate position of the onset of a defect, and to cleave the fibre precisely at this point is paramount to investigate its characteristics origin, and longitudinal evolution. I developed a setup (shown in Figure 3.4) to cleave the fibre under test at a scattering point. This setup has been built around a top-of-the-range commercial cleaver (Fujikura CT-100) which produces high quality cleaves [133]. The added real time defect position monitoring is paramount to this study, which is not available in any commercial cleaver to the best of my knowledge.

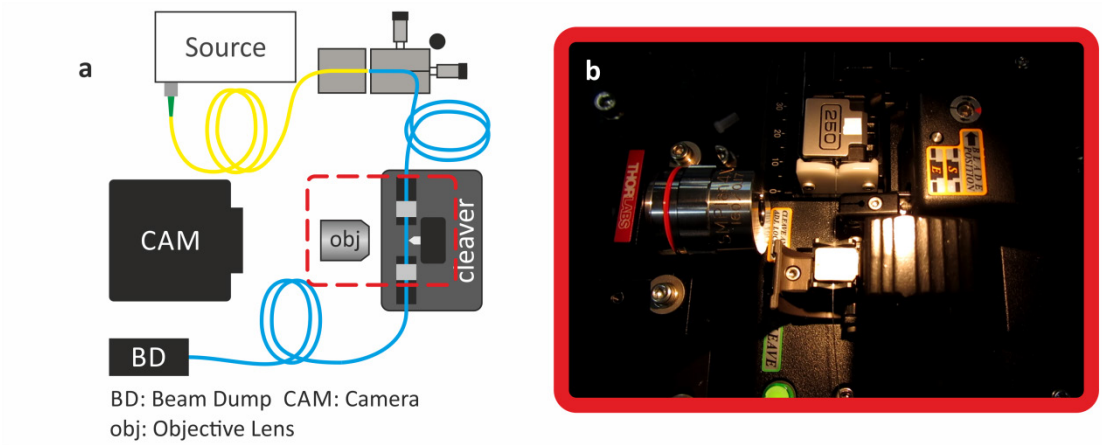

Figure 3.4: A setup to monitor and cleave a fibre under test at the position of a fibre scattering point. **a**, Schematic of the setup. **b**, Image of the part of the setup highlighted by the red dashed box.

As Figure 3.4 **a** shows, the fibre under test (FUT) is held inside a fibre cleaver and is monitored from the side using an IR camera. The light from a source is coupled into one end of the FUT, while its other end is terminated into a beam dump (BD). The combination of the camera and a microscope objective provides a magnified image of the FUT. Figure 3.4 **b** shows an image of the part of the setup highlighted by the red dashed box in the schematic. The bright light in the image is generated by an illuminator that I used to light up the FUT for alignment purpose. The position of the cleaver's blade is marked on the screen, and the FUT is moved, as required, to locate the position of the maximum out-scattered light intensity under the blade position marker. Figure 3.5 **a** shows a photo of the monitoring screen of the setup with the blade position marker highlighted by the red oval. The IR camera images of an example defect are shown in Figure 3.5 **b** and **c** when the source is off and on, respectively. Using this setup, I managed to cleave many sample fibres accurately (+/-10µm) at the position of maximum scattering of their defects.

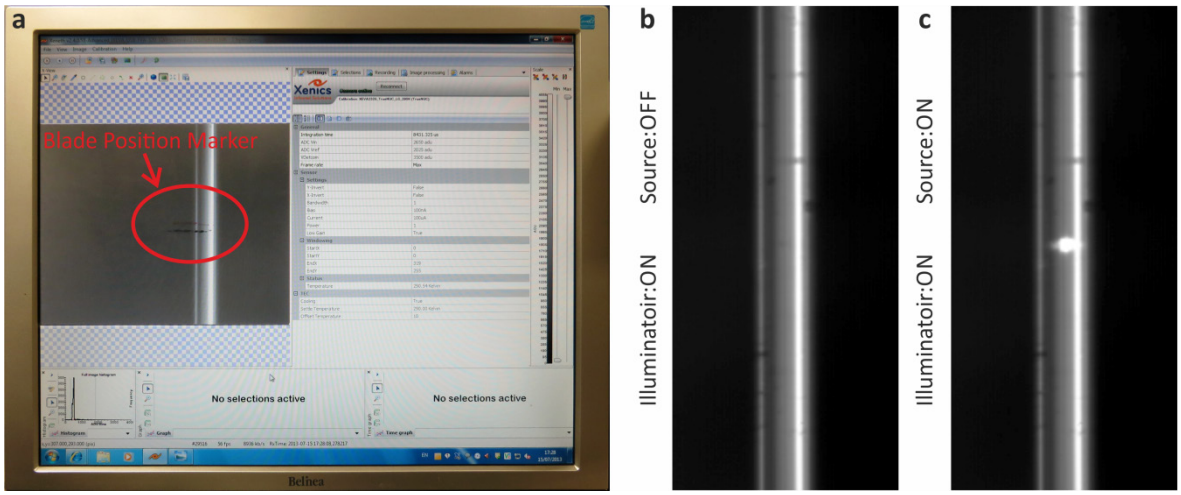

Figure 3.5: Monitoring fibres in the accurate cleaving setup. **a**, Monitoring screen of the setup with a marker showing the position of the cleaver's blade. **b**, The IR image of an example fibre with defect captured by the setup while the source is off. **c**, Similar image to **b** while source is on.

3.3.1 Structural defects in HC-PBGFs

I studied several defect points along numerous fibres using the techniques described above. Three examples of different defect types identified are shown in Figure 3.6 **b**-**d**. The geometry of the unperturbed fibre, from which the examples are selected, is shown in Figure 3.6 **a**. The first defect type (Figure 3.6 **b**) shows a transient imbalance in the differential pressure between the core and the microstructured cladding, causing a sudden expansion of the core and associated uneven compression of the first two rings surrounding it. In the second type of defect (Figure 3.6 **c**) two of the cladding holes close to the core have over-expanded. The third type (Figure 3.6 **d**) appears to

be the opposite of the first type, with a core collapse and correspondingly an overexpansion of some core surrounding holes. It should be noted that in all these instances no appreciable variation of the fibre draw parameters, in particular fibre outer diameter, and core and cladding pressure was detected. Figure 3.7 shows two example fibres, one with a clean OTDR trace (image **a**) and the other with several OTDR features (image **b**). Despite the very different OTDR traces, the traces of the variation of the OD of the fibres (shown by blue curves) do not show any noticeable correlated difference.

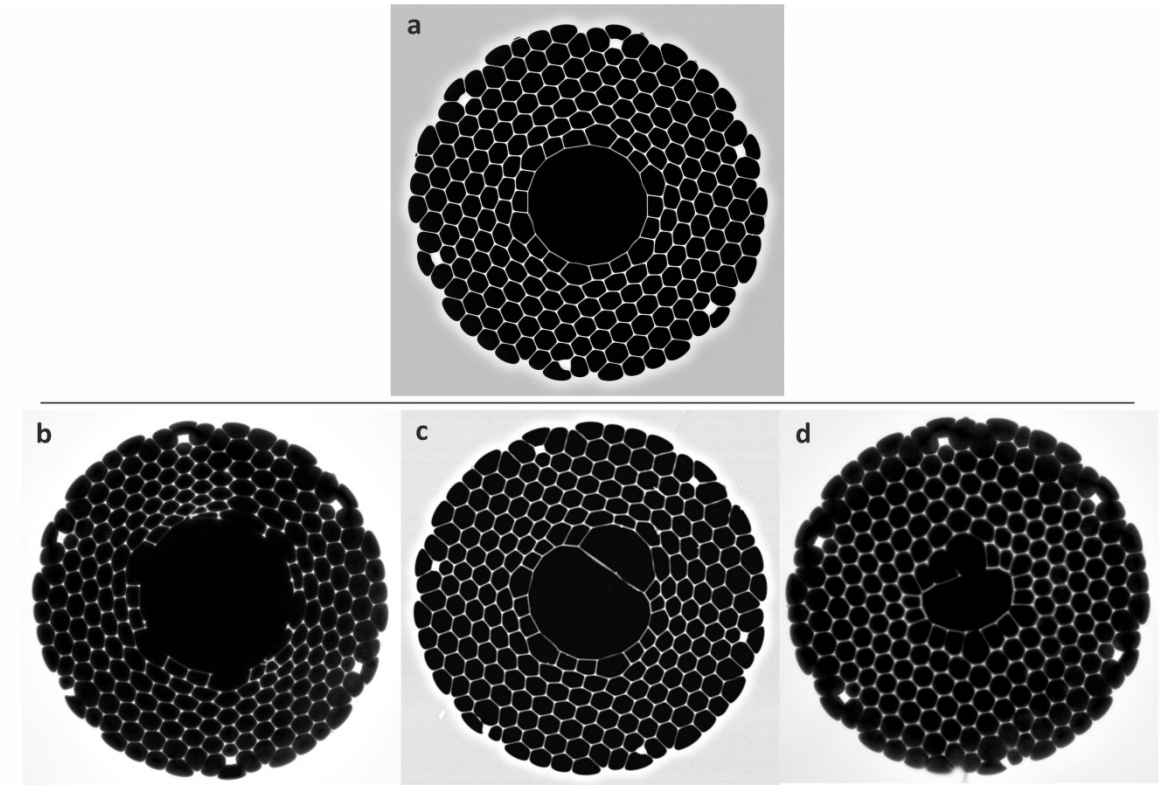

Figure 3.6: An example of a fibre and different defect types. **a**, a SEM image of the cross-section of one of the tested HC-PBGFs in defect study work. **b**-**d**, different defect types identified in HC-PBGFs where **b** is over-expanded core, **c** is over-expanded corner hole and **d** is shrunk core.

Scattering points caused by defects, such as those in Figure 3.6 that correspond to a severe structural deformation, can substantially degrade the transmission quality of the fibre. We observed in many cases that by removing such defects the transmission properties of the remaining fibre are substantially improved. For example, Figure 3.8 shows the spectral transmission and modal behaviour of a particularly bad fibre with two groups of closely spaced scattering points (as shown in Figure 3.8 **c**), before and after the removal of its defects. In order to obtain these results, light from a laser diode was coupled into the fibre under test (FUT) via a standard single mode fibre (i.e., SMF28e). The SSMF was butt-coupled to the FUT using a 3-axis nano-positioner. I equipped the positioner with two digital microscopes to monitor the coupling accurately. Additionally, the intensity pattern of the FUT's output was monitored continuously

during the optimisation of the coupling conditions. After achieving the optimum coupling conditions to generate maximum output power, the laser diode was swapped with a white light source and the output of the FUT was connected to an optical spectrum analyser (OSA). A spectral transmission test was then carried out.

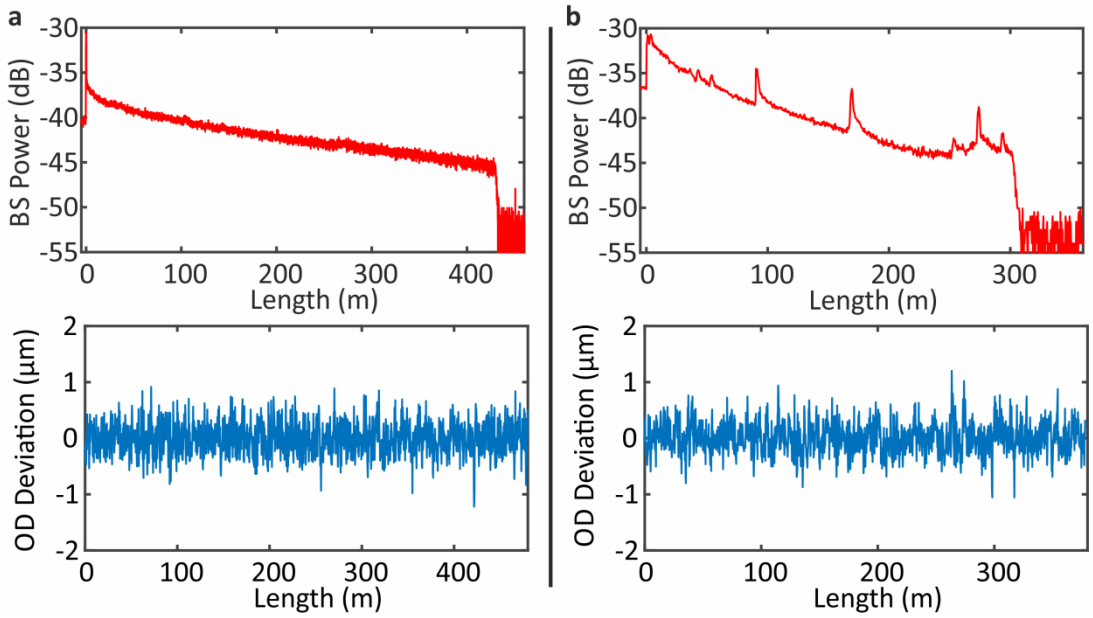

Figure 3.7: The outer diameter (OD) variation and the OTDR trace of two HC-PBGFs. **a**, An example of a uniform fibre. **b**, An example of a defective fibre.

The dark-blue curve in Figure 3.8 **a** shows the transmission spectrum of the fibre with both groups of the scattering points, G1 with five distinct scattering points and G2 with four distinct scattering points detected by the IR camera technique described earlier in this chapter. The test was repeated after removing the first group (G1) and then the second group (G2) of the defects, which generated the green and light-blue transmission spectrums, respectively. Micrographs of the modal output of the fibre are shown in Figure 3.8 **b,** colour coded according to their relevant transmission curve. As I discussed in Section 2.6.1.2, surface modes can strongly affect the transmission quality of fibre and its maximum available bandwidth. As can be seen in these images, these defects can couple light almost completely from the fundamental mode into some higher order modes (like LP11 in the green case) and surface modes. After the removal of the defective sections, with the coupling conditions maintained untouched, a mode closely resembling the fundamental mode was observed. The defect-induced coupling to surface modes is obvious in the dark-blue and green curves (as compared to the light-blue curve). The spectral traces show that this mode coupling also caused a severe reduction in bandwidth and an increase in loss.

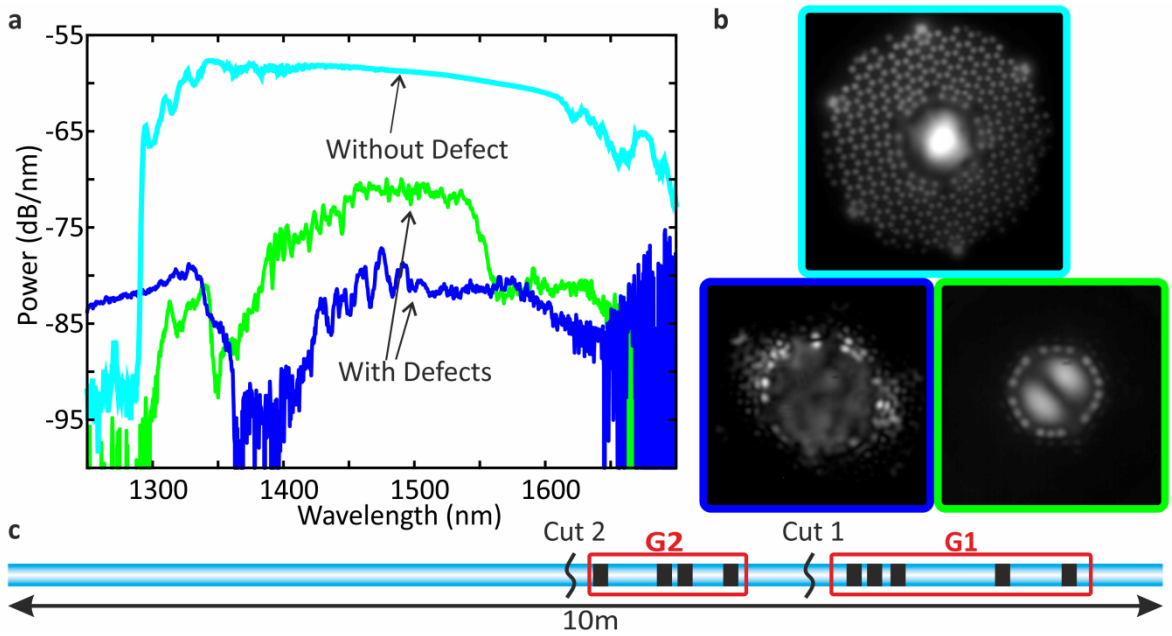

Figure 3.8: The spectral transmission and modal behaviour of a HC-PBGF with and after removal of defects. **a**, Spectral transmission curves. **b**, Micrographs of the output intensity pattern. (The launch was not modified throughout the measurement.)

Next, to investigate in more detail the origin of the observed defects and possibly, to try to prevent their occurrence, I also studied their longitudinal evolution along the fibre. Early studies immediately showed that the onset of defects happened over length scales of a few mm, i.e. too short for a commercial cleaver to be useable. Hence, I developed a custom-built fibre cleaver that allowed fine sectioning of fibres. Figure 3.9 **a** shows the top view of the cleaver. It consists of a 3-axis flexure stage with two fibre clamps with adjustable tension. Additionally, it has a linear micrometre driven stage with a ceramic blade installed on it. All the components are labelled in the figure. The fibre under test is held inside the first clamp and by adjusting the flexure stage in z-direction the fibre waste length is set, measured against the edge of the blade. Then the second clamp holds the free end of the FUT. Next, the blade is moved toward the FUT until it touches the side of the fibre. The blade scribes a crack in the FUT by a single knock on the metal bar (by taking the advantage of the bar's oscillation). By bending the fibre away from the blade side using the x-axis actuator of the flexure stage, the crack propagates through the cross section of the FUT and a fibre cleave is obtained.

As several 10s of cleaves are needed to study the evolution of a single defect, and many of such defects needed to be studied, I made a custom-built microscope setup to facilitate imaging of the cleaved end of the FUT. The top view of the setup is shown in Figure 3.9 **b**. The main advantage of this setup is in its specimen stage. I used a 3-axis flexure stage with a standard v-groove fibre holder. The optical path of the microscope and the stage are horizontal. In addition, this configuration allows easy installation of the FUT, especially when the sample length is longer than

a few centimetres, which often is the case in this study. This setup uses transmitted illumination to light up the specimen. As Figure 3.9 **b** shows, the FUT is illuminated from the side by a torch and/or in some cases from its other end by another light source. The optical path is highlighted in the figure. A microscope objective creates an image on the image sensor of a full-frame digital camera. A mirror is used to align the image position on the sensor and optimise the use of space. A concave lens installed on a flip holder in the optical path can switch between high and low image magnification. This setup made the repetitive task of imaging the FUT's cross-section in this particular study very easy.

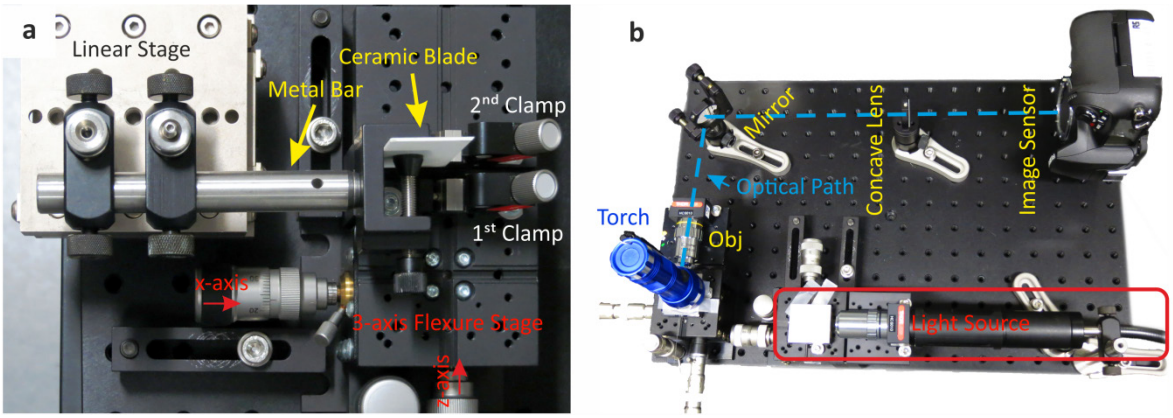

Figure 3.9: Sample slicing and imaging setups. **d**, A fibre slicing setup designed for defect evolution study. **e**, A microscope setup specifically designed for defect evolution study.

The sequence of images in Figure 3.10 **a**, which was selected from a cross-section image collection of more than 50 consecutive cleaves, illustrates the evolution of a defect of the second type (Figure 3.6 **c**). A schematic of the corresponding position along the drawn fibre is shown in Figure 3.10 **b**. One may notice the strut thickness appear so different between the two groups 1-4 and 5-8. This is because the first group (1-4) has been imaged using reflected illumination (episcopic illumination), whereas the other group (5-8) has been imaged using a different setup by transmitted illumination (diascopic illumination). At position 1 and 2, which are ~2m apart, the fibre shows an unperturbed structure. Less than 25mm away from position 2 (Figure 3.10 **a**, image 3) the onset of the defect is observed, with the two corner holes undergoing an overexpansion. The fibre then enters a meta-stable condition where the defective geometry does not substantially change: image 4 is taken 10mm away from image 3 and the defect remains unchanged for 325mm until sample 5. Images 6 and 7, obtained at 2.5 and 5mm away from sample 5, respectively, which show the rapid reversal of the defect back to normal structure. Image 8 shows the fibre cross-section 35cm away from positon 7. At a drawing speed of ~18m/minute, the whole defect, from beginning to end would have only taken about 1.2s to happen, which we believe is too fast a transient to be caused by fluctuations in drawing parameters (which were monitored and logged, and showed no variation). Accounting for the

draw down-ratio (preform feed rate of 4mm/minute), the defective fibre length corresponds to a length of just 81µm in the preform from which the fibre is drawn, which strongly hints at the possibility of discrete, small scale inhomogeneity or contamination within the microstructured cane as the most likely cause of such defects.

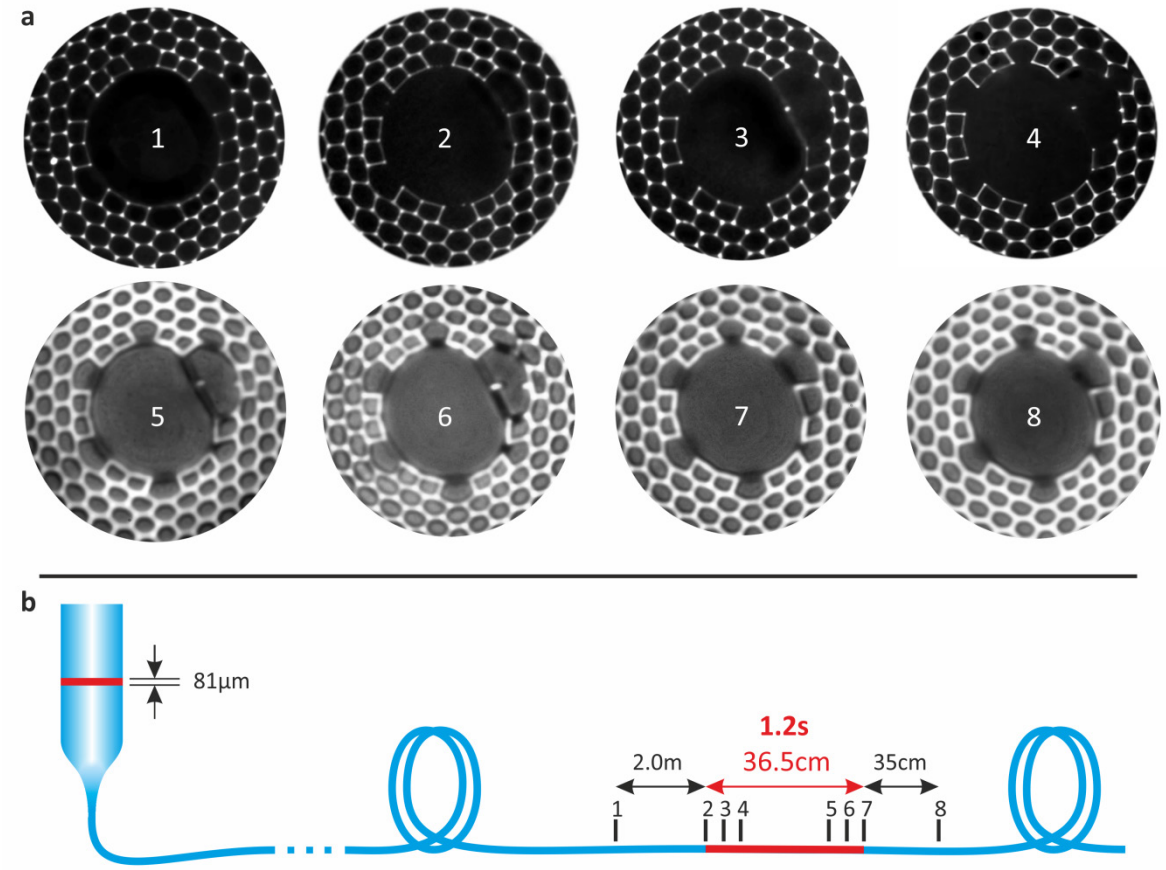

Figure 3.10: Evolution of a defect in a HC-PBGF. **a**, The sequence of cross sectional images showing the longitudinal evolution of a defect in a HC-PBGF. **b**, The schematic illustration of the defect formation and length scale during a fibre draw.

In order to distinguish the minute structural changes in the cross-section images, I used some image processing technique in which sequential images are coloured and overlaid on top of each other. Based on the colour superposition it is possible to distinguish where different images overlap, or otherwise which samples shows a particular deformation. Figure 3.11 shows an example of a shrunk core defect. Three consecutive cross-section images are coloured in red, green and blue, showing a transition from shrunk to normal structure respectively. The green and blue images were collected at 15cm and 36cm away from the red image, respectively. Then images are aligned, rotated and overlaid on top of each other to produce the image on the right hand side. The uniform expansion in the microstructure can be easily seen while the core is contracting. It also allows identifying the order of images.

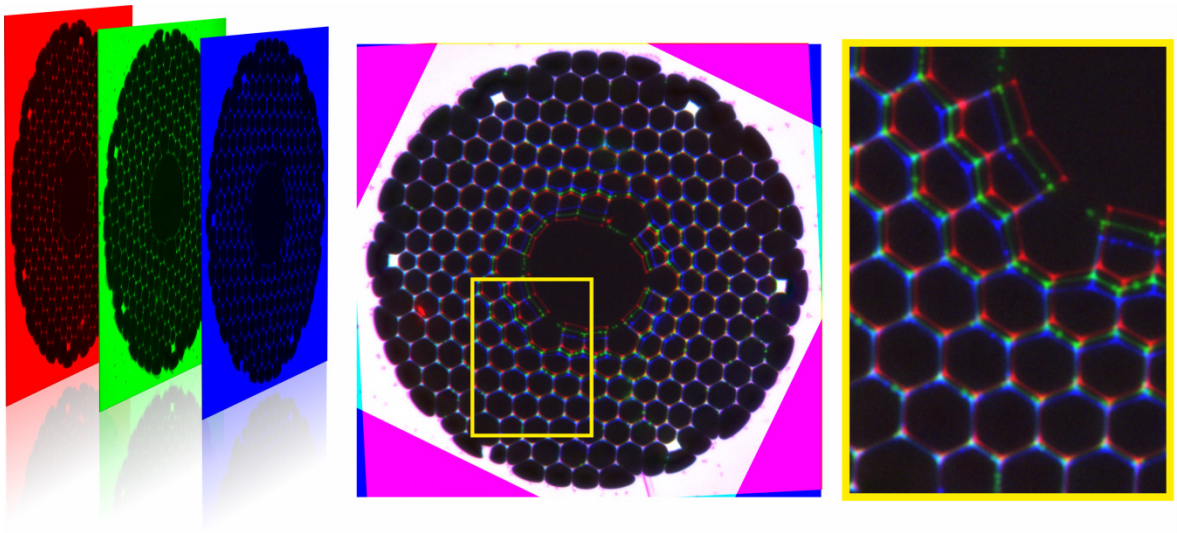

Figure 3.11: An effective image processing technique to highlight minute structural changes. An image stacking technique is used to extract minute structural changes.

3.3.2 Contamination inside HC-PBGFs

In addition to the case previously discussed, where scattering points were associated with fibre defects, in my IR camera and OTDR observations, I also came across some very strong scattering points that were not associated with any structural deformation within the fibre. Instead, I observed particulate contamination of sub-micron size, on the cross-section of the microstructure cladding and jacketing glass, right after cleaving the fibre at the scattering point. Figure 3.12 shows an example of such contamination. The IR image of the defect, shown in Figure 3.12 **a**, illustrates a very strong scattering that is stretched over ~3cm. I cleaved the fibre at a few points across the scattering trace and every time I observed a cross-section image like Figure 3.12 **b** and **c**, showing powder-like particles all across the fibre end face, sometimes including features similar to liquid droplets. Cleaving the fibre away from the scattering point resulted in a clean cross-section image without particles as shown in Figure 3.12 **c**. We speculate the liquid-like droplets are water attracted to the surface from the surrounding atmosphere, and the powder-like particles are either silica sooth or a type of salt formed from the reaction of water with chemical contents emerging/diffusing out of glass. This is discussed in more detail later in this section. The observed light scattering pattern implies the particles may exist inside the fibre before cleaving, however this needs to be confirmed.

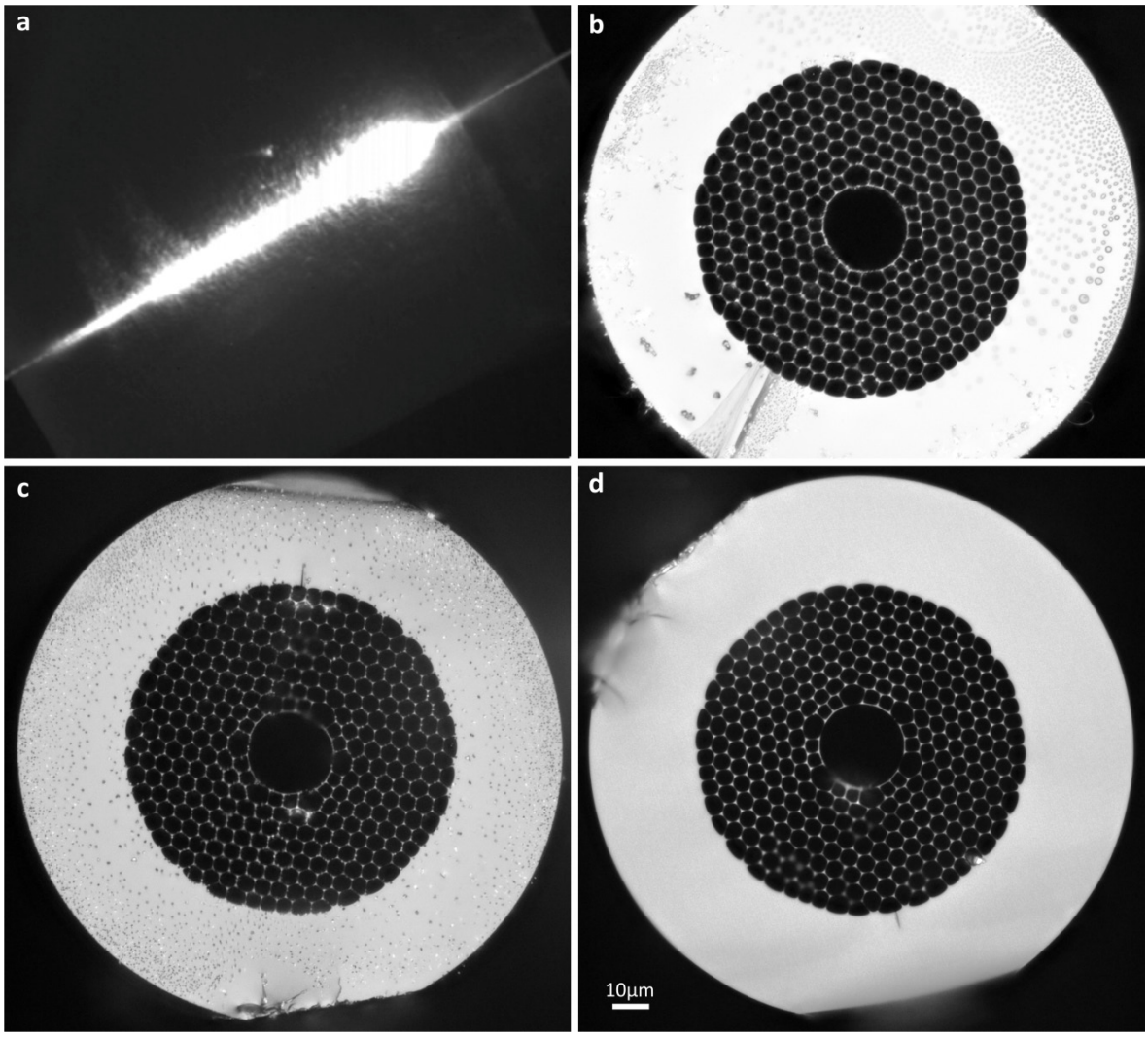

Figure 3.12: An example of a contamination defect in a HC-PBGF. **a**, An IR image of the strong scattering by a contamination defect. **b** and **c**, Cross-section images of the fibre at defect position showing micron and submicron size particles/droplets all over the fibre end face. **d**, Cross-section image of the fibre away from the defect, showing a clear particle-free fibre end-face.

Like the structural defects presented earlier in this chapter, this contamination defect (occurring at a position ~6m away from the beginning of the fibre) was observed to create an associated pronounced OTDR peak (as highlighted in Figure 3.13 **a**). Besides, it was found to have a very strong influence on the modal quality and transmission characteristics of the fibre, as shown by the red trace and inset with red frame in Figure 3.13 **b**. After removing the contamination defect, I observed a wider surface mode free transmission band, as shown by the blue trace, with a clear fundamental mode pattern and reduced surface modes, as seen in the inset with blue frame.

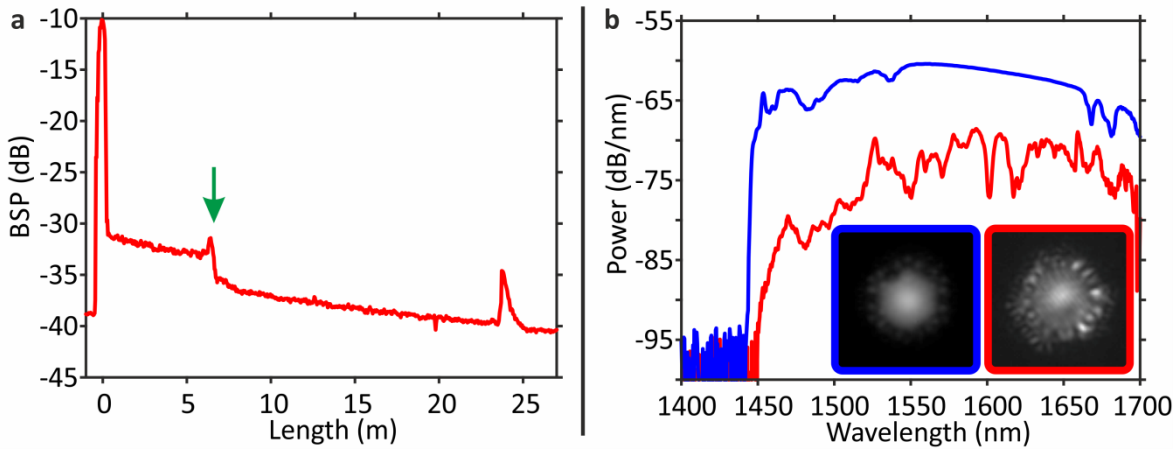

Figure 3.13: Optical characteristics of a fibre with a contamination defect. **a**, The OTDR trace of the fibre with defect position highlighted by the green arrow. **b**, Spectral transmission traces of the fibre before and after removing the defect. The modal behaviour of the fibre in both cases is shown in the insets.

I attempted to obtain information about the composition of the contaminant through Energy-dispersive X-ray spectroscopy (EDX) measurement, however the particles disappeared after the usual sample preparation for this experiment, suggesting plasma coating and vacuum operation can vaporise or disperse the particles. I analysed the contamination defects using an optical microscope, before cleaving the fibre. However, I could not find any noticeable feature in the side micrographs of contamination defects; one needs to consider that the visibility of the inner layers of a microstructure cladding is very limited through the side of fibre by an optical microscope analysis.

In addition to the localised discrete contamination defects, I also observed some form of distributed defects that are likely to be caused by contamination. During the examination of some fibre samples, I identified in some cases, a part of the beginning and end of the fibres that glowed relatively brightly in IR images, when the fibre was illuminated. Figure 3.14 **a** shows, for example, an IR image of a two-year-old 300m long fibre with relatively brighter bands at the top and bottom of the spool. The OTDR trace of the fibre in Figure 3.14 **b** highlights regions with a sharper backscattered power drop at the beginning and end of the fibre, in agreement with the IR image. Similarly to the localised contamination defect type, I could not identify any structural deformation as the cause of the excessive scattering; however, I found particulate contamination at the surface of both ends of the fibre, following a cleave.

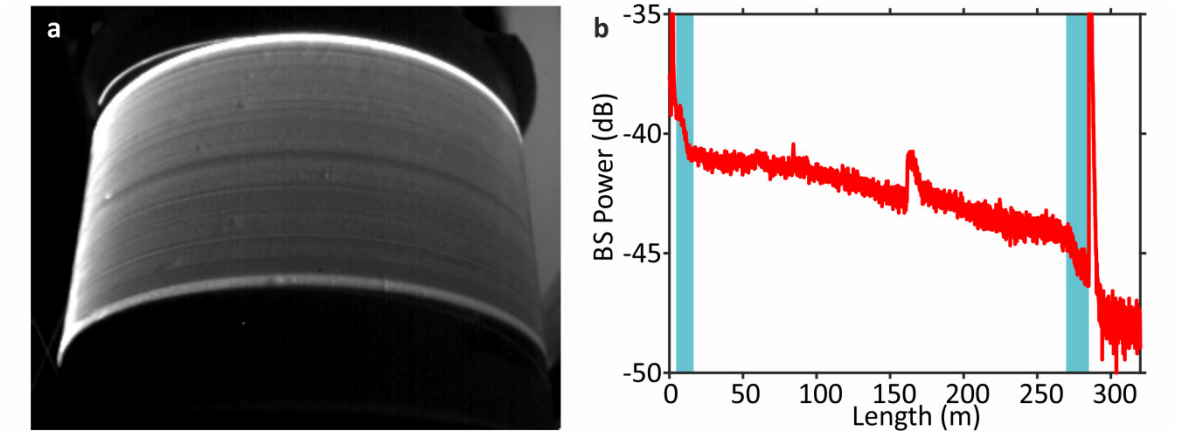

Figure 3.14: An example of distributed contamination defect. **a**, An IR image of the fibre. **b**, The OTDR trace of the fibre

I believe a possible root of the observed contamination defect lies in the finding of a recent study by Lyngsø *et al* [134]. They suggest the possibility of chemical reactions between a chlorine-containing compound in the glass used for optical fibres and atmospheric gases to be the reason for the formation of contamination at the end face of the fibre over time (~25hours in an example shown by them). Chlorine is conventionally used to reduce OH content and consequently the optical loss of the glass forming optical fibres in the wavelength range of 800nm to beyond 2.5µm (mainly to remove the 1380nm peak and lower the loss at adjacent wavelengths). It has been suggested that in an optical fibre having voids, such as HC-PBGFs, chlorine from the glass surrounding a void diffuses into the void, and reaches to the end facet of the fibre through the void, where it reacts with water in the atmosphere and forms crystalline hydrates. The amount of chlorine in the glass and water in the atmosphere can change the time scale of the appearance of the contamination. I have observed extreme cases where degradation at the end facet happened in less than an hour.

In the case of the defect contamination, I speculate that atmospheric water that slowly diffuses inside the fibre from its end facets over a long time (month/year) have undergone similar chemical reactions and have formed similar contamination near the extremities of the fibre. Although, isolating the contamination and testing its composition has proved to be challenging, I found that sealing the ends of a fibre immediately after its fabrication effectively minimizes the length of the contaminated regions. More work is needed to arrive at a solid conclusion about the properties of the contamination particles and their origin.

3.3.3 Classification of scattering points

Through numerous tests, I have obtained an extensive collection of images of scattering points, within which I observed repeating patterns of scattering signatures. I have been able to categorise

them based on their light intensity distribution. So far, I have identified three major categories, which are shown in Figure 3.15 with an example from each category; directional (left), lump (right) and mixed (middle). The top horizontal row shows a schematic of the intensity signature footprint whereas the middle row shows an example of each category obtained by an IR camera. I have observed evidences of a correlation between the defect types and these scattering signatures, suggesting a directional scattering pattern is mainly caused by structural defects whereas a lumped scattering pattern points to a contamination defect and a mixed scattering pattern simply implies a defect that is caused by both structural deformation and contamination. The last horizontal row in the figure shows an example of a fibre cross-section image for each category. This finding allows early identification of the origin of the defects in our fibres based on their scattering pattern. It will be an interesting future work to arrange for theoretical and simulation studies to verify and explain the observed correlation.

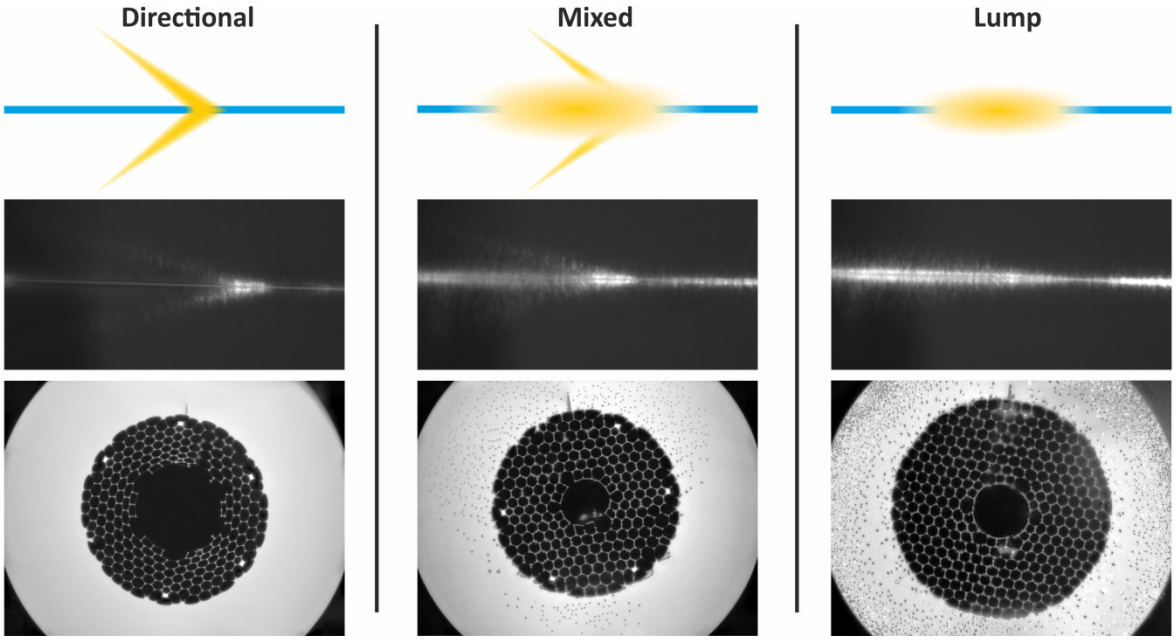

Figure 3.15: The three categories of scattering points based on the light intensity distribution from left to right: Directional, Mixed and Lump.

3.3.4 Analysis of canes

As proposed in section 3.3.1, a discrete, small-scale inhomogeneity or particle contamination of several 10s to a few 100s of micron size within the microstructured cane is likely to cause defects similar to what I studied earlier. Conventionally, canes are examined visually to check for any obvious defect or problem. However, the suggested particle contamination size is very likely to be missed by a simple visual inspection, aiming to find any trace of the contamination in the cane. I explored the bulk light scattering properties of the glass to find a better inspection method. Figure 3.16 shows the method. I coupled both IR and visible light (each in a different test) into one

end of a cane and looked for any non-uniformity in the side scattered light. I examined several canes, specifically the ones adjacent to the canes that produced the fibres with many defects that I studied earlier (see section 3.3.1). I found some isolated scattering points along the length of canes shining considerably more brightly than their surroundings, such as the one highlighted with blue arrows in Figure 3.16, and then I marked their position. Next, I examined the marked positions with an optical microscope. This method can easily pick up any contamination and defects that are close to the outer surface of the cane under test. However, the visibility of defects in the inner rings and in inner most layers of the microstructured cane is low, which is mainly due to the fact that the scattered light from these regions has to go through several reflections and refractions to reach to the observer, and is therefore blurred out.

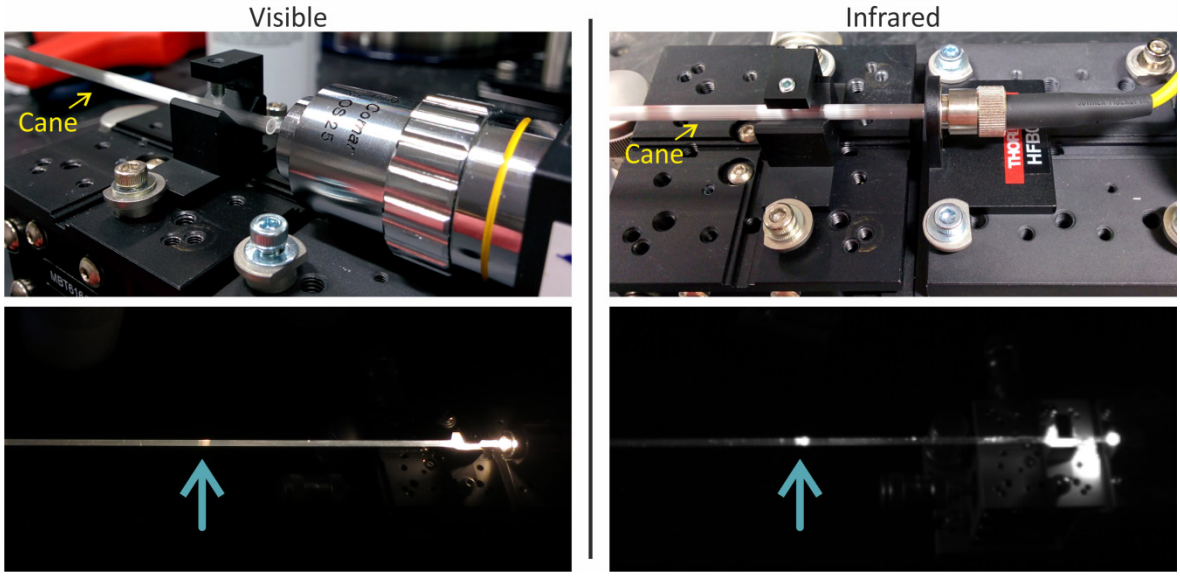

Figure 3.16: Cane analysis method. IR and visible light is coupled to a cane and the position of scattering points is marked.

Nonetheless, my preliminary observations showed evidence of some contamination of similar length scale to what I expected based on the defect sizes I had observed in the examined HC-PBGFs. Figure 3.17 shows microscope images of a few such contamination features in the cane. The red and green colours on the surface of the canes show the points marked after the scattering analysis. These findings provide useful evidence for my early speculation about contamination in preforms (either first stage or second stage) as the cause of discrete short time scale defects in the examined fibres.

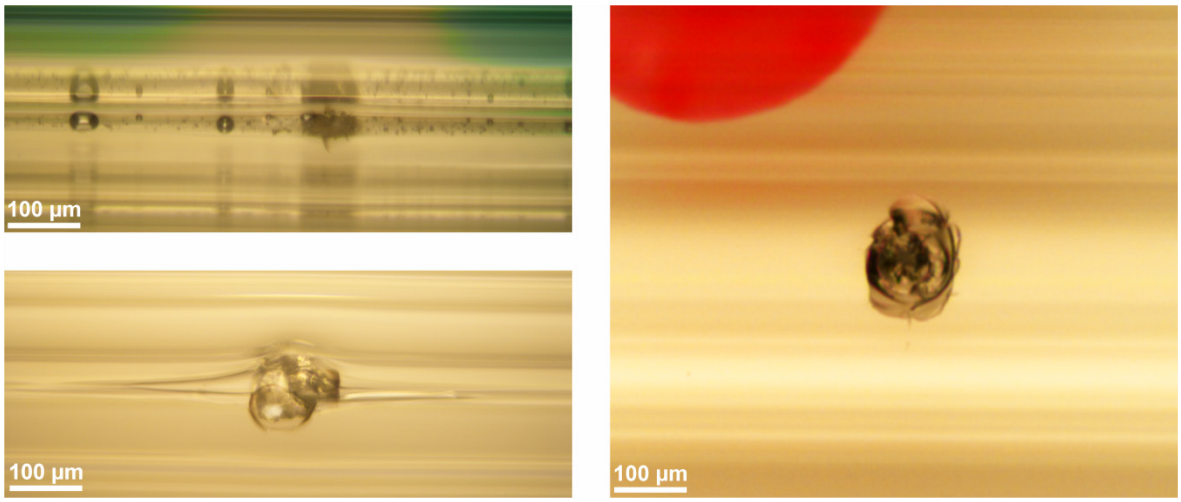

Figure 3.17: The micrograph of three defects in a microstructured cane.

In the next chapter, I will introduce a non-destructive examination method based on X-ray computational tomography that helps us characterise the particle contamination in the cane without damaging the canes, even if the contamination is obscured within the structure. A non-destructive investigation of canes allows interesting future studies such as fabricating fibres from the canes and correlating the observed defects (and their position) in the cane with possible defects that occur in the fabricated fibre.

3.3.5 Automation of fibre defects detection

As pictured earlier, the fabrication of a long length of defect free HC-PBGF (and equally of any other type of microstructure fibre) is important in their future application. A system that provides a real-time in-situ feedback about the uniformity and integrity of the fibre during the fibre fabrication is therefore highly desirable. The IR camera method with the setup configuration presented above provides a solution to check the uniformity and to identify defects in a stationary fibre after its fabrication.

In another method, as shown in Figure 3.18 **a**, I fixed the camera and moved the fibre under test, while light was coupled into the fibre. I captured a movie of the illuminated moving fibre at 16 frames per second. This test was done on a short fibre sample (5m). I defined 'frame intensity' to be the sum of the intensity value of all the pixels in a single frame. The frame intensity can be normalised against the maximum possible frame intensity (i.e. frame width times frame height times maximum pixel value, which in this experiment are 320 x 240 x 2^{16} respectively). Figure 3.18 **b**, shows the curve of the normalised frame intensity against time, which can be interpreted as a scattering trace of the fibre against the fibre length, if the time axis is replaced with displacement according to the translation speed of the fibre under the camera. At the position of a scattering point, a sharp increase in the frame intensity is produced. The gradual drop of power is also seen

in the figure as the distance from source increases. This method can be used to identify scattering points, their position and their strength in scattering light out of the fibre, which provides a measure of the uniformity and integrity of the fibre. This method brings us one step closer to the ultimate method of real-time in-situ monitoring of the fibre quality during the fabrication process.

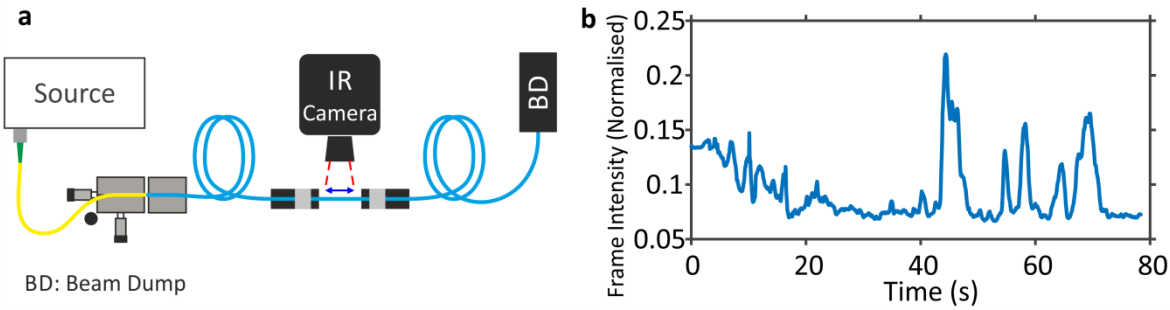

Figure 3.18: Measuring the out-scattered intensity vs length trace of fibres. **a**, The schematic of the setup. **b**, The scattering trace of a short length HC-PBGF.

In principle, this method does not have the fibre length limitation of the earlier method. However, at this stage, I could only measure the scattering traces of short fibre samples (up to a practical length of ~10m) as the fibre is loose on the optical bench. Longer fibre samples are usually kept on fibre spools and coupling light into a fibre on a moving spool is challenging. In Chapter 5, I introduce my solution to the coupling issue, which resulted in a novel approach to measure the longitudinally resolved scattering map of a fibre.

3.4 Conclusion

In summary, I have investigated for the first time the structural defects that occasionally arise in a HC-PBGF, degrading its transmission properties through increased loss and intermodal coupling. To circumvent the limited spatial resolution of standard OTDR techniques, I used an IR camera to precisely locate the scattering points along the fibre. The sub-millimetre resolution offered by this approach allows identification of clusters of finely spaced defects (which appear as a single unresolved peak in an OTDR trace), or even of defects that would be hidden in an OTDR trace. IR camera inspection, combined with accurate fibre cleaving, has enabled us to directly visualize and categorize the structural deformation of several fibres at the point of their defects. Different types of defects were identified and their longitudinal evolution was studied in more detail (with one example reported in detail). The study has highlighted that structural defects can form and disappear over very short time scales of the order of ~1s, corresponding to only several tens of µm long sections in the fibre preform. This provides a strong indication that inhomogeneity or contamination in the microstructured cane from which fibres are drawn (rather than drawing parameter fluctuations) are likely to be responsible for the defect's origin. To confirm this

hypothesis, I developed some characterization methods and studied several canes and indeed, I identified some defects. These methods were used both to determine the source of defects and eliminate them, and to identify canes/preforms with defect and abandon them. Arrangements have been made to incorporate these techniques into the routine fibre fabrication process, in order to aid selection of canes without defects. Although quantitative correlation between preform defect type/density with final fibre performance has not been done to date, such correlation has been observed qualitatively. A HC-PBGF fabrication is very costly and requires heavy investment in resources in particular in terms of time and energy of a number of people. If a defective cane/preform is identified, it will be abandoned to save these resources and because of this, such correlation study has been delayed.

Besides the structural defects in HC-PBGFs, I found another equally important defect type caused by contamination in the fibres, the origin of which I believe is caused by chemical reactions between Chlorine from the glass and atmospheric water. I found a correlation between the defect types and their scattering signature, which allows us to predict the defect type based on their scattering intensity pattern. Finally, I demonstrated a preliminary setup to measure the length resolved scattering map of a fibre based on the out-scattered light, which can be used for fibre quality monitoring. This method has been re-engineered and developed further in Chapter 5.

In conclusion, the work presented in this chapter has helped us to identify and study systematically for the first time to my knowledge defects in HC-PBGFs, a topic somehow ignored previously but an important aspect of the fibre fabrication, and to learn about their origin, which I hope can sheds light into some possible effective mitigation strategies.

Chapter 4: X-ray tomography

4.1 Overview

The fabrication of conventional optical fibres has undergone more than 40 years of continuous development and the various preform fabrication techniques and fibre-drawing processes used to produce the hundreds of millions of kilometres of low-loss transmission fibre installed each year are now highly engineered and optimized for mass production. In addition, many special fibres have also been devised and developed over the past few decades (e.g. various PM fibres, dispersion shifted/ compensating/ flattened fibres, highly nonlinear fibres, etc.) which have now reached the same level of maturity as single mode fibres. However, currently there is a strong requirement for novel fibres that can address emerging needs, for instance increased capacity in optical telecommunications, new fibres to deliver the output of high average/peak power lasers, or novel fibres for short (e.g. UV) or long (Mid-IR) wavelengths. A number of evermore-complex fibres are being pursued in order to address these emerging requirements, including for instance microstructured optical fibres (MOFs), multicore fibres (MCFs), and multimode fibres (MMFs). For most of these fibres the fabrication techniques are not as well developed. Therefore, there is a requirement for new characterisation techniques (e.g. to assess their optical properties) but there is also an urgent need for new methods to assess the fabrication itself. Hollow-core MOFs are a very good example of such emerging fibres, which potentially can better performance of conventional fibres in many ways. These fibres require a very complex internal structure to achieve their desired optical properties. Their fabrication is substantially more complex than that of conventional fibres [9, 41], and significantly different from the “chemical deposition techniques” used for SSMF and other mainstream fibres, which demands new ways of e.g. assessing structural quality of the fibre during the various fabrication steps.

As discussed in Chapter 2, the fabrication of MOFs, typically involves a multi-stage fabrication process that requires the manual stacking of preform assemblies (in some instances even comprising materials with very different thermal and mechanical properties, see for instance the case of a metal filled MOF discussed in section 4.5.1) and then their drawing, first to canes and then, in a second step, to fibres. Due to complexity and the lack of established quality control procedures in the fabrication of MOFs, there is, therefore, potential to introduce defects into the fabrication process, for instance by the way of stacking errors, or accidental inclusions of contaminants within the stacked preforms. Such defects, as I have shown in Chapter 3, can affect optical performance, mechanical properties and very often reduce the yield of useful fibre that can be produced from a single preform [135].

It is therefore highly desirable to develop non-destructive techniques capable of accurately capturing high resolution three-dimensional (3D) structural images of the internal structure of preforms and canes used to form MOFs, as well as, if possible, the final fibres. However this is quite challenging because: structures are very complex, made of up to several hundred holes, often of different sizes; furthermore, the dimensions of the features that need to be imaged varies from ~mm in the preform to ~μm (or few hundred nm) in the final fibre, a factor of over 1000x variation in scale. Therefore, a technique able to achieve the required measurement accuracy for these very different length scales is required. Very few attempts are reported in the literature. Possible techniques include standard optical index profiling methods or other non-standard techniques like Fourier domain optical coherence tomography [136], Doppler assisted tomography [137], and optical computed tomography [138]; however, they all have resolution/accuracy limitations when complicated structures with many features and/or structures with high index contrast are involved.

This work is the first demonstration of the potential of X-ray Computed Tomography (in short, XCT) for the structural analysis of both preforms and fibres, which enables non-destructive measurements that have not yet, to date, achieved by other means (particularly for preforms and canes).

In this chapter, I describe the use of cutting edge XCT to achieve for the first time detailed and accurate high-resolution analysis of the internal structure of preforms, canes and fibres, thus characterising the full fabrication flow of hollow core MOFs. The results have been facilitated by recent developments in X-ray computed tomography (CT) technology and systems [139]. More importantly, this technique can be applied to virtually all types of fibres, ranging from the more conventional to the most exotic special fibres types. Notable examples that will be shown in the following include for instance multi-material optical fibres (e.g. incorporating different glasses, metals and polymer elements) (MMOFs) and multi core fibres.

The chapter is structured as follows. I begin with a discussion on the conventional methods used to inspect fibres and preforms, and then briefly explain the concepts and operating principle of X-ray CT. This is followed by a description of the experimental setups and equipment I used. Next, I discuss the X-ray CT analysis of two particular examples of special fibres (non HC-MOFs), which have been selected to show the versatility and usefulness of X-ray CT for the analysis of fibres and preforms. In particular, I apply XCT to study the structural uniformity and consistency in a metal incorporated soft-glass fibre and the internal arrangement of fibre elements in a multi-element fibre. Then I discuss the main topic of this chapter, i.e. the use of XCT to preform non-destructive

structural analysis of hollow core photonic bandgap fibres (HC-PBGFs), arguably one of the most structurally complex optical fibre types produced to date, and their preforms. In this section, I show X-ray CT as a valuable tool for inspection of first stage preforms and canes, which provides unparalleled details about their consistency and uniformity. I highlight the advantages of this method for the study of fibre defects, examples of which have been discussed in Chapter 3. I then report other exemplar applications of the technique in other areas of studying HC-PBGFs. More in detail, I use the technique to understand the internal deformations caused during the splicing process of HC-PBGFs, and to study the end facet damage induced by coupling light from a high peak-power pulsed laser source in to Kagome fibres.

The work described in this chapter provided the basis for a paper presented at the 40th European Conference on Optical Communication (ECOC 2014) [140], and a journal article published in Optics Express [141]. The latter paper was highlighted by Spotlights in Optics in October 2014 [142] and has already accumulated 10 citations.

4.2 Conventional methods of identifying structural non-uniformities

The standard way to analyse the structure of conventional solid optical preforms and fibres is generally through either optical microscopy or refractometric techniques (also known as transverse profiling methods) [60, 143]. In refractometry, for instance, an optical wave is passed through a fibre or preform. In its path, any single wavefront undergoes distortion due to the differential phase delays induced by the refractive index profile of the specimen. One can then use the information carried by the distorted wavefront to retrieve the refractive index profile. This technique is simple, fast and non-destructive, however it suits simple structures, typically with cylindrical symmetry; it is not easily applicable to the case of complex structures, for instance where multiple interfaces exist within the fibre structure – plus in a HC-PBGF there would be problems associated to the very large index contrast air/glass. Optical and electron microscopy are the most commonly used techniques for accurate structural measurements and are suited for the analysis of complex fibres. However, these techniques normally require a “clear line of sight” to the target under inspection. Therefore, to image the internal structure of the fibre or preform, one should create a flat cross section, e.g. by cleaving, sawing, or polishing the fibre/preform. These procedures are in most cases destructive, i.e. they affect the produced yield in the case of fibres and, in the case of MOF preforms, completely prevent further use due to accumulation of dust and debris within the holes. This is usually the case when polishing and/or sawing are used. Scribe-and-break and scribe-and-tension cleaving techniques are often considered as a quick method to produce a high quality cross-section and usually introduce the least contamination.

However, these cleaving techniques do not work for larger diameters (e.g. preforms and, in some instances, canes).

Another situation that is difficult to investigate via the “multiple sectioning & imaging approach” is that of a rapidly changing structure. This could be the case for instance, of a preform at the necking point (see Chapter 2), or a fibre or cane where the structure is unintentionally changing e.g. due to a perturbation of the process or a defect or imperfection in the preform. An example of this was discussed in Chapter 3 where I discussed the formation and longitudinal evolution of defects in a HC fibre. In this case, the ability to investigate the variation is limited by the minimum physical distance at which two subsequent sections can be obtained. This is typically a few cm in the case of a cane or a 10-15mm in the case of a fibre when using standard equipment and procedures, or a few mm using the tools I developed and discussed in Chapter 3 [135]. Moreover, studying features that require knowledge of the angular alignment of the fibre samples, such as twists or bends, is difficult to capture through “multiple sectioning & imaging approach” as the fibre is often repositioned during the cleaving process and its angular orientation is difficult to maintain.

4.3 Tomographic methods

Tomography, as inferred from its roots ‘τόμος (tómos)’ (from Greek, slice) and ‘γρᾰ́φω (gráphō)’ (to write), is in its wider scope any imaging technique to generate cross-sectional images of an object [144, 145]. Although there are invasive variants of tomography in which the object is physically sliced and then imaged [144], non-invasive tomography involves: i) illuminating the sample with a form of radiation at a particular angle; ii) collecting the transmitted fraction; iii) repeating the previous steps for a number of angles; and iv) computing the cross-section image of the object from the plurality of projections [146]. In the rest of this chapter, I always refer to non-invasive tomographic methods, which is also termed computed tomography (CT). Depending on the illuminating radiation e.g. X-ray, optical waves, radio waves, and ultrasound, different tomography methods have been developed and demonstrated [138, 146].

X-ray CT is a well-established versatile method for getting information on the specimen’s size, density, structure, material and can achieve fairly high (sub-micron) image resolution [144-146]. X-ray CT provides a virtual slice / cross-sectional image, representing the mass density of the specimen. It is typically reconstructed from a collection of conventional radiographs acquired from hundreds or even thousands of different angles. Each virtual slice has a thickness, which depends on the width of the X-ray beam and the resolution of radiographs. Similar to the definition of pixels (picture elements) in a 2D image, voxels (volume elements) are used to define

the unit measurement cube (with known dimensions) in 3D datasets. Each voxel in an X-ray CT reconstructed volume contains the value of the mass density of the object under analysis at a specific spatial point. This method can capture complex internal geometries, composed e.g. of regions characterised by different materials/compositions, provided there is sufficient contrast between the density of the materials[147]. Advanced XCT setups allow voxel sizes smaller than 50nm [144, 148].

The intensity level in the radiographs (or voxel values in the reconstructed dataset) provides a measure of the total attenuation of the X-rays through everything along their path, from the source to the detector [146]. The attenuation of X-rays as a function of the thickness traversed follows a Lambert-Beer type exponential law, where the attenuation is a strong function of the density/atomic number of the material. Each intensity level represents a specific mass density and directly depends on the average atomic number of the specimen. As the dimensions of a voxel are much larger than a single atom, the captured X-ray intensity represents the average density of all atoms within the voxel and thus of its chemical composition; therefore, different attenuation levels, and thus different intensity levels in the final image, correspond to different materials.

An X-ray CT scanner is used to acquire the radiographs. This machine has three main parts: an X-ray source, a platform (that holds and rotates the sample) and an X-ray detector. A common configuration of the parts is shown in Figure 4.1.

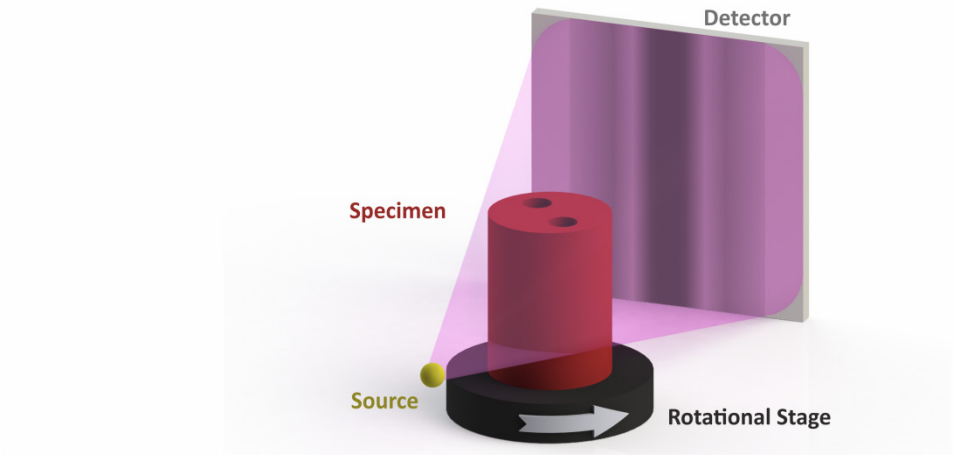

Figure 4.1: Schematic of the typical layout of a X-ray computed Tomography (XCT) setup.

The source emits a beam of X-ray (with sufficient flux and either a narrow or wide energy spectrum/wavelength) that propagates towards the detector interacting with the specimen along its path [149]. In general, high-energy X-rays are less attenuated by matter. Additionally, high X-ray flux is required for thicker samples (to ensure enough photons reach the detector). The detector collects a radiograph image and the process is repeated as the sample is rotated by 360 degrees at very small intervals (if a high resolution is sought). Based on the intensity of the transmitted X-rays, the “exposure time” of the detector is adjusted to achieve a higher SNR.

Tomographic images of the specimen are then reconstructed from the collected radiographs, using reconstruction methods such as the back projection method [149]. Figure 4.2 shows a schematic of a reconstructed image from sixteen 1D profiles based on the back projection method.

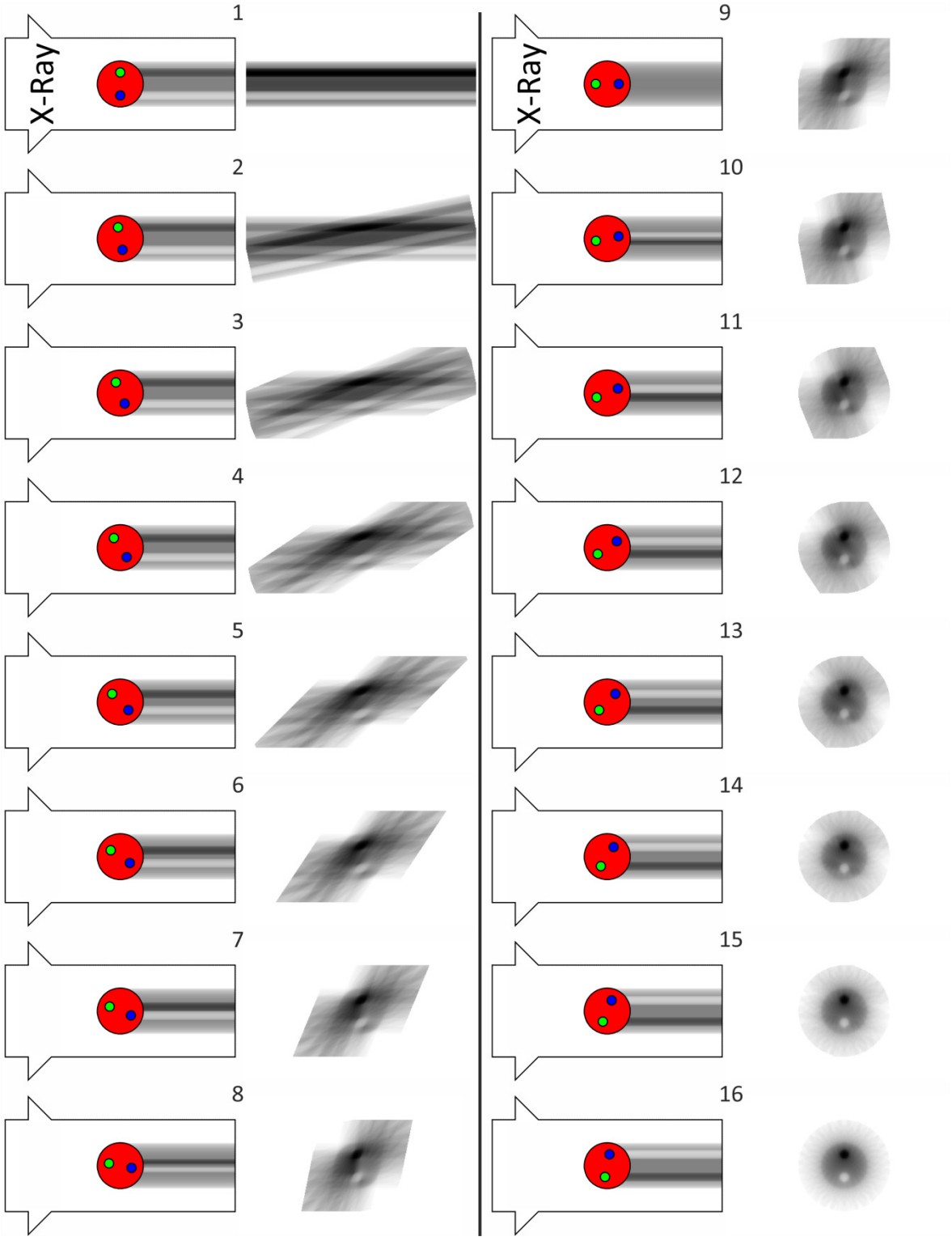

Figure 4.2: Example illustrating how the 2D reconstruction of an object is obtained from XCT using a back projection method.

The detector can be a linear array where a virtual cross-sectional 2D image of a specimen is reconstructed from the line profiles (similar to the example in Figure 4.2); by repeating this sampling along the third dimension of the specimen, a sequence of 2D images is produced which generates a 3D map of the specimen. On the other hand, a 2D array /area detector reconstruct a 3D image of the specimen directly.

X-ray CT is mostly used in the two key areas of medical applications (to image organs in the human body), and industrial applications (e.g. to study material integrity, defects, flaws etc.), however it is finding increasing scientific applications e.g. in science and engineering of materials archaeology, and marine biology [150, 151]. In section 4.6 we will discuss how X-ray CT is particularly suited for the observation of the internal structure of hollow core microstructured preforms, canes and fibres; in the next section we describe in some detail the different machines available at the University of Southampton which have been crucial to carrying out the present study. .

4.4 Description of experimental XCT setups used

In this work, I performed a set of X-ray CT scans at the μ-VIS Centre at the University of Southampton using three different X-ray CT machines [152]. All these setups have a similar configuration similar to the schematic in Figure 4.1 (e.g. they use a fixed source, a fixed 2D detector array and a rotational stage), however they differ significantly in terms of their overall size, the measurement volume and thus the energy of the X-ray source, and their resolution. In more detail, the three machines are:

(a) **Custom 450kVp / 225kVp "Hutch"**: This is the biggest of the three instruments, which is designed to measure specimens as large as 1m width × 1m length × 1.5m height weighing up to 100kg (this limitation is imposed by the sample rotation/translation stage). Figure 4.3 shows this large machine that can easily fit a few people inside to prepare the test. It is equipped with two X-ray sources, including one high energy (100-450kVp – where kVp stands for kV peak and indicates the X-ray tube voltage of the source, which can be varied between the two values above), which is required to analyse very large samples, and one lower energy source (20-225kVp). It should be noted that increasing the X-ray tube voltage would in turn produce higher energy X-rays, i.e. the X-ray spectrum grows larger toward higher energies/shorter wavelengths. This instrument uses a 2000x2000 pixels Flat Panel detector and its resolution varies from ~3μm for the low225kVp source and 50μm for the 450kVp source. For the analysis of HC-PBGF preforms, I used the low energy source, which provided

higher resolution and enough energy to image through the ~cm thick preforms, as will be discussed in detail in section 4.6.1.

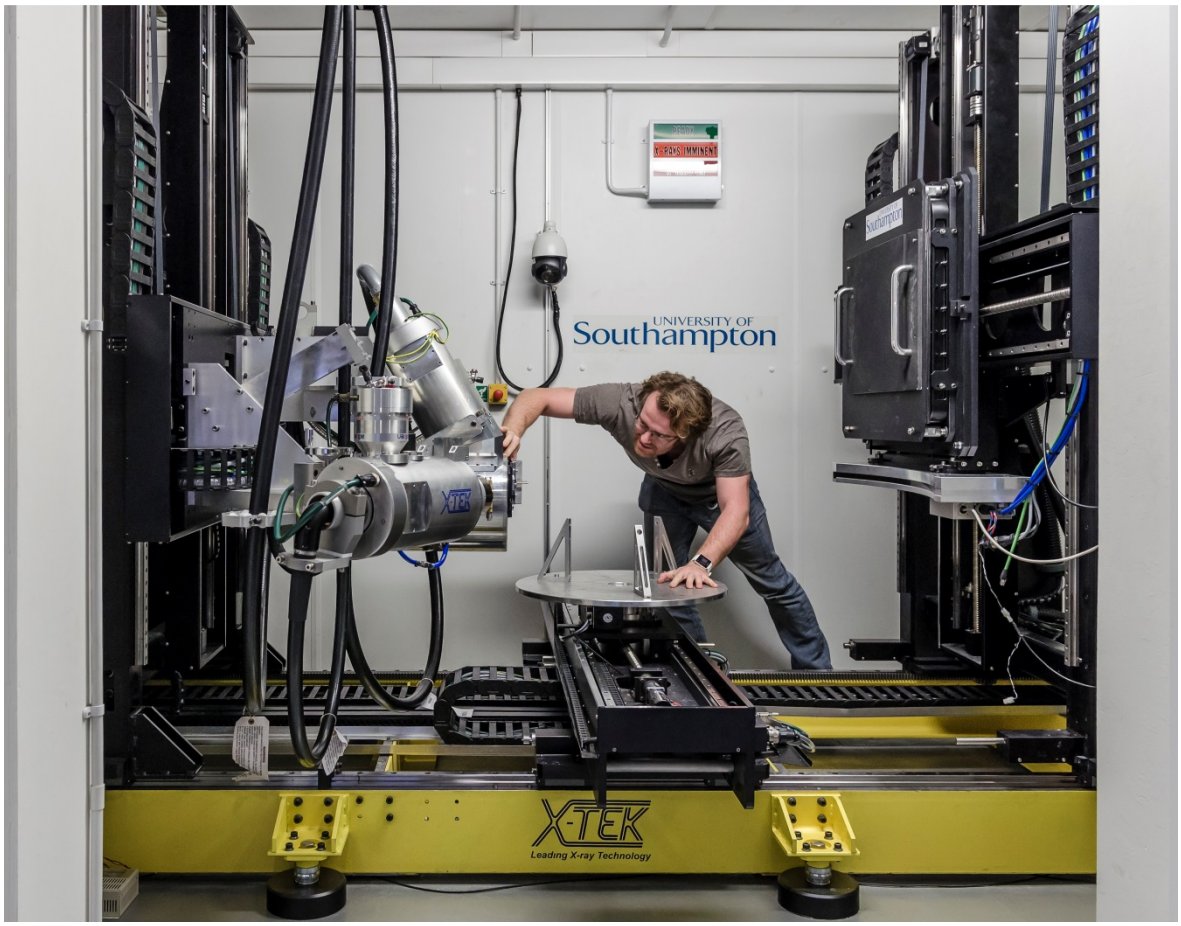

Figure 4.3: The Hutch X-ray CT scanner at the µ-VIS Centre at the University of Southampton

(b) **225kVp HMX ST**: This system is a Nikon XTEK XTH 225kVp micro-focus CT scanner [153] that is designed to measure specimens with relatively smaller size (≤300x300x300mm) and smaller weight (no more than 50kg). Figure 4.4 shows the instrument with its control desk beside it. The 20-225kVp source of this system can be configured for high resolution (1µm) or high X-ray flux (up to 5x 'normal' flux), for which a low flux or low resolution (10µm) is achieved respectively. I used the HMX scanner for the study of small preforms and canes, an example of which is discussed in detail in section 4.6.2.

(c) **Xradia Versa 510**: This scanner is the finest of the three systems, which can achieve submicron resolution down to 0.7µm, and voxel size as small as 70nm. This machine employs various advanced technologies to allow imaging of low Z contrast structures and is designed for the measurement of relatively small specimens. Its sample holder allows for a specimen of 50mm width x 50mm length x 300mm height with up to a maximum weight of 15kg to be measured. Figure 4.5 shows this system. As can be seen, the size of sample holder is relatively small. Since the small specimen, this system uses a 30-160kVp source. This machine

also utilise a 2048x2048 pixels flat panel detector. I used the Versa scanner mainly to scan fibre samples.

Figure 4.4: The HMX X-ray CT scanner at the µ-VIS Centre at the University of Southampton

Table 4.1 below presents a comparison of the main characteristics of these three machines.

Table 4.1 Summary of available X-ray CT systems available at µ-VIS Centre.

	450kVp / 225kVp Hutch	**225kVp HMX**	**Xradia 510 Versa**
Manufacturer	Nikon / Metris	Nikon / Metris	Zeiss
Source(s)	20-225kVp , 100-450kVp	20-225kVp	30-160kVp
Detector	Panel (2000x2000)	Panel (2048x2048)	Panel (2048x2048)
Best Spatial Resolution	3µm	1µm	0.7µm
Maximum Sample Size	1.0 x 1.0 x 1.5m	300 x 300 x 150mm	50 x 50 x 300mm
Maximum Sample Weight	100kg	50kg	15kg

As seen in Figure 4.1, the specimen is held on the rotational stage and the scan is collected as the stage is rotated. A scan can take anywhere from ~30 minutes to 12 hours, depending on the size of the sample and required resolution (which is determined by system parameters like, exposure time and the number of angular projections). During a scan, it is therefore paramount that the sample is held very firmly in place through the use of an appropriate holder to avoid vibrations and/or sample movement. As a part of my activity, I designed a series of custom holders designed

specifically for HC-PBG preform, cane and fibre samples, as will be discussed in the following section. The general principle is that if the holder interjects the beam path (as was unavoidable in the case of the analysis of a PBGF preform), it obviously needs to be made out of a low-Z material (such as plastic) in order to reduce X-ray attenuation; it is also essential that the holder is cylindrically symmetric in order to avoid introducing measurement artefacts, as will be detailed later. In the case of canes and fibres, the holder was designed to not interject the measurement beam, and could be made out of metal (aluminium, or stainless steel). The holders were physically manufactured by ORC technicians/ external manufacturers to match my design and technical drawings.

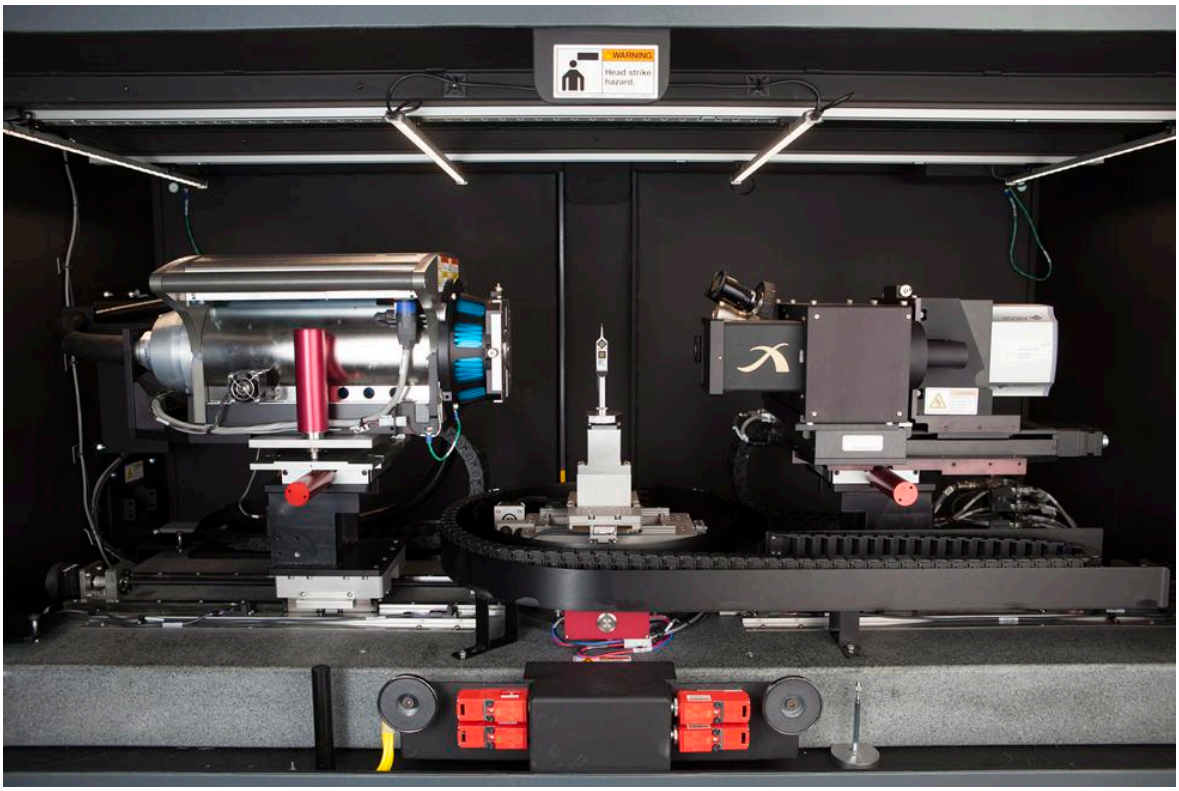

Figure 4.5: The Xradia Versa X-ray CT scanner at the µ-VIS Centre at the University of Southampton (courtesy of µ-VIS Centre).

The analysis of the reconstructed data is done through use of suitable post-processing software (such as VG Studio, Aviso and Fiji Image J). Our radiographs usually have a grayscale bit-depth of 16-bit, producing tomographic images in which voxel intensity values range between 0 to 2^{16}- 1. The intensity value of each voxel then correlates with the mass density of the specimen at that particular position. A useful tool in post-processing of CT data is the image histogram. This is a very useful tool to enhance the visualisation of those particular elements of the XCT measurement that are of most interest. It allows identifying the voxels corresponding to a particular material (with a specific X-ray attenuation coefficient) and select the matching data

within the measurement dataset for further processing. The use of this feature will be explained in more detail in the next section (e.g. the section on multi-material optical fibres)

4.5 Exemplar studies

In the next section, I use X-ray CT as a non-destructive tool to investigate the integrity of HC-PBG fibres, canes and preforms. This will help us to take the defect investigation study that I introduce in Chapter 3 to a next level, where I gain a better understanding and insight into the origin of non-uniformities, defects and contamination. Nevertheless, before I move on to those details, here in this section I will discuss the versatility and capabilities of the X-ray CT analysis through measurement and analysis of a few exemplar cases.

X-ray attenuation, ΔI, by a sample is highly dependent on the atomic number Z of its constituent material ($\Delta I \propto Z^3$) [154]. Such strong Z dependence of the XCT measurement results in the contrast between different materials (each having a specific Z (or equivalent)) in any specimen. For instance, X-ray CT analysis of a lead silicate MOF with tin electrodes inside the fibre (that I discuss in the following subsection) fully exploit this property to reveal the internal structure of the fibre. The Z contrast between silica (SiO_2, Z_{Si} = 14, Z_O = 8) and air (Z_N = 7, Z_O = 8) in silica HC-MOFs is another good example, which shows the advantage of exploiting Z contrast to creates a clear distinction between air holes and glass structure in these fibres. Additionally, this strong Z dependence provides the ability to discriminate materials with relatively small difference in composition, if therein a small quantity of an element(s) with relatively large Z contrast exists. In fact, the technique is able to image the core of a conventional fibre, which only contains a relatively small amount of Ge (Z_{Ge}=32). In the following subsection, I demonstrate another example in which I have explored this sensitivity to distinctively show the core and cladding of an SMF.

4.5.1 Illustration of XCT for structural analysis of special fibres: Metal-incorporated fibres and Multi-element Fibres.

Metal-Incorporated Fibres (MIFs) are a niche type of optical fibre that incorporates metal wires or electrodes, opening up the possibility of controlling the optical properties of the fibre itself via electrical signals [155-158]. Another group at the ORC has been working towards a very novel type of MIF, comprising two glass cores, where the relative position of the cores can be controlled by an actuation mechanism based on electrostatic forces [155, 159]. The fibre and its preform are shown in Figure 4.6. In summary, the fibre is fabricated via a dual stage drawing process (refer to Chapter 2), in which a cane containing the innermost structure (comprising the two cores

suspended on very thin glass membranes, see the schematic in Figure 4.6 **a**) is first fabricated by extrusion and then stacked together with solid glass rods and 4 glass-jacketed tin metal rods, which will provide the metal electrodes in the final fibre. The whole array is then placed in a further retaining glass tube. All glass elements are made out of Schott F2 glass (a commercial lead silicate soft glass). The photo in Figure 4.6 **a** shows the actual stacked composite MIF preform. Figure 4.6 **b** shows SEM pictures of the fibre with the two suspended cores clearly seen in the fibre centre and the top image. Each core is ~2.0×3.1µm and they are separated by an air gap of 200nm and suspended on two 500nm thick glass membranes. The average diameter of the four tin wires is about 50µm and the fibre OD is ~285µm.

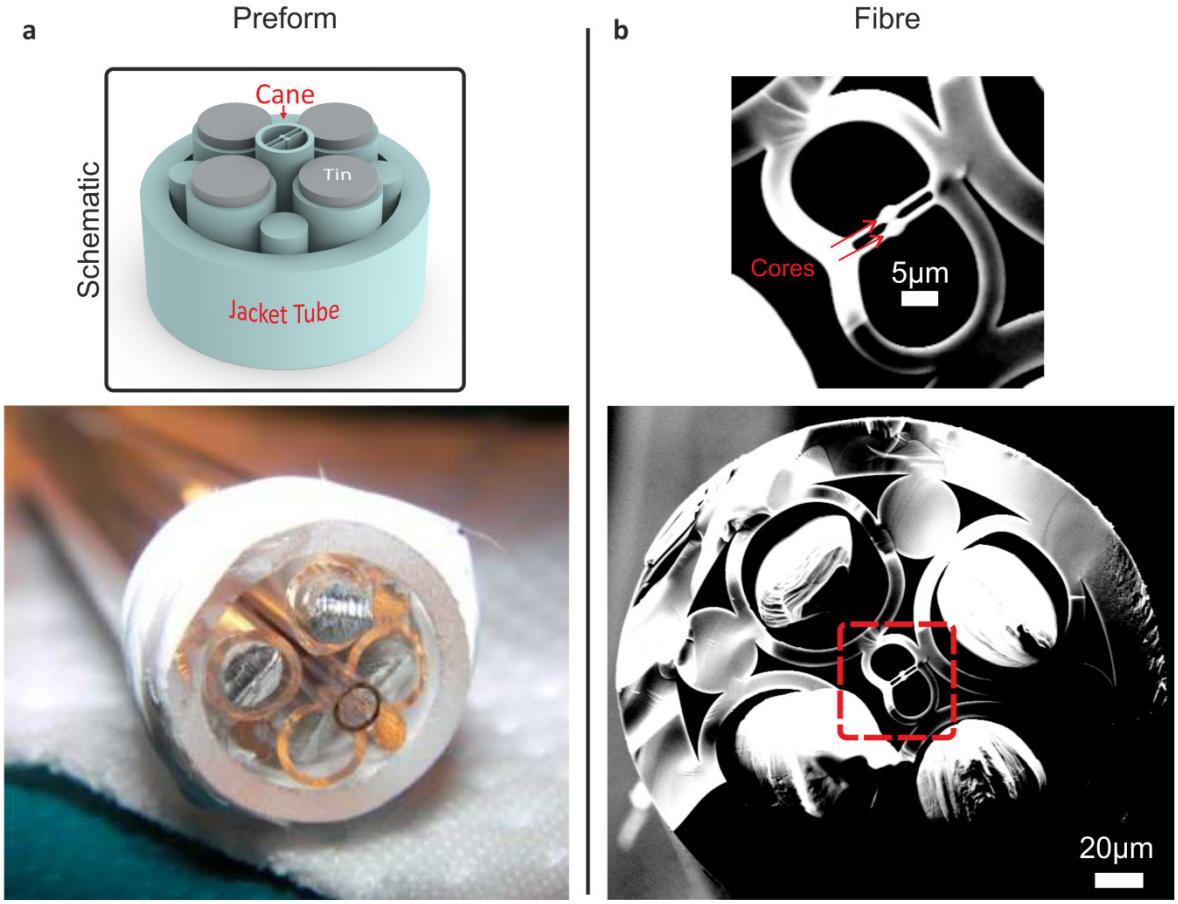

Figure 4.6: A dual-suspended-core Metal incorporated Fibre (MIF): **a** Stacked preform (bottom) and its schematic (Top) highlighting the central extruded cane (containing the two cores), tin rods and jacket tube. **b**, A SEM image of: (bottom) the metal incorporated fibre and (top) a magnified image of the two suspended cores.

The fabrication of this fibre presented a number of challenges. The process of co-drawing materials (e.g. glass, metal) with vastly different thermo-mechanical properties (e.g. viscosity, coefficient of thermal expansion, etc.) is in itself difficult (though at the drawing temperature of the F2 glass the tin metal is completely liquid). In addition, the microstructure needs to be preserved and in fact enhanced via tuning of the diameter and separation of the two cores and

thickness of the membranes (all need to be made small in order to enhance the mechanical response of the cores to the electrostatic stimulus). Another important aspect relates to the uniformity, continuity and adherence of the metal wires. The evaluation of the structural quality of the fibre is made very difficult because the metal wires, differently from the glass, do not cleave easily, but tend to taper, deform and break (as shown in Figure 4.6 **b**) and thus is practically very hard to obtain a fibre cross-section suitable for direct imaging (via SEM or optical microscope). I proposed and demonstrated X-ray CT as a viable way to gain structural information about this complex fibre type. The large density contrast between the various materials (air, Lead-containing glass and Tin wires) provides an ideal case study for demonstrating XCT for the analysis of special optical fibres.

Figure 4.7 and Figure 4.8 show the result of the CT measurement of the MIF introduced above. A virtual cross-section image of the fibre is shown in Figure 4.7 **a**; from such reconstructed images the geometrical of the different parts composing the structure can be investigated in detail. The "virtual cleave" obtained in this way is free from any damage and distortion typically observed in a mechanical cleave, and enables the pristine internal structure to be visualized. A full reconstruction of the 3D structure of fibre from the CT data is seen in Figure 4.7 **c**, where the voids, metal wires and glass materials were separated, based on the histogram in Figure 4.7 **b**. As can be seen in the virtual cross section image, because of the large Z contrast (and associated large difference in X-ray attenuation coefficient) between the elements of the different materials of the fibre (e.g. tin wires, lead silicate glass and air), each material has been clearly resolved with a distinct intensity level (grey shade). The histogram represents the number of voxels (within the 3D dataset) for each intensity level, revealing three clearly distinct Gaussian distributions and peaks for each material. Figure 4.7 **c** is generated by selecting the voxels within each material window using the histogram and then attributing a specific colour property to it. Note that the same process has been repeated for similar X-ray CT analysis performed in other fibres discussed in this chapter.

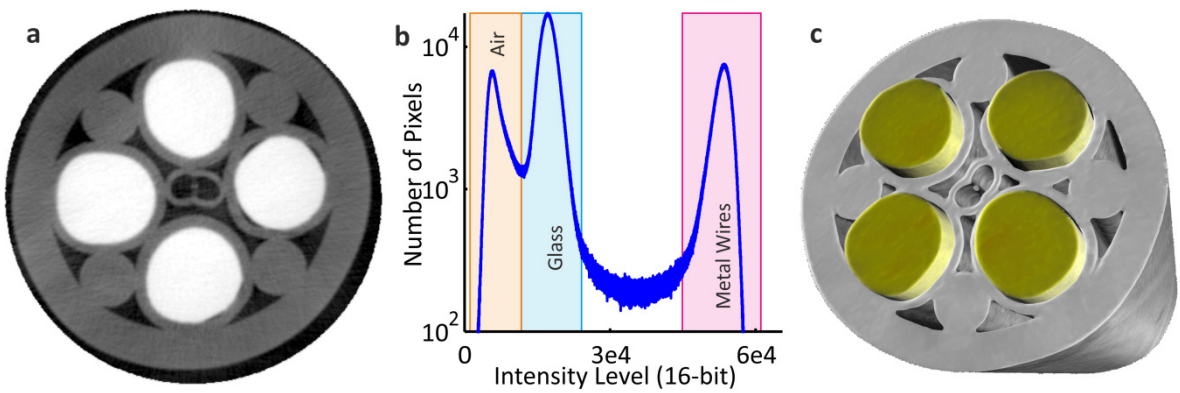

Figure 4.7: X-ray CT analysis of MIF described above. **a**, A virtual cross-section image of the dual-core MIF. **b**, The histogram graph of the measurement with identified region of interests. **c**, The reconstructed 3D structure based on the histogram from the CT data.

A more careful analysis of the full CT data set allows for instance carrying out a detailed investigation of the integrity of the metal wires within the fibre. Figure 4.8 **a** shows an image of an isolated wire. The image clearly shows small disuniformities and multiple features (like bumps and dents) at its surface. Moreover, this data set allows for the investigation of the homogeneity of the tin wires. For instance, a possible air void (bubble) is seen in Figure 4.8 **b** highlighted by the red circle. This analysis was carried out using the Versa setup and the voxel size in this measurement is 0.706µm. The number of projections used was 1601 and the source voltage was set at 80kV with 20s exposure time at 7W source power. The detector was used in 2-pixel binned mode resulting in a 1024x1024x1024 voxels dataset. The fibre cross-section is therefore covered by 604x604 pixels and the scan height was about 700µm. The results of this test show very clearly the potential of the XCT technique to analyse the structural integrity of complex optical fibres.

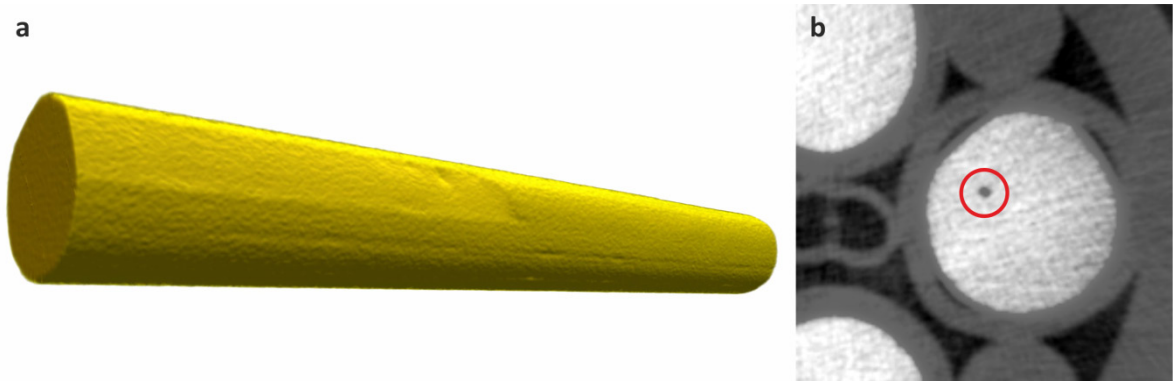

Figure 4.8: Analysis of the metal wires in the MIF. **a**, A single tin wire isolated from the CT data. **b**, A part of a virtual cross-section image, showing a possible defect in one of the tin wires.

The second example of "other" special fibre discussed here, namely the **Multi-Element Fibres (MEFs)** are a novel technological approach to enable multiple spatial data carrying channel within a single fibre (known as SDM), which has been proposed for next generation high capacity optical transmission networks [160]. MEFs are made of several individual solid optical fibres (elements), which are embedded in a common polymer coating to form a single fibre and provide different spatial channels for data transmission. Typically, two concentric layers of polymer coating are used: the first used to embed the different elements (which typically have reduced diameter as compared to SSMF); the so-formed single strand is then coated with a second layer or slightly different polymer material. Figure 4.9 shows a few examples of MEFs.

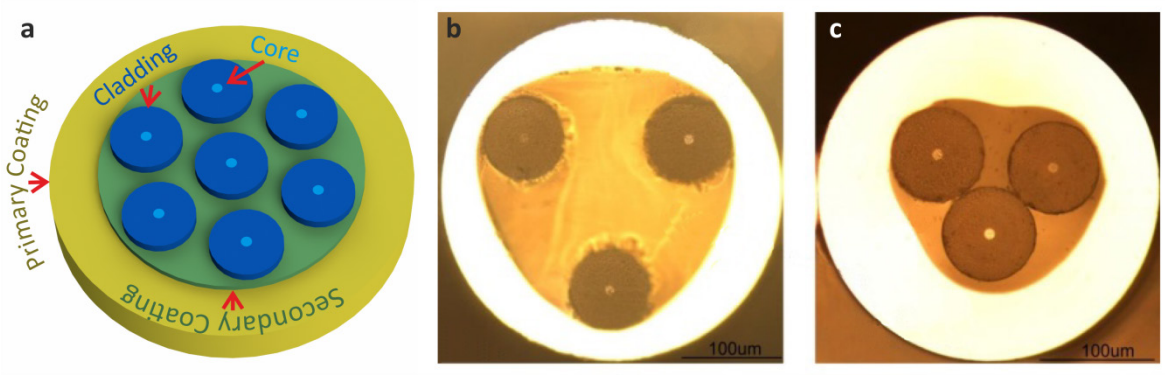

Figure 4.9: Multi element fibres. **a**, Detailed 3D CAD model of a 7-element MEF. **b** and **c**, Optical micrographs of two examples of 3-element passive (**b**) and active (**c**) MEF. Note the different separation between elements in the two cases (see text for discussion)

The structural and compositional analyses of MEFs are important. The arrangement of the elements, for instance, is a determining factor on the structural strength of MEFs. Also, active MEFs (doped with Erbium/ Ytterbium) designed for cladding-pumped SDM optical amplifiers require optical contact between the pump and signal fibre-elements to be maintained for efficient pump transfer. In contrast, in passive MEFs, a minimum separation between the elements must be ensured in order to keep the cross talk between the different spatial channels low. Additionally, any bubbles formed by gas trapped within either of the two layers of coating can affect both optical properties and strength of these fibres.

Similarly to the MIF discussed earlier in this section, cleaving MEFs by conventional scribe and tension method to produce a flat cross-section for structural inspection is non-trivial because the polymer coating does not allow the crack to propagate across all elements. This makes analysis of MEFs through conventional structural inspection method, like microscopy and refractometry, very difficult. The micrographs in Figure 4.9 **c** have been achieved through many attempts with a high precision saw and focus stacking (that combines micrographs taken at different focus depth to form a sharp image with a longer depth of field) which do not assure the fidelity of small details. XCT offers a useful alternative. From the point of view of the structural analysis via XCT, however, the main challenge of MEFs lies in the very small density difference between the two layers of polymer coating and between core/cladding within the various fibre elements.

I used the Xradia 510 Versa to look at a passive 7-element MEF with a hexagonal arrangement of elements. The achieved voxel size in this measurement was 0.71µm. The number of projection used was 1601 and the source voltage was set at 40kV with 12s exposure time at 3W source power. The detector was used in 2-pixel binned mode resulting in a 1024x1024x1024 voxels dataset. The fibre cross-section is therefore fully covered by 570x570 pixels and the scan height was about 690µm Figure 4.10 **a** shows a virtual cross-sectional image of the MEF, in which the

polymer (dark grey) fibre cladding and core (brightest spots) can be discerned. In Figure 4.10 **b**, data corresponding to the fibre elements has been removed from the full structure in order to separate the polymer coating region from the glass and to help with identifying features more precisely. This allows the uniformity of the polymer to be checked, i.e. to determine whether any air bubble or contaminant has been trapped within it. Figure 4.10 **c** is a 3D view of the sample, where half of the data is cut away to illustrate the post-processing functionalities and to visualize the physical features of this structure.

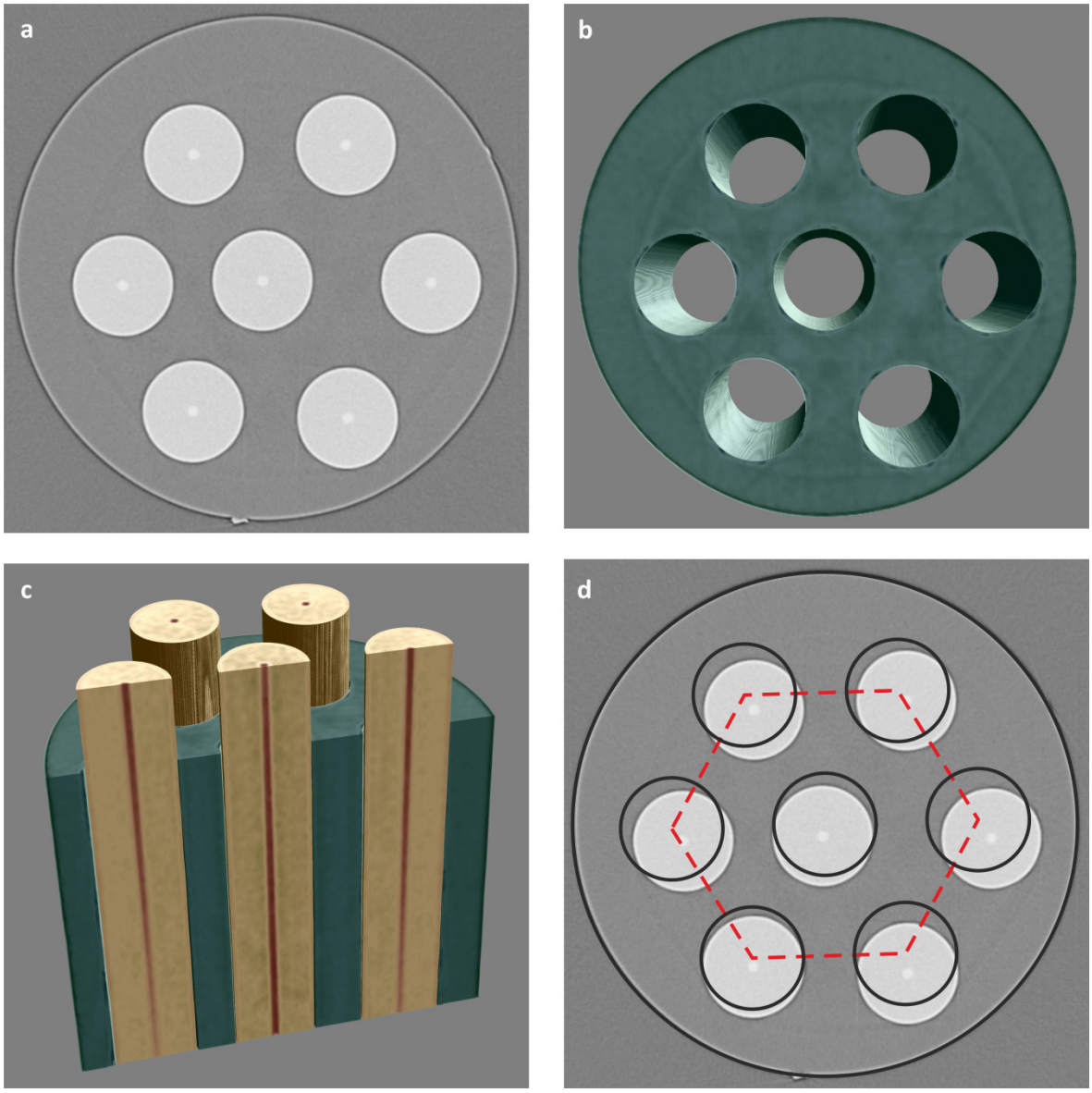

Figure 4.10: X-ray CT analysis of a 7-element MEF. **a**, A virtual cross-section image produced from the CT data. **b**, The polymer coating region only. **c**, A 3D view of the MEF structure showing the Ge doped cores within the three diagonal elements. **d**, Real Vs desired MEF structure: the XCT allows to identify deviations from target design in the real fibre.

The MEF diameter was measured 400µm and the cladding diameter of each element is ~80µm. The average core size of the elements is about 8.5µm. A dual-coating process was used in the fabrication of this MEF. The element cores were doped with ~3.7 mole% of Ge representing Δn=0.0055. Despite the low concentration of Ge, the sensitivity of X-ray CT to material density allowed distinguishing between the core and cladding of each element, as well as differentiating between the two polymer coating materials. Figure 4.10 **d** compares an ideal structure against the actual fibre, highlighting asymmetries in the location of the seven elements.

4.6 X-ray CT analysis of HC-PBG fibres, canes and preforms

This section describes the large body of work that I have carried out during my project in order to achieve for the first time a precise characterisation of the full fabrication flow of Hollow Core Microstructured Fibres using the XCT technique. My target was thus to identify new ways to analyse the presence of potential structural defects, contaminations or stacking imperfections of stacked PBGF preforms, canes and of the final fibre using a technique capable of measuring all the three stages with their very different scale factors, in particular non-destructively in the case of canes and preforms. Therefore, preforms, canes and even fibres can be used following such measurement. In the following, I discuss in detail the three types of analysis, which are carried out along similar lines but also have some important differences.

As introduced in Chapter 2, HC-PBGFs belong to the family of microstructured fibres. They have a complex cross-sectional structure with a central large hole as their core and a microstructured cladding with a few hundred holes surrounded by sub-µm glass nodes connected via very thin (~100nm) glass membranes (as shown in Figure 4.11 **d**). These features extend uniformly along the entire length of fibre. The electromagnetic resonances of the nodes of the HC-PBGF determine the guiding mechanism and therefore their consistency and uniformity both axially and transversally are paramount [9].

As explained in detail in Chapter 2, HC-PBGFs are fabricated through a complex, labour-intensive fabrication process. A plurality of ~mm diameter high purity glass capillaries are stacked in a hexagonal lattice and inserted into a glass tube to form the first stage preform with a typical OD of a few cm. Figure 4.11 **b** shows an example of a first stage preform with 25mm OD. The first stage preform is drawn down to a microstructured cane with an OD of a few mm. An example of PBGF cane is shown in Figure 4.11 **c**, (diameter in this case is ~3mm). The cane is then inserted into another jacketing tube to form the second stage preform. This final preform is then drawn on a fibre-drawing tower to produce the final HC-PBGF with a typical OD ranging from 100-300 microns depending on the target structure and operating wavelength of choice [9].

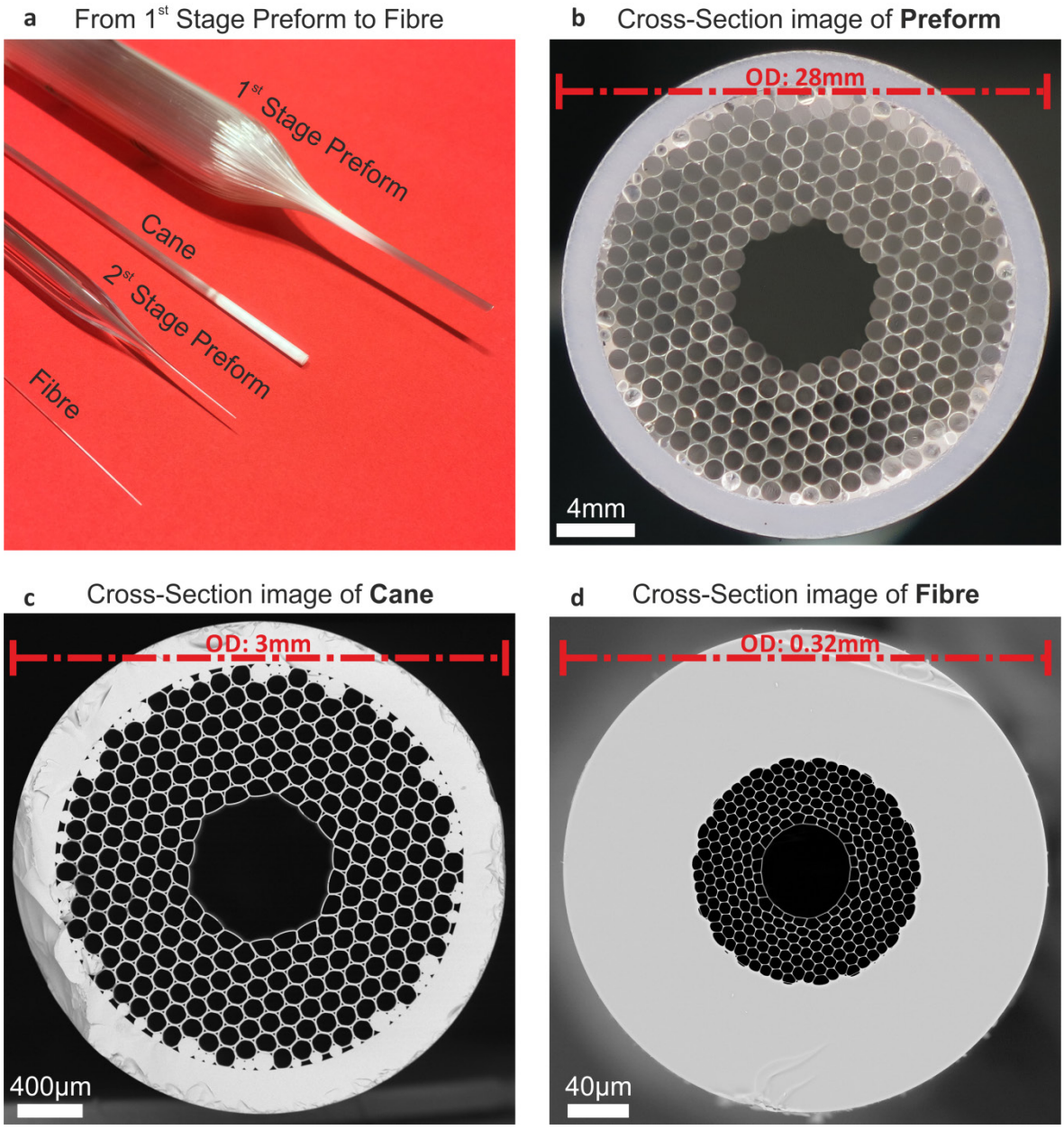

Figure 4.11: Different fabrication stages of HC-PBGFs. **a**, A photo showing the three fabrication stages of a HC-PBGFs, including 1st stage preform, cane and the final fibre. **b**, A cross-section (optical microscope) image of a 1st stage HC-PBG preform (37-cell structure); the image was obtained by cutting the preform itself with a diamond saw. **c**, A SEM image of a 37-cell HC-PBG cane. **d**, a SEM image of a 37-cell HC-PBGF.

As highlighted in Chapter 3, longitudinal consistency and absence of defects are required in both preform and cane to produce a long length of uniform fibre that is longitudinally uniform and free from inconsistencies. The transmission loss of the fibre can be significantly increased by defects [135]. At the onset of such fibre defects, the microstructure might have been altered significantly over a short distance scale of just a few centimetres or less, so rapid that its evolution is hard to capture by cleaving the fibre section and direct imaging of the fibre structure. Moreover, defects such as the one shown in Chapter 3 (e.g. see Figure 3.6) with overall length of up to several tens

of centimetres can be initiated from sub-millimetre defects (e.g. contaminants/cracks etc.) in preforms and canes, which can easily be missed during cross sectional inspection/imaging. CT provides a tool to image the full structure of preforms, canes and fibres allowing the longitudinal consistency to be examined with high resolution.

To highlight the above capabilities I examined each key fabrication stage of HC-PBGFs, i.e. the preform, cane and fibre by X-ray CT.

4.6.1 Analysis of preform

As mentioned in Chapter 2, the first stage preforms are still obtained by manual stacking of bundles of hundreds of capillaries. Though the manufacturing procedure is typically carried out by skilled people and in a cleanroom environment, due to the complexity of the structure and to the multiple steps involved in assembling it, there is a chance for defects to be introduced in the form of geometrical (stacking) errors and/or inclusions of foreign particles (e.g. – fibres, grains of non-vitreous materials e.g. refractory materials present in the furnace when capillaries are made, metal particles from tools and burners, etc.). Following the stacking process, the preforms are visually checked by skilled people before the cane draw process. However, this inspection is not helpful to identify fine particles and internal structural irregularities. It is worth mentioning that destructive inspection methods are out of question as they compromise the whole preforms, not just a small section of it.

XCT is the ideal solution to find if such problems exist, because: preforms are reasonably large-scale bodies; they are single material with a large Z/density contrast vs. air; moderate resolution is required ($\sim$100μm for features in the preform; $\sim$10μm for smaller defects such as point inclusions); and importantly, XCT is a non-destructive method.

HC-PBG preforms are usually about a meter long and have an OD of 20-30cm. They are rigid enough to be held on their own on the specimen stage (from one end) without experiencing vibrations that have impact on the measurement. Therefore, their installation on the stage is easy (care need to be taken to avoid putting excessive force on the glass, usually by using rubber pads). Following the sample installation on the XCT stage, one need to assure that the equilibrium spatial position is achieved before the scan process begins. An equilibrium spatial position is where the sample settles and experiences no further movement due to the mechanical relaxation of materials and devices used in the positioning of the sample. This is usually the case when the clamps of specimen holder grab the plastic protection tapes around the preforms or canes/the polymer coating of the fibre samples. Due to the specimen height restriction, we can only use the Hutch scanner to measure a full-size preform. The Hutch has a 3μm resolution, which is well

beyond the requirement of this measurement. A specific short preform sample (e.g. a leftover preform from the cane draw process, or to further investigate the origin of problem in a scrapped preform), we could use the other two XCT scanners to gain better resolution.

A tomographic image of a preform is shown in Figure 4.12 **a**-**b**. The voxel size and scan length are 18.4µm and 36.8mm respectively. The preform was scanned by the Hutch setup. The source voltage was set at 70kV and filament current of 99µA producing 6.9W source power. The detector was used at its full 2000x2000 pixels resolution and the number of projection used was 3142 with 4 frames per projection and frame exposure time of 354ms. The preform was also scanned by the HMX setup under exactly similar setup condition.

The XCT analysis is helpful to identify any longitudinal inconsistencies and irregularities in the arrays of capillaries such as twist, bend or misplaced elements, if present at all. Figure 4.12 **b** shows a virtual cleave at the middle of the scanned section. There are a number unintentional excess interstitial gaps, some of which is highlighted, formed by some row of elements within the stack drifting across the structure; this is caused by imperfect tight packing of the structure and leads to more important stacking errors such as misplaced capillaries or packing rods. In Figure 4.12 **c** I super imposed three cross-section images from virtual cleaves obtained at the top, middle and bottom of the XCT dataset (as marked with the white dashed lines on Figure 4.12 **a**). The images are coloured red, green and blue from top to bottom respectively. The colours mix where there are overlaps between the structures (e.g. the white areas show where all the three colours overlap, like the jacketing tube or core plug tube). One can notice a form of a helical twist in the structure and more specifically in the outer ring of capillaries. It is worth mentioning that this dislocation is not visible from the free ends of the preform, which is the usual method of checking the preform.

Additionally, it is possible to identify contamination in the preform based on its shape or material density, and to detect failure of any part of the structure such as any broken glass capillaries or cracks. All this helps substantially improving time and cost management of the fibre fabrication process by preventing costly and time-consuming fabrication of canes and fibres from a problematic preform.

Based on the result I obtained, I believe XCT analysis of preforms is the best inspection method that one could achieve given no constraints.

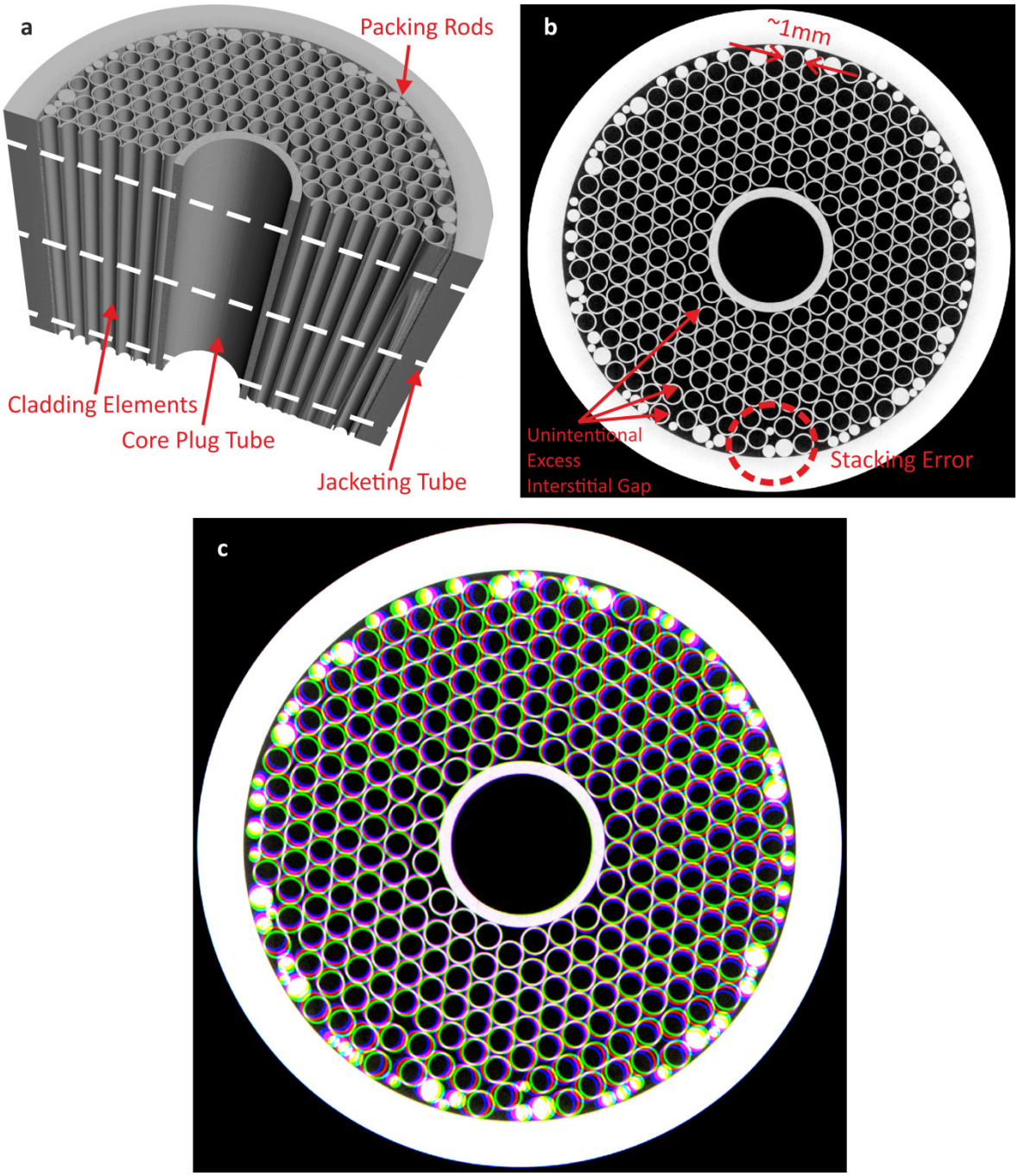

Figure 4.12: **a**, (top left) X-ray CT image of a 37-cell first stage preform incorporating a core plug **b**, virtual cross section showing problems in the tight packing leading to excess gaps between the elements, dislocations of whole rows of capillaries etc. **c**, Superposition of three cross-section images from virtual cleaves obtained at the top, middle and bottom of the XCT dataset, showing a form of helical twist in the preform

4.6.2 Analysis of HC-MOF canes

The first stage preform problems described above can cause unintentional structural irregularities and/or can transfer foreign particle or contamination to the canes. In particular, the particles or contaminants may survive the cane draw process and leave residuals in the cane. In addition, the

irregularities may happen by fabrication instabilities or variations in the fabrication control parameters (as discussed in Chapter 2). Before the canes can be used to make second stage preforms, canes should ideally be quality checked. This in principle should include detection of any irregularities and/or foreign particle or contamination. Currently there is no standard (or easy) inspection method to detect these problems and all checks are done visually from outside by an expert fabricator. As discussed before, the quality checks need to be non-destructive and should be able to resolve fine internal structural details.

Similar to the case of preforms, XCT is the ideal solution to find if such problems exist, because the internal structure of the canes can be well resolved by XCT analysis. This is mainly due to the fact that the required resolution for cane inspection is well within the capacity of XCT systems (~10 μm for features in the preform and a few microns for smaller defects such as point inclusions); and canes' large Z/density contrast (air/glass) resolves features sharply in the XCT images. In addition, XCT analysis is non-destructive, allowing the cane to be used for fibre fabrication process.

HC-PBG canes are nearly a meter long and have an OD of only a few mm. This large dimensional aspect ratio (~100:1) is susceptible to vibrate when it is hold from one end on the rotating stage of the XCT scanner. The vibration is getting worse as we move further away from the stage (where the cane end is fixed). To tackle this problem, we wrapped Teflon tape around the cane and inserted it inside a larger diameter carbon fibre tube – both Teflon tape and carbon fibre tube have minimal effect on the XCT measurements due to their low mass density/Z. This solution was good enough to reduce movement well below the required scan resolution. Because of the specimen's height restriction of the scanners, we used the Hutch XCT scanner for the inspection of full-size canes. When we had a specific short cane samples (e.g. leftover cane from a fibre draw process, or to further investigate the origin of problem in a scrapped cane), we could use the other two XCT scanners to gain better resolution.

Figure 4.13 shows the X-ray CT image of a HC-PBG cane (which, as seen above, is about 10 times smaller in diameter as compared to its first stage preform). I used the Xradia 510 Versa to measure this sample. The voxel size and scan length are 3.35μm and 3.39mm respectively. Other scan parameters include 2501 projections, source voltage of 50kV, 1s exposure time and source power of 4W. The size of obtained dataset was 1012x1012x1012 voxels.

This is an example of a cane presenting an excellent consistency and longitudinal uniformity. The cross-section image in Figure 4.13 **b** obtained via a 'virtual cleave' at the middle of the XCT data set (where is marked with the red dashed line in Figure 4.13 **a**) does not show any specific distortion. A cross section image obtained from a physical cleave (such as Figure 4.11 **c**), suffers

from distortion caused by the cleaving process, which can be totally avoided with XCT analysis. Moreover, XCT result in this case provides a cross-section image per every 3.35µm in longitudinal direction, which cannot be obtained by conventional physical cleaving process. This advantage, in particular, is more helpful in the analysis of particles and contamination, which can be easily missed in a physical sectioning with long separations, an example of which is shown in the following.

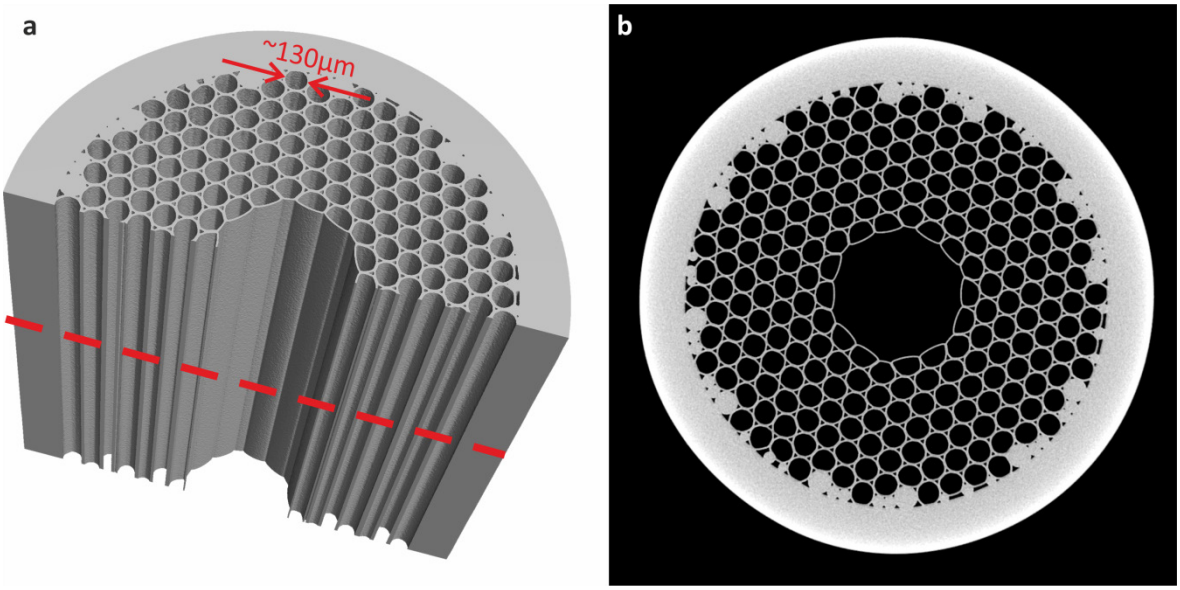

Figure 4.13: **a**, X-ray CT images of a 19-cell cane. **b**, Cross sectional image.

Next, I studied a full-size cane using the Hutch setup. This sample was particularly chosen to test the density-dependent response of XCT in the study of contamination and foreign particles within the preforms, canes and fibres. We measured the cane we studied in Chapter 3 using XCT. Figure 4.14 **a** shows a high-density contaminant found in between the outer ring of the microstructure cladding and the jacketing glass tube in one of the canes I examined. The density of this defect would seem to indicate it is a high-density material, (I speculate a metal particle), which may have accidentally been incorporated during the first stage preform assembly. As mentioned above, there is a chance for defects to be introduced in the form of geometrical (stacking) errors and/or inclusions of foreign particles (e.g. – fibres, grains of non-vitreous materials e.g. refractory materials present in the furnace when capillaries are made, metal particles from tools and burners, etc.) during the assembly and manufacturing of the first stage preform.

Based on these findings, we are investigating the change of the lathe burner from a metal burner to a glass burner, which reduces the chance of incorporating metal contaminates in the capillaries that are used for stacking. In addition, antistatic blowers that are used above the stacking rig can shed metal particles originating from their internal components such as their electrical motors.

We are investigating the use of other charge-neutralizing solutions like long-range antistatic bars. Moreover, we are looking into better grade cleanroom solutions, such as laminar flow bench and soft wall cleanrooms to reduce the chance of incorporating particles in to the capillary stacks and preforms.

The deformation induced by the particle on the wall of its adjacent hole is shown in Figure 4.14 **b**. I showed the optical microscope image of this defect in Chapter 3, Figure 3.17 (lower left). Here I could analyse the defect with much more details about its shape, material properties and its exact position. A particle like this, which has survived the cane fabrication process, is likely to cause a fibre break during fibre fabrication. Additionally, if such a structural deformation were to happen in the vicinity of the core, it would almost certainly introduce a number of undesirable degradation in the transmission properties of the resulting fibre, including additional loss and intermodal coupling, localized surface modes, etc. Moreover, one would have missed such defect as the inner layers of the cane are not accessible through non-destructive optical microscope inspection methods.

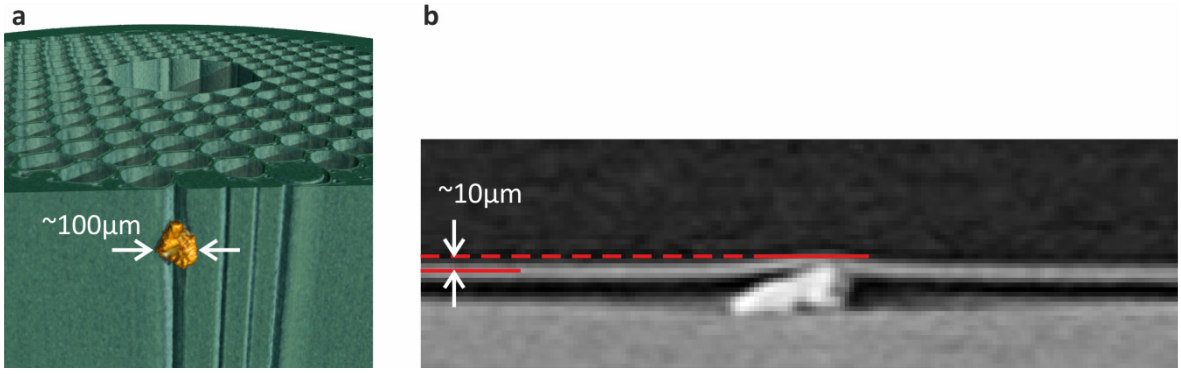

Figure 4.14: X-ray CT images of a contamination in HC-PBG cane. **a**, 3D image of a Metal-like particle in the cane. **b**, Deformation induced by the particle on the wall of its adjacent hole.

4.6.3 Analysis of fibre

Cleaving a HC-PBGF and imaging its cross-section is not considered destructive in most cases after the fibre draw. However, avoiding a physical cut can be crucial in a number of circumstances such as:

- During the fibre draw process, where cleaving the fibre will interrupt the process and/or reduce the single-piece fibre yield.
- Analysing a fibre where no physical cutting of the fibre is possible, e.g. cleaving somewhere in the middle of a sample that needs to remain in a single piece, for instance in gas-cells or when fusion splicing is not possible.

Additionally, in order to study a fibre feature that sharply changes over a few cm (or less), a number of cross-section images is required with very small separations (see Chapter 3 for an example). Achieving such spacing using conventional cleave-and-image method is not possible.

Again XCT is an ideal solution in these situations to address such requirements. It is mainly because, an XCT measurement is a non-destructive process; HC-PBGFs have large Z/density contrast (air/glass); and the fine resolution requirement for the fibre defect analysis (a few µm for large features and ~0.5µm for subtle changes, similar to a standard optical microscope resolution) is still within the capabilities of XCT systems (as small as 50nm). Furthermore, one could potentially consider the possibility of measuring the structure as the fibre is drawn, assuming an image/radiogram with sufficient detail could be collected in a short enough time, compatible with the speed at which these fibres are drawn. At a fibre drawing speed of $30m/s$, which is equivalent to $0.5\mu m/\mu s$, an exposure of $\sim 1\mu s$ to X-ray source is sufficient to produce a radiograph with micron scale resolution. This requires high power X-ray source [161] and high-sensitivity fast X-ray detectors [162]. Nearly real-time, bench-top commercial XCT solutions are emerging such as Bruker SkyScan 1275 micro-CT, however they need further improvement in terms of scan time and resolution in order to provide a viable solution for inline monitoring during fibre draw.

HC-PBGF samples to be inspected by XCT can be as short as a few cm to several hundred meters long (or even longer). Their fibre OD varies between 150µm (for fibres operating at ~1550nm wavelength) to ~350µm (for mid-IR applications). They have a polymer coating with ~50-100µm thickness, adding up to a few hundred microns to the overall thickness of the sample. Because of their large dimensional aspect ratio, they can mechanically vibrate and/or easily bend during an XCT scan. Therefore, they are required to be properly mounted. I have used and/or designed various fibre mount to address this issue. The required scan resolution to study fibres is only possible using the Xradia 510 Versa among the three XCT scanners. This machine offers a suitable specimen holder (as shown in Figure 4.15 **a** and **b**) for our short fibre sample – in some cases for very short fibre samples with no coating I designed an intermediary device like the one showed in Figure 4.15 **c** to install the fibre in the holder.

The short samples (up to ~5cm) are rigid enough to be on their own on the specimen stage (being held from one end) without experiencing vibrations that have impact on the measurement. In mounting the short fibre samples with polymer coating, one should avoid putting excessive force on the glass, usually by using rubber pads. Following the sample installation, one should assure that the sample is settled in equilibrium position, and it experiences no further movement due to

the mechanical relaxation of the polymer coating (which usually takes up to a few hours. I usually left the sample for half a day).

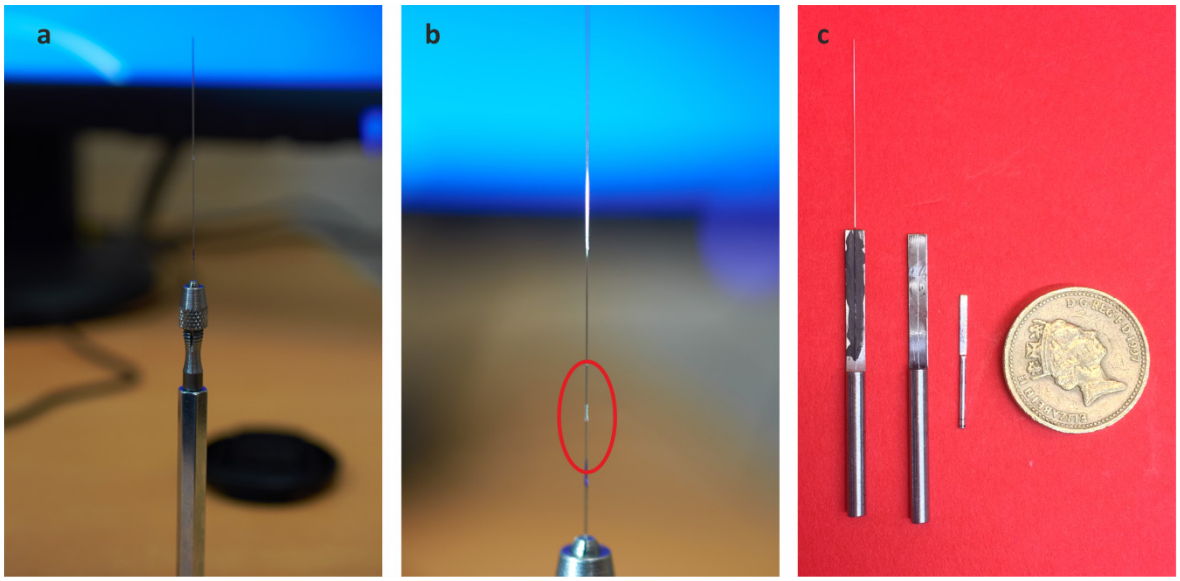

Figure 4.15: **a**, A short HC-PBGF sample mounted in the Xradia Versa sample holder. As highlighted by the red oval in **b**, this sample holder is suitable for fibres that have polymer coating – below the bright section inside the oval, the fibre sample has polymer coating. **c**, The intermediary devices that I use for mounting the short uncoated fibre samples.

For long fibre samples, fibre needs to be clamped from both sides (top and bottom). I designed a specific mount to provide the required support for our samples longer than 5cm. In addition, using this mount, I should be able to scan sample that are several hundred meters long. Figure 4.16 **a** shows the CAD design of the mount, which was made by the ORC workshop (Figure 4.16 **b**).

Figure 4.17 **a** shows a virtual cross-section image of a Mid IR 19-cell HC-PBGF obtained via the Xradia 510 Versa. In Figure 4.17 **b** I cut-away a section of the structure during the post processing of the data in order to show the internal structure of the fibre. This is an example of a large diameter uniform fibre. The voxel size here is set to 0.418µm and the scanned length of the sample is 407µm. Other scan parameters include 1601 projections, source voltage of 40kV, 15s exposure time and source power of 5W. The size of obtained dataset was 973x973x973 voxels. parameters for this scan include 801 projections, source voltage of 80kV, 11s exposure time and source power of 5W. The size of obtained dataset was 974x974x974 voxels, with a voxel size 0.360µm.

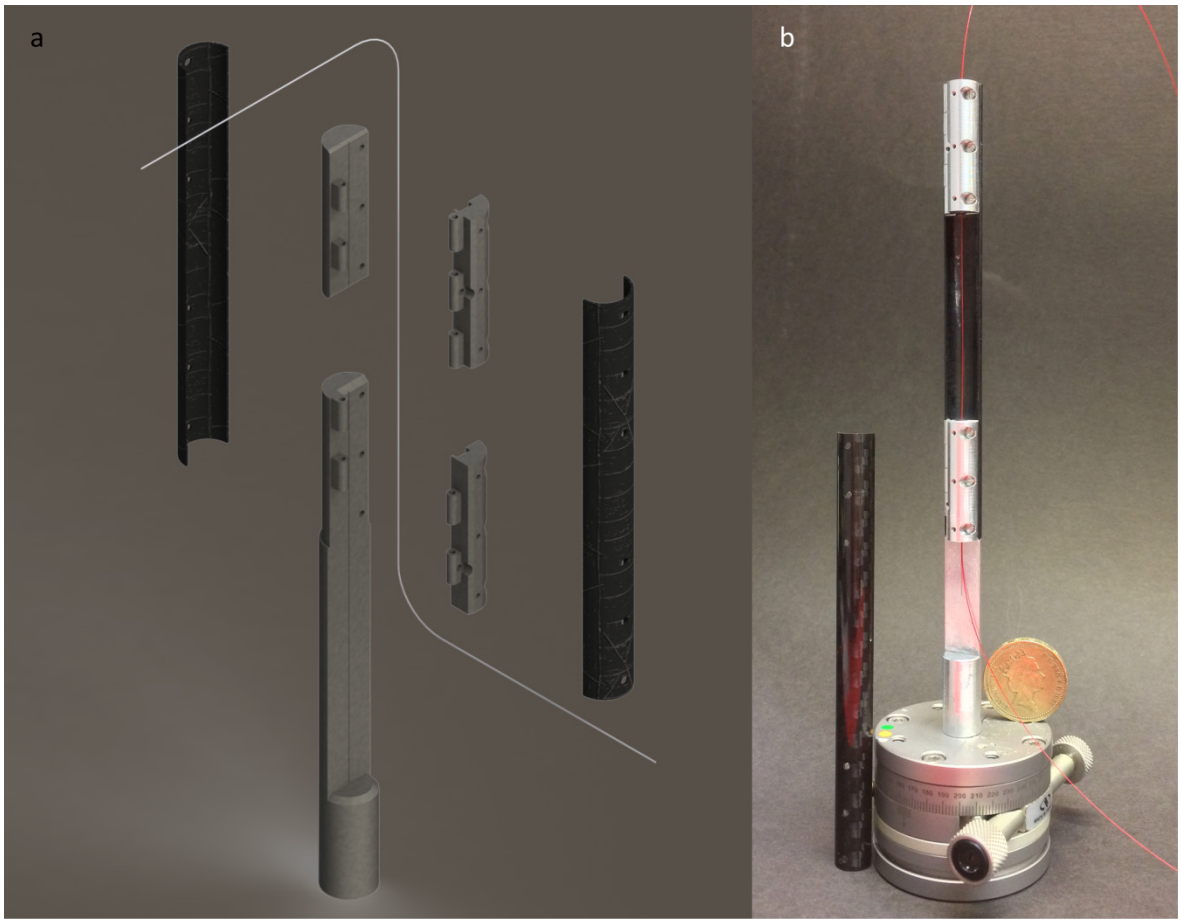

Figure 4.16: (Right) A detailed schematic of the parts composing the custom made fibre mount I designed to hold long fibre samples; (left) the finite product.

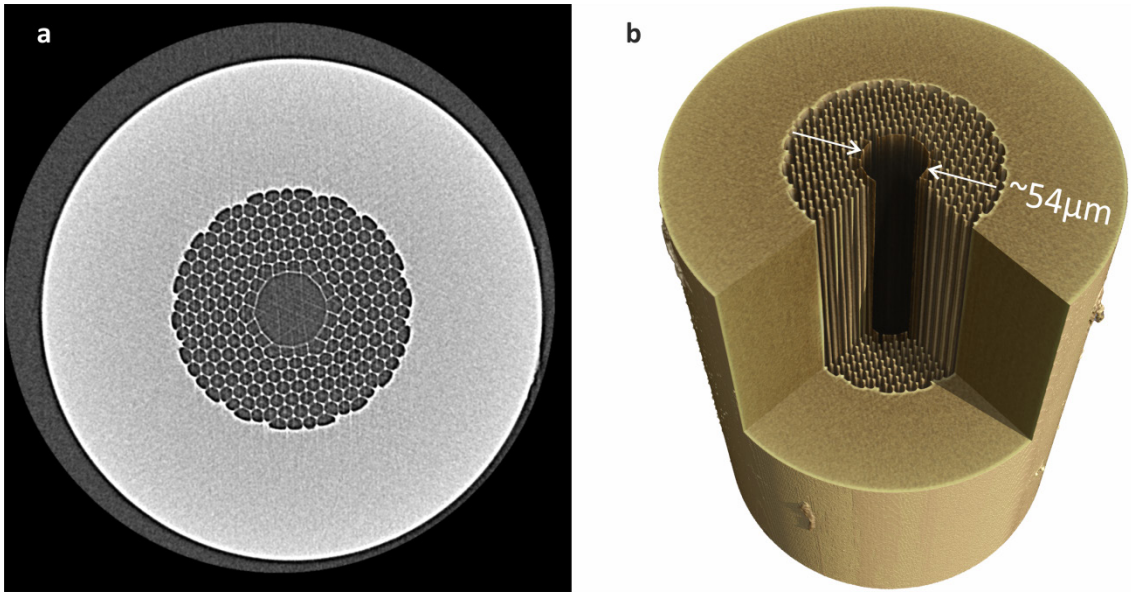

Figure 4.17: X-ray CT image of a 19-cell fibre. **a**, "virtual cleave" cross sectional image of the fibre; **b**, Reconstructed image with a quarter slice removed to show the inner microstructure.

In another attempt, I used XCT to look at the fibre I studied in Chapter 3. Figure 4.18 **a** shows the virtual cross-section image of a sample section of the fibre with uniform structure. The polymer coating around the sample is also seen in the figure. I scanned another piece of the fibre that has a scattering point based on the IR imaging method (discussed in Chapter 3). Figure 4.18 **b** shows a virtual cross section image of the piece with structural distortion in the microstructure surrounding the core. As there is no mechanical cleave is involved, one can infer that the distortion is solely due to an event inside the fibre related to its draw process. The scan

One could use XCT systems with higher resolution (like e.g. the Xradia 810 Ultra [148]) to see more details of the microstructure. In general, any structural defects or contaminants from small foreign objects are identifiable as long as they are larger than a voxel. Unfortunately, the fibre section containing the transition region from normal to distorted structure was lost during the sample preparation. However, based on my findings in Chapter 3 and considerations on the length scales typically associated with the formation of these defects, I am fully confident that the XCT is the best tool to study such quickly evolving structural transitions.

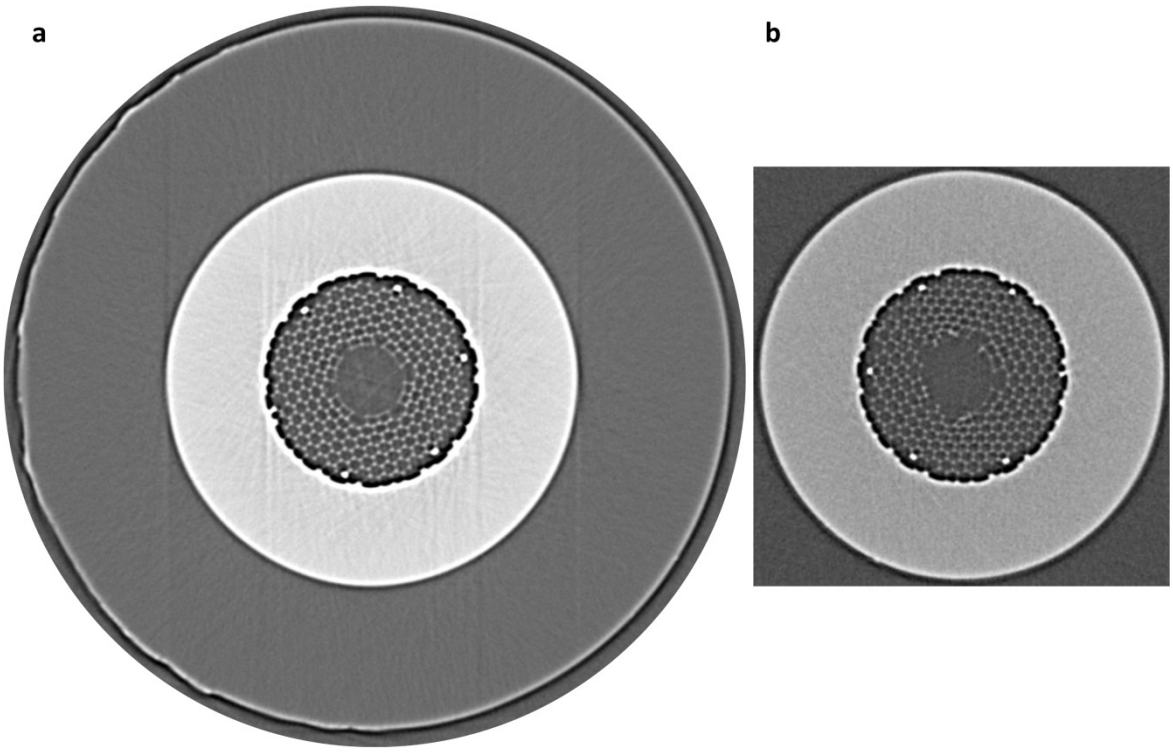

Figure 4.18: XCT image of a structural defect in the microstructure surrounding the core of a 19-cell HC-PBGF. where **a** shows the normal and **b** shows the distorted structure respectively. This fibre was studied in Chapter 3.

4.6.4 Analysis of preform transition regions

Since I have shown that the XCT technique is able to analyse all the fabrication stages namely preforms, canes and fibres, of even the most complex MOF structure, a natural consequence is that the same technique also offers a way to analyse the transition between any two of these stages. Such transitions occur e.g. when a preform is drawn into cane (first stage draw), or a cane preform is drawn into the final fibre (second stage draw). The region in which the scale of the overall structure is reduced is often referred to as the "neck-down region". It is important to recognize that the scale reduction generally happens along with significant changes of the inner structure, for example: some larger holes may grow, smaller holes may collapse, and the shape of some glass struts may change and so on. Some of these changes are controlled via external parameters, and some others are dictated by the physics of the drawing process/fluid dynamics. Here I need to stress the importance of capturing these changes, as through understanding their underpinning mechanism and behaviour we should be able to engineer the preforms in such a way that a fibre with desired shape and performance is produced. Until not long ago, such changes were not very well understood (as the transition happens in the hot zone inside a furnace, where standard imaging techniques are unsuitable). A group colleague at the University of Southampton, Dr Greg Jasion, has produced a fluid dynamic computational model to describe the cane and fibre draw processes [58, 163]. One of the aims to develop this model was that of being able to capture the structural modifications occurring during these processes without need to perform an actual draw. However, the task of checking the reliability of the model and performing the necessary parameter calibrations appeared initially to be a very difficult task, due to the lack of suitable experimental data. However, XCT provide an elegant way tool to validate the model, by collecting detailed structured data of a full neck-down region, e.g. from preform to cane (all the way through the transition region). Suitable samples were obtained by interrupting the drawing process and extracting the neck-down region from the furnace, thereby "freezing" it in the configuration identical to that inside the furnace. More in detail, I used the HMX setup to analyse the first stage transition and the Xradia 510 Versa system for the second stage transition, where their corresponding preforms evolves to make the cane and fibre respectively.

In order to install the 1st stage preform neck-down sample (which is ~40 cm long with the transition region in its bottom 10cm section) on the specimen stage of the X-Ray instrument, I needed to use a special mount. The mount was designed to hold the preform with its tip pointing downward, mainly because the movement range of the specimen stage along the preform axis is limited. A similar situation also applies to the installation of the 2nd stage preform neck-down sample on the specimen holder of the Xradia 510 Versa setup. Figure 4.19 shows the mount I designed for this purpose (it was manufactured by the ORC workshop technician). This design

allows close to uniform X-ray exposure over 360˚ rotation of the stage – depending on the uniformity of the plastic tube surrounding the sample. The low mass density of plastic materials would have minimal interaction with the X-ray flux – therefore it is my material of choice for the tube.

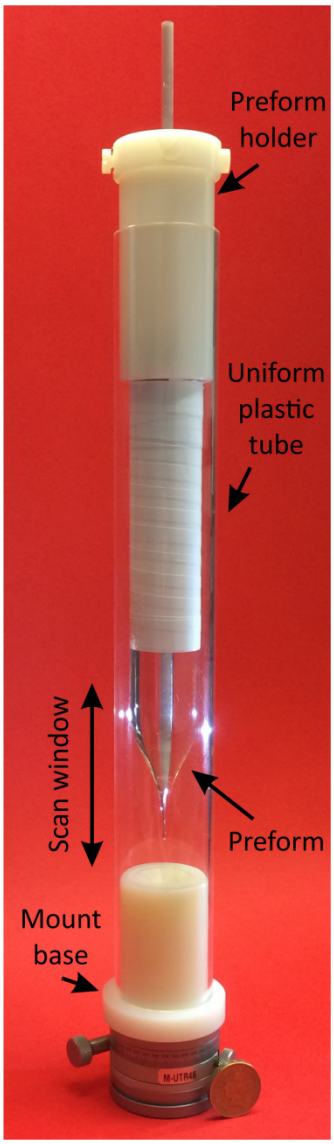

Figure 4.19: Custom designed holder for performing XCT analysis of the transition region of a 1st stage draw using XCT.

The XCT technique provides an ideal technique to obtain an unprecedented set of structural data across the full transition region and changes associated with the scale transition from preform to cane and likewise from 2nd stage preform to the final fibre. Figure 4.20 shows the result XCT analysis of the transition region of a 1st stage 19-cell HC-PBG preform. On the top left, a photograph of the neck-down is shown. The dashed white lines show the relative position of a number of virtual slices I have chosen to illustrate starting from 0 on top and extends to 66mm at the bottom. The cross-section images (cut to half along the symmetry axis) on the left correspond

to the position of virtual slices. One can observe how the core tube deforms and expands and finally fuses to the capillaries of the microstructure cladding. Also, the small relative expansion of core and contraction of the cladding in the final cane with respect to the preform arrangement is observable. One can follow these changes (with more details) in the 3D representation of the dataset shown on the left bottom of the figure.

The above dataset is generated by joining two other datasets, one covers the upper section of the preform and the other covers the lower section with a small region of overlap between the two scan for alignment purposes. For both these scans, the voxel size and scan length are 18.4µm and 36.8mm, respectively. The source voltage was set at 70kV and filament current of 99µA producing 6.9W source power. The detector was used at its full 2000x2000 pixels resolution and the number of projection used was 3142 with 4 frames per projection and frame exposure time of 354ms.

Figure 4.21 shows the analysis of a 2nd stage transition region of a preform obtained from a 19-cell cane. On the top left corner of the figure, a photograph of the transition (neck-down) region is shown. The fuzzy structure in the middle of the glass tube is the cane. Below the photo, on the left side of the figure, a lateral cross-section image of the preform is shown. The image includes three distinct sections (based on the image contrast of the sections), each of which corresponds to a dataset covering a section of the preform. In order to reconstruct the transition region, three scans were preformed (with similar scan settings) and the datasets were concatenated to produce the full geometry of the transition region. For these scans, the voxel size and scan length are ~10µm and ~20mm, respectively. The source voltage was set at ~130kV and filament current of ~53µA producing 6.9W source power. The detector resolution was 2000x2000 pixels and the number of projection used was 3142 with 16 frames per projection and frame exposure time of 354ms.

The red dashed lines correspond to the position where the cross-section images on the right side have been obtained. On the top (0% dashed line), the can has already fused to the jacketing tube, however its structure has not considerably changed. At a position 25% of the scan length lower, the core has significantly contracted and the microstructure cladding has expanded. The core contraction continues until the 50% of scan length. The core starts to expand as it approaches to the 75% position. The expansion of cores is the maximum, as it reaches to the end of scan. One can also notice the relative expansion of the microstructure region as compared to the thickness of the jacketing glass.

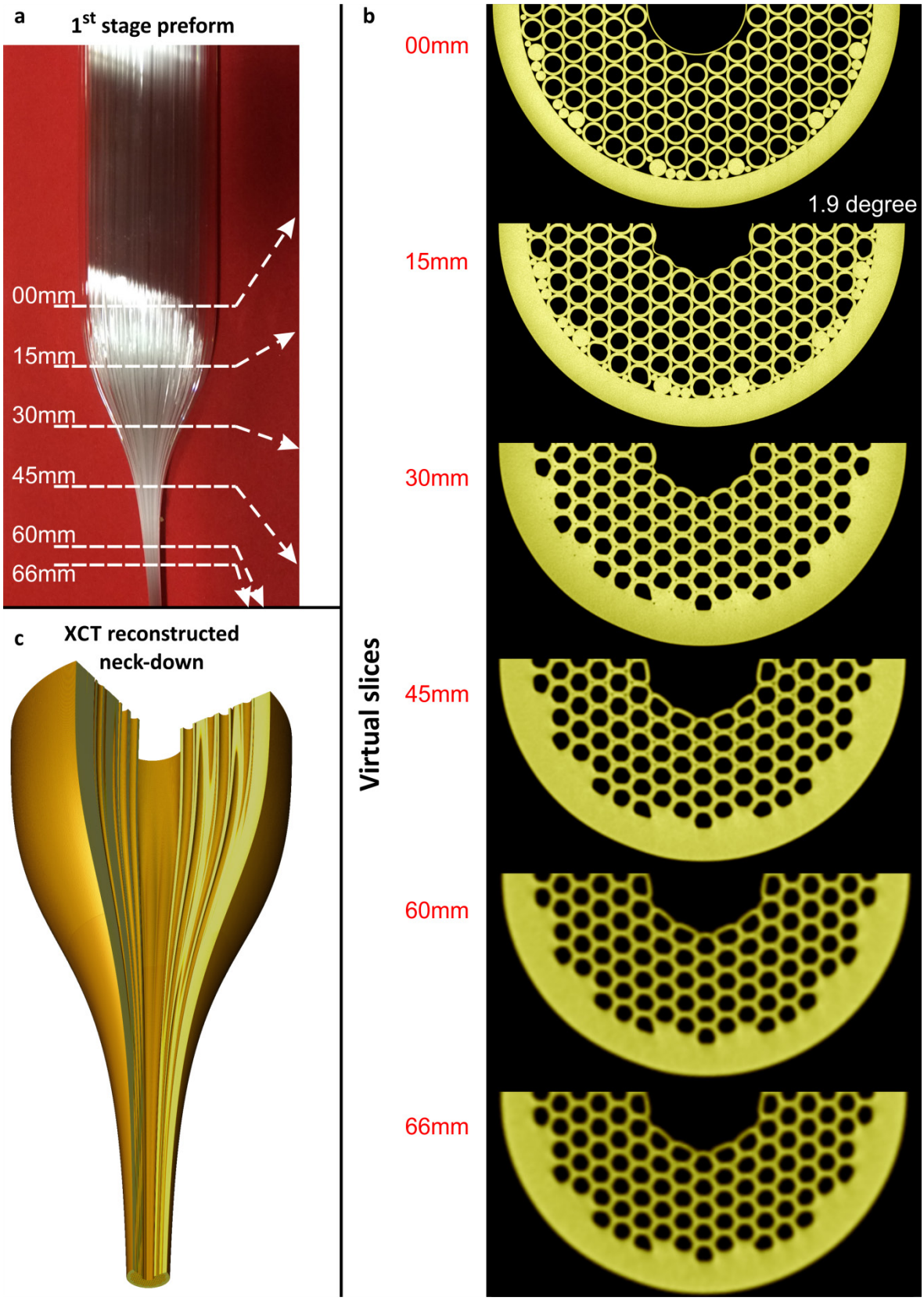

Figure 4.20: XCT analysis of preform to cane (1st stage draw) transition region. **a**, 1st stage preform photo with white arrows highlighting the position of virtual cleaves. **b**, Virtual cleave showing the half the cross-section of the preform across the neck-down. **c**, XCT reconstructed neck-down – quarter data cut-away to expose the internal structure.

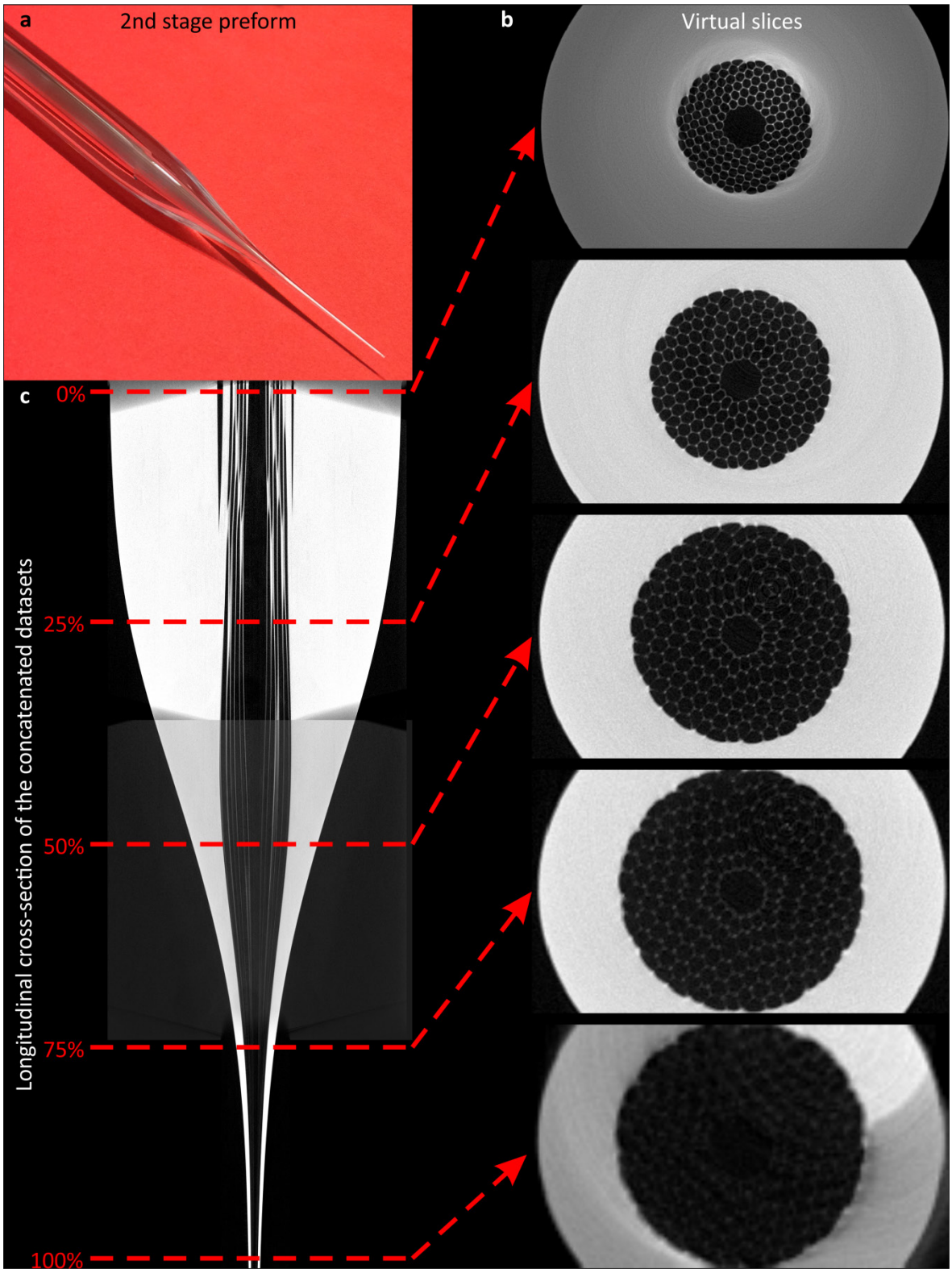

Figure 4.21: XCT analysis of cane preform to fibre (2nd stage draw) transition. **a**, 2nd stage preform photo. **b**, Virtual cleave showing the cross-section of the preform across the neck-down at the position shown by arrows. **c**, Virtual longitudinal cross-section of the concatenated datasets covering the whole transition region, with red arrows showing the position of virtual slices in **b**.

4.7 More exemplar cases

In this section, I demonstrate a few other very enabling applications of the X-Ray CT technique in the context of HC-PBGF development. These applications have been selected to highlight the power and usefulness of the approach its general applicability. Obviously, the application of X-Ray CT is not limited to these few examples – a few other possible areas for future development are mentioned in the conclusions chapter. While the measurements described in the previous sections mainly related to controlling the quality of the fibre fabrication procedures, the examples I discuss in the following are very important for the fabrication of devices based on HC-PBGFs.

4.7.1 Exploring the inner structure of HC-PBGF splices to itself

Fusion splicing is the standard method of creating a permanent joint between two optical fibres with low additional loss. Typical loss in SMF is ~0.05dB. In the case of specialty fibres, fusion splicing is still applicable in most cases, however it often presents more complications in terms of the additional loss, increased fragility and sensitivity of the splice point to external perturbations (such as bends, temperature variations, vibrations, etc.). Splicing microstructured fibres is particularly challenging because of the structural deformation, which can be potentially introduced in the microstructured by the high temperature processing required by the fusion splicing process. To achieve a robust and low loss splice, I have developed (as a part of a team) a special procedure to join HC-PBGFs together [164], and to fuse a HC-PBGF to a solid fibre [165-167]. However, careful choice of the splice recipe in order to avoid damage to the microstructure is essential. The recipe has been designed to fuse the peripheral solid region of the HC-PBGF while avoiding the collapse of the delicate central microstructure. Some qualitative information on the effect of the splice can be gained, for example, from imaging the splice from its side and/or by breaking the splice point carefully and inspecting each of the two sides for indications e.g. about the extent and uniformity of the fused zone, any modifications of the fibre microstructure, etc. [166], however, this requires an amount of guesswork in telling which deformations were caused by the splicing and which by the breaking of the splice. A non-destructive method that does not alter the structure in the slightest is much more preferable for the study and optimization of the splice process. X-ray CT offers such a non-destructive solution, which allows, as will be shown in the following, investigating the quality of the bond and the induced structural deformation in unprecedented detail.

Figure 4.22 shows micrographs of a 19-cell HC-PBGF that has been cleaved and fusion spliced to itself. The outer diameter of the fibres is measured as 211µm ± 0.7µm. Figure 4.22 **a** and **b** are dark field and bright field optical images of the splice point, respectively. The vertical discontinuity

in the middle of the images shows the merging point of the two fibres, which in the case of a perfect splice should not be visible. This can be due to the fact that no particular effort was made in this instance to align the two microstructured claddings, and alignment is only with respect to the outer diameter of the fibre. Possible small lateral misalignments as well as the deformation of the microstructure due to the fusion splicing also contribute to the visible discontinuity. The heat during the splice causes the microstructure (at the position of the joint) to retract slightly into the respective fibres, which forms a funnel-like region in the cladding of each fibre and thus a cavity between the two. Figure 4.22 **c** is an electron microscope image of the HC-PBGF cross section showing some deformation at the splice point. Tilting the fibre helps me picture the inward retraction of the microstructure; however, from a tilted SEM image it is not straightforward to quantify the magnitude of the deformation and to correlate it with the splicing parameters.

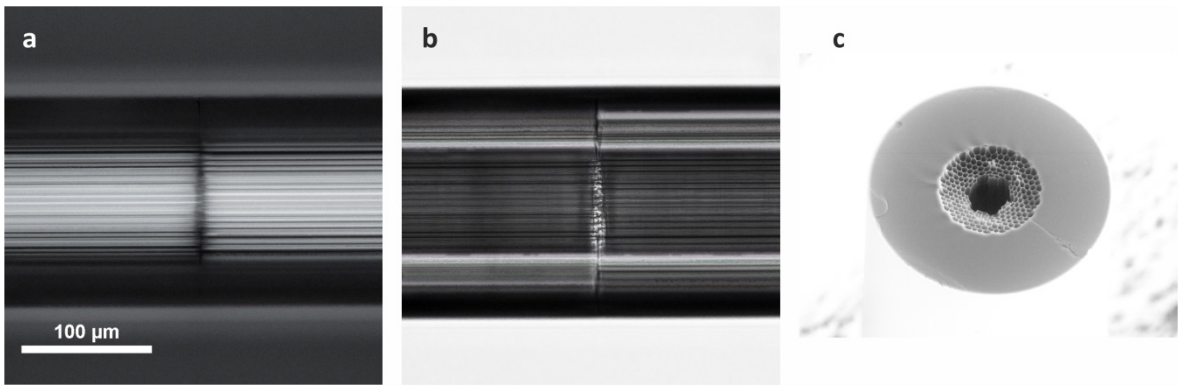

Figure 4.22: Microscope images of a HC-PBGF to HC-PBGF splice. **a** and **b**, Bright field and dark field optical microscope images of the side of a splice respectively. **c**, A SEM image of a side of the splice at angle.

Optical images such as those that are shown in Figure 4.22 represent the standard way to get qualitative information on the quality of a splice – a larger structural deformation almost invariably correlates with a higher loss of the splice. By comparing different images one can modify and optimize the splicing parameters available in the splicing machine (e.g. temperature and/or duration of the arc, etc.). However, for a more in-depth and quantitative details, X-ray CT can be used to assess the impact of the splicing process on the structure of the fibres on either side of a splice. I used the Xradia 510 Versa (0.7um resolution) for this analysis as described in the following.

Figure 4.23 shows the result of the XCT measurement. In Figure 4.23 **b**, data from a quarter of the structure are clipped out to expose the internal structure of the fibre and show the splice region. The position of the joint where the jacketing glass was fused together is visible in the centre of the image. The distance between the two microstructured claddings, or width of the gap at the splice point, varies between 0 (where they are touching) and 21µm in the middle close to the fibre

centre axis. The achieved voxel size in this scan is 0.714µm. Other scan parameters include 1601 projections, source voltage of 50kV, 10s exposure time and source power of 4W. The size of obtained dataset was 484x484x484 voxels, as the detector was used in 4-pixel binned mode.

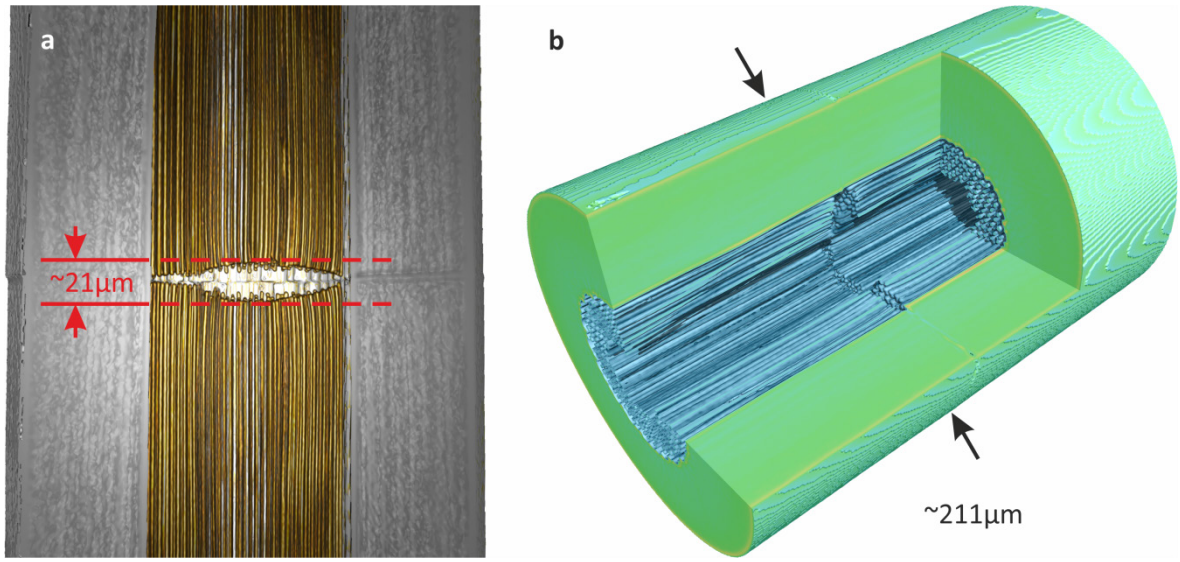

Figure 4.23: X-ray CT images of a HC-PBGF to HC-PBGF splice. **a**, CT image of the cavity formed at a splice point. **b**, Detailed tomographic image of a splice.

The CT data set of the splice contains vast amounts of information that can be post-processed in many different ways, some of which are shown in the examples below. A slight misalignment of the two cladding boundaries of very few µm can be clearly seen in the inset of Figure 4.24 **a**. The angular misalignment (~51˚) between the microstructures of the fibres is seen in Figure 4.24 **b** observed through the virtual cross-sections obtained before and after the splice point without physically cutting the fibre. The coloured dot in the outer cladding (which is one of the microstructure holes) is to demonstrate the relative orientation of one fibre to another. The concentricity of the core-to-core alignment is also measurable. The structural deformations due to the heating process are highlighted up to 165µm before and after the splice point. For example, in this splice the core has expanded from a nominal 38µm to 41µm near the joint over this distance scale. Yellow lines in Figure 4.24 **a** highlight the boundary of the core. At the point where the two fibres meet, on the left of the image the core boundary looks straight without any noticeable deviation from the ideal shape. However, a strong structural deformation is seen along the right core boundary. Moreover, I can observe the impact of the cleave quality on the strength of the bond; the uneven surface generated by the cleaving crack has caused a gap (the dark patch highlighted by the red ovals) in the bond between the fibres (Figure 4.24 **c**). The central part of the virtual cross-section image has been removed to avoid visual distraction. Any deviations from the original structure can affect fibre performance, similar to the structural defects I discussed in Chapter 3, and must be minimized using often-complex splice parameters in the recipe. This analysis thus provides a very powerful way to assess the impact of individual steps in the splice

recipe. As a result of this understanding, I managed to reduce the splice loss from a few dBs to ~0.2dB [164, 166].

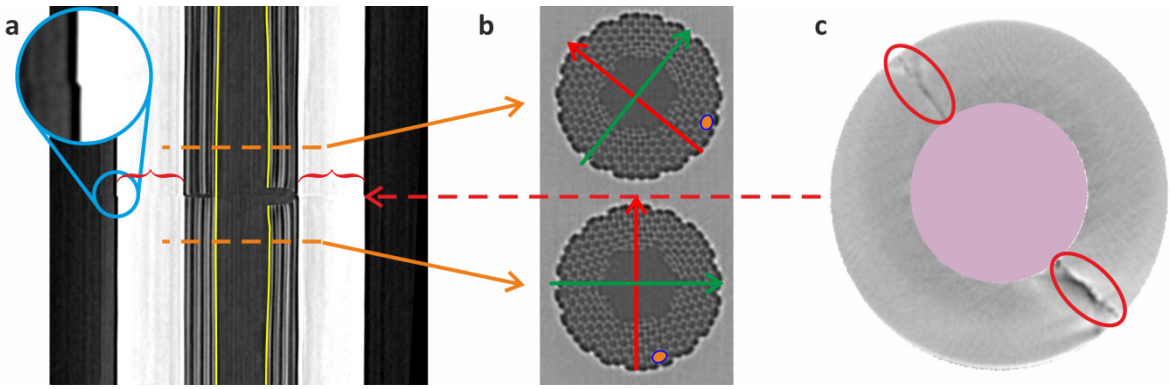

Figure 4.24: Some data analyses on the X-ray CT result of a HC-PBGF to HC-PBGF splice. **a**, Core boundary deformation induced by the splice and; misalignment of fibres at the joint. **b**, Angular (rotational) misalignments of the splice. **c**, Inconsistency in the bond that is induced by cleaving features.

4.7.2 Preliminary investigation into laser damage mechanism

Optical fibres are now widely used in the generation and delivery of high power/intensity optical radiation from fibre lasers. Delivery through an optical fibre has enabled a number of applications from industrial machining, welding and marking to sensing, microscopy and imaging to name just a few. However, physical phenomena associated to thermal damage (typically observed for longer laser pulses up to the CW regime) and nonlinear dielectric breakdown (relevant to ultrashort laser pulses) put a bound to the amount of power that can be transmitted by an optical fibre. In conventional fibres, such limit is imposed by the properties of silica glass, which, though it is a very resilient material, can undergo damage for high enough powers. Several hollow core fibre types, including both HC-PBGFs and anti-resonant HCFs such as Kagome Fibres (see Figure 4.25) are being investigated in this context as they promise to better the power delivery performance of solid fibres [7, 168-170]. Indeed, the damage thresholds of most gases are orders of magnitude higher than for any glass material and furthermore HC-MOFs could potentially be evacuated to remove any effects related to the gas normally present in these fibres.

However, even HCFs can undergo damage. This typically occurs when too high a fraction of power is coupled into the tiny glass membranes, which constitute the microstructured cladding. This can happen due to either poor fibre design, or poor alignment and/or beam wandering. Damage of HCFs is a very complex and as of yet poorly understood effect, with just a handful of studies describing experimental observation[7, 170].

Due to the stochastic nature of damage, it is important to be able to collect as much information as possible on how and where damage occurs and on how it evolves along the fibre. Damage generally occurs at or near the input facet but can then propagates for some length through the fibre. Direct visualisation techniques such as microscopy struggle to capture the fine detail of the damaged regions. XCT offer a non-destructive way to analyse these effects with sufficient resolution to capture enough detail.

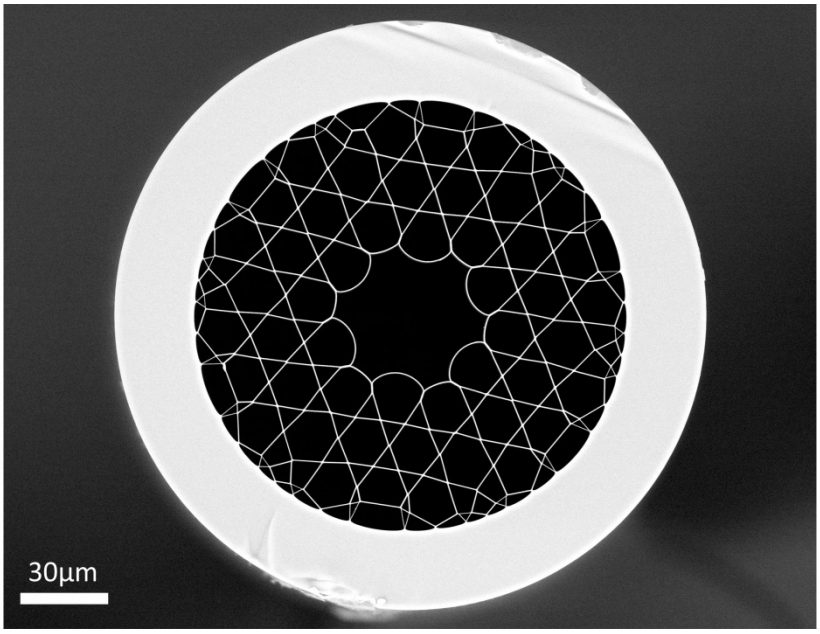

Figure 4.25: The SEM image of a Kagome fibre used in high power laser light delivery at a wavelength of 1µm.

I used the Xradia 510 Versa to analyse a damaged sample (in this case the HC fibre was a Kagome fibre developed by other colleagues in the group [171]). In order to install the samples on the XCT stage, I used the sample holders I introduced in section 4.6.3 for the study of fibres. Here, the sample are often short (less than 5cm) and can be mounted on the standard XCT sample holder using the intermediary devices shown in Figure 4.15 **c**.; one can use the fibre mount in Figure 4.16 for more delicate samples. To cover the full length of damaged section, as will be described shortly, ten scans were performed and for each scan, the voxel size and scan length were 0.33µm and ~324µm respectively.

Figure 4.26 a shows an optical microscope image of the input end of a hallow core Kagome MOF, which has been damaged as a results of a high peak power laser delivery experiment (7ps pulses, 45W average power, 200MW peak). The image was obtained by stitching four high-magnification bright-field microscope images. Not much can be seen from the region of interest inside the fibre, apart from dark green patches that stretch down to 2.2mm of the fibre – possibly caused by the damage.

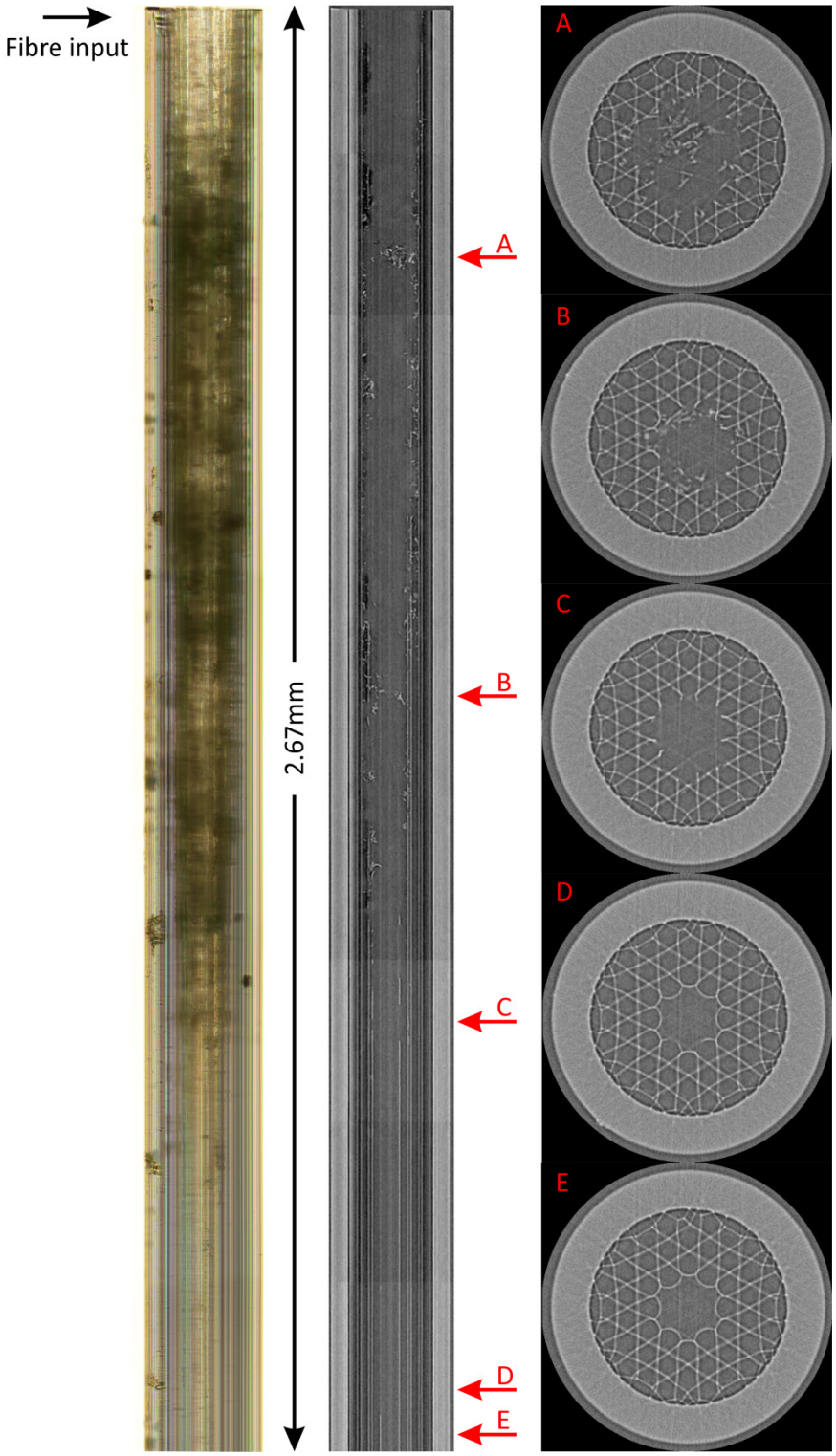

Figure 4.26: Damaged input facet of a Kagome fibre by a high power pulsed laser.

Next to the optical image, a lateral cross-section image of the sample (obtained by XCT analysis) is shown in Figure 4.26 **b**. At the points highlighted by the arrows alongside the lateral image (labelled with letters from A to E), the virtual cross-section image of the fibre is shown in Figure 4.26 **c**. These points are chosen where there is a sudden change in the extent of damage in the microstructure. The depth of damaged region (from the fibre tip to where the microstructure is back to normal) in this sample is ~2.5mm. This requires an elaborative complex XCT analysis,

which here includes concatenating 10 datasets to capture the full length of damage. The whole scan has taken more than 40 hours to complete and 10s of hours of data post processing. Figure 4.27 shows a 3D illustration of the concatenated data, to better visualise the extent of the captured information about the damage. In Figure 4.27 **b**, the fibre is viewed from its laser input face (a physical end of the sample), from a perspective angle. The data corresponding to a half of the fibre is removed to expose the internal structure of the sample. Figure 4.27 **a** shows the sample from a similar perspective, but from the other side of the dataset where the fibre structure is normal – this is a virtual end.

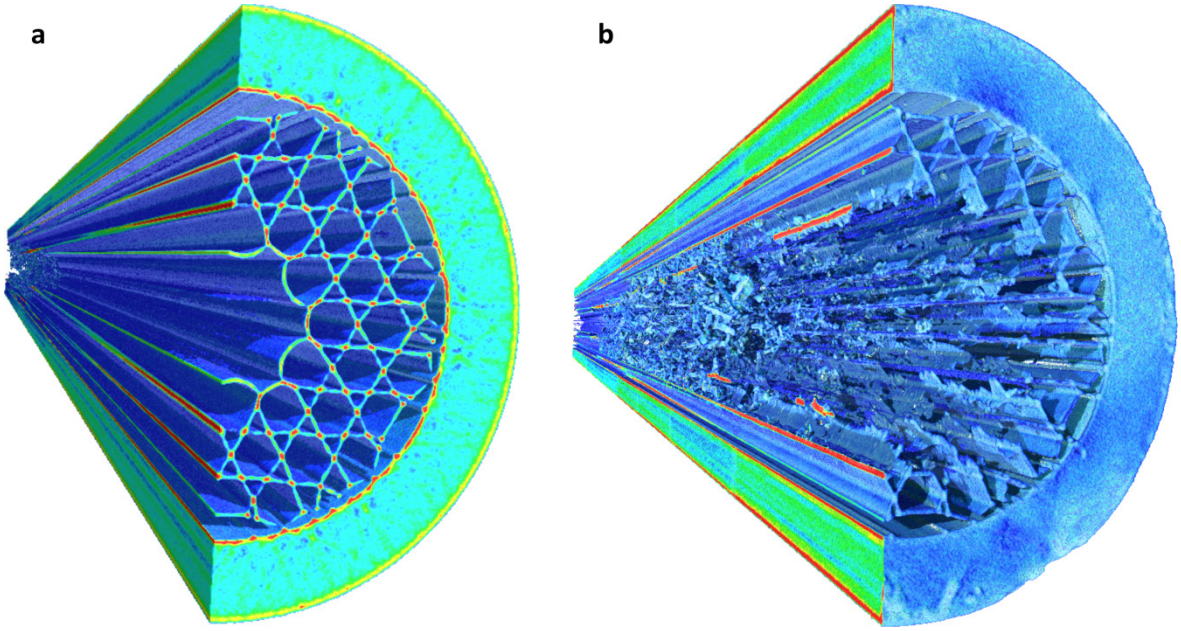

Figure 4.27: 3D illustration of the damaged fibre sample, where half of the structure is virtually cut away to reveal the internal structure. **a**, A perspective view of the concatenated dataset from the undistorted virtual end of the fibre. **b**, A similar view to the data set from the physical end of the sample where the pulsed laser was coupled and damaged the fibre.

4.8 Conclusions

In this chapter, I have presented the first demonstration of non-destructive X-ray CT to inspect the internal features of microstructured HC-PBGFs. XCT offers a powerful tool to evaluate the structure of both preforms, canes and the final fibre, opening up the possibility of analysing the full multistage fabrication process of these fibres, which is wholly impractical by using more standard techniques such as optical and electron microscopy.

I have shown results relating to a HC-PBG preform in which I identified some stacking errors via XCT analysis, which resulted in drift in the arrangement of capillaries and unintentional gaps

between various elements of the cladding region. These are relatively simple problems which can however have a catastrophic effect on the performance of the fibre, which relies on near-perfect geometry for its guidance mechanism. This type of analysis allow in principle the possibility to capture much smaller deviations and effects such as twist, small gaps, dislocations and missing elements without recurring to damaging the preform itself. I have also presented results on a specific HC-PBG cane (that I previously introduced in Chapter 3 in the context of defect identification) in which I have identified a contamination in from of minute particles, likely of metal. This analysis was again performed non-destructively providing unprecedented details, which enabled me to make a reasonable guess as to the nature and origin of the inclusion defect. In addition, I have analysed a specific HC-PBGF sample from a fibre that I studied in Chapter 3, in which I could identify similar microstructure deformation. Next, I have looked at the 1st stage transition region (necking region of a HC-PBG preform to cane) where the capillaries arrangement in the preform undergoes substantial structural change as it is scaled down to cane. I have also looked at the 2nd stage transition region (necking region of a HC-PBG cane preform to fibre) where the microstructure region expands and take up much wider cross-section area in the final fibre. None of above analysis was easily achievable using other conventional characterisation techniques. Based on these findings, we are investigating a number of modifications/ changes to our current fabrication steps and tools, such as improving the cleanroom grade where the first stage preform is assembled, changing the burners from metal to glass on the glass working lathe and replacing antistatic blowers to antistatic bars. Meanwhile we have introduced more stringent requirements on the cleanroom coveralls, in order to reduce various sources of contamination. Moreover, some of the results presented were used to validate a novel fluid dynamic model that predicts the draw process of HC-PBGFs, through a virtual draw [58, 163].

I have also presented how this non-destructive technique can be utilized to visualize and measure macroscopic and microscopic deformations within a HC-PBGF to HC-PBGF splice (an example of one of the most complicated fibre processes and devices). Here, this technique unveils structural changes induced by the splice process hidden to other conventional inspection methods.

Another “first demonstration” analysis that I was able to carry out was that of the damaged region of a HCF used for the delivery of very high peak-power laser pulses, a theme of great current interest. Following this preliminary investigation, my colleague Dr. Gregory Jasion applied for and was awarded a Research Fellowship from the Royal Academy of Engineering to design and develop hollow core fibres for high power laser delivery. In his work he will make constant use of the technique described in this Chapter.

I also carried out analysis of a 7-element MEF, which highlighted well the capability of the technique to discern between layers of different polymer coating, as well as any deviations in the fibre structure from the design target. Moreover, I have presented the analysis of a metal incorporated fibre, for which the presence of wires of a ductile metal complicates the fibre cleaving process to the point of preventing in practice to obtain clean and uniform cross sections suitable for visualisation/imaging. In the MIF we identified flaws within the metal wires. Our results illustrate the capability and value of using X-ray CT techniques in the ongoing refinement of various aspects of Microstructured and Multi-Material fibre fabrication and technology.

Chapter 5: Optical side scattering radiometry

5.1 Overview

In Chapter 3, I have discussed how structural defects might be present at specific locations along a HC-PBGF and how their presence can be detrimental to the fibre performance. In the same chapter, I have also shown simple ways to isolate, image and characterize each individual local defect. Those techniques are perfectly adequate to study a small number of defects but they are mostly qualitative, time consuming and limited to short lengths of fibres (i.e. those that can fit on a single spooled layer). As the performance of HC-PBGF technology improves in terms of loss and fabricated lengths, it is essential to be able to rely on better inspection methods that can measure longer fibres reproducibly and possibly in an automated way. As discussed in Chapter 2, the state-of-the-art techniques to perform these tasks on solid core fibres are typically based on back-scattering reflectometry methods like optical time domain reflectometry (OTDR) and optical frequency domain reflectometry (OFDR). The dynamic range and spatial resolution of these two techniques, however, whilst adequate for most mainstream telecoms fibres, cannot fulfil the requirements of current HC-PBGFs, with losses in the range of a few dB/km and lengths in excess of several km, where cm-scale spatial resolutions are needed to locate defect points accurately (see Chapter 3).

In this chapter, I present the method I have developed to measure the longitudinally resolved optical out-scattered fibre power with high spatial resolution (∼cm scale) and large dynamic range (>50dB). The study presented in this chapter follows the experiment discussed at the end of Chapter 3 in section 3.3.5, through which I developed a setup to automatically measure scattering map of long fibres. This data can then be used to infer information on the locally propagating signal and to obtain information on both local and distributed forms of loss. The method is validated through measurements on a standard telecoms fibre (Corning SMF28e) and subsequently used to examine an 11km HC-PBGF, which would not have been possible with any standard high-resolution reflectometry technique. I then use the technique to examine another HC-PBGF with unusually high loss, and finally I demonstrate the flexibility of the method by measuring a HC-PBGF operating at a wavelength of 2μm, at which no commercial OTDR is currently available.

5.2 Background

Backscattered power represents only a very small portion of the total light power scattered by a fibre. By way of an example, it is only ~0.13% in the case of commercial low loss single mode fibres operating at wavelengths around 1550nm [60]. In OTDRs and OFDRs, the light backscattered at a given position along the fibre length then has to travel all the way back to the fibre end in order to reach the detector. Therefore, it is further attenuated due to fibre loss and can also undergo other potentially undesirable propagation effects along its path. For instance, in a few-moded fibre, on its way back to the detector the backscattered power can be recaptured by a mode different from the one that has been initially excited, thus experiencing a different attenuation on its return path. All these issues, combined with practical limitations, e.g. on the maximum injected power and pulse width in OTDRs [60, 62], or the sampling frequency and wavelength range of the scan in OFDRs [64], limits in practice the resolution and dynamic range of commercial instruments.

In Table 5.1, Table 5.2 and Figure 5.1 I have thoroughly collected and analysed the performance of most known commercial OTDR and OFDR instruments operating at a wavelength of 1550nm. As can be seen, their performance is restricted to the points/shaded regions shown in Figure 5.1.

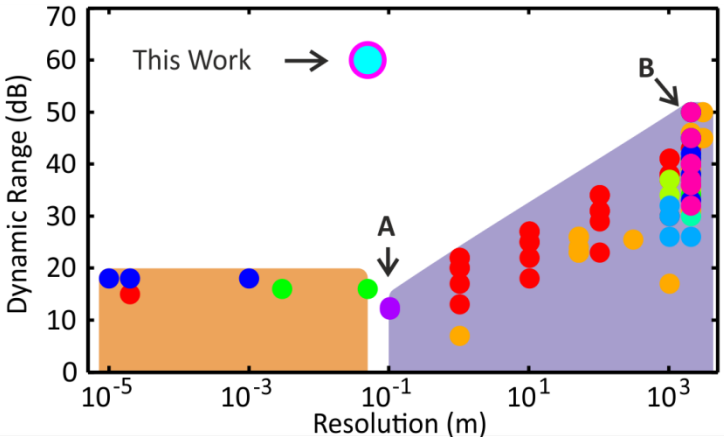

Figure 5.1: Visual representation of the dynamic range vs. longitudinal resolution of commercial reflectometry systems (> 70 instruments) as compared to the OSSR method described in this work. Different colours in OTDRs and OFDRs sections show different brands and instruments respectively. Point A refers to Luciol LOR-220 IR and Luciol v-OTDR and point B refers to Anritsu MW9087D, EXFO FTB-7600E, JDSU 8100D and Yokogawa AQ7285A. OFDR systems in this plot belong to Luna Technologies. The detailed list of devices analysed for this figure is presented in Table 5.1 and Table 5.2.

Table 5.1 shows the dynamic range (in dB) at a specific pulse width/ spatial resolution for the commercial OTDR solutions by Agilent, Anritsu, Corning, EXFO, Fluke, Fujikura, JDSU, Luciol and

Yokogawa. The table is left blank wherever the dynamic range information and/or the pulse width options are not available. The table represents 71 instruments and 100 entry points in Figure 5.1. The resolution has been calculated from the pulse widths based on the Equation (2.7) for a group index of 1.46.

Table 5.1: List of the OTDR systems with their corresponding dynamic range at a specific pulse width/spatial resolution. The dynamic range values are in dB.

Model	1ns (0.1m)	10ns (1m)	100ns (10m)	500ns (50m)	1µs (100m)	3µs (300m)	10µs (1km)	20µs (2km)	30µs (3km)
Agilent E6020B-013	-	13	18	-	23	-	30	-	-
Agilent N3910AM	-	17	22	-	29	-	37	39	-
Agilent N3910AL	-	22	27	-	34	-	41	43	-
Agilent N3911AL	-	22	27	-	34	-	41	43	-
Agilent N3914AL	-	20	25	-	31	-	38	41	-
Agilent N3916AL	-	20	25	-	31	-	38	41	-
Anritsu CMA5302	-	-	-	-	-	-	-	38	-
Anritsu CMA5225	-	-	-	-	-	-	-	36	-
Anritsu CMA5245	-	-	-	-	-	-	-	-	45
Anritsu CMA5246	-	-	-	-	-	-	-	-	45
Anritsu CMA5254	-	-	-	-	-	-	-	-	50
Anritsu MT9083C2-053	-	-	-	-	-	-	-	46	-
Anritsu MT9083C2-057	-	-	-	-	-	-	-	46	-
Anritsu MT9083B2-053	-	-	-	-	-	-	-	41	-
Anritsu MT9083B2-055	-	-	-	-	-	-	-	41	-
Anritsu MT9083B2-056	-	-	-	-	-	-	-	41	-
Anritsu MT9083B2-057	-	-	-	-	-	-	-	39	-
Anritsu MT9083B2-058	-	-	-	-	-	-	-	41	-
Anritsu MT9083B2-063	-	-	-	-	-	-	-	41	-
Anritsu MT9083A2-073	-	-	-	-	-	-	-	37.5	-

Model	1ns (0.1m)	10ns (1m)	100ns (10m)	500ns (50m)	1µs (100m)	3µs (300m)	10µs (1km)	20µs (2km)	30µs (3km)
Anritsu MT9083A2-055	-	-	-	-	-	-	-	37	-
Anritsu MT9083A2-057	-	-	-	-	-	-	-	35.5	-
Anritsu MT9083A2-063	-	-	-	-	-	-	-	37.5	-
Anritsu MU909011A3	-	7	-	-	-	-	-	-	-
Anritsu MU909015C/C6-057	-	-	-	26	-	-	-	37	-
Anritsu MU909015C/C6-058	-	-	-	26	-	-	-	37	-
Anritsu MU909015C/C6-059	-	-	-	24	-	-	-	35	-
Anritsu MU909014C/C6-057	-	-	-	23	-	-	-	31	-
Anritsu MU909014C/C6-058	-	-	-	23	-	-	-	31	-
Anritsu MU909015B/B1-056	-	-	-	26	-	-	-	36	-
Anritsu MU909014B/B1-056	-	-	-	23	-	-	-	31	-
Anritsu MW9077A1	-	-	-	-	-	-	-	40	-
Anritsu MW9077B	-	-	-	-	-	25.5	-	38	-
Anritsu MW9087D	-	-	-	-	-	-	-	50	-
Anritsu MW90010A C-OTDR	-	-	-	-	-	-	17	-	-
Corning 400-SD34	-	-	-	-	-	-	34	35	-
Corning 400-SD37	-	-	-	-	-	-	37	38	-
EXFO FTB-7200D	-	-	-	-	-	-	-	34	-
EXFO FTB-7300E	-	-	-	-	-	-	-	37	-
EXFO FTB-7400E	-	-	-	-	-	-	-	41	-
EXFO FTB-7500E	-	-	-	-	-	-	-	45	-
EXFO FTB-7600E	-	-	-		-	-	-	50	-
Fluke OptiFiber Pro	-	-	-	-	-	-	-	30	-
Fujikura Noyes C850	-	-	-	-	-	-	26	-	-
Fujikura Noyes CS260-20	-	-	-	-	-	-	30	-	-

Model	1ns (0.1m)	10ns (1m)	100ns (10m)	500ns (50m)	1µs (100m)	3µs (300m)	10µs (1km)	20µs (2km)	30µs (3km)
Fujikura FLX380-300	-	-	-	-	-	-	-	42	-
Fujikura Noyes M700-20	-	-	-	-	-	-	-	38	-
Fujikura Noyes M700-24	-	-	-	-	-	-	-	37	-
Fujikura Noyes M700-25	-	-	-	-	-	-	-	26	-
Fujikura OFL280	-	-	-	-	-	-	32	-	-
JDSU 8100B	-	-	-	-	-	-	-	40	-
JDSU 8100C	-	-	-	-	-	-	-	45	-
JDSU 8100D	-	-	-	-	-	-	-	50	-
JDSU 8100 CWDM1E	-	-	-	-	-	-	-	42	-
JDSU E4126MA	-	-	-	-	-	-	-	38	-
JDSU E4126MP	-	-	-	-	-	-	-	41	-
JDSU SmartOTDR	-	-	-	-	-	-	-	33	-
Luciol LOR-220 IR	12	-	-	-	-	-	-	-	-
Luciol v-OTDR	12.5	-	-	-	-	-	-	-	-
Yokogawa AQ1200A	-	-	-	-	-	-	-	32	-
Yokogawa AQ1200E	-	-	-	-	-	-	-	36	-
Yokogawa AQ1205A	-	-	-	-	-	-	-	40	-
Yokogawa AQ1205E	-	-	-	-	-	-	-	40	-
Yokogawa AQ1205F	-	-	-	-	-	-	-	40	-
Yokogawa AQ7277	-	-	-	-	-	-	-	37	-
Yokogawa AQ7282A	-	-	-	-	-	-	-	36	-
Yokogawa AQ7283A	-	-	-	-	-	-	-	40	-
Yokogawa AQ7284A	-	-	-	-	-	-	-	45	-
Yokogawa AQ7285A	-	-	-	-	-	-	-	50	-

In Table 5.2, I have listed the three OFDR systems I found in the market, manufactured by Luna. Based on the specification sheets of the instruments, I obtained the operation points listed in the table. Although the dynamic range of each device is fixed for the different resolutions, the distance range of scans decreases for finer resolution.

Table 5.2: List of OFDR systems in the market with their corresponding measurement limitations in terms of resolution, dynamic range and distance range.

Model	Resolution (m)	Dynamic Range (dB)	Range (m)
OBR 5T-50	2.00E-05	15	8.5
OBR 4200	3.00E-03	16	500
OBR 4200	5.00E-02	16	500
OBR 4600	1.00E-05	18	30
OBR 4600	2.00E-05	18	70
OBR 4600	1.00E-03	18	2000

Commercial OTDRs can achieve high spatial resolution (~10cm) with relatively modest (12dB) dynamic range (point A in Figure 5.1), or greater dynamic ranges (up to ~50dB) at the expense of an extremely coarse resolution (~3km), point B, by using longer pulses. On the other hand, OFDRs provide even finer spatial resolution but only at the expense of a low dynamic range and a reduced measurable fibre length, e.g. a resolution of 10µm over a length of up to 30m of fibre with an 18dB dynamic range. These performances are inadequate with respect to the high spatial resolution, high dynamic range requirements of HC-PBGFs.

Besides, currently, there is no commercial reflectometry equipment available operating at the 2µm wavelength range, where HC-PBGFs have minimum loss, and a system capable of characterizing the fabricated fibre for this wavelength region would be highly desirable given the recent interest in this waveband [172, 173].

5.3 Optical side scattering radiometry

General Description: In this work, I improve and automate a well-known characterization approach for the study of locally out-scattered light [3, 174] to provide accurate length-resolved

measurements of the out-scattered fraction of light from a fibre under test (FUT). I name this technique (longitudinally resolved) Optical Side Scattering Radiometry (OSSR). Figure 5.2 shows the schematic of the OSSR setup. The FUT is passed through an integrating sphere (IS) which collects the out-scattered light and directs it a low noise detector.

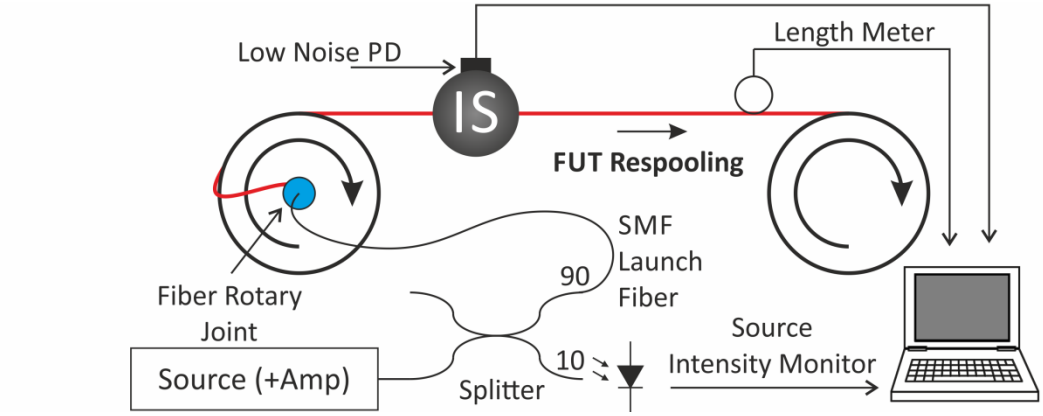

Figure 5.2: The schematic of my proposed OSSR setup.

In Chapter 3, I used an IR camera to look at the out-scattered light by the fibre. The IR camera provides the scattering pattern of the defect by collecting a small portion of the out-scattered light, however in OSSR, I prefer to collect the out-scattered light as efficiently as possible and the information on the scattering pattern is less important. An integrating sphere allows efficient integration of the out-scattered light in almost all directions over the section of the FUT inside the sphere. Therefore, with a similar detector specification, a better SNR is achieved. Also, because of the adjustable saturation level of a single large area photo diode as compared to the full-well capacity (the amount of charge an individual pixel can hold before saturating) of each pixel in a camera, the detection dynamic range of the IS configuration is far better than the camera. The only down side to the IS configuration is its cm resolution as compared to the sub-millimetre resolution of the IR camera configuration.

My implementation: In my implementation, the FUT is re-spooled from one bobbin (pay-off bobbin) to another bobbin (take-up bobbin) on a fibre-rewinding machine while light is coupled into the fibre via an arrangement incorporating a fibre optic rotary joint. On the rewinding machine, as shown in Figure 5.3, the FUT is unwound from the pay-off bobbin, is passed through a number of pulleys, and finally is wound on a the take-up bobbin. In this path, the position of the FUT is fixed between the two highlighted pulleys, where there is space to place the IS. (The rewinding machine I used here is not the optimum implementation as the FUT is passed through small diameter pulleys that can cause macro-bend in some fibres).

In order to couple light into the FUT while it is being rewound, I considered a number of solutions:

1. A battery powered portable laser source attached to the bobbin which is directly connected to the FUT;
2. A small mains powered laser source attached to the bobbin which is connected directly to the FUT;
3. A fibre optics rotary joint that delivers light to the FUT from a fixed table-top source.

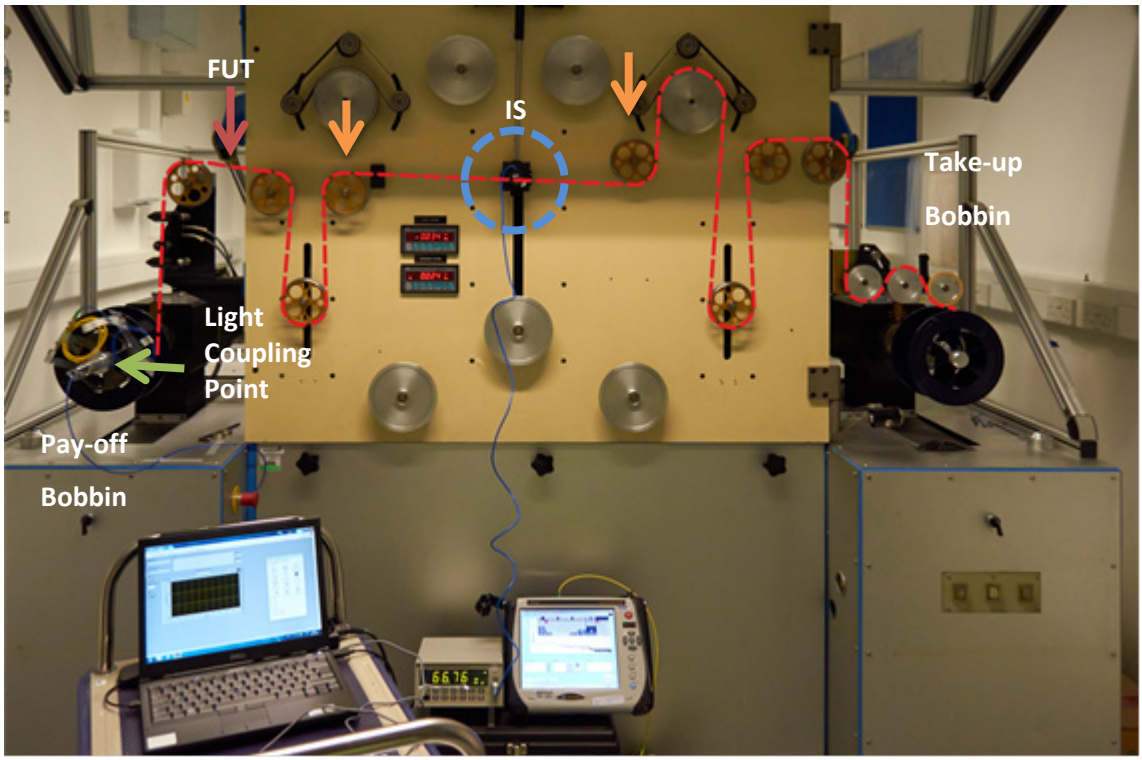

Figure 5.3: OSSR setup.

Solution 1, commercial battery operated portable laser sources (handheld laser sources), are limited to low output powers (~1mW) and restricted wavelengths (635nm, 1310nm and 1550nm) – as they are mainly used either as fault locator or for single wavelength loss measurement. Also monitoring the source output power is rather complicated and requires other portable devices to be fixed on the rotating bobbin, where the space is limited. In addition, battery life can be problematic in lengthy experiments.

The mains powered source in Solution 2 provides relatively higher output power, however they are bulky and usually sensitive to mechanical instabilities during the bobbin rotation. Also, in order to supply power to the rotating laser on the bobbin, I need to design a device incorporating an electrical rotary joint. Moreover, monitoring the source output brings similar complications as discussed above in Solution 1.

I considered Solution 3 as the best choice for the following reasons, lending itself to the stationary condition of source and monitoring equipment:

1. Very stable light sources are available at the various wavelength of my interest;
2. The highest output power is achieved among these solutions, by using high power amplifiers.
3. Source output monitoring is done easier and with better accuracy.
4. It is the lightest and least complex solution to couple light to the rotating drum.

In order to couple light from the stationary source to the FUT on the rotating drum, I designed a device that incorporates a fibre optic rotary joint (FORJ). FORJs allow uninterrupted transmission of an optical signal while rotating along the fibre axis. FORJs are widely used in robotic systems, remotely operated vehicles (ROVs), oil-drilling systems, sensing systems, medical devices, broadcasting and many other field applications [175]. The FORJ I used allows for low insertion loss (~0.8dB), versatility (any source with fiberized output can be used for the measurement) and high stability (the rotary joint provides consistent coupling for a few hundred million rotations), properties which are essential for this measurement.

In order to utilize the FORJ in my OSSR setup, I designed and fabricated a rotary joint device that allows the integration of the FORJ with my rewinding machine. Figure 5.4 shows the device and the rotary joint. The CAD drawings of the device are shown in Figure 5.5. The device is made of aluminium to keep the weight of the assembly low. The device fits at the end of the rewinding machine's bobbin shaft. I designed the assembly in such a way that the rotation axes of the FORJ, the device and the bobbin shaft coincide. This ensures minimum movement of the device and the attached fibres. Three spring-loaded screws, highlighted in the figure, fix the device to the shaft. In this design, I considered including enough room for the fibres at the both sides of the FORJ to bend gently around their contact point, in order to avoid bend loss.

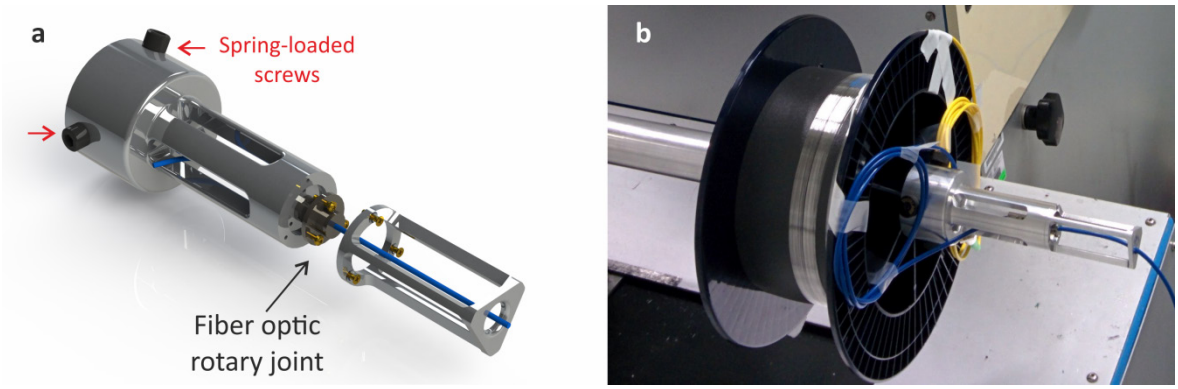

Figure 5.4: The light coupling assembly. **a**, The designed arrangement. **b**, The fabricated device, which has been installed on the ORC rewinding machine.

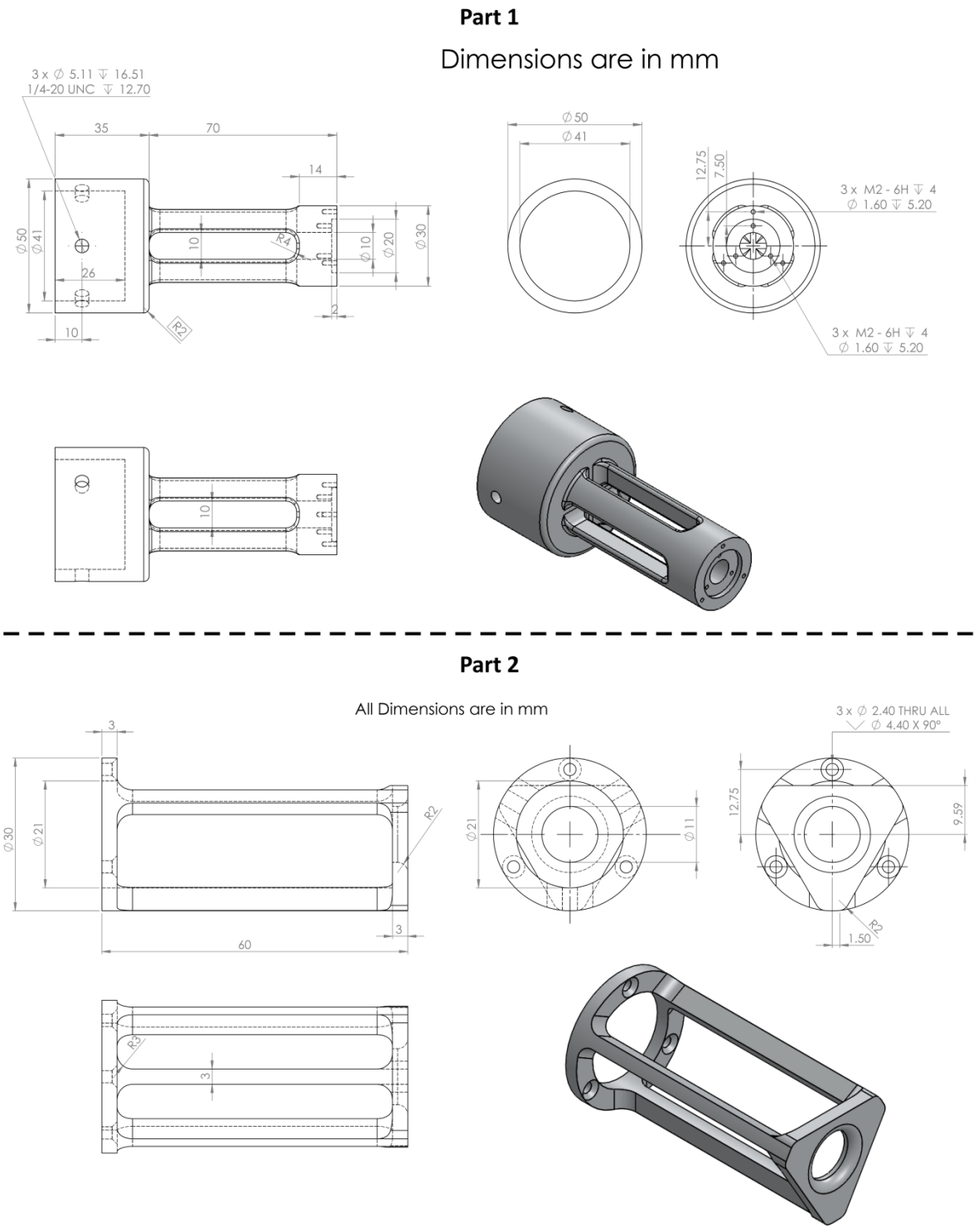

Figure 5.5: My CAD drawings of the rotary joint device.

In order to track and compensate for any intensity fluctuations of the laser source, a small portion of the generated light is tapped out and monitored. Here, I used a 10/90 fibre splitter and connected its 10% arm to a photodiode. The 90% arm is connected to the FORJ fibre input by angle published connectors (APCs) to minimize the back reflection to the source – which can otherwise cause power fluctuations or damage to the laser/amplifier.

The whole system is interfaced to a personal computer, which continuously collects readings of the scattered power from IS, the output power of the reference arm and position along the fibre. I developed a LabVIEW program to control the instruments and collect their data. I designed a graphical user interface (GUI) for the LabVIEW code, which generates real-time graphs of scattered power and reference power against length. Figure 5.6 shows the latest version of the GUI.

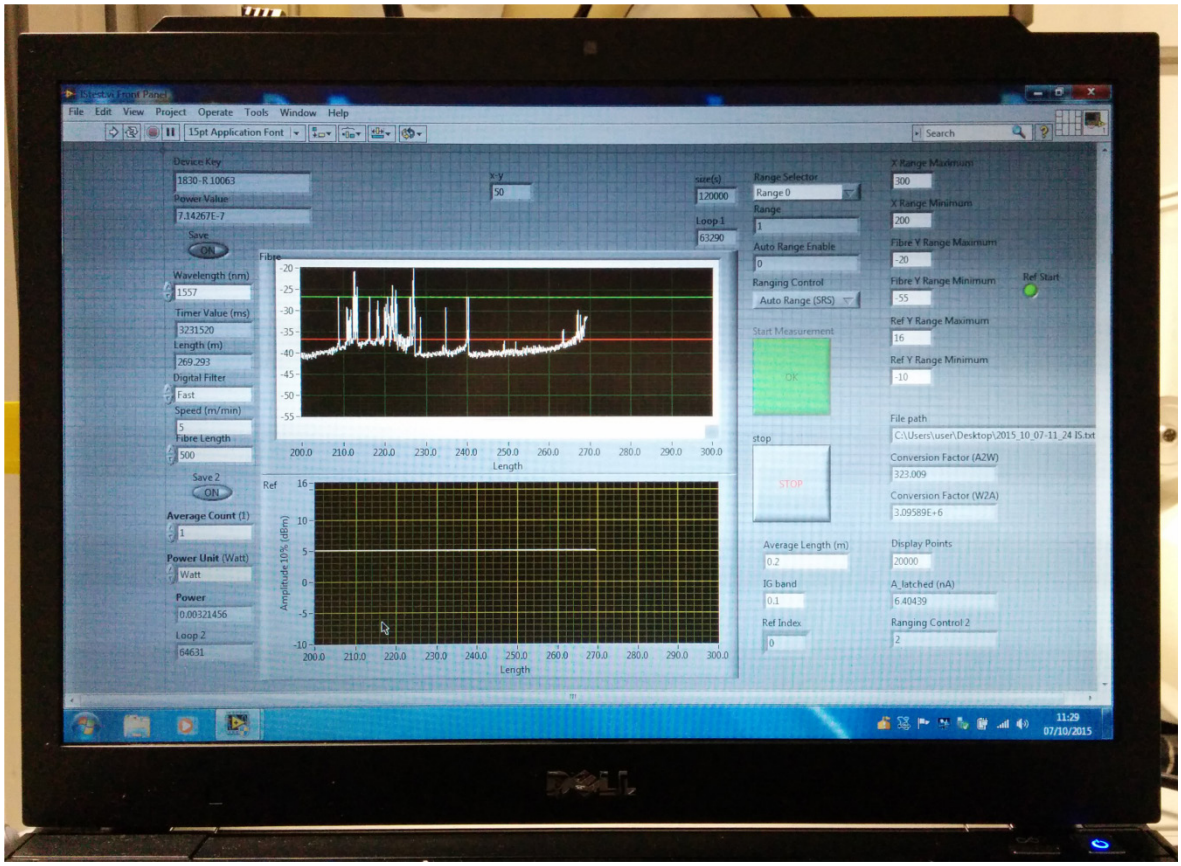

Figure 5.6: The GUI of the LabVIEW code that controls and collects data form the OSSR setup.

It is worth noting that, the scattered light is locally detected and does not need to travel back along the fibre length, providing a better SNR as compared to an OTDR with a similar detector. This in turn increases the dynamic range. To achieve an even wider dynamic range the use of a lock-in amplifier could also be implemented [60].

I used an optical amplifier to boost up the power injected into the FUT. Maximizing the input power will correspondingly increase the dynamic range of the system as its upper bound is determined by the absolute maximum power collected by the IS. This depends on the maximum handling power of the connectors and components as well as the scattering coefficient of the FUT, similar to OTDRs and OFDRs.

Performance of my implementation: To configure my OSSR setup at the wavelength of 1.5µm, first I needed a suitable integrating sphere. I used an off-the-shelf detector, attached to a ~5cm diameter 4-port IS with Spectralon coating from Newport (Newport calibrated IS, 819C-IG-2-CAL). The power handling range of this device is 100nW-1.5W – which is equivalent to an inherent dynamic range of ~92dB. I optimized the light-collecting capability of the IS by improving the reflectivity of the ports (by replacing the standard port plugs with Spectralon coated port plugs) and calibrated the device against several commercial low noise detectors. After calibration, I could detect light levels as low as ~100pW.

The fibre optic rotary joint I used for this configuration is a compact 1-channel single-mode slip ring by MOFLON (MFO100), which only weights 50g. It operates in the wavelength band 1310nm to 1550nm, with typical insertion loss of 0.8dB. This rotary joint can handle up to 200mW (23dBm) of input power, which in my current OSSR configuration, sets the maximum input power to the FUT and therefore determines the upper limit for the dynamic range of my system. The maximum rotation speed of the MFO100 is ~2000 revolutions per minute, which allows a scan speed of up to 2km/min using a standard fibre spool with 1m circumference. The estimated life cycle of the FORJ is about 300milion rotations, which in my system allows testing over more than 150,000km length of optical fibres.

I tested a few laser sources and fibre amplifiers, including:

- a tunable laser source (OSICS ECS 1560 from Yenista Optics) with a maximum output power of +6dBm. Its wavelength tuning range varies from 1520nm to 1600nm at 0dBm output level. Its power stability is +/-0.01dB/h at 0dBm.
- a laser diode (HP 81554SM) with fixed output power at about -1dBm and 6 hours power stability of +/-0.05dB.
- a high power fibre amplifier (EAD-5-C by IPG photonics) with 5W maximum output power and operated in automatic power/current control mode to stabilise the output level. I mainly used it in auto current control mode that delivers a smooth (but slowly decaying) output.

The rewinding machine I used is an old bulky system. A safe rewinding speed for delicate HC-PBGFs using this machine can be as high as 15m/min, which ensures no fibre breaks during the process. Various bobbin sizes can fit on to this machine, the most common we use are the ones with 0.5m and 1.0m circumference.

The optical power meter I used for measuring the signal from the IS is the model 1830-R USB from Newport. The input signal (photocurrent) range of this system can vary by up to 8 decades, with a

maximum cap at 10mA. Its measurement rate per second is as high as 20Hz at its minimum detectable low light level. In addition, it has a USB computer interface that allows integration with LabVIEW.

The detector and power meter for the reference arm can be a generic power meter solution with suitable computer interface, mainly because the level of light on this arm is ~10% of the source. Even in the case of only 1mW source power, this is large enough (10µW) for a generic detector to pick up. I used a Thorlabs S145C detector and PM100USB power meter (which was available in my lab) for this purpose. The detection range of this detector is between 1µW to 3W and the power meter allows integration with LabVIEW through its USB interface. The measurement rate per second can be as high as 500Hz.

The resolution of the measurement depends on the size of the IS, the sampling frequency and the rewind speed. The diameter of the IS determines the minimum possible spatial resolution. With a rewinding speed of V and a sampling frequency of Fs, a spatial sampling interval of Xs = V/Fs is obtained, which at low speed and high sampling frequency leads to over-sampling of the trace. At high rewinding speed and/or low sampling frequency, under-sampling occurs and therefore the resolution of the measurement is determined by the spatial sampling interval.

Differently from other remotely operated reflectometry methods, OSSR requires access to the full length of the FUT and must therefore be applied before the fibre is installed, ideally during fabrication or immediately after it, when a newly fabricated fibre is re-spooled on its final bobbin.

5.4 Technique validation via a standard fibre at wavelength of 1.5µm

To verify the accuracy of the OSSR set-up I tested a standard telecoms single mode fibre. I used 3km of Corning SMF28e, which has a datasheet loss of ≤0.20dB/km at 1550nm. A tunable laser source (TLS) with +2dBm output power at 1550nm was used as the source. An Erbium doped fibre amplifier (EDFA) was used to amplify the light up to +7dBm. The FUT was collected on a bobbin with 0.5m circumference. The fibre input and output port of the IS were protected by long black tubes to avoid interference due to ambient stray light. Figure 5.7 shows the long tubes attached to the IS.

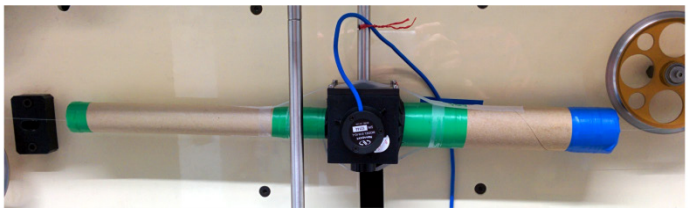

Figure 5.7: reducing the noise caused by ambient light using the tubes attached to the IS. The inside of the tubes are covered in a black material.

Mechanical limitations of my rewinding machine set the maximum rewinding speed to 15m/min. The diameter of the IS sets the practical spatial resolution of my experiment to ~5cm. By adopting an integrating cube [174] or a sandwich-detector [176] arrangement to operate at this wavelength, or using a smaller IS the resolution can be further reduced. A frequency of 20Hz was set to over sample the signal with 4 samples per resolution length. Figure 5.8 shows the OSSR result with an inset showing a magnified part of the trace. Periodic noise at the revolution frequency of ~1Hz with average amplitude of 0.4dB can be seen. This is a known artefact (insertion loss ripple) generated by the rotary joint, which can easily be filtered out. According to the specification sheet of the MFO100, this oscillation should be no more than +/-0.25dB. The scattering trace shows a ~0.6dB linear power drop over 3km, which corresponds to ~0.2dB/km.

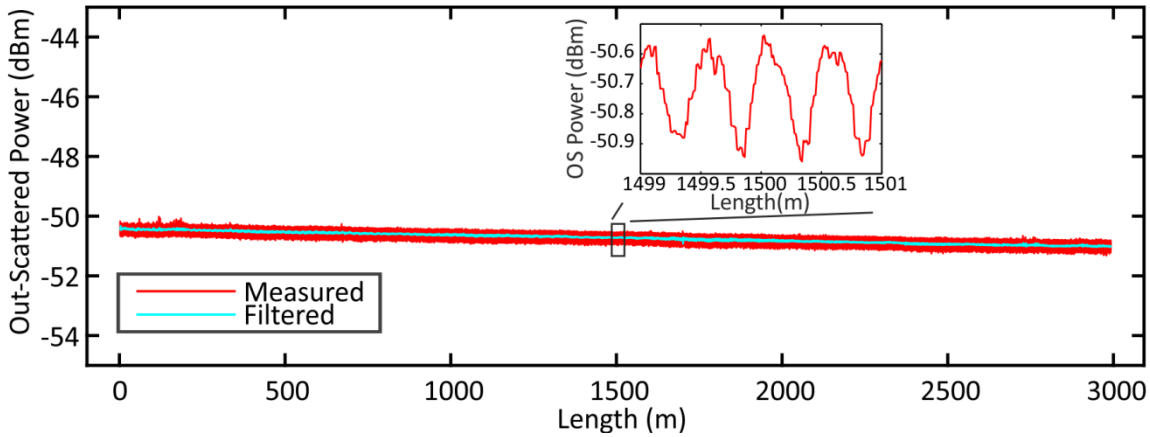

Figure 5.8: Scattering trace of the SMF28e. The inset shows a magnified part of the trace.

For a more precise measurement, the loss can be estimated through the cumulative sum of the out-scattered power (CP), expressed by $F(x)$, over the length of the measured fibre. For a fibre with loss factor of α (unit: dB/km) passing through an IS with L_{IS} (unit: m) diameter, the $F(x)$ (unit: W) can be expressed analytically via

$$F(x) = \frac{1}{L_{IS}} \int_0^x 10^{\left(\frac{-\alpha x+\beta}{10}\right)} dx = \frac{10}{L_{IS}\,\alpha \ln(10)} 10^{\frac{\beta}{10}} \left(1 - 10^{\frac{-\alpha x}{10}}\right) \tag{5.1}$$

Here, β (unit: dB) is the out-scattered power at x=0. First, the CP is calculated from the measured OSSR trace, red curve in Figure 5.9. The loss is then obtained by making a fit to the CP using Equation (5.1) with L_{IS} and β known from the measurement and α as the fit parameter. For the fibre under test I obtained a loss value of α=0.20dB/km, in good agreement with the fibre's nominal loss value. The curve of $F(x)$ for α=0.20dB/km, shown by the black dotted trace in Figure 5.9, sits exactly on the calculated CP. I used a dB scale here to better visualize the difference. Additionally, to demonstrate the sensitivity of the fit parameter (α), I have shown two dashed lines corresponding to 0.20±0.02dB/km (fibre's nominal loss ± 10%).

The calculation of the CP largely eliminated the periodic noise shown in Figure 5.8, and removed the need for any filtering in the present case. Based on the level of input and out-scattered power, I estimated that at the wavelength under the test, 78% of the lost power has been captured by the IS (the rest being absorbed by the glass and coating or is not captured by the detector). This yields a fibre scattering coefficient of 0.91dB/km/μm^{-4} that agrees well with the reported value of 0.94dB/km/μm^{-4} [59].

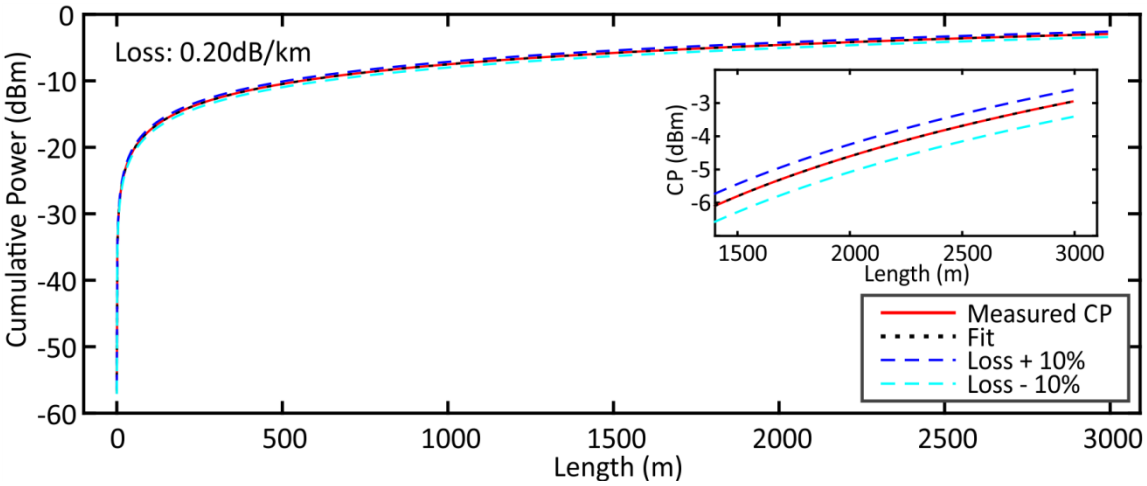

Figure 5.9: The cumulative power trace of the examined SMF28e. Inset shows a magnified view of the second half of the trace.

OTDR is commonly used to characterise SSMF, in particular to measure the loss and check the fibre integrity/consistency. Figure 5.10 shows a comparison between the OTDR and OSSR traces of the 3km SMF28e. OTDR pulse width used for this measurement is 30ns at the wavelength of 1550nm (equivalent to ~3m spatial resolution). Measured fibre loss by the OTDR is 0.19dB/km, which is very close to the measured loss by OSSR. Although both traces have very similar slopes, OTDR signal is much (~3 times) nosier than unfiltered OSSR.

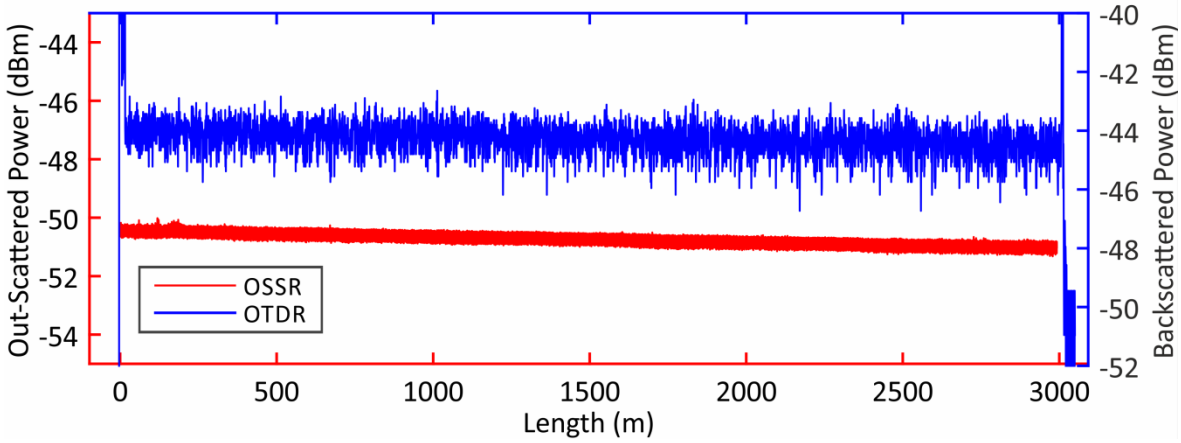

Figure 5.10: A comparison between OSSR and OTDR result of the 3km SMF28e.

5.5 Dynamic range testing

As discussed in Chapter 2, HC-PBGFs have a microstructured cladding made of sub-µm nodes connected by very thin glass membranes. Generally, a multi-step stack and draw technique is used for their fabrication, which has gone through tremendous improvements in recent years [9], resulting in a record length ~11km HC-PBGF (cross section shown in Figure 5.11 **a**) with 5.2dB/km cutback loss and >200nm bandwidth around the central wavelength of ~1550nm, as shown in Figure 5.11 **b** [13, 25]. The cutback loss was measured from the initial fibre length 11070m cut back to 20m. This fibre is an interesting test-bed to demonstrate the dynamic range capability of my system. The high end-to-end loss of the 11km span (~57dB) means that conventional reflectometers can only probe a relatively short subsection of the fibre from each end, as shown in Figure 5.13 **a** using a state of the art OTDR set to provide the maximum dynamic range at a reasonable resolution (~15dB dynamic range and ~15m resolution).

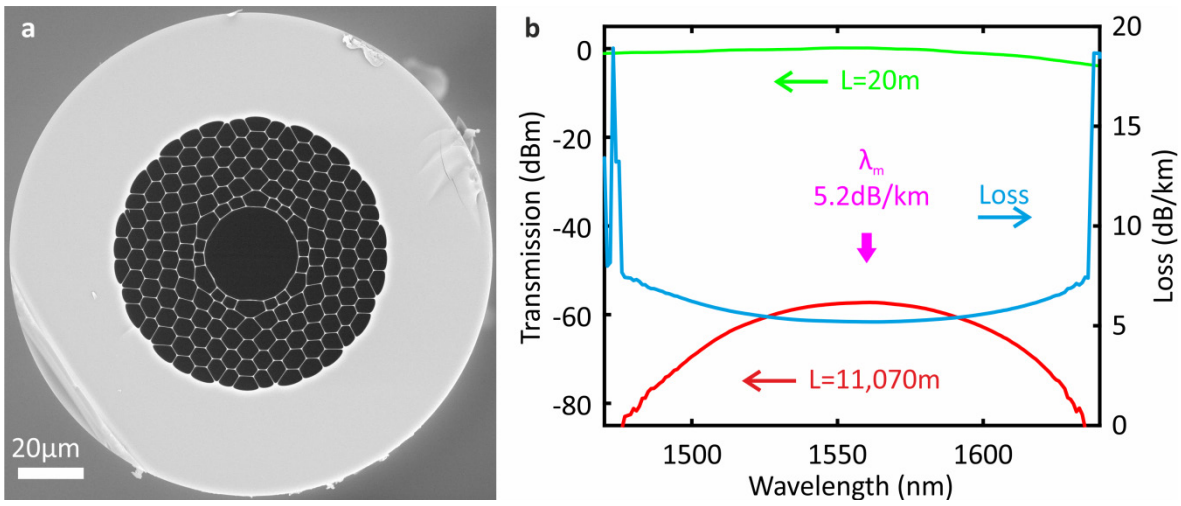

Figure 5.11: The record-length HC-PBGF in [25]. **a**, The SEM cross-section image of the fibre. **b**, Transmission characteristics of the fibre. The thick arrow in the middle shows the position of minimum loss.

For the OSSR measurement I used a high-power Er/Yb fibre amplifier with +26.5dBm power at 1560nm, 15m/min rewinding speed and 20Hz sampling frequency. The usable signal spans from -10 to -70dBm, providing a ~60dB dynamic range in this test (See Figure 5.12). As shown in the inset of Figure 5.12, over the first ~30m of the fibre, the out-scattered power drops by ~10dB. This is believed to be mainly due to the mode mismatch between the launch fibre and the HC-PBGF, which results in excitation of higher order guided modes that have higher loss and hence scatter more than the fundamental mode, which explains the steeper slope at the beginning of the trace. As they lose power, after a certain length, the out-scattered trace is dominated by scattering from the fundamental mode.

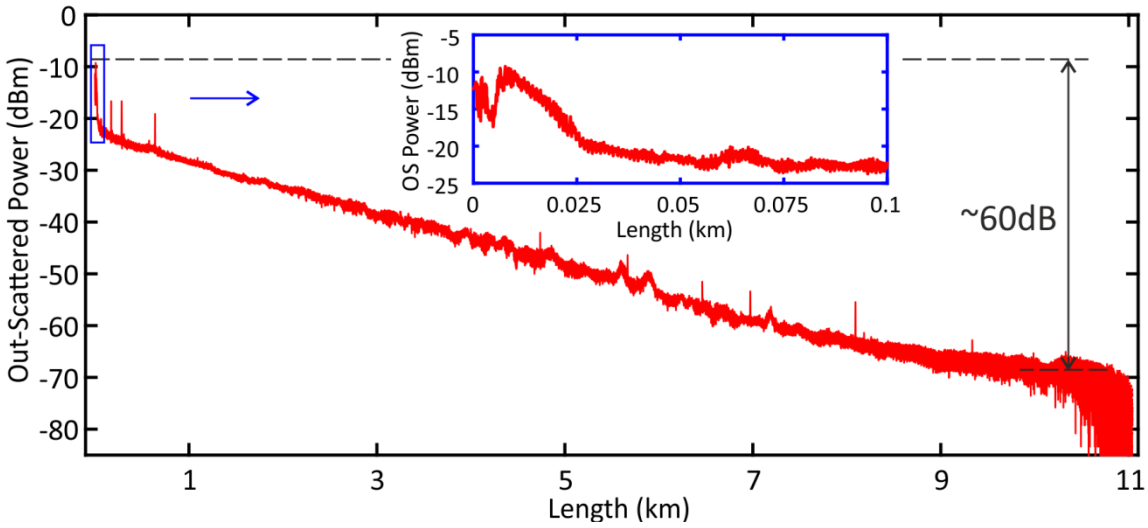

Figure 5.12: The OSSR result of end-to-end measurement of the record-length HC-PBGF. The inset shows the very first section of the fibre.

To couple light into the HC-PBGF, I spliced an angle polished connectorized single mode fibre attached to a suitable large mode area (LMA) fibre which acts as a buffer fibre that was then connected to the HC-PBGF using a specialized splicing recipe [166]. The mode field diameter of the buffer fibre and of the HC-PBGF are ~15µm and ~22µm respectively. With these input conditions, the OSSR result indicates that an accurate cutback loss measurement can be achieved only if the cutback length is longer than the transition length. I have found that coiling the fibre around a small diameter (~7mm) mandrel to strip out high order modes is effective in reducing this initial transition length to a few meters only [177].

Near the end of the fibre, the signal drops to below the noise floor and thus to achieve an accurate measurement of the full fibre span I performed another test by swapping the launch end around. Figure 5.13 **b** shows the two combined traces (where for ease of visualization, the second trace has been plotted upside down, and with an arbitrary offset so that the two traces match up at the joint) alongside measurements obtained via a state of the art OTDR which show a considerably reduced dynamic range (in Figure 5.13 **a**). The measured OSSR loss achieved from

the fit using Equation 1 is 5.14dB/km, which agrees well with the measured cutback loss of 5.2dB/km (see Figure 5.11 **b**).

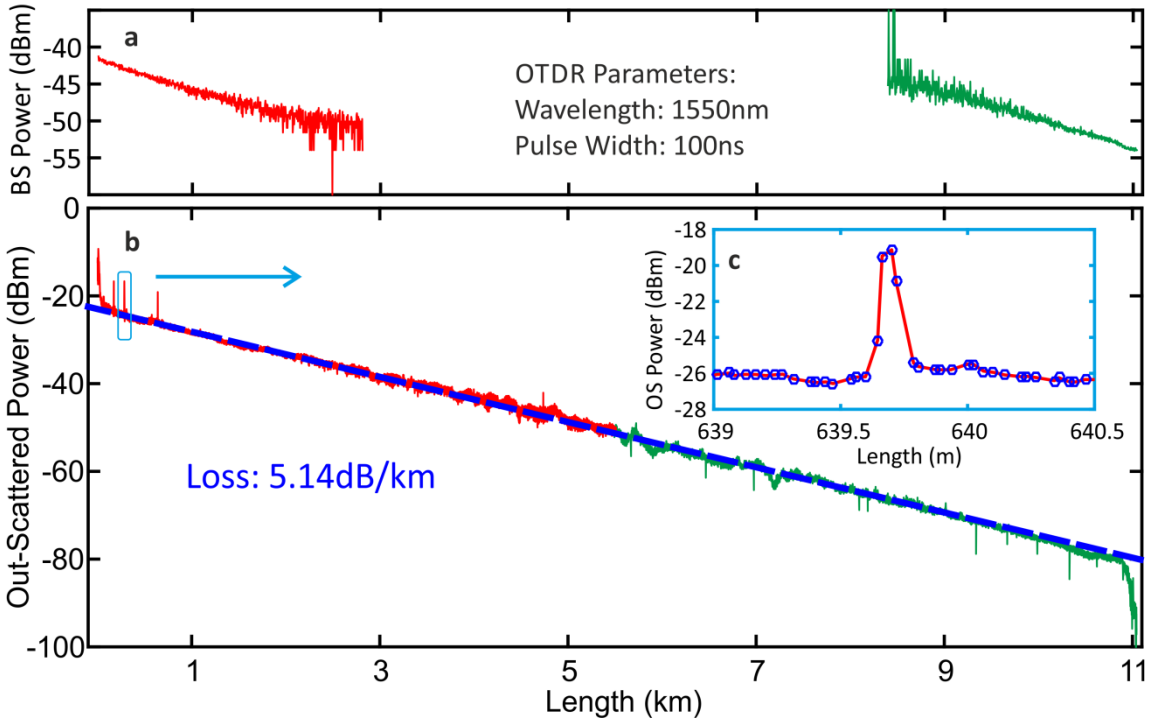

Figure 5.13: The measurement of the scattering trace of the record length HC-PBGF. **a**, OTDR traces from both ends of the fibre. **b**, OSSR measurements obtained by launching from both ends. **c**, (The inset) shows a magnification of a discrete scattering event.

A small number of features can be identified in the measured OSSR traces, including 16 discrete narrow scattering peaks (a magnified plot of one of which is shown in the inset of Figure 5.13 **c**). I speculate that they are caused by some small scale structural inconsistencies, the origin of which can be studied using a number of techniques such as precision cleaving and fibre side-imaging with an IR camera (presented in Chapter 3 [135]) and X-ray tomography (discussed in Chapter 5 [141]). In any case, by using the procedure described below, I estimate that the cumulative impact of all the peaks on the fibre loss is <1dB (out of the 57dB of total measured loss).

To calculate the loss of a peak, I integrate the out-scattered intensity along the length of the defect and compare it with the scattered light from the clean section of adjacent fibre. Here, I assume coupling to other modes to be negligible. The assumption holds if the rate of change of the out-scattered power remains the same before and after the inconsistency point. Additionally, I also assume, almost all the lost light scatters out and has been captured effectively by the detector. This is the case for HC-PBGFs, as the glass absorption (and the coating absorption) gives a negligible contribution to loss in these fibres. For example, in the case of the defect shown in Figure 5.14, the total out-scattered power is 28.1µW over the defect length of 0.26m. The out-scattered intensity of the adjacent fibre section is 48.3µW/m. This implies that the defect out-

scatters an amount of power equivalent to 0.58m of fibre. With the estimated fibre loss of 5.14dB/km, the defect loss is obtained:

$$\alpha_{Defect} = \frac{28.1\mu W}{48.3\mu W\ m^{-1}} \times 5.14 \times 10^{-3} dB\ m^{-1} = 0.003 dB \quad (5.2)$$

This loss includes the actual loss of the fibre over the defect length, which is 0.26m × 5.14e−3dB/m = 0.0013dB. Therefore, the excess loss caused by the defect is 0.003 − 0.0013 = 0.0016dB, which is extremely low. The effect of coupling to other guided modes will manifest itself by raising the scattering level and changing the rate of change of the out-scattered power, an example of which is discussed in the next section.

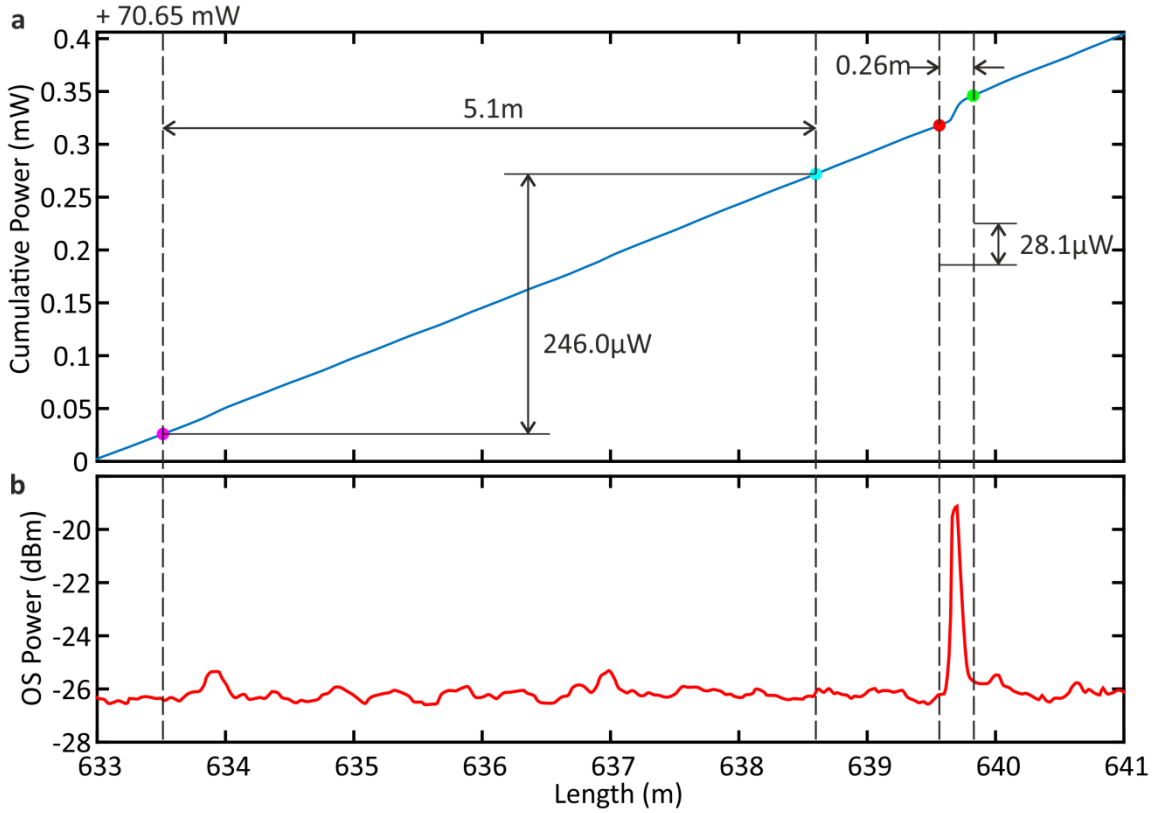

Figure 5.14: Analysis of the highlighted defect of Figure 5.13 **c** in the 11km HC-PBGF. **a**, The cumulative power trace across the defect. **b**, Its corresponding OSSR trace.

As discussed in Chapter 3, I have identified that the structural deformation, which causes similar scattering points, happens only over a short fibre length (a few 10s of cm to a few meters) [135] which implies that fluctuations in fabrication control parameters are unlikely to be the cause of the anomalies. The multistage fabrication process of microstructured fibres increases the chance of incorporation of contamination and inconsistencies in the preform, which are the most likely origin of such points in the fibre. Depending on the size of the preform, and the expansion ratio, the length scale of the scattering points implies inconsistencies of the order of 10s to a few 100s of micron [141].

In addition to these localized peaks, wider peaks and troughs are also visible in the trace, indicating regions with a non-uniform scattering pattern, which likely correlate with small variations in fabrication control parameters like differential pressure or drawing speed, which I am investigating through a number of purposely developed techniques, such as the methods presented in Chapter 3 and 4 [141].

The work I presented in this section, led to two prestigious publications for my group, an OFC post-deadline paper and an invited paper at the Journal of Lightwave Technology [13, 25]. In particular, OSSR provided a tool to count the number of defects per unit length and measure the distributed loss of the fibre using its scattering pattern, through which we could quantitatively assess the uniformity of the fibre and study the detrimental impact of defects.

5.6 Demonstration of high spatial resolution in a high-loss HC-PBGF

While the consistency of HC-PBGF fabrication has improved considerably in the last few years, occasionally some fabricated HC-PBGFs still show a higher length-averaged loss (e.g. measured via the cutback technique) than expected. As discussed in Chapter 3, their OTDR trace is often either clean or shows only a few small discontinuity points and therefore it cannot provide a clear explanation as to the reason for the high loss. Using OSSR, I can gain more information about the inconsistencies and issues within these defective fibres, one example of which is shown below.

Here, I tested an HC-PBGF similar to the defective fibre that I studied in Chapter 3. In fact, this fibre was pulled from the same preform. The transmission properties and cross sectional image of this high-loss HC-PBGF are shown in Figure 5.15. The minimum cutback loss is ~20dB/km, which is high for this type of fibre, despite the fact that the cross sectional image in Figure 5.15 **b** does not show any obvious structural distortion. The transmission curve of the 300m length presents obvious anomalies if compared to the transmission curve of a 10m length, which suggests the presence of discrete longitudinal defect(s). The OTDR traces in Figure 5.16 **a** and **d** indeed show some features, including a strong discontinuity near the end of the fibre. Figure 5.16 **d** shows the measurement in the opposite direction. To gain more insight I have also measured the fibre with OSSR at a wavelength of 1557nm (at which the cutback loss is ~37dB/km, as highlighted by the pink arrow in the figure).

The OSSR results in Figure 5.16 **b** and **c** give a much clearer indication of the longitudinal problems in the fibre, showing more than 56 points with strong scattering, which are 3dB larger than the average intermediate scattering level. A comparison between Figure 5.16 **c**, which is the measurement in the other direction, and Figure 5.16 **b**, shows that all the scattering events are reproducible and the measurement is also robust in terms of identifying the scattering events.

Additionally, the amplitude of like-to-like scattering events is different as the fibre properties on either side of the event, such as modal content and loss, are different. Moreover, there is a good agreement with the overall scattering pattern of the similar OTDR and OSSR traces. However, the pattern varies by changing the light coupling direction.

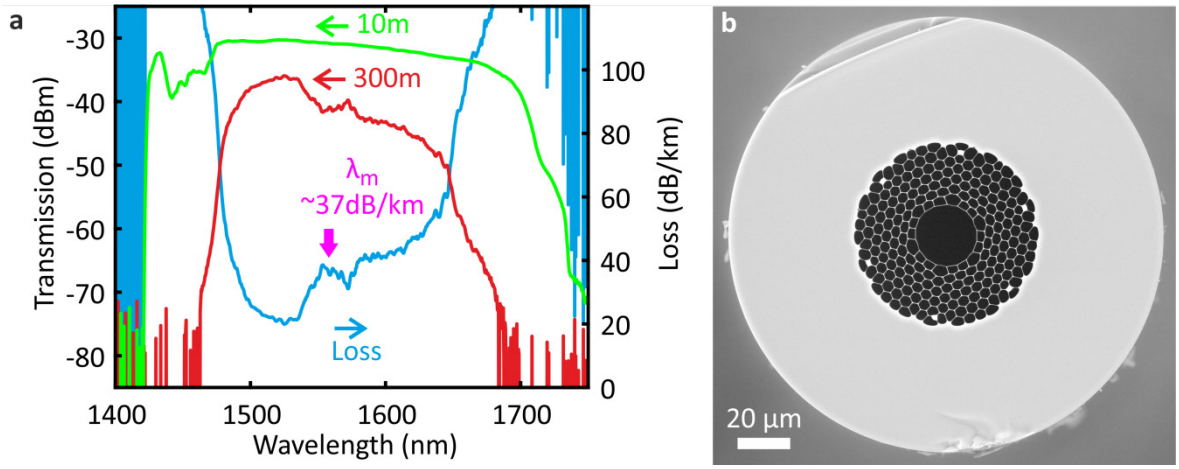

Figure 5.15: An example of a high-loss HC-PBGF. **a**, The transmission properties of the fibre. **b**, The SEM image of the cross-section showing a uniform and undistorted structure. This fibre originates from the same batch of fibre that I studied in Chapter 3.

The features in the OTDR traces match very closely with some of the scattering events in the OSSR traces, however there are many other events that are not visible even at the finest resolution of my OTDR, showing the usefulness of the high spatial resolution and sensitivity of the OSSR. Here I emphasize another unique advantage of OSSR in the detection of possible non-isotropic scattering events, in particular those that do not backscatter the light and therefore can only be seen by OSSR and not by OTDR. This effect is independent of any spatial resolution.

It is noticeable that in this instance, the measurement does not start at zero and hence misses the transition at the coupling point (the transition region has been effectively reduced by the coiling technique introduced in section 5.5). Mechanical limitations of the rewinding machine that I used also impose a dead-zone of ~2m right at the beginning and end of the fibre, where it is not accessible with the IS. With other rewinding machine designs, this can be reduced to as short as $0.5\times L_{IS}$. Additionally, the dead zone can be completely suppressed if the machine allows the spliced joint to pass through it. In this case, even an arbitrary sequence of different fibres can be examined.

As is clearly seen in the OSSR traces in Figure 5.16, after the stronger defects, a raised out-scattered power is observed, indicating a defect-mediated coupling of light to higher order or cladding modes (HOMs/CMs). In the case of weak coupling, the scattering level stabilizes after a few 10s of meters as the light coupled into the HOMs decays much faster. However, the set of

very strong scattering points near the end of the fibre (~230m) cause significant power coupling to the HOMs, which dominate the out-scattered power trace and follow a faster decay rate. This mechanism was also confirmed in a separate time-of-flight experiment [178].

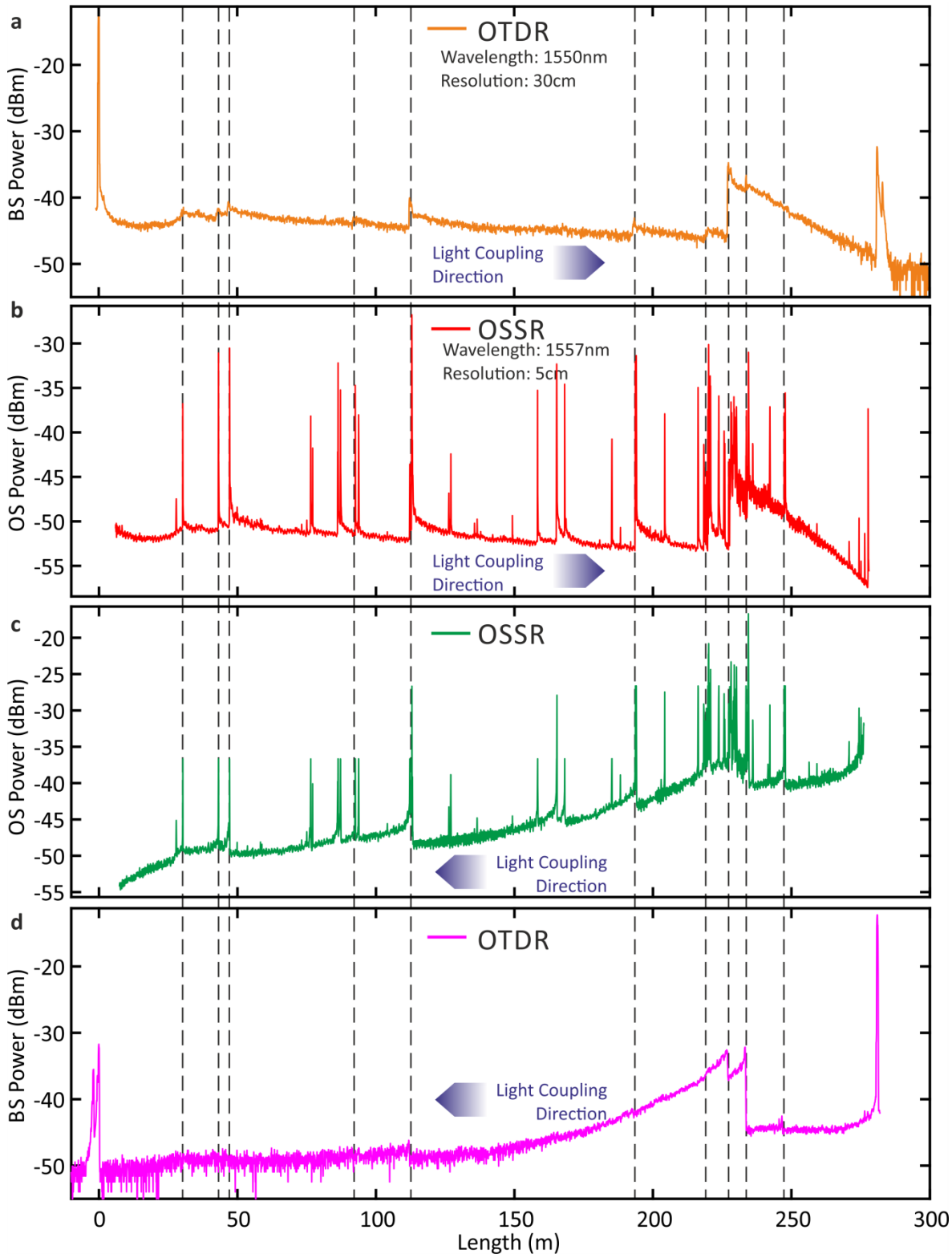

Figure 5.16: The analysis of a high-loss, defective HC-PBGF. **a**, The OTDR trace of the fibre. **b**, The OSSR trace of the fibre in the same direction as **a**. **c**, The OSSR measurement in the opposite direction as compared to **a**. **d**, The OTDR result in the reverse direction as

compared to **a**. The wavelength is 1550nm for the OTDR (2ns pulse width) and 1557nm for the OSSR.

In this instance, it is not possible to measure the loss of individual defects using the procedure described earlier in section 5.5 mainly because the preliminary assumptions on the fibre properties and its scattering pattern immediately before and after defect are not held. However, one can make a rough estimation of the contribution of the 56 strong defects by comparing the background scattering level of the fibre and the average scattering level of all defects. Assuming the 56 defects cover an overall length of about 20% with average strength of 10dB above the background level, one can calculate the contribution of defects to be:

$$Loss\ of\ Defects + Loss\ of\ defectfree\ Fibre = (0.20 \times 10 \times \alpha) + \alpha = 37dB/km$$

$$Loss\ of\ defectfree\ Fibre = \alpha = 12.3dB/km \equiv 3.4dB$$

$$Loss\ of\ Defects = 2\alpha = 24.6dB/km \equiv 6.7dB$$

This is in agreement with the end-to-end (insertion) loss of ~10dB for the ~280m total length of the fibre based on OTDR and OSSR.

A figure of merit indicating the quality of these HC-PBGFs can be defined based on the number of scattering points per unit length. For comparison, the 11km fibre of Figure 5.13 had 1.5 defects/km as compared to 206 defects/km for the fibre in Figure 5.16.

The relatively short length of this sample allows it to fit in a single layer on the white polystyrene bobbin we used for IR camera investigation method. We measured the fibre scattering using the IR camera setup, the result of which is shown in Figure 5.17. There is a good agreement between the scattering signatures captured by this method and OSSR, both in terms of the position and strength of the discrete scattering events.

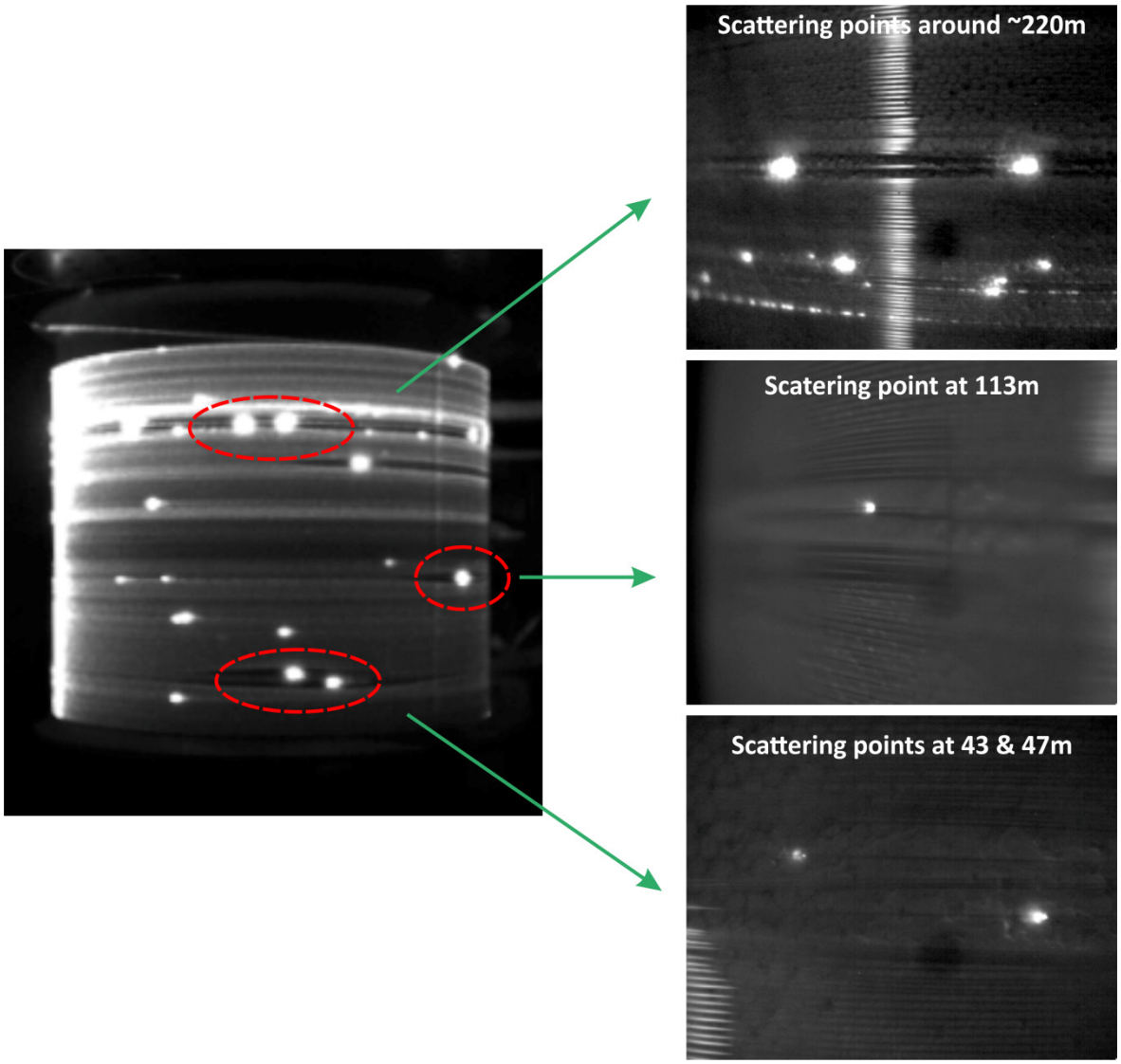

Figure 5.17: IR camera images of the scattering points from the fibre studied in this section.

5.7 Wavelength scalability demonstration

Besides the large dynamic range and fine spatial resolution, another advantage of the OSSR technique is that it is readily extendable to perform measurements at other wavelengths. In my setup, the IS has a Spectralon coating which provides very high reflectivity (≥95%) over the wide wavelength range from 250nm to 2500nm. Thus, by using suitable sources and detectors, measurements over this whole wavelength range can in principle be obtained. As an example, I reconfigured the previous system to measure at wavelengths around 2000nm, the waveband of expected minimum loss for HC-PBGFs and promising for some future optical data communications applications [173]. Whilst highly sensitive photodetectors for these wavelengths are already commercially available in the market from manufacturers like Hamamatsu, Teledyne and EOS, for this demonstration I used a Mercury Cadmium Telluride (MCT) camera that I had available in the lab. The MCT array detector is cooled (by 4-stage thermoelectric cooler) to ~−63˚C and had a cut

off wavelength of ~2.7µm and a peak sensitivity at 2.5µm. The detector array size is 320×256 pixels with 30µm pitch and 14-bit data output. I bin all the pixels together to get a single large area detector. The fibre rotary joint I used at 1550nm is still functional at the wavelength of ~2µm, albeit with slightly more sensitivity to bends. The schematic of the setup is similar to the schematic in Figure 5.18 except that the low noise photodetector is replaced with the MCT camera. I used a laser diode [179] generating light at the wavelength of 1989nm followed by a Thulium doped fibre amplifier (TDFA) as the source. I also used an extended InGaAs detector (working over the wavelength range 1.2µm to 2.6µm, Teledyne J23-5I-R02M-2.6) to monitor the source power variation. I calibrated the detector at ~1.5µm and based on the responsivity curve provided by the manufacturer I extrapolated the calibration factor at ~1989nm. The output of the camera is in analog-to-digital units (ADU) and is transferred to the personal computer via a 16-bit bus. I calibrated the combination of the IS and camera by using the extended InGaAs detector that I had calibrated earlier. I obtained a calibration factor of 4.58nW/ADU. The noise floor of this detector was found to be very sensitive to changes in temperature, with a measured sensitivity of ±100ADU (0.46µW) per degree Celsius. Thermal stabilization and measurement of the noise level was therefore necessary, particularly for low light level measurements (i.e. for signals close to the noise level). The noise level of the detector was in the several microwatts range. To improve performance here, one could either increase the SNR e.g. by using a coherent detection scheme, or use a more suitable detector with a lower noise level and with less sensitivity to thermal fluctuations.

I tested a HC-PBGF designed to operate at a central wavelength of ~2050nm, with 195nm transmission bandwidth and a minimum cutback loss of 4.2dB/km at 2041nm. Figure 5.18 shows the SEM image of the cross-section and transmission characteristics of the fibre. Note that the test wavelength of 1989nm is sufficiently far from the surface mode group positioned around 1900nm. At the test wavelength, the cutback loss is ~4.8dB/km. In this test, due to my source limitations, the out-scattered light level is close to the noise level of the detector. I used the coiling method to reduce the transition region at the coupling point effectively. I allowed the detector temperature to stabilize before the beginning of the test and once stabilized, I measured ~1260ADU (an equivalent of 5.77µW or −22.39dBm) for the noise level. The result of the OSSR measurement including a suitable noise floor calibration can be seen in Figure 5.19. The fibre is seen to be almost defect-free over the 425m tested length, with only a ~35m section at ~410m with a slightly increased out-scattered level (not more than 2dB above the average). I estimated the loss of the fibre over its defect-free region (highlighted by the blue line) to be 4.72dB/km, in very good agreement with the cutback loss at this wavelength, which confirms that accurate

distributed measurements can be also acquired at different wavelengths with relatively minor modifications to the setup.

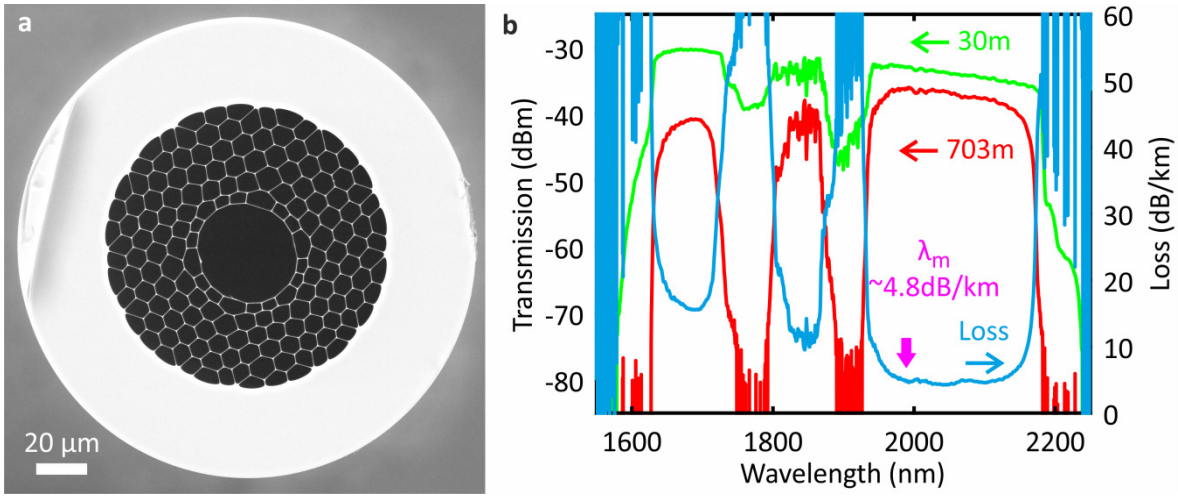

Figure 5.18: An example of a HC-PBGF designed to operate at the wavelength of 2µm. **a**, The SEM image of the cross-section. **b**, The transmission properties of the fibre.

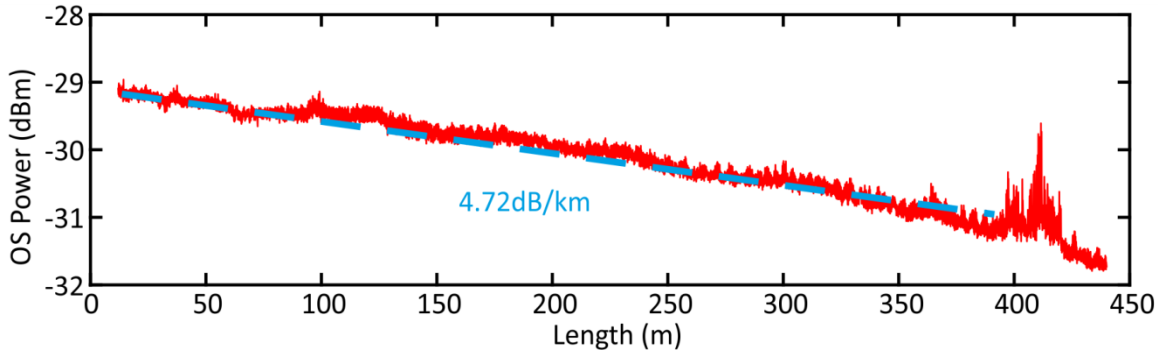

Figure 5.19: The OSSR result of the 2µm HC-PBGF with the loss estimation over the clean section of the fibre.

5.8 Conclusions

In this chapter, I discussed a method I developed for a long-range, high spatial resolution measurement of the longitudinal scattering pattern of HC-PBGFs – which I called OSSR. This method, can measure the distributed loss of fibres with ~50mm fixed resolution and ~60dB dynamic range, well beyond the capability of the best commercial fibre measurement systems. The characterization of virtually any type of special fibre and measurements at different wavelength ranges are possible.

I validated the method in measurements on 3km of SMF28e, showing an accurate loss measurement within the tolerance of the manufacturer's data. Then, I used the OSSR to measure a record-length (11km) HC-PBGF, providing for the first time accurate quantitative information about the longitudinal properties of these fibres despite the very large (~57dB) fibre span loss. I

exploited the high spatial resolution of OSSR to obtain detailed information on the presence/absence of small scattering points and defects (similar to the ones I studied in Chapter 3) along the fibre. X-ray technique could be used to study the identified scattering points in order to measure whether they are structural deformations or are caused by a form of contamination (similar to the fibre defects in Chapter 3), through which a reasonable guess could be made about their origin. Although such study was planned for the defects in the 11km HC-PBGF it could not be completed without damaging the fibre, due to current restrictions with the way the fibre needs to be mounted inside a suitable X-ray CT machine.

This technique can also help to establish improvements in the fabrication process. As an example, I used OSSR to identify >200 scattering defects/km in a HC-PBGF with an unusually high loss of 37dB/km, which provided a reasonable explanation for the excessive loss of the fibre. This measurement shows excellent agreement with the results from IR camera inspection method I introduced in Chapter 3. The main advantages of OSSR over the IR camera are the very high dynamic range of measurement, quantitative measure of defects' loss and the maximum length of FUTs.

The knowledge of fibre integrity, uniformity and consistency is crucial in assessing the process of fibre fabrication and optimising the fabrication steps toward the production of a uniform long-length low loss fibre. The record-breaking 11km HC-PBGF is a result of such process optimising; its uniformity and consistency can only be appreciated thanks to the technique presented in this chapter, i.e. OSSR.

I demonstrated the wavelength flexibility of the setup through a measurement at a wavelength of 2µm, which shows the ability of OSSR to address measurements at wavelengths for which no commercial tool currently exists. Also in this wave band, the loss estimate was in excellent agreement with the cutback loss measurements.

I believe that OSSR could ultimately provide an excellent solution for the longstanding issue of fibre quality monitoring directly during the fabrication process of optical fibres [180] – a future work direction which I would like to explore and demonstrate, in particular its implementation directly on a fibre drawing tower.

Chapter 6: Conclusion

The fabrication of low-loss, long-length, uniform HC-PBGFs is an important technological goal with the potential to deliver transformative performance in several areas of telecoms and datacomms. Two key challenges that need to be overcome in order to realise widespread application of the technology are the elimination of fibre breaks during the fibre draw, and the occurrence of high loss scattering points along the fibre length, both of which effectively limit the maximum amount of usable fibre from a given draw. Both fibre breakage and local scattering points can occur due to contamination and structural inconsistencies/defects within the starting preform yet little was known at the start of this thesis work about the origin of such potential contamination and defects. In order to better understand such issues it is necessary to examine preforms and fibres, identify the issues and find the clues that point to the origin of the problems. This defines the goal of the studies in this work.

In this Thesis I conceived of, and developed, characterisation methods and setups to identify defects and imperfections in HC-PBGFs and their preforms, to study their properties and ultimately ways to reduce/eliminate them.

Using a simple intuitive inspection method based on a sensitive IR camera, I measured and studied the distributed and discrete scattering of propagating light within HC-PBGFs. The former scattering relates to the uniform optical attenuation of the fibre (dominated by surface scattering due to capillary waves) and the latter is caused by inconsistencies/defects along the fibre length. A low loss fibre shows nothing more than gradually decaying distributed scattering along the fibre length (potentially with the occasional low intensity discrete scattering points). However, in fibres with exceptionally high loss, and often distorted spectral transmission profiles, many discrete scattering points/regions with strong scattering intensity are observed, varying in size from sub-millimetre to a few millimetres in the case of point scattering, to several centimetres up to several meters in the case of discrete scattering regions. I examined the internal structure of the fibres by means of a precision cleaving setup that I developed for cutting the fibres at the position of the discrete scattering points. Using this I found some structural deformations (defects) near/at the core surround, which were responsible for the excessive local scattering. Additionally, I found scattering spikes that indicate the onset of the deformations after/before which defective structure exists. I studied the evolution of the fibre structure from where it is normal through where it is defective up until where it returns to normal. To enable this study I developed a sequential fibre cleaving setup that allows for wasted fibre lengths as short as a few millimetres. By means of this setup, I found that the transition from the normal to the defective structure (or

vice versa) happens only over distance scales of just a few centimetres, although the entire defective length can be as long as several tens of centimetres. The length of the observed defect regions suggests that the cause of these defects is likely to be imperfections/contaminants (of a few 100s µm size) in the fibre preforms, rather the sudden variations in the fabrication control parameters. I also found a form of particulate contamination inside the fibres, associated with some of the discrete scattering points and the distributed scattering regions, which I speculate relate to preform contamination by chlorine compounds reacting with atmospheric water. We are investigating the use of glass with low chlorine and monitoring the atmospheric water more strictly to minimize the issue. Subsequently, I inspected some HC-PBGF canes from the same batch from which the examined fibres were made. The optical microscope images of the cane revealed the existence of foreign particles and contamination of the same dimensions as speculated from the length of the defective regions, leading me to conclude the origins of the scattering anomalies (and likely susceptibility to fibre breakage) is due to contamination and particles inadvertently incorporated inside the fibre preforms.

At this point, two areas of further investigation were pursued. In an attempt to gain more information from the evolution of defects in HC-PBGFs and to find a suitable inspection method to study canes and preforms non-destructively, I employed X-ray computed tomography, which allows for measurement of the internal structure of the fibres, canes and preforms without cutting or damaging the samples. The other area for further investigation led to the development of the optical side scattering radiometry technique, through which the position of scattering points along the length of the fibre sample can be mapped in a manner similar to an OTDR trace, however with much higher resolution and dynamic range.

I provided a first demonstration of non-destructive X-ray CT to inspect the internal features of microstructured HC-PBGFs. XCT offers a powerful tool to evaluate the internal structure of preforms, canes and the final fibre. It opens up the possibility of analysing the full multistage fabrication process of HC-PBGFs, which is wholly impractical using more standard techniques such as optical and electron microscopy.

I obtained results relating to a HC-PBGF preform in which I identified some stacking errors via XCT analysis that resulted in a variation from the intended arrangement of capillaries and unintentional gaps between various elements of the cladding region. Although these problems may look relatively benign, they can have a catastrophic effect on the performance of the fibre: in particular in terms of the loss, which relies on a near-perfect geometry for its guidance mechanism. XCT analysis allows in principle the possibility to capture much smaller deviations and effects such as twist, existence of small gaps, dislocations and missing elements without imparting

damage to the preform itself. Additionally, I obtained results on a specific HC-PBGF cane (that I previously introduced in Chapter 3 in the context of defect identification) in which I have identified contamination in the form of minute particles, likely of metal. The presence of such particles in the second stage preform, leads to a very high chance of a fibre breaks during the fibre draw process. This analysis was again performed non-destructively, which opens up the possibility of using this cane in a fibre draw to study the correlation of fibre breakage and contamination. The unprecedented detail of this result also enabled me to make a reasonable guess as to the nature and origin of the inclusion, which has helped to reduce/eliminate the recurrence of such contaminants in our future canes. Moreover, I analysed a specific HC-PBGF sample from a fibre that I studied in Chapter 3, in which I was able to identify similar microstructure deformation.

Next, I looked at the first stage transition region (necking region of a HC-PBGF preform to cane) where the capillary arrangement in the preform goes through substantial structural changes as it is drawn to cane. I also looked at the second stage transition region (necking region of a HC-PBGF cane preform to fibre) where the microstructured region expands and takes up a much greater cross-sectional area in the final fibre. None of the above analysis would be easily achievable using other conventional characterisation techniques. The result of the latter analysis was used to validate our advanced fluid dynamic model (developed by an ORC colleague Dr. G. T. Jasion) that allows us to study the behaviour of the fibre preforms in the process of upscaling the fibre yield.

Although not immediately relevant to the goals of this study, I have also described how this non-destructive technique can be utilized to visualize and measure macroscopic and microscopic deformations within a HC-PBGF to HC-PBGF splice (an example of one of the most complicated fibre processes and devices). Here, this technique unveils the structural changes induced by the splice process and that is otherwise hidden using other conventional inspection methods. I managed to reduce the loss down to few tenths of dB by the captured details in this study.

Another “first demonstration” analysis that I was able to carry out was that of imaging the damaged region of a HCF used for the delivery of very high peak power (>100 MW) picosecond laser pulses, a theme of great current interest. The finding of this study is used to design and develop hollow core fibres for high power laser delivery – a Research Fellowship from the Royal Academy of Engineering pursued by my ORC colleague Dr. G. T. Jasion. I also carried out an analysis of a 7-element MEF, which highlighted the capability of the technique to discern between layers of different polymer coating, as well as to identify deviations in the fibre structure from the design target. Moreover, I presented the analysis of a metal incorporated fibre (MIF), for which the presence of wires of a ductile metal complicates the fibre cleaving process to the point of

preventing clean and uniform cross section cleaves as required for conventional visualisation/imaging. In the MIF, I identified flaws within the metal wires. Our results illustrate the capability and value of using X-ray CT techniques in the ongoing refinement of various aspects of Microstructured and Multi-Material fibre fabrication and technology.

I believe, as demonstrated by these examples, that XCT is an invaluable tool in the study and diagnosis of imperfections in HC-PBGFs and their preforms, through which we can obtain unprecedented information about each and every stage of the HC-PBGF fabrication process, to identify the origin of imperfections and to explore possible mitigation strategies to eliminate them. Based on these findings, we are investigating a number of modifications/ changes to our current fabrication steps and tools, such as upgrading the cleanroom to a higher grade, in particular where the first stage preform is assembled, changing the burners from metal to glass on the glass-working lathe and replacing antistatic blowers to antistatic bars. In addition, we have introduced stringent requirements on the cleanroom coveralls used by our fabricators, in order to reduce various sources of contamination.

In parallel with the XCT analysis, I developed a technique for long-range, high spatial resolution measurement of the longitudinal scattering pattern of HC-PBGFs – which I called OSSR. This method can measure the distributed loss of fibres with ~50mm fixed resolution and ~60dB dynamic range: performance well beyond the capability of the best commercial fibre measurement systems. In principle, it can be used to measure any type of specialty fibre at any wavelength of choice. I validated the method in measurements on 3km of SMF28e, showing an accurate loss measurement to within the tolerance of the manufacturer's data. Then I used the OSSR to measure a record-length (11km) HC-PBGF, providing for the first time accurate quantitative information about the longitudinal properties of these fibres despite the very large (~57dB) fibre span loss. I exploited the high spatial resolution of OSSR to obtain detailed information on the presence/absence of small scattering points and defects (similar to the ones I studied in Chapter 3) along the fibre. Arrangements have been made to use XCT to study the identified scattering points in order to measure whether they are structural deformations or are caused by a form of contamination (similar to the fibre defects in Chapter 3). The knowledge of fibre integrity and longitudinal consistency is crucial in assessing the process of fibre fabrication and optimising the fabrication steps toward the production of a uniform long-length low loss fibre. The record-breaking 11km HC-PBGF is a result of such process optimising and such a result can be appreciated because of its uniformity and consistency, which both could not have happened without the presented technique, i.e. OSSR.

This technique can also help to establish improvements in the fabrication process. As an example, I used OSSR to identify >200 scattering defects/km in a HC-PBGF with an anomalous loss of 37dB/km, which provided a reasonable explanation for the excessive loss of the fibre. This measurement shows excellent agreement with the results from the IR camera inspection method I introduced in Chapter 3. I demonstrated the wavelength flexibility of the setup through a measurement at a wavelength of 2µm, where the lowest loss operation of HC-PBGFs is predicted. This measurement showed the ability of OSSR to address measurements at wavelengths for which no commercial tool currently exists. Also in this wave band, the loss estimate was in excellent agreement with the cutback loss measurements. As shown by these examples, OSSR is proving to be an invaluable tool in the course of HC-PBGF development, playing a significant role similar to OTDR in the development of standard single mode fibre in checking fibre uniformity and integrity.

Next, I would like to point out a few directions for expanding the use of the methods and techniques I have developed, including some interesting ideas that will help us to learn more about HC-PBGFs and their fabrication.

I believe OSSR could ultimately provide an excellent solution for the longstanding issue of fibre quality monitoring directly during the fabrication process of optical fibres. In the near future, I would like to explore and demonstrate its implementation directly on a fibre-drawing tower.

Also, I would like to study short-length HC-PBGFs using OFDR and compare the backscattered power traces against the OSSR trace, in particular for fibre samples that have defects. In particular, I am interested to study the scattering signature of the fibre defects to conclude my findings on scattering pattern of different types of defects that I introduced in Chapter 3.

In addition, I would like to capture the evolution of microstructure deformation at the onset of a defect in HC-PBGFs using XCT. Such an analysis would allow us to study the impact of defects on the transmission properties of these fibres.

The study of first stage and second stage transition regions requires more structural resolution near the narrower sections, which require mores more elaborate XCT scans – this is an area of further study that I would like to explore. The finding s of such a study would help to improve the fluid dynamic model and predictions of the behaviour of these fibres and their preforms during the draw process.

I would also like to employ this technique in the study of other microstructured fibres, in particular, tubular lattice antiresonant MOFs which represent an attractive solution for high-power laser light delivery, and which are also finding new applications in the area of data communications, as their loss is improved.

Appendices

Appendix A: Scanning electron microscopy

Appendix B: Publications

Appendix A: Scanning electron microscopy

A.1 SEM application

Scanning electron microscopy (SEM) is used extensively for a number of reasons including:

- Large magnification range (10 to 3,000,000X), with a maximum magnification much higher than what is achievable by standard optical microscopy;
- Large depth of field (4mm to 400nm, depending on magnification – ~500 times better than optical microscopy at an equivalent magnification); and
- High resolution (down to sub-nanometre at the very best, but in any case, well below the diffraction limit of optical microscopy).

In the case of HC-PBGFs, SEM is the only technique that allows reliable, accurate, repeatable measurements of the fibre microstructure. As we discussed in Chapter 2, some key geometrical parameters within the fibre microstructure determines the optical properties of the fibre. If the microstructure is measured correctly, there exist modelling and simulation tools that allow an accurate estimation of all the optical properties of the fibre, such as loss, bandwidth, and modal properties among others. These methods are extremely powerful; however, they require a clean, high contrast, high SNR SEM image that accurately portrays the structural details of the fibre. Due to the importance of this aspect for the overall development work of HC-PBGFs within our group, I have devoted a very substantial amount of time to improving the quality of sample preparation and image acquisition methods. This appendix outlines the main achievements in this area of my work and links into what other development it has unlocked.

Optical fibres are typically made of dielectric material such as various types of glasses. In SEM, a beam of electron (with energy ranging from sub keV to a few tens of keV) is scanned in a raster pattern over the sample surface. The incident electrons interact with the sample and are either back reflected, or absorbed – thus exciting secondary electrons from the regions at and immediately below the surface of the sample. This process works extremely well for high conductivity samples (i.e. metals and semiconductors), where the excess charge deposited by the beam is rapidly dissipated via the sample and the metallic holder. In the case of insulators and dielectric materials, however, electro static charges can build up on the surface of sample. These charges, unless they are removed (e.g. via a suitable coating or through gas molecules present in the measurement chamber) can cause an artefact known as “charging effect”. This effect builds up in time and can be so severe to render the SEM image completely useless as all the structural details of the fibre are either lost or substantially deformed. To minimize the charging effect, in

particular for high-resolution imaging, one solution is to coat the fibre samples with a conductive metal like gold, palladium, platinum (or, in some instances, carbon). This method normally works well, however in the case of HC-PBGFs two challenges arise: i) if the coating is too thick the image may not accurately portray the fibre structure – for instance the thin struts present in the cladding may appear thicker than they are; ii) furthermore, the presence of air holes means that the side surfaces inside of the hollow channels do not get coated by the metal, and thus they can get charged up.

Two typical detectors that are often found in SEM machines are Secondary Electron (SE) detectors and Backscattered Electron Detector (BSD). Secondary electrons are produced when the main electron beam hits the samples surface. Multiple secondary electrons are generated per single incident electron, thus ensuring a good SNR. On the other hand, SEs have relatively low energy and can be more easily deflected by e.g. charge building up in the sample. Using a SE detector under optimum conditions, a high-resolution imaging of fine surface morphology can be obtained. For an ideal SEM sample, the SE detector should be able to produce image resolution as fine as ~3nm for a tungsten-filament or ~0.6nm for field emission SEM [181]. In contrast, BS electrons are primary beam electrons deflected by the atoms constituting the sample. These electrons have much higher energy than SEs, although their number and thus SNR is generally not as high. The image contrast of micrographs collected via the BSD is determined by a combination of the atomic number (material composition) of the material and its surface topography. The number of backscattered electrons (BSE) produced during the imaging process is proportional to the sample material's mean atomic number. Therefore, a material with a higher atomic number appears brighter than a low atomic number material in an image obtained by BSD. The best resolution achievable with BSD under ideal conditions is about 4nm[181], thus lower than for the SE detector; however, it can be preferable for the analysis of non-conductive samples since the BS electrons have higher energy and are this less sensitive to surface charging effects, often resulting in a sharper contrast. The low energy of SEs (i.e. <50eV and typically 2 to 5eV) implies that a surface charge of the same magnitude (causing only 2 to 5V electric potential difference) on the specimen can significantly alter the number of detected SEs, resulting in imaging artefacts. In contrast, the average energy of BSEs is much higher than SEs and is typically within 50 to 80% of the energy of the incident electron beam [182]. Therefore, the specimen should have been electro-statistically charged to an electric potential difference of more than 10kV (for incident beam energy of ~20keV) before the BSD becomes considerably affected by charging artefacts, which usually does not happen.

Figure A.1 **a** shows an example of a HC-PBGF imaged with SE detector and no particular precautions. The charging effect (due to the dielectric nature of the glass samples) has obscured

the structural details around the fibre core and its surrounding microstructure. By using a lower detector bias voltage, the charging effect can be hidden away as shown in Figure A.1 **b**. However, this inevitably leads to a substantial drop in the signal to noise ratio, and, since longer scan times are typically required, this method is more prone to image distortions due to external disturbances such as vibrations. The image in Figure A.1 **b** represent an example of the best quality image that was collected (by my colleague Naveen Baddela) before I was given responsibility over this type of measurements within the Microstructured Fibre Group in late 2012.

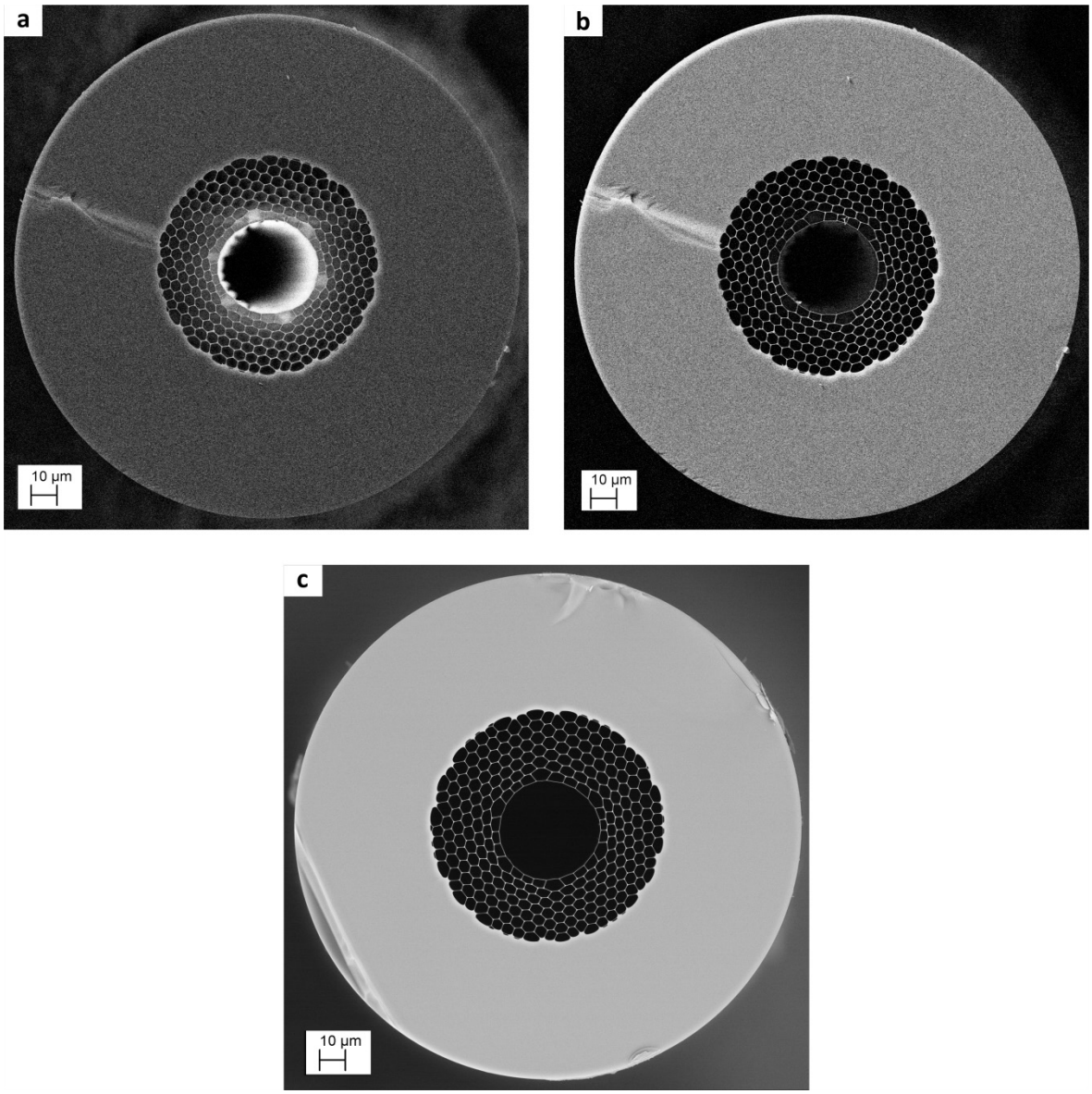

Figure A.1: Comparing the result of SEM images of HC-PBGFs using different imaging techniques. **a**, Image collected in Secondary Electrons (SE) mode without suitable precautions for avoiding surface charging effects. Substantial image distortion is present in the region surrounding the core, which renders the image of limited utility. **b**, SE imaging method using low bias voltage to reduce charging effects: poor SNR is clearly visible. **a** and **b**

are collected by Naveen Baddela. **c**, High SNR, high contrast image collected via backscattered electron imaging.

I have extended and further developed our sample preparation method, through introducing steps and modifications that ensure fibre samples with high quality cleaves are collected and then are coated with platinum, a material that I have identified as a suitable choice for high resolution measurements. The advantage of Pt is that a thinner uniform layer can be deposited as compared to the more commonly used gold (3-5nm vs. >10nm). More importantly, I have been using BSD extensively to eliminate the charging artefacts and reduce image distortion caused by external distortions. Through these adjustments to the conventional SEM imaging process, I can reliably use the BS detector to obtain high resolution and high fidelity images that are free from/have minimum both artificial structural distortions due to sample preparation, and image distortion because of imaging artefacts and external disturbances.

A.2 Method

In order to image the cross section of a fibre sample using SEM, one needs to follow the three main steps below. In a logical order these are:

i. Mounting the sample on a SEM stub;
ii. Coating the samples with a conductive material;
iii. Imaging the sample using a SEM system.

The first two steps together are referred to as sample preparation, which is then followed by imaging step. Depending on the equipment used, there would be some little differences as what should be considered a good practice. However, one should be able to replicate what I have achieved, by following the procedures I describe here.

A.2.1 Mounting samples on a SEM stub

In order to install fibre samples in the SEM microscope available at the ORC, I use a standard pin type SEM mount (stub). An image of the pin stub is shown in Figure A.2 **a**. I attach a hexagonal M8 zinc plated steel nut (Figure A.2 **b**) on top of the pin stub using a double-sided carbon tape (Figure A.2 **c**). I stick a cut-to-size piece of double-sided carbon tape on one of the side-faces of the nut. I use the other sticky side of the tape for mounting the fibre samples, as shown in Figure A.2 **d**. I carefully prepare each fibre sample one by one, as I explain in the following.

Each fibre sample that is mounted on the customized pin stub requires a careful preparation to ensure it is not contaminated. For this, I prepare my samples in a cleanroom environment where I also have access to an optical microscope. Once I cleaved a fibre (usually hand cleaved), I inspect

its end face under the microscope at high magnification (50x microscope objective times 20x eyepiece that is ~1000x). At this stage, I make sure no visible damage has happened to the microstructure and the end face is clean from dust particles and contamination. Using electrostatic charge management devices (such as an anti-static gun) to neutralize the charged fibre samples may improve the quality of sample cleanliness. Each sample is about 3-5cm long when I mount it on the pin stub. Once I fixed the sample in position, I cut the remaining bottom section. It is very important to leave only a very small fibre length protruding from the top of the nut. This ensures no sample vibration at very high magnification (>20,000x) during SEM imaging. I prepare 3 to 5 samples for each specific fibre that I like to measure. This is mainly due to the fact that, features of the microstructure are not clearly resolved by the optical microscope during the end face inspection and there is always a chance that some part of the microstructure in one or two samples is broken. I have found, in most case, one out of the three samples is definitely clean.

Once all the samples are attached to the side of the pin stub (similarly to Figure A.2 **d**), the side of the fibres are covered with carbon adhesive paste. However, the paste should stay well away from the tips of samples (as seen in Figure A.2 **e**). The carbon paste helps conducting the electrostatic charge that is build up on the samples during the SEM imaging. At this point, the samples are ready for coating process.

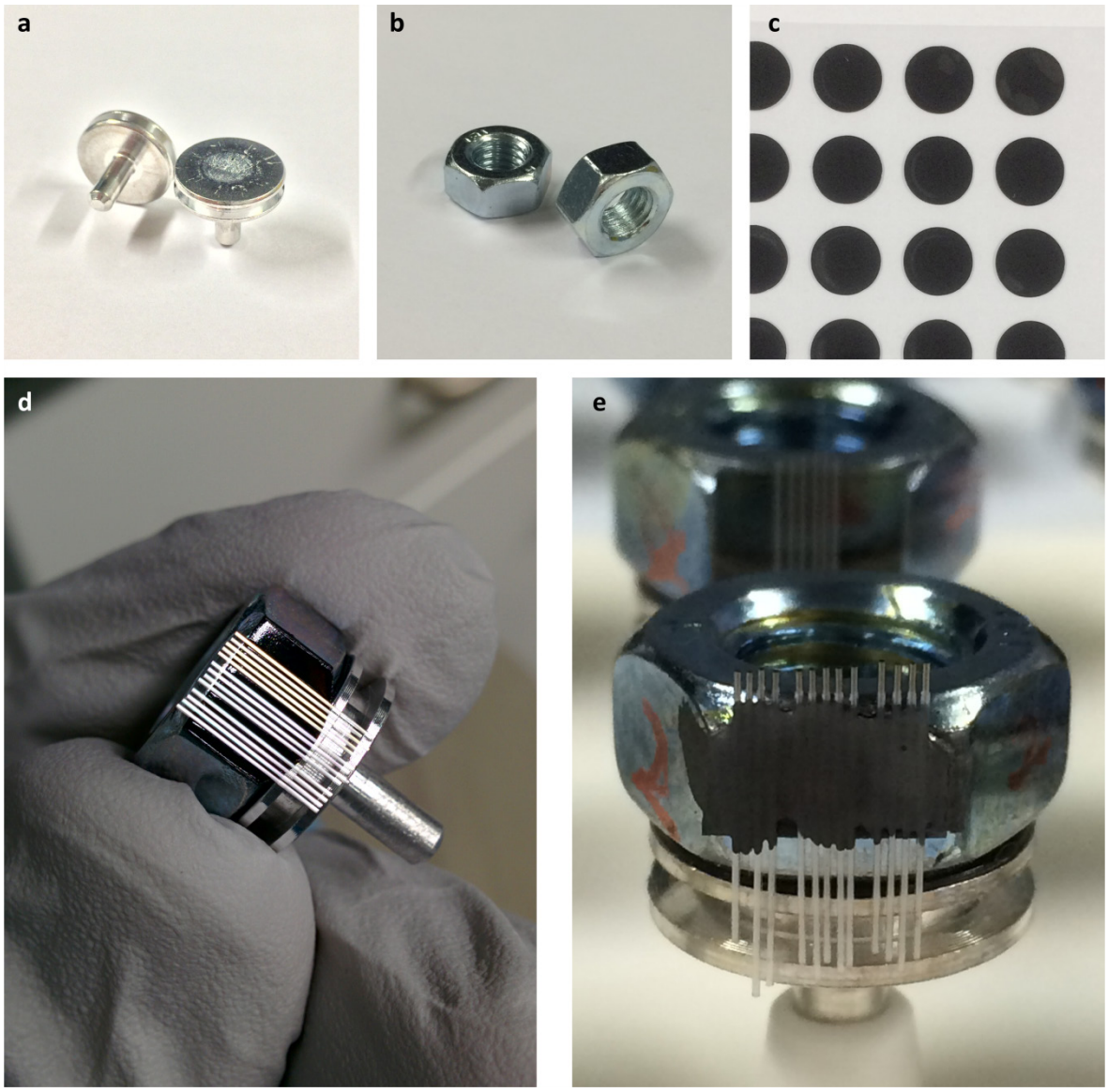

Figure A.2: SEM sample preparation procedure. **a**, SEM pin stubs. **b**, Zinc-plated steel M8 nuts. **c**, Double sided carbon tape. **d**, customized pin stub with 3 sets of fibre samples. **e**, The samples are partially covered by carbon paste.

A.2.2 Coating samples

In this step, samples are coated by a very thin (5-15nm) layer very high quality conducting material. This is again to facilitate neutralising the surface charges built up during the SEM imaging. Several coating materials are available for this purpose, such as Gold, Platinum, and the mixture of Gold-Palladium. Depending on the material, the thickness of coating may vary. Among these options, I am using Platinum as it allows the minimum coating thickness (~5nm) to be used. Also, because of its high density, it produces more backscattered electrons.

I have coated my samples using an “Agar automatic sputter coater B7341” which was available in the ORC SEM lab. Other machines also can be used for this purpose. Once the samples are coated, the stub is ready to be transferred into the SEM machine.

I have prepared hundreds of fibre samples, through which I have perfected our sample preparation technique, in particular through identifying both samples with minimum artificial distortions and (more importantly) suitable coating material and thickness, in order to achieve reliable capture and measurement of high resolution and high fidelity images using SEM. I have imaged fibre samples of various sizes (from ~120-350µm with features as thin as a several tens of nanometres), and different structures (HC-PBGFs, Kagome fibres, and antiresonant tubular lattice fibres among other). I have also image larger (~3mm OD) structure like HC-PBG canes. Figure A.3 shows examples of the samples I have prepared and imaged. Figure A.3 **a** shows a SEM image from the top of one of the pin stubs that I have prepared, which includes 4 different sets of fibres (each set has 3 to 4 sample of a particular fibre) , sitting neatly side by side. In Figure A.3 **b**, a SEM stub that includes two HC-PBG canes is shown. Figure A.3 **c**, shows my collection of more than 50 SEM stubs, each of which has several fibre samples on its side.

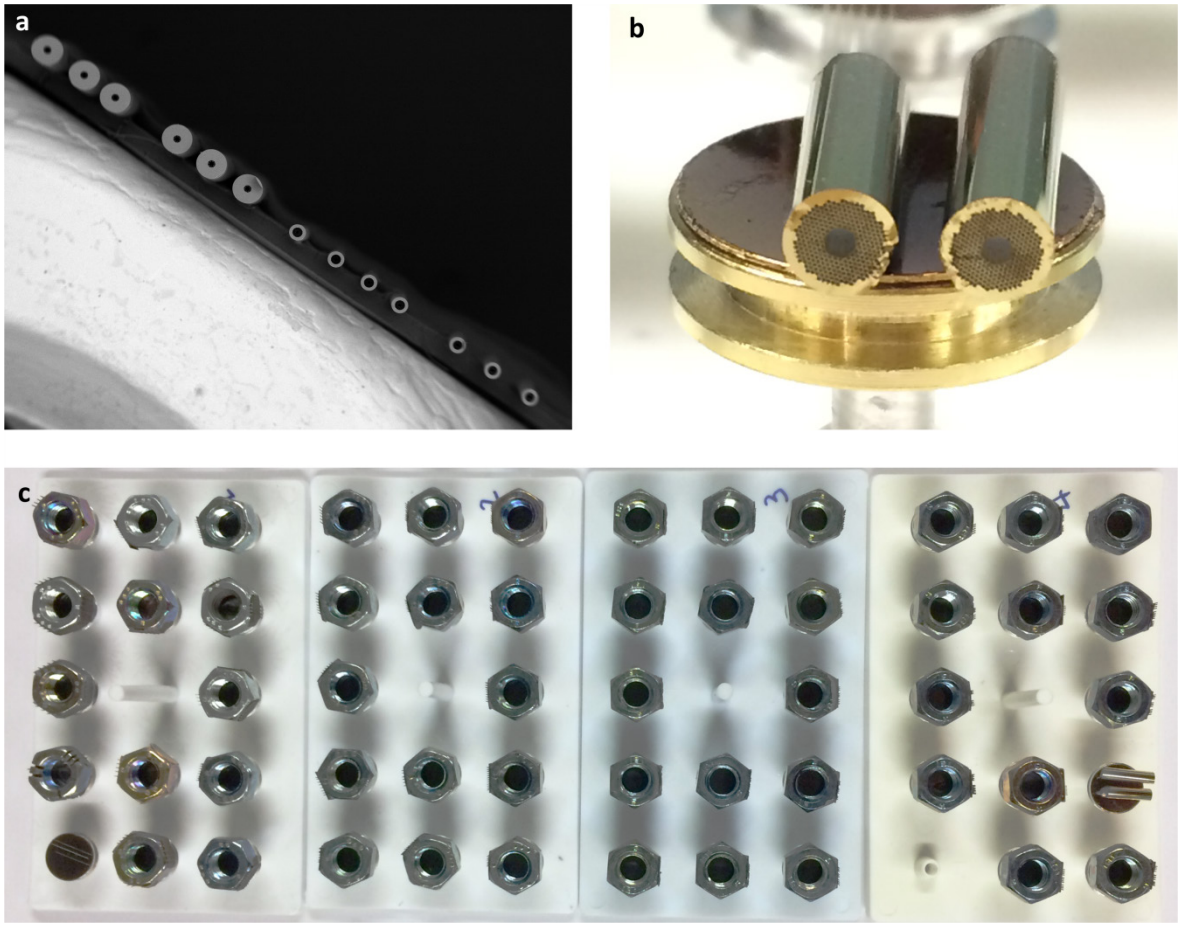

Figure A.3: Various SEM samples mounted and tested, through which I have perfected my sample preparation method.

A.2.3 Setting up the SEM machine and imaging

In order to obtain reliable SEM images, it is important to develop a recipe that should be used for all subsequent measurements. There are several standard configurations to initialize an SEM machine; two of the most common ones are High Vacuum (HV) or Variable Pressure (VP). For dielectric samples that often suffer from charging artefacts, VP configuration is recommended because (unlike HV mode) it is possible to have a considerable amount of gas molecules inside the SEM chamber to neutralise the charges that have built up on the surface of the specimen. However, VP mode requires a larger beam limiting aperture size (e.g., 100µm as compared to 20µm for HV mode) that results in an increased beam spot size and therefore reduced resolution. Also, the SNR decrease in VP mode due to the scattering/absorption by the gas molecules in the chamber. Although fibre samples are dielectric, considering the fact that charging artefacts can be avoided using BSD, I have selected HV configuration.

The accuracy of SEM measurements depends on a number of parameters that may require fine adjustment before each measurement session. Although it is not a common practice, in order to do accurate SEM measurements, I use two calibration samples, a “gold on carbon” sample, which is used for accurate beam alignment, and a silicon specimen that is used for size measurement calibration. These calibration samples have been installed on pin stubs and can be used alongside the fibre samples during a SEM session. The nanometre-size gold particles in the carbon substrate produce a very high contrast object that allows very accurate beam alignment to achieve very high-resolution imaging. Figure A.4 **a** shows the gold on carbon calibration sample at 5000x magnification with SE detector and 8mm working distance(WD) and 100pA probe current (I_p). Figure A.4 **b** shows the silicon specimen, captured using the same imaging parameters (i.e., WD=8mm and I_p=100pA) at 3000x magnification. This sample consists of a pattern with 10µm pitch size both vertically and horizontally that allows calibration of the accuracy of SEM measurements. In the standard protocol to use these calibration samples, SE detector is used. Once these adjustments are done, any detector can be used for imaging.

Another important step in achieving an accurate SEM measurement is the alignment of fibre samples under the electron beam. In particular, it is very important to ensure the fibre cross-section is perpendicular to the electron beam, otherwise a part of the side of the strut membranes in HC-PBGFs are also imaged, causing false membrane thickness reading. This alignment has been a standard practice in our group; however, this procedure needs to be done using SE detector, prior to the use of BSD for imaging.

At the end of the angular alignment, the fibre image using the SE detector at normal operation condition (detector bias voltage 300V) looks similar to the Figure A.1 **a** with a strong charging

effect in the core (the white patches inside the core which has affected the air hole rings close to the core as well) . Figure A.1 **b** has been obtained under similar condition using the SE detector however at detector bias voltage of -70V. This setting hides the charging effect characteristic at the expense of increased scan time (~4 times longer) as the signal to noise drops drastically. However, in Figure A.1 **c**, through the use of BSD the charging effect has been completely removed, and because of the high density Platinum coating more BSEs have been generated. The large Z contrast between the air holes and silica sample coated with Pt results in a high contrast image and the accurate beam alignment using the calibration samples ensures high resolution and accurate measurements.

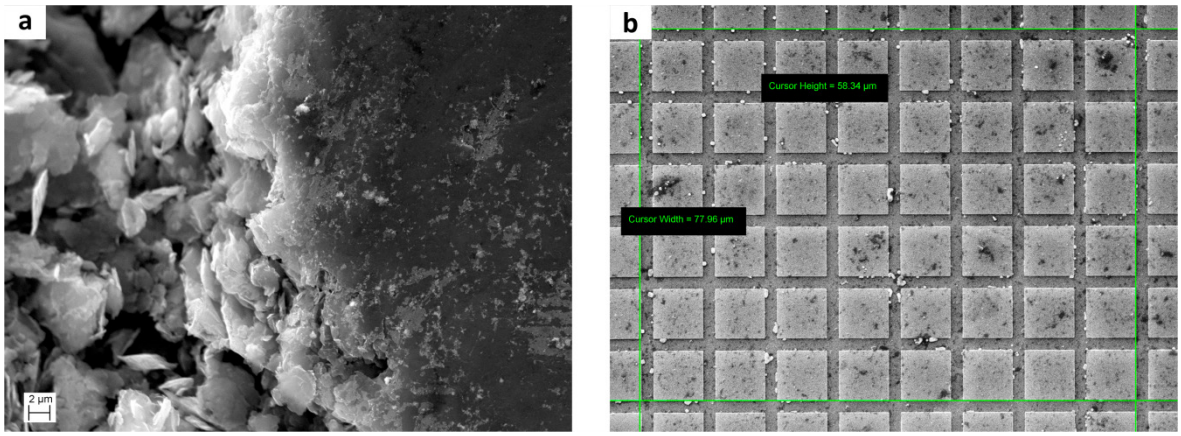

Figure A.4: Calibration samples for initializing SEM machine. **a**, Gold on carbon sample. **b**, Silicon specimen.

I have used two scanning electron microscopes from Zeiss, namely EVO LS 25 and EVO 50. The procedure to use these machines is very similar. I mainly used EVO 50 and in the following, I describe my imaging procedure using this particular machine.

A.3 Results and discussion

Figure A.5 **a** shows the gold on carbon calibration sample at 50,000x magnification, where the cluster of gold particles in carbon substrate is seen with high detail using the SE detector at the end of beam alignment procedure. As discussed above, this calibration at each and every SEM session ensures a high resolution imaging. In Figure A.5 **b** and **c,** parts of the outer edge of the microstructured cladding of two different HC-PBGFs are shown at 95,000x and 200,000x magnifications. In Figure A.5 **d** a node in the microstructure cladding is imaged at 90,000x magnification. These three images have been obtained using the BSD detector after a proper calibration, which show no charging artefacts.

These particular samples are coated with 10nm thickness of gold, which in fact is not thin as compared with the thickness of struts. Also, the gold thickness need to be increased in order to

remove the graininess on the silica surfaces caused by the gold particles. Considering the fact that HC-PBGFs contain features that are well below 100nm, using gold as the coating material is not suitable. Using platinum however, a uniform thin film with 5nm thickness on the surface of the fibre can be achieved. Also, the higher density of platinum, increases the number of produced BSEs which provides better SNR.

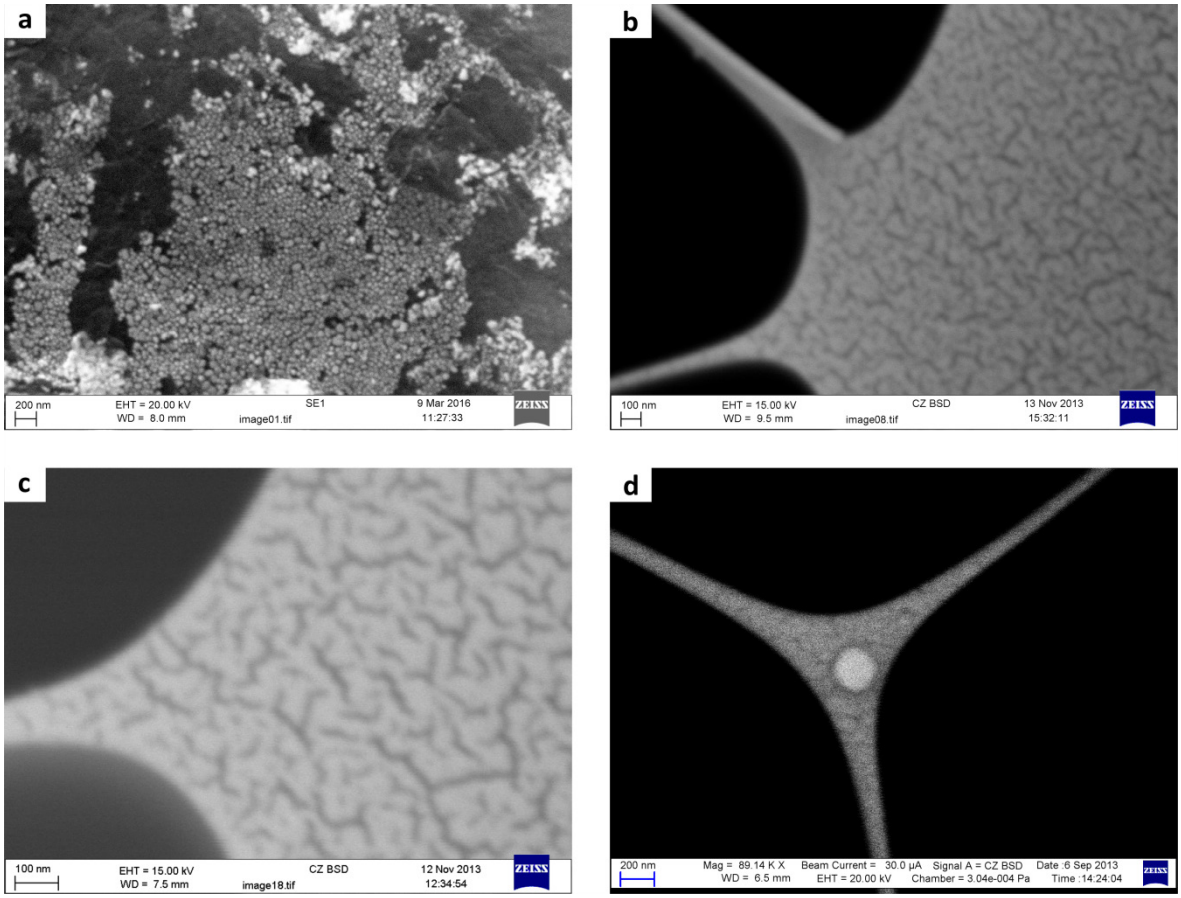

Figure A.5: High resolution imaging by SEM. **a**, Gold on carbon calibration sample at 50,000x magnification using SE detector, showing a resolution of ~10nm, after calibration. **b**, **c** and **d**, different parts of the microstructure cladding in different HC-PBGF samples at 95,000x, 200,000x and 90,000x magnifications using BSD detector, respectively. As highlighted by these images, HC-PBGFs may contain features that are only several tens of nanometres. Gold coating with 10nm thickness has been used for these samples. The grainy texture of gold film indicates even higher thickness is required for having a uniform coating film. This indicates gold may not be a suitable choice for accurate length/size measurement. The bright dot in the middle of image **d** indicates a different material composition (possibly a contaminant particle) with higher density than it surrounding; another benefit of BSD, which can be explored to identify contamination.

By means of the images shown in Figure A.6 **a**-**e** I compare the quality and sharpness of the images obtained by BSD and SE detectors. Figure A.6 **a** and **b** show images of a part of the

microstructure cladding and core of an HC-PBGF using SE and BSD detectors respectively. As the images show, apart from the low SNR in the image captured by the SE detector, there is no difference in the amount of structural details between these two images. In figure A.6 **c**, a window in the middle of an image captured by SE detector has been recaptured by BSD detector. Close to the position of recaptured node, where the image is not blurred, the structural edges follow, demonstrating similar measurement precision by the two detectors. In Figure A.6 **d** and **e**, a part of the core boundary has been captured by SE and BSD detectors, at similar scan speed. The high SNR in image captured by BSD results very clearly from the image.

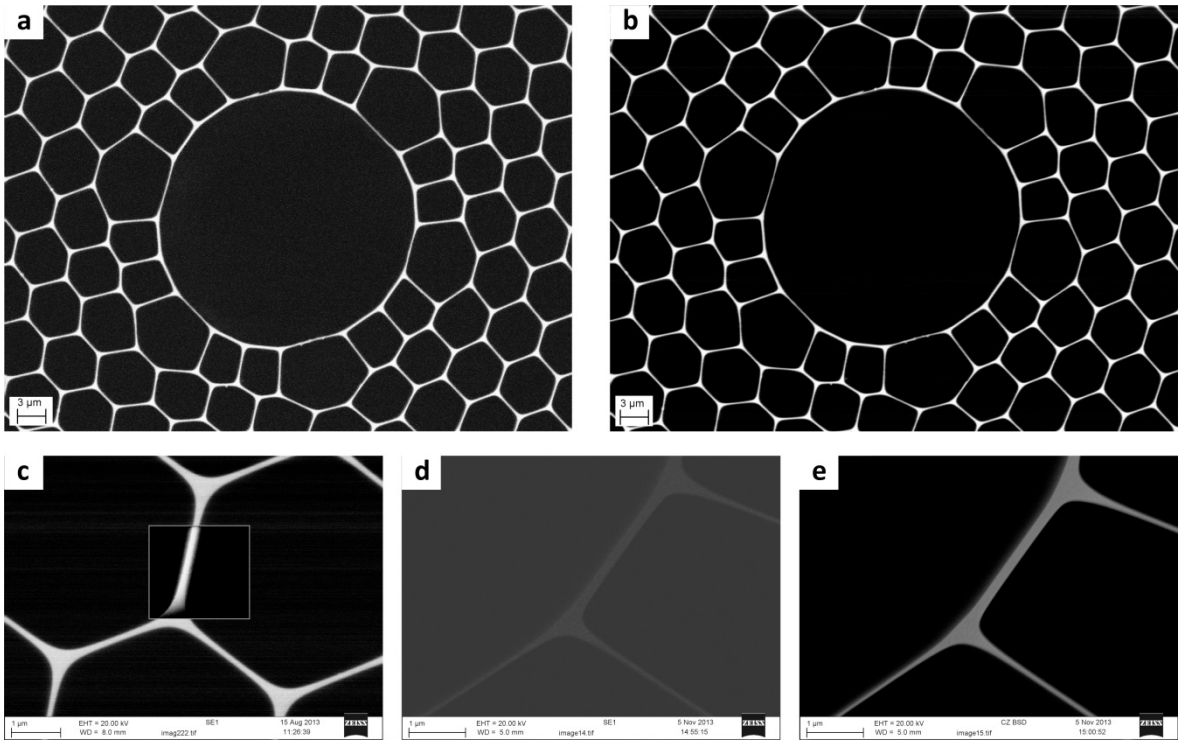

Figure A.6: Comparison of two HC-PBGF images collected by SE and BSD detector **a** and **b**, show the microstructure around the core in a HC-PBGF captured by SE detector and BSD, respectively. The obtained structural information using both detector is almost the same, however BSD provides improved SNR. This is seen well in **d** and **e**, showing the struts at the core surround captured by SE and BSD with similar scan speed, respectively. **c**, a part of the microstructured cladding captured by SE detector. A window in the middle of this image has been recaptured by BSD.

Using these accurate and sharp SEM images combined with our powerful modelling and simulation tool we have developed, we presented a new approach to simulate the characteristics of fabricated HC-PBGFs [183]. As discussed in section 2.2 and 2.3, optical properties of HC-PBGFs, such as loss, bandwidth, and modality and so on, can be determined from the fibre's structural parameters, e.g. pitch size, hole diameter, strut thicknesses of core and cladding, node sizes and core diameter among others. The accuracy of estimated properties by modelling tools very much

depends on the accuracy of the fibre structure that is given to the model. This method obtains the geometrical irregularities of the fibre cross-section from the SEM images. This tool can achieve remarkable accuracy in estimating the experimental loss of HC-PBGFs as a result of the reliable high resolution images that have been obtained by the presented SEM technique. Besides the loss, for the very first time, the method can reproduces accurately both the spectral and the spatial position of the surface modes. The spectral position of SMs, as discussed in different sections in this thesis, in particular in section 2.6.1.2, is key to an accurate estimate of wavelength dependent modal parameters such as group delay, differential loss and group velocity dispersion. The spatial position of SMs can enable the identification of the geometrical deformations responsible for SMs. We believe this method will be a powerful tool in the development of wider bandwidth, lower loss HC-PGFs [183]. Figure A.7 shows an example of the SEM images used for this model.

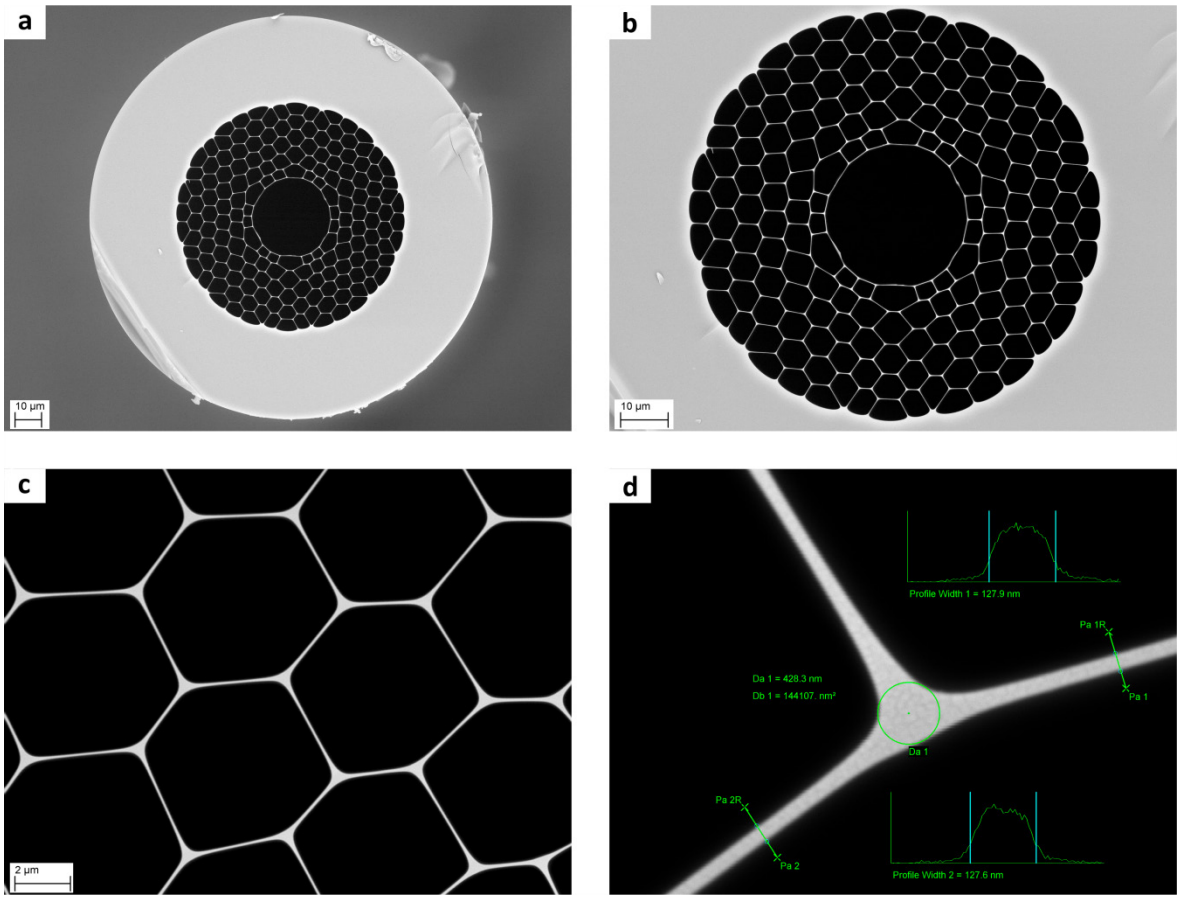

Figure A.7: SEM images and measurements for modelling and simulation of the optical performance of HC-PBGFs. a, The full fibre cross-section image. b, The microstructured cladding. c, A magnification of a part of microstructured cladding . d, A node and its connected struts at the core surround.

Figure A.7 **a** shows the full fibre cross section. In Figure A.7 **b** the microstructured cladding is shown, which allows finding the accurate position of the nodes. Figure A.7 **c** shows a part of

microstructured cladding, which is used in the estimation of pitch size and Figure A.7 **d** shows a node at the core surround to measure the node size and the strut thickness of the core surround. A number of other images are also taken to help measuring other structural parameters.

I use the presented SEM technique to image HC-PBG canes and other microstructured fibres like Kagome and antiresonant tubular lattice fibres, images of which are shown in Figure A.8. These images are useful for other research activities in our group. In particular, cane images such as Figure A.8 **a**, are used in developing a modelling to model realistic fibre draws (i.e. virtual fibre draw). Images of Kagome sample (see Figure A.8 **b** and **c**) are used to measure their important fibre parameters such as the thickness and curvature of the core surround struts [171, 184, 185]. The thickness of the internal tubes in an antiresonant tubular lattice fibre (figure A.8 **d**) is also measured using SEM [186, 187].

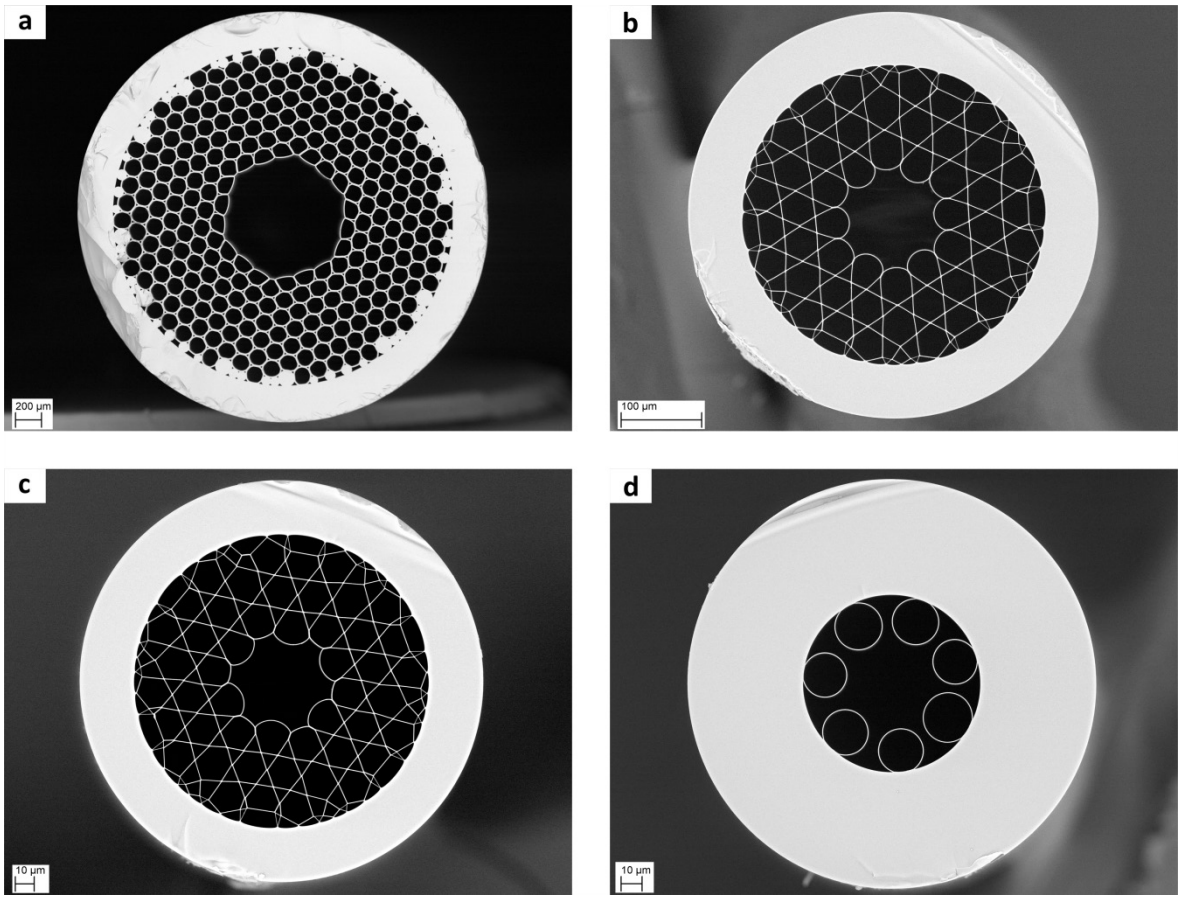

Figure A.8: **a**, SEM image of HC-PBG cane. **b** and **c**, SEM images of two different Kagome fibre. **d**, SEM image of an antiresonant tubular lattice fibre .

In conclusion, through the choice of platinum as a suitable coating for BS analysis, and by including additional steps in the imaging protocol in order to ensure that the sample images are providing well-calibrated lengths/thicknesses readings, it is now possible to use the BS detector reliably for high-resolution high-fidelity images.

Appendix B: Publications

Here I provide the list of the publications, which both resulting from the work and/or include an element of the work I presented in this PhD Thesis.

1. Poletti, F., M.N. Petrovich, N.V. Wheeler, N.K. Baddela, E.R. Numkam Fokoua, J.P. Wooler, D.R. Gray, S.R. **Sandoghchi**, J.R. Hayes, Y. Jung, R. Slavik, S.U. Alam, V.A.J.M. Sleiffer, M. Kuschnerov, and D.J. Richardson. *Hollow core fibres for high capacity data transmission*. in *18th OptoElectronics and Communications Conference held jointly with 2013 International Conference on Photonics in Switching (OECC/PS)*. 2013.

2. Poletti, F., N.V. Wheeler, N.K. Baddela, Y. Jung, J.P. Wooler, D.R. Gray, E.R. Numkam Fokoua, J.R. Hayes, R. Slavik, S.U. Alam, S.R. **Sandoghchi**, V.A.J.M. Sleiffer, M. Kuschnerov, M.N. Petrovich, and D.J. Richardson. *Recent Advances in Photonic Bandgap Fiber Technology*. in *2013 IEEE Photonics Society Summer Topical Meeting Series*. 2013.

3. Poletti, F., J.P. Wooler, N.V. Wheeler, N.K. Baddela, D.R. Gray, E.R. Numkam Fokoua, J.R. Hayes, Y. Jung, S.U. Alam, S.R. **Sandoghchi**, V.A.J.M. Sleiffer, M. Kuschnerov, M.N. Petrovich, and D.J. Richardson. *Transmitting Data Inside a Hole: Recent Advances in Hollow Core Photonic Bandgap Technology*. in *Workshop on Specialty Optical Fibers and their Applications*. 2013. Sigtuna: Optical Society of America.

4. Richardson, D.J., N.V. Wheeler, N.K. Baddela, J.R. Hayes, Y. Chen, E.R. Numkam Fokoua, S.R. **Sandoghchi**, D.R. Gray, J.P. Wooler, Y. Jung, S.U. Alam, V.A.J.M. Sleiffer, M. Kuschnerov, M.N. Petrovich, and F. Poletti. *Advances in photonic bandgap fiber technology for optical communications* in *Extremely Advanced Optical Transmission Technologies (EXAT) Symposium*. 2013. Hokkaido, Japan.

5. Wheeler, N.V., A.M. Heidt, N.K. Baddela, J.R. Hayes, S.R. **Sandoghchi**, E.R. Numkam Fokoua, F. Poletti, M.N. Petrovich, and D.J. Richardson. *Low Loss, Wide Bandwidth, Low Bend Sensitivity HC-PBGF for Mid-IR Applications*. in *Workshop on Specialty Optical Fibers and their Applications*. 2013. Sigtuna: Optical Society of America.

6. Wooler, J.P., F.R. Parmigiani, S.R. **Sandoghchi**, N.V. Wheeler, D.R. Gray, F. Poletti, M.N. Petrovich, and D.J. Richardson, *Data transmission over 1km HC-PBGF arranged with microstructured fiber spliced to both itself and SMF*, in *European Conference on Optical Communication*. 2013: London, United Kingdom. p. Tu.3.A.3.

7. Wooler, J.P., S.R. **Sandoghchi**, D.R. Gray, F. Poletti, M.N. Petrovich, N.V. Wheeler, N.K. Baddela, and D.J. Richardson, *Overcoming the Challenges of Splicing Dissimilar Diameter Solid-Core and Hollow-Core Photonic Band Gap Fibers*, in *Workshop on Specialty Optical Fibers and their Applications*. 2013, Optical Society of America: Sigtuna, Sweden. p. W3.26.

8. Chen, Y., M.N. Petrovich, N.V. Wheeler, A.M. Heidt, N.K. Baddela, S.R. **Sandoghchi**, F. Poletti, and D.J. Richardson. *High Sensitivity Gas Sensing Using Hollow Core Photonic Bandgap Fibres Designed for Operation at mid-IR Wavelengths*. in *3rd EPSRC Manufacturing the Future*. 2014. Glasgow, UK.

9. Chen, Y., N.V. Wheeler, N.K. Baddela, J.R. Hayes, S.R. **Sandoghchi**, E.R. Numkam Fokoua, M. Li, F. Poletti, M.N. Petrovich, and D.J. Richardson. *Understanding Wavelength Scaling in 19-Cell Core Hollow-Core Photonic Bandgap Fibers*. in *2014 Optical Fiber Communications Conference and Exhibition (OFC)*. 2014.

10. Gray, D.R., S.R. **Sandoghchi**, N.V. Wheeler, G.T. Jasion, J.P. Wooler, M.N. Petrovich, F. Poletti, and D.J. Richardson. *Towards real-time mode content characterization of multimode fibers*. in *2014 European Conference on Optical Communication (ECOC)*. 2014.

11. Jasion, G.T., S.R. **Sandoghchi**, Y. Chen, N.V. Wheeler, T.D. Bradley, N.K. Baddela, J.R. Hayes, M.N. Petrovich, D.J. Richardson, J.S. Shrimpton, and F. Poletti, *Novel fluid dynamics model to predict draw of hollow core photonic band-gap fibres*, in *European Conference on Optical Communication*. 2014: Cannes, France. p. Th.2.4.3.

12. Numkam Fokoua, E.R., S.R. **Sandoghchi**, Y. Chen, N.V. Wheeler, N.K. Baddela, J.R. Hayes, M.N. Petrovich, D.J. Richardson, and F. Poletti. *Accurate Loss and Surface Mode Modeling in Fabricated Hollow-Core Photonic Bandgap Fibers*. in *2014 Optical Fiber Communications Conference and Exhibition (OFC)*. 2014.

13. Numkam Fokoua, E.R., S.R. **Sandoghchi**, Y. Chen, N.V. Wheeler, N.K. Baddela, J.R. Hayes, M.N. Petrovich, D.J. Richardson, and F. Poletti. *Accurate Modelling of Hollow Core Photonic Bandgap Fibre*. in *Advanced Photonics Congress*. 2014. Barcelona: Optical Society of America.

14. Petrovich, M.N., N.K. Baddela, S.R. **Sandoghchi**, N.V. Wheeler, J.R. Hayes, Y. Jung, E.R. Numkam Fokoua, F. Poletti, and D.J. Richardson. *Development of Large Core Hollow Core Photonic Bandgap Fibres for Telecommunications Applications*. in *2014 16th International Conference on Transparent Optical Networks (ICTON)*. 2014.

15. Petrovich, M.N., N.V. Wheeler, A.M. Heidt, N.K. Baddela, S.R. **Sandoghchi**, Y. Chen, F. Poletti, and D.J. Richardson. *High sensitivity gas detection using Hollow Core Photonic Bandgap Fibres designed for mid-IR operation*. in *IEEE SENSORS 2014*. 2014. Valencia: IEEE.

16. Poletti, F., G.T. Jasion, E.R. Numkam Fokoua, S.R. **Sandoghchi**, Y. Chen, N.V. Wheeler, N.K. Baddela, J.R. Hayes, T.D. Bradley, M.N. Petrovich, and D.J. Richardson. *Hollow Core Fibre Technology for Data Transmission*. in *Asia Communications and Photonics Conference 2014*. 2014. Shanghai: Optical Society of America.

17. Richardson, D.J., Y. Chen, E.R. Numkam Fokoua, N.V. Wheeler, N.K. Baddela, J.R. Hayes, S.R. **Sandoghchi**, G.T. Jasion, J.P. Wooler, D.R. Gray, M.N. Petrovich, and F. Poletti. *Recent Advances in Hollow-Core Photonic Bandgap Fibres*. in *Advanced Photonics Congress*. 2014. Barcelona: Optical Society of America.

18. **Sandoghchi**, S.R., G.T. Jasion, N.V. Wheeler, S. Jain, Z. Lian, J.P. Wooler, R.P. Boardman, N.K. Baddela, Y. Chen, J.R. Hayes, E.R. Numkam Fokoua, T.D. Bradley, D.R. Gray, S.A. Mousavi, M.N. Petrovich, F. Poletti, and D.J. Richardson, *X-ray tomography for structural analysis of microstructured and multimaterial optical fibers and preforms.* Optics Express, 2014. **22**(21): p. 26181-26192.

19. **Sandoghchi**, S.R., G.T. Jasion, N.V. Wheeler, J.P. Wooler, R.P. Boardman, N.K. Baddela, Y. Chen, J.R. Hayes, E.R. Numkam Fokoua, T.D. Bradley, D.R. Gray, S.A. Mousavi, M.N. Petrovich, F. Poletti, and D.J. Richardson, *X-ray tomography for structural analysis of microstructured optical fibres and preforms*, in *European Conference on Optical Communication*. 2014: Cannes, France. p. Th.2.4.2.

20. **Sandoghchi**, S.R., G.T. Jasion, N.V. Wheeler, J.P. Wooler, R.P. Boardman, N.K. Baddela, Y. Chen, J.R. Hayes, E.R. Numkam Fokoua, T.D. Bradley, D.R. Gray, S.A. Mousavi, M.N. Petrovich, F. Poletti, and D.J. Richardson, *X-ray computational tomography of hollow core photonic bandgap fibre*, in *3rd EPSRC Manufacturing the Future Conference*. 2014.

21. **Sandoghchi**, S.R., T. Zhang, J.P. Wooler, N.K. Baddela, N.V. Wheeler, Y. Chen, G.T. Jasion, D.R. Gray, E.R. Numkam Fokoua, J.R. Hayes, M.N. Petrovich, F. Poletti, and D.J. Richardson, *First Investigation of Longitudinal Defects in Hollow Core Photonic Bandgap Fibers*, in *Optical Fiber Communication Conference*. 2014, Optical Society of America: San Francisco, California, United States. p. M2F.6.

22. Wheeler, N.V., A.M. Heidt, N.K. Baddela, E.R. Numkam Fokoua, J.R. Hayes, S.R. **Sandoghchi**, F. Poletti, M.N. Petrovich, and D.J. Richardson, *Low-loss and low-bend-sensitivity mid-infrared guidance in a hollow-core photonic-bandgap fiber.* Optics Letters, 2014. **39**(2): p. 295-298.

23. Wheeler, N.V., M.N. Petrovich, A.M. Heidt, N.K. Baddela, E.R. Numkam Fokoua, J.R. Hayes, S.R. **Sandoghchi**, F. Poletti, and D.J. Richardson. *Low Loss, Tightly Coilable, Hollow Core Photonic Bandgap Fibers for Mid-IR Applications*. in *2014 IEEE Photonics Society Summer Topical Meeting Series*. 2014.

24. Wheeler, N.V., M.N. Petrovich, A.M. Heidt, N.K. Baddela, E.R. Numkam Fokoua, J.R. Hayes, S.R. **Sandoghchi**, F. Poletti, and D.J. Richardson. *Hollow Core Photonic Bandgap Fibers for Mid-IR Applications*. in *Advanced Photonics Congress*. 2014. Barcelona: Optical Society of America.

25. Zhang, H., Z. Li, N. Kavanagh, J. Zhao, N. Ye, Y. Chen, N.V. Wheeler, J.P. Wooler, J.R. Hayes, S.R. **Sandoghchi**, F. Poletti, M.N. Petrovich, S.U. Alam, R. Phelan, J. O'Carroll, B. Kelly, D.J. Richardson, B. Corbett, and F.C. Garcia Gunning. *81 Gb/s WDM transmission at 2μm over 1.15 km of low-loss hollow core photonic bandgap fiber*. in *2014 European Conference on Optical Communication (ECOC)*. 2014.

26. Chen, Y., Z. Liu, S.R. **Sandoghchi**, G.T. Jasion, T.D. Bradley, E.R. Numkam Fokoua, J.R. Hayes, N.V. Wheeler, D.R. Gray, B.J. Mangan, R. Slavik, F. Poletti, M.N. Petrovich, and D.J. Richardson, *Multi-kilometer long, longitudinally uniform Hollow Core Photonic Bandgap Fibers for broadband low latency data transmission.* Journal of Lightwave Technology, 2015. **PP**(99): p. 104-113.

27. Chen, Y., Z. Liu, S.R. **Sandoghchi**, G.T. Jasion, T.D. Bradley, E.R. Numkam Fokoua, J.R. Hayes, N.V. Wheeler, D.R. Gray, B.J. Mangan, R. Slavik, F. Poletti, M.N. Petrovich, and D.J. Richardson, *Demonstration of an 11km hollow core photonic bandgap fiber for broadband low-latency data transmission*, in *Optical Fiber Communication Conference - Post-Deadline Papers*. 2015, Optical Society of America: Los Angeles, California, United States. p. Th5A.1.

28. Gray, D.R., S.R. **Sandoghchi**, N.V. Wheeler, N.K. Baddela, G.T. Jasion, M.N. Petrovich, F. Poletti, and D.J. Richardson, *Accurate calibration of S^2 and interferometry based multimode fiber characterization techniques.* Optics Express, 2015. **23**(8): p. 10540-10552.

29. Gray, D.R., S.R. **Sandoghchi**, N.V. Wheeler, N.K. Baddela, G.T. Jasion, M.N. Petrovich, F. Poletti, and D.J. Richardson. *Mitigating Spectral Leakage and Sampling Errors in Spatial and Spectral (S^2) Imaging*. in *Optical Fiber Communication Conference*. 2015. Los Angeles, California: Optical Society of America.

30. Kuschnerov, M., V.A.J.M. Sleiffer, Y. Chen, E. de Man, Y. Chen, Z. Liu, S.R. **Sandoghchi**, G.T. Jasion, T.D. Bradley, E.R. Numkam Fokoua, J.R. Hayes, N.V. Wheeler, D.R. Gray, R. Slavik, Y. Jung, N.H.L. Wong, B.J. Mangan, F. Poletti, M.N. Petrovich, and D.J. Richardson. *Data transmission through up to 74.8 km of hollow-core fiber with coherent and direct-detect transceivers*. in *2015 European Conference on Optical Communication (ECOC)*. 2015.

31. Mousavi, S.A., D.J. Richardson, S.R. **Sandoghchi**, and F. Poletti. *First design of high birefringence and polarising hollow core anti-resonant fibre*. in *2015 European Conference on Optical Communication (ECOC)*. 2015.

32. Numkam Fokoua, E.R., S.R. **Sandoghchi**, Y. Chen, G.T. Jasion, N.V. Wheeler, N.K. Baddela, J.R. Hayes, M.N. Petrovich, D.J. Richardson, and F. Poletti, *Accurate modelling of fabricated hollow-core photonic bandgap fibers.* Optics Express, 2015. **23**(18): p. 23117-23132.

33. Petrovich, M.N., Y. Chen, T.D. Bradley, S.R. **Sandoghchi**, N.V. Wheeler, J.R. Hayes, G.T. Jasion, E.R. Numkam Fokoua, F. Poletti, Z. Liu, R. Slavik, and D.J. Richardson. *Demonstration of long lengths of longitudinally uniform hollow core Photonic Bandgap fibre and their demonstration for low latency data transmission*. in *2015 17th International Conference on Transparent Optical Networks (ICTON)*. 2015.

34. Richardson, D.J., Y. Chen, N.V. Wheeler, J.R. Hayes, T.D. Bradley, Z. Liu, S.R. **Sandoghchi**, G.T. Jasion, T.D. Bradley, E.R. Numkam Fokoua, D.R. Gray, R. Slavik, Y. Jung, N.H.L. Wong, F. Poletti, and M.N. Petrovich. *Photonic bandgap fibres for low-latency data transmission*. in *2015 European Conference on Optical Communication (ECOC)*. 2015.

35. **Sandoghchi**, S.R., D.R. Gray, Y. Chen, N.V. Wheeler, T.D. Bradley, J.R. Hayes, E.R. Numkam Fokoua, G.T. Jasion, S.A. Mousavi, M.N. Petrovich, F. Poletti, and D.J. Richardson. *High dynamic range technique for discrete and distributed scattering loss measurement in microstructured optical fibres*. in *2015 European Conference on Optical Communication (ECOC)*. 2015.

36. **Sandoghchi**, S.R., M.N. Petrovich, D.R. Gray, Y. Chen, N.V. Wheeler, T.D. Bradley, N.H.L. Wong, G.T. Jasion, J.R. Hayes, E.R. Numkam Fokoua, M.B. Alonso, S.A. Mousavi, D.J. Richardson, and F. Poletti, *Optical side scattering radiometry for high resolution, wide dynamic range longitudinal assessment of optical fibers.* Optics Express, 2015. **23**(21): p. 27960-27974.

37. Wong, N.H.L., Y. Jung, S.R. **Sandoghchi**, T.D. Bradley, N.K. Baddela, N.V. Wheeler, J.R. Hayes, M.N. Petrovich, F. Poletti, S.U. Alam, P. Petropoulos, and D.J. Richardson, *Modal characterization of hollow-core photonic bandgap fibers in the time-domain*, in *Siegman International School on Lasers: 2015*. 2015.

38. Wong, N.H.L., S.R. **Sandoghchi**, Y. Jung, T.D. Bradley, N.V. Wheeler, N.K. Baddela, J.R. Hayes, F. Poletti, M.N. Petrovich, S.U. Alam, P. Petropoulos, and D.J. Richardson, *Inspection of defect-induced mode coupling in hollow-core photonic bandgap fibers using time-of-flight*, in *Conference on Lasers and Electro-Optics*. 2015, Optical Society of America: San Jose, California, United States. p. STu1N.6.

39. Zhang, H., N. Kavanagh, Z. Li, J. Zhao, N. Ye, Y. Chen, N.V. Wheeler, J.P. Wooler, J.R. Hayes, S.R. **Sandoghchi**, F. Poletti, M.N. Petrovich, S.U. Alam, R. Phelan, J. O'Carroll, B. Kelly, L. Grüner-Nielsen, D.J. Richardson, B. Corbett, and F.C. Garcia Gunning, *100Gbit/s WDM transmission at 2μm: transmission studies in both low-loss hollow core photonic bandgap fiber and solid core fiber.* Optics Express, 2015. **23**(4): p. 4946-4951.

40. Bradley, T.D., N.V. Wheeler, G.T. Jasion, D.R. Gray, J.R. Hayes, M.A. Gouveia, S.R. **Sandoghchi**, Y. Chen, F. Poletti, D.J. Richardson, and M.N. Petrovich, *Modal content in hypocycloid Kagomé; hollow core photonic crystal fibers.* Optics Express, 2016. **24**(14): p. 15798-15812.

41. Bradley, T.D., N.V. Wheeler, M.N. Petrovich, G.T. Jasion, D.R. Gray, J.R. Hayes, S.R. **Sandoghchi**, Y. Chen, F. Poletti, D.J. Richardson, and M.A. Gouveia, *S^2 Measurement of*

Higher Order Mode Content in Low Loss Hypocycloid Kagomé Hollow Core Photonic Crystal Fiber, in *Conference on Lasers and Electro-Optics*. 2016, Optical Society of America: San Jose, California, United States. p. STu4P.8.

42. Buet, X., C. Brun, J. Gâteau, B. Bresson, S.R. **Sandoghchi**, E.R. Numkam Fokoua, M.N. Petrovich, F. Poletti, D.J. Richardson, D. Vandembroucq, and G. Tessier, *Nondestructive measurement of the roughness of the inner surface of hollow core-photonic bandgap fibers.* Optics Letters, 2016. **41**(21): p. 5086-5089.

43. Chen, Y., H.C. Mulvad, S.R. **Sandoghchi**, E.R. Numkam Fokoua, T.D. Bradley, J.R. Hayes, N.V. Wheeler, G.T. Jasion, S.U. Alam, F. Poletti, M.N. Petrovich, and D.J. Richardson. *First Demonstration of Low Loss, Bend Insensitive 37-Cell Hollow-Core Photonic Bandgap Fiber at 1µm for High Power Delivery Applications*. in *Conference on Lasers and Electro-Optics*. 2016. San Jose, California: Optical Society of America.

44. Chen, Y., M.N. Petrovich, S.R. Sandohgchi, T.D. Bradley, J.R. Hayes, N.V. Wheeler, E.R. Numkam Fokoua, G.T. Jasion, H.C. Mulvad, Z. Liu, S.U. Alam, R. Slavik, F. Poletti, and D.J. Richardson. *Recent advances in the development of high performance hollow-core photonic bandgap fibres*. in *2016 18th International Conference on Transparent Optical Networks (ICTON)*. 2016.

45. Chen, Y., S.R. **Sandoghchi**, E.R. Numkam Fokoua, T.D. Bradley, J.R. Hayes, N.V. Wheeler, G.T. Jasion, D.R. Gray, F. Poletti, M.N. Petrovich, and D.J. Richardson. *Detailed study of macrobending effects in a wide transmission bandwidth hollow-core photonic bandgap fiber*. in *Micro-Structured and Specialty Optical Fibres IV*. 2016. Brussels, Belgium.

46. Gray, D.R., M.N. Petrovich, S.R. **Sandoghchi**, N.V. Wheeler, N.K. Baddela, G.T. Jasion, T.D. Bradley, D.J. Richardson, and F. Poletti, *Real-Time Modal Analysis via Wavelength-Swept Spatial and Spectral (S^2) Imaging.* IEEE Photonics Technology Letters, 2016. **28**(9): p. 1034-1037.

47. Hayes, J.R., S.R. **Sandoghchi**, T.D. Bradley, Z. Liu, R. Slavik, M.A. Gouveia, N.V. Wheeler, G.T. Jasion, Y. Chen, E.R. Numkam Fokoua, M.N. Petrovich, D.J. Richardson, and F. Poletti, *Antiresonant Hollow Core Fiber with Octave Spanning Bandwidth for Short Haul Data Communications*, in *Optical Fiber Communication Conference - Post-Deadline Papers*. 2016, Optical Society of America: Anaheim, California, United States. p. Th5A.3.

48. Hayes, J.R., S.R. **Sandoghchi**, T.D. Bradley, Z. Liu, R. Slavik, M.A. Gouveia, N.V. Wheeler, G.T. Jasion, Y. Chen, E.R. Numkam Fokoua, M.N. Petrovich, D.J. Richardson, and F. Poletti, *Antiresonant Hollow Core Fiber with an Octave Spanning Bandwidth for Short Haul Data Communications.* Journal of Lightwave Technology, 2016. **35**(3): p. 437-442.

49. Numkam Fokoua, E.R., G.T. Jasion, Y. Chen, S.R. **Sandoghchi**, T.D. Bradley, D.R. Gray, N.V. Wheeler, J.R. Hayes, M.N. Petrovich, D.J. Richardson, and F. Poletti. *Recent advances in hollow fiber technology for telecoms applications*. in *2016 IEEE Photonics Society Summer Topical Meeting Series (SUM)*. 2016.

50. Wheeler, N.V., T.D. Bradley, J.R. Hayes, M.A. Gouveia, Y. Chen, S.R. Sandohgchi, F. Poletti, M.N. Petrovich, and D.J. Richardson, *Low Loss Kagome Fiber in the 1 µm Wavelength Region*, in *Advanced Photonics Congress*. 2016, Optical Society of America: Vancouver, Canada. p. SoM3F.2.

51. Wheeler, N.V., T.D. Bradley, J.R. Hayes, G.T. Jasion, Y. Chen, S.R. **Sandoghchi**, P. Horak, F. Poletti, M.N. Petrovich, and D.J. Richardson. *Dual hollow-core anti-resonant fibres*. in *Micro-Structured and Specialty Optical Fibres IV*. 2016. Brussels, Belgium.

52. Wheeler, N.V., Y. Chen, J.R. Hayes, S.R. **Sandoghchi**, G.T. Jasion, T.D. Bradley, E.R. Numkam Fokoua, N.K. Baddela, D.R. Gray, Z. Liu, Y. Jung, S.U. Alam, R. Slavik, F. Poletti, M.N. Petrovich, and D.J. Richardson. *High Capacity, Low Latency Data Transmission Using Hollow Core-Photonic Bandgap Fibers*. in *Optical Fiber Communication Conference*. 2016. Anaheim, California: Optical Society of America.

List of references

[1] D. J. Richardson, "New optical fibres for high-capacity optical communications," *Philosophical Transactions of the Royal Society A: Mathematical, Physical and Engineering Sciences,* vol. 374, 2016.

[2] K. C. Kao and G. A. Hockham, "Dielectric-fibre surface waveguides for optical frequencies," *Proceedings of the Institution of Electrical Engineers,* vol. 113, pp. 1151-1158, 1966.

[3] F. P. Kapron, D. B. Keck and R. D. Maurer, "Radiation losses in glass optical waveguides," *Applied Physics Letters,* vol. 17, pp. 423-425, 1970.

[4] T. Miya, Y. Terunuma, T. Hosaka and T. Miyashita, "Ultimate low-loss single-mode fibre at 1.55 µm," *Electronics Letters,* vol. 15, pp. 106-108, 1979.

[5] P. Sillard, "New fibers for ultra-high capacity transport," *Optical Fiber Technology,* vol. 17, pp. 495-502, 2011.

[6] R. F. Cregan, B. J. Mangan, J. C. Knight, T. A. Birks, P. S. J. Russell, P. J. Roberts and D. C. Allan, "Single-mode photonic band gap guidance of light in air," *Science,* vol. 285, pp. 1537-1539, 1999.

[7] X. Peng, M. Mielke and T. Booth, "High average power, high energy 1.55 µm ultra-short pulse laser beam delivery using large mode area hollow core photonic band-gap fiber," *Optics Express,* vol. 19, pp. 923-932, 2011.

[8] F. Poletti, N. V. Wheeler, M. N. Petrovich, N. K. Baddela, E. R. Numkam Fokoua, J. R. Hayes, D. R. Gray, Z. Li, R. Slavik and D. J. Richardson, "Towards high-capacity fibre-optic communications at the speed of light in vacuum," *Nature Photonics,* vol. 7, pp. 279-284, 2013.

[9] F. Poletti, M. N. Petrovich and D. J. Richardson, "Hollow-core photonic bandgap fibers: technology and applications," *Nanophotonics,* vol. 2, pp. 315-340, 2013.

[10] R. G. H. van Uden, C. M. Okonkwo, H. Chen, N. V. Wheeler, F. Poletti, M. N. Petrovich, D. J. Richardson, H. de Waardt and A. M. J. Koonen, "8.96Tb/s (32×28GBaud×32QAM) Transmission over 0.95 km 19 cell Hollow-Core Photonic Bandgap Fiber," presented at the Optical Fiber Communication Conference, San Francisco, California, United States, 2014.

[11] B. J. Mangan, L. Farr, A. Langford, P. J. Roberts, D. P. Williams, F. Couny, M. Lawman, M. W. Mason, S. Coupland and R. Flea, "Low loss (1.7 dB/km) hollow core photonic bandgap fiber," presented at the Optical Fiber Communication Conference - Post-Deadline Papers, Los Angeles, California, United States, 2004.

[12] P. J. Roberts, F. Couny, H. Sabert, B. J. Mangan, D. P. Williams, L. Farr, M. W. Mason, A. Tomlinson, T. A. Birks and J. C. Knight, "Ultimate low loss of hollow-core photonic crystal fibres," *Optics Express,* vol. 13, pp. 236-244, 2005.

[13] Y. Chen, Z. Liu, S. R. Sandoghchi, G. T. Jasion, T. D. Bradley, E. R. Numkam Fokoua, J. R. Hayes, N. V. Wheeler, D. R. Gray, B. J. Mangan, R. Slavik, F. Poletti, M. N. Petrovich and D. J. Richardson, "Multi-kilometer long, longitudinally uniform Hollow Core Photonic Bandgap Fibers for broadband low latency data transmission," *Journal of Lightwave Technology,* vol. PP, pp. 104-113, 2015.

[14] N. V. Wheeler, M. N. Petrovich, R. Slavik, N. K. Baddela, E. R. Numkam Fokoua, J. R. Hayes, D. R. Gray, F. Poletti and D. J. Richardson, "Wide-bandwidth, low-loss, 19-cell hollow core photonic band gap fiber and its potential for low latency data transmission," presented at the National Fiber Optic Engineers Conference, Los Angeles, California, United States, 2012.

[15] A. Bjarklev, J. Broeng and A. Sanchez Bjarklev, *Photonic crystal fibres*. Boston: Kluwer Academic Publishers, 2003.

[16] N. A. Mortensen and M. D. Nielsen, "Modeling of realistic cladding structures for air-core photonic bandgap fibers," *Optics Letters,* vol. 29, pp. 349-351, 2004.

[17] F. Poletti, N. G. R. Broderick, D. J. Richardson and T. Monro, "The effect of core asymmetries on the polarization properties of hollow core photonic bandgap fibers," *Optics Express,* vol. 13, pp. 9115-9124, 2005.

[18] R. Amezcua-Correa, N. G. R. Broderick, M. N. Petrovich, F. Poletti and D. J. Richardson, "Optimizing the usable bandwidth and loss through core design in realistic hollow-core photonic bandgap fibers," *Optics Express,* vol. 14, pp. 7974-7985, 2006.

[19] C. M. Smith, N. Venkataraman, M. T. Gallagher, D. Muller, J. A. West, N. F. Borrelli, D. C. Allan and K. W. Koch, "Low-loss hollow-core silica/air photonic bandgap fibre," *Nature,* vol. 424, pp. 657-659, 2003.

[20] J. A. West, N. Venkataramam, C. M. Smith and M. T. Gallagher, "Photonic crystal fibers," presented at the European Conference on Optical Communication, Amsterdam, Netherlands, 2001.

[21] F. Benabid, J. C. Knight, G. Antonopoulos and P. S. J. Russell, "Stimulated Raman Scattering in Hydrogen-Filled Hollow-Core Photonic Crystal Fiber," *Science,* vol. 298, pp. 399-402, 2002.

[22] NKT Photonics. (2016, Dec. 20). *Hollow core photonic crystal fibers* [Specification Sheet]. Available: http://www.nktphotonics.com/product/hollow-core-photonic-crystal-fibers/

[23] P. S. J. Russell, P. J. Roberts and D. P. Williams, "Photonic bandgap optical waveguide with anti-resonant core boundary," United States Patent US 7346249 B2, Mar. 18, 2008.

[24] E. R. Numkam Fokoua, "Ultralow loss and wide bandwidth hollow-core photonic bandgap fibres for telecom applications," Doctoral thesis, Faculty of Physical Sciences and Engineering, University of Southampton, 2015.

[25] Y. Chen, Z. Liu, S. R. Sandoghchi, G. T. Jasion, T. D. Bradley, E. R. Numkam Fokoua, J. R. Hayes, N. V. Wheeler, D. R. Gray, B. J. Mangan, R. Slavik, F. Poletti, M. N. Petrovich and D. J. Richardson, "Demonstration of an 11km hollow core photonic bandgap fiber for broadband low-latency data transmission," presented at the Optical Fiber Communication Conference - Post-Deadline Papers, Los Angeles, California, United States, 2015.

[26] P. S. J. Russell, T. A. Birks and F. D. Lloyd-Lucas, "Photonic bloch waves and photonic band gaps," in *Confined Electrons and Photons: New Physics and Applications*, E. Burstein and C. Weisbuch, Eds., ed Boston, MA: Springer US, 1995, pp. 585-633.

[27] J. D. Joannopoulos, *Photonic crystals : molding the flow of light*, 2nd ed. New Jersey: Princeton University Press, 2008.

[28] S. John, "Strong localization of photons in certain disordered dielectric superlattices," *Physical Review Letters,* vol. 58, pp. 2486-2489, 1987.

[29] E. Yablonovitch, "Inhibited Spontaneous Emission in Solid-State Physics and Electronics," *Physical Review Letters,* vol. 58, pp. 2059-2062, 1987.

[30] T. A. Birks, P. J. Roberts, P. S. J. Russell, D. M. Atkin and T. J. Shepherd, "Full 2-D photonic bandgaps in silica/air structures," *Electronics Letters,* vol. 31, pp. 1941-1943, 1995.

[31] P. Yeh, A. Yariv and C.-S. Hong, "Electromagnetic propagation in periodic stratified media. I. General theory*," *Journal of the Optical Society of America,* vol. 67, pp. 423-438, 1977.

[32] P. Yeh, A. Yariv and E. Marom, "Theory of Bragg fiber*," *Journal of the Optical Society of America,* vol. 68, pp. 1196-1201, 1978.

[33] Y. Fink, J. N. Winn, S. Fan, C. Chen, J. Michel, J. D. Joannopoulos and E. L. Thomas, "A Dielectric Omnidirectional Reflector," *Science,* vol. 282, pp. 1679-1682, 1998.

[34] B. Temelkuran, S. D. Hart, G. Benoit, J. D. Joannopoulos and Y. Fink, "Wavelength-scalable hollow optical fibres with large photonic bandgaps for CO2 laser transmission," *Nature,* vol. 420, pp. 650-653, 2002.

[35] M. Plihal and A. A. Maradudin, "Photonic band structure of two-dimensional systems: The triangular lattice," *Physical Review B,* vol. 44, pp. 8565-8571, 1991.

[36] R. D. Meade, K. D. Brommer, A. M. Rappe and J. D. Joannopoulos, "Existence of a photonic band gap in two dimensions," *Applied Physics Letters,* vol. 61, pp. 495-497, 1992.

[37] A. A. Maradudin and A. R. McGurn, "Out of Plane Propagation of Electromagnetic Waves in a Two-dimensional Periodic Dielectric Medium," *Journal of Modern Optics,* vol. 41, pp. 275-284, 1994.

[38] P. R. Villeneuve and M. Piché, "Photonic band gaps in two-dimensional square and hexagonal lattices," *Physical Review B,* vol. 46, pp. 4969-4972, 1992.

[39] T. A. Birks, D. M. Bird, T. Hedley, J. Pottage and P. S. J. Russell, "Scaling laws and vector effects in bandgap-guiding fibres," *Optics Express,* vol. 12, pp. 69-74, 2004.

[40] P. S. J. Russell, "Photonic-Crystal Fibers," *Journal of Lightwave Technology,* vol. 24, pp. 4729-4749, 2006.

[41] F. Benabid and P. J. Roberts, "Linear and nonlinear optical properties of hollow core photonic crystal fiber," *Journal of Modern Optics,* vol. 58, pp. 87-124, 2011.

[42] T. A. Birks, G. J. Pearce and D. M. Bird, "Approximate band structure calculation for photonic bandgap fibres," *Optics Express,* vol. 14, pp. 9483-9490, 2006.

[43] T. A. Birks, J. C. Knight and P. S. J. Russell, "Endlessly single-mode photonic crystal fiber," *Optics Letters,* vol. 22, pp. 961-963, 1997.

[44] K. Schuster, S. Unger, C. Aichele, F. Lindner, S. Grimm, D. Litzkendorf, J. Kobelke, J. Bierlich, K. Wondraczek and H. Bartelt, "Material and technology trends in fiber optics," *Advanced Optical Technologies,* vol. 3, pp. 447-468, 2014.

[45] B. J. Ainslie, "A review of the fabrication and properties of erbium-doped fibers for optical amplifiers," *Journal of Lightwave Technology,* vol. 9, pp. 220-227, 1991.

[46] U. C. Paek, "High-speed high-strength fiber drawing," *Journal of Lightwave Technology,* vol. 4, pp. 1048-1060, 1986.

[47] G. P. Agrawal, *Nonlinear fiber optics*, 4th ed.: Academic press, 2006.

[48] W. B. Gardner and D. Gloge, "Microbending loss in coated and uncoated optical fibers," presented at the Optical Fiber Transmission, Williamsburg, Virginia, United States, 1975.

[49] S. R. Schmid, P. Shah, L. Han and X. Wu, "Development and Characterization of a Superior Class of Microbend Resistant Coatings for Today's Networks," presented at the International Wire & Cable and Connectivity Symposium, Charlotte, North Carolina, United States, 2009.

[50] A. S. Webb, F. Poletti, D. J. Richardson and J. K. Sahu, "Suspended-core holey fiber for evanescent-field sensing," *Optical Engineering,* vol. 46, pp. 010503-010503-3, 2007.

[51] M. Becker, M. Werner, O. Fitzau, D. Esser, J. Kobelke, A. Lorenz, A. Schwuchow, M. Rothhardt, K. Schuster, D. Hoffmann and H. Bartelt, "Laser-drilled free-form silica fiber preforms for microstructured optical fibers," *Optical Fiber Technology,* vol. 19, pp. 482-485, 2013.

[52] K. M. Kiang, K. E. Frampton, T. M. Monro, R. C. Moore, J. Tucknott, D. W. Hewak, D. J. Richardson and H. N. Rutt, "Extruded singlemode non-silica glass holey optical fibres," *Electronics Letters,* vol. 38, pp. 546-547, 2002.

[53] R. T. Bise and D. J. Trevor, "Sol-gel derived microstructured fiber: fabrication and characterization," presented at the Optical Fiber Communication Conference, Anaheim, California, United States, 2005.

[54] K. Cook, J. Canning, S. Leon-Saval, Z. Reid, M. A. Hossain, J.-E. Comatti, Y. Luo and G.-D. Peng, "Air-structured optical fiber drawn from a 3D-printed preform," *Optics Letters,* vol. 40, pp. 3966-3969, 2015.

[55] J. C. Knight, T. A. Birks, P. S. J. Russell and D. M. Atkin, "All-silica single-mode optical fiber with photonic crystal cladding," *Optics Letters,* vol. 21, pp. 1547-1549, 1996.

[56] R. J. Tonucci, B. L. Justus, A. J. Campillo and C. E. Ford, "Nanochannel Array Glass," *Science,* vol. 258, pp. 783-785, 1992.

[57] M. N. Petrovich, F. Poletti, A. van Brakel and D. J. Richardson, "Robustly single mode hollow core photonic bandgap fiber," *Optics Express,* vol. 16, pp. 4337-4346, 2008.

[58] G. T. Jasion, E. R. Numkam Fokoua, J. S. Shrimpton, D. J. Richardson and F. Poletti, "Studying the limits of production rate and yield for the volume manufacturing of hollow core photonic band gap fibers," *Optics Express,* vol. 23, pp. 32179-32190, 2015.

[59] K. Nagayama, M. Kakui, M. Matsui, T. Saitoh and Y. Chigusa, "Ultra-low-loss (0.1484 dB/km) pure silica core fibre and extension of transmission distance," *Electronics Letters,* vol. 38, pp. 1168-1169, 2002.

[60] R. Hui and M. S. O'Sullivan, *Fiber optic measurement techniques*. London: Academic Press, 2009.

[61] M. Ohashi, K. Shiraki and K. Tajima, "Optical loss property of silica-based single-mode fibers," *Journal of Lightwave Technology,* vol. 10, pp. 539-543, 1992.

[62] M. K. Barnoski, M. D. Rourke, S. M. Jensen and R. T. Melville, "Optical time domain reflectometer," *Applied Optics,* vol. 16, pp. 2375-2379, 1977.

[63] K. Takada, T. Kitagawa, M. Shimizu and M. Horiguchi, "High-sensitivity low coherence reflectometer using erbium-doped superfluorescent fibre source and erbium-doped power amplifier," *Electronics Letters,* vol. 29, pp. 365-367, 1993.

[64] B. Soller, D. Gifford, M. Wolfe and M. Froggatt, "High resolution optical frequency domain reflectometry for characterization of components and assemblies," *Optics Express,* vol. 13, pp. 666-674, 2005.

[65] W. V. Sorin and D. M. Baney, "Measurement of Rayleigh backscattering at 1.55 mu m with 32 mu m spatial resolution," *IEEE Photonics Technology Letters,* vol. 4, pp. 374-376, 1992.

[66] J. P. von der Weid, R. Passy, G. Mussi and N. Gisin, "On the characterization of optical fiber network components with optical frequency domain reflectometry," *Journal of Lightwave Technology,* vol. 15, pp. 1131-1141, 1997.

[67] P. Oberson, B. Huttner, O. Guinnard, L. Guinnard, G. Ribordy and N. Gisin, "Optical frequency domain reflectometry with a narrow linewidth fiber laser," *IEEE Photonics Technology Letters,* vol. 12, pp. 867-869, 2000.

[68] G. W. Day and D. L. Franzen, "Optical Fiber Metrology," *Journal of Lightwave Technology,* vol. 26, pp. 1119-1131, 2008.

[69] M. Nakazawa, "Rayleigh backscattering theory for single-mode optical fibers," *Journal of the Optical Society of America,* vol. 73, pp. 1175-1180, 1983.

[70] H. H. Gilgen, R. P. Novak, R. P. Salathe, W. Hodel and P. Beaud, "Submillimeter optical reflectometry," *Journal of Lightwave Technology,* vol. 7, pp. 1225-1233, 1989.

[71] D. R. Anderson, L. Johnson and F. G. Bell, *Troubleshooting Optical-fiber Networks: Understanding and Using Your Optical Time-domain Reflectometer*, 1st ed.: Academic Press, 2004.

[72] M. Tateda and T. Horiguchi, "Advances in optical time domain reflectometry," *Journal of Lightwave Technology,* vol. 7, pp. 1217-1224, 1989.

[73] W. Eickhoff and R. Ulrich, "Optical frequency domain reflectometry in single-mode fiber," *Applied Physics Letters,* vol. 39, pp. 693-695, 1981.

[74] R. I. MacDonald, "Frequency domain optical reflectometer," *Applied Optics,* vol. 20, pp. 1840-1844, 1981.

[75] U. Glombitza and E. Brinkmeyer, "Coherent frequency-domain reflectometry for characterization of single-mode integrated-optical waveguides," *Journal of Lightwave Technology,* vol. 11, pp. 1377-1384, 1993.

[76] R. Passy, N. Gisin, J. P. von der Weid and H. H. Gilgen, "Experimental and theoretical investigations of coherent OFDR with semiconductor laser sources," *Journal of Lightwave Technology,* vol. 12, pp. 1622-1630, 1994.

[77] W. V. Sorin, D. K. Donald, S. A. Newton and M. Nazarathy, "Coherent FMCW reflectometry using a temperature tuned Nd:YAG ring laser," *IEEE Photonics Technology Letters,* vol. 2, pp. 902-904, 1990.

[78] D. K. Gifford, M. E. Froggatt, M. S. Wolfe, S. T. Kreger, A. K. Sang and B. J. Soller, "Millimeter Resolution Otpical Reflectometry Over Up to Two Kilometers of Fiber Length," presented at the IEEE Avionics, Fiber-Optics and Photonics Technology Conference, Victoria, British Columbia, Canada, 2007.

[79] A. W. Snyder and J. D. Love, *Optical waveguide theory*. London: Chapman and Hall, 1983.

[80] J. Broeng, S. E. Barkou, T. Søndergaard and A. Bjarklev, "Analysis of air-guiding photonic bandgap fibers," *Optics Letters,* vol. 25, pp. 96-98, 2000.

[81] M. J. F. Digonnet, H. K. Kim, G. S. Kino and S. Fan, "Understanding Air-Core Photonic-Bandgap Fibers: Analogy to Conventional Fibers," *Journal of Lightwave Technology,* vol. 23, p. 4169, 2005.

[82] H. K. Kim, J. Shin, S. Fan, M. J. F. Digonnet and G. S. Kino, "Designing air-core photonic-bandgap fibers free of surface modes," *IEEE Journal of Quantum Electronics,* vol. 40, pp. 551-556, 2004.

[83] T. Murao, K. Saitoh and M. Koshiba, "Realization of single-moded broadband air-guiding photonic bandgap fibers," *IEEE Photonics Technology Letters,* vol. 18, pp. 1666-1668, 2006.

[84] X. Chen, M.-J. Li, N. Venkataraman, M. T. Gallagher, W. A. Wood, A. M. Crowley, J. P. Carberry, L. A. Zenteno and K. W. Koch, "Highly birefringent hollow-core photonic bandgap fiber," *Optics Express,* vol. 12, pp. 3888-3893, 2004.

[85] J. D. Shephard, P. J. Roberts, J. D. C. Jones, J. C. Knight and D. P. Hand, "Measuring Beam Quality of Hollow Core Photonic Crystal Fibers," *Journal of Lightwave Technology,* vol. 24, pp. 3761-3769, 2006.

[86] D. R. Gray, S. R. Sandoghchi, N. V. Wheeler, N. K. Baddela, G. T. Jasion, M. N. Petrovich, F. Poletti and D. J. Richardson, "Accurate calibration of S^2 and interferometry based multimode fiber characterization techniques," *Optics Express,* vol. 23, pp. 10540-10552, 2015.

[87] D. R. Gray, M. N. Petrovich, S. R. Sandoghchi, N. V. Wheeler, N. K. Baddela, G. T. Jasion, T. D. Bradley, D. J. Richardson and F. Poletti, "Real-Time Modal Analysis via Wavelength-Swept Spatial and Spectral (S^2) Imaging," *IEEE Photonics Technology Letters,* vol. 28, pp. 1034-1037, 2016.

[88] F. Poletti, E. R. Numkam Fokoua, M. N. Petrovich, N. V. Wheeler, N. K. Baddela, J. R. Hayes and D. J. Richardson, "Hollow Core Photonic Bandgap fibers for Telecommunications: Opportunities and Potential Issues," presented at the Optical Fiber Communication Conference, Los Angeles, California, United States, 2012.

[89] E. A. J. Marcatili and R. A. Schmeltzer, "Hollow metallic and dielectric waveguides for long distance optical transmission and lasers," *The Bell System Technical Journal,* vol. 43, pp. 1783-1809, 1964.

[90] M. Wegmuller, M. Legré, N. Gisin, T. P. Hansen, C. Jakobsen and J. Broeng, "Experimental investigation of the polarization properties of a hollow core photonic bandgap fiber for 1550 nm," *Optics Express,* vol. 13, pp. 1457-1467, 2005.

[91] F. Poletti, "Direct and inverse design of microstructured optical fibres," Doctoral thesis, Optoelectronic Research Center, University of Southampton, 2007.

[92] K. Saitoh, N. A. Mortensen and M. Koshiba, "Air-core photonic band-gap fibers: the impact of surface modes," *Optics Express,* vol. 12, pp. 394-400, 2004.

[93] D. C. Allan, N. F. Borrelli, M. T. Gallagher, D. Müller, C. M. Smith, N. Venkataraman, J. A. West, P. Zhang and K. W. Koch, "Surface modes and loss in air-core photonic bandgap fibers," presented at the Photonic Crystal Materials and Devices, San Jose, California, United States, 2003.

[94] J. A. West, C. M. Smith, N. F. Borrelli, D. C. Allan and K. W. Koch, "Surface modes in air-core photonic band-gap fibers," *Optics Express,* vol. 12, pp. 1485-1496, 2004.

[95] G. Humbert, J. C. Knight, G. Bouwmans, P. S. J. Russell, D. P. Williams, P. J. Roberts and B. J. Mangan, "Hollow core photonic crystal fibers for beam delivery," *Optics Express,* vol. 12, pp. 1477-1484, 2004.

[96] P. J. Roberts, F. Couny, T. A. Birks, J. C. Knight, P. S. J. Russell, B. J. Mangan, H. Sabert, D. P. Williams and L. Farr, "Achieving Low Loss and Low Nonlinearity in Hollow Core Photonic Crystal Fibers," presented at the Conference on Lasers and Electro-Optics, Baltimore, Maryland, United States, 2005.

[97] M. J. F. Digonnet, H. Kyun Kim, J. Shin, S. Fan and G. S. Kino, "Simple geometric criterion to predict the existence of surface modes in air-core photonic-bandgap fibers," *Optics Express,* vol. 12, pp. 1864-1872, 2004.

[98] H. K. Kim, M. J. F. Digonnet, G. S. Kino, J. Shin and S. Fan, "Simulations of the effect of the core ring on surface and air-core modes in photonic bandgap fibers," *Optics Express,* vol. 12, pp. 3436-3442, 2004.

[99] R. Amezcua-Correa, F. Gérôme, S. G. Leon-Saval, N. G. R. Broderick, T. A. Birks and J. C. Knight, "Control of surface modes in low loss hollow-core photonic bandgap fibers," *Optics Express,* vol. 16, pp. 1142-1149, 2008.

[100] R. Amezcua-Correa, N. G. R. Broderick, M. N. Petrovich, F. Poletti and D. J. Richardson, "Design of 7 and 19 cells core air-guiding photonic crystal fibers for low-loss, wide bandwidth and dispersion controlled operation," *Optics Express,* vol. 15, pp. 17577-17586, 2007.

[101] Y. Y. Wang, P. S. Light and F. Benabid, "Core-Surround Shaping of Hollow-Core Photonic Crystal Fiber Via HF Etching," *IEEE Photonics Technology Letters,* vol. 20, pp. 1018-1020, 2008.

[102] P. J. Roberts, F. Couny, H. Sabert, B. J. Mangan, T. A. Birks, J. C. Knight and P. S. J. Russell, "Loss in solid-core photonic crystal fibers due to interface roughness scattering," *Optics Express,* vol. 13, pp. 7779-7793, 2005.

[103] P. J. Roberts, D. P. Williams, B. J. Mangan, H. Sabert, F. Couny, W. Wadsworth, T. A. Birks, J. C. Knight and P. S. J. Russell, "Realizing low loss air core photonic crystal fibers by exploiting an antiresonant core surround," *Optics Express,* vol. 13, pp. 8277-8285, 2005.

[104] A. Argyros, S. G. Leon-Saval, J. Pla and A. Docherty, "Antiresonant reflection and inhibited coupling in hollow-core square lattice optical fibres," *Optics Express,* vol. 16, pp. 5642-5648, 2008.

[105] B. J. Mangan, J. K. Lyngsø and P. J. Roberts, "Realization of Low Loss and Polarization Maintaining Hollow Core Photonic Crystal Fibers," presented at the Conference on Lasers and Electro-Optics, San Jose, California, United States, 2008.

[106] M. E. Lines, "Can the minimum attenuation of fused silica be significantly reduced by small compositional variations? I. Alkali metal dopants," *Journal of Non-Crystalline Solids,* vol. 171, pp. 209-218, 1994.

[107] A. Q. Tool, "Relation between inelastic deformability and thermal expansion of glass in its annealing range," *Journal of the American Ceramic Society,* vol. 29, pp. 240-253, 1946.

[108] M. G. Drexhage, B. Bendow, R. N. Brown, P. K. Banerjee, H. G. Lipson, G. Fonteneau, J. Lucas and C. T. Moynihan, "Extended IR absorption of multicomponent glasses based on the fluorides of thorium, barium, and other metals," *Applied Optics,* vol. 21, pp. 971-972, 1982.

[109] F. Urbach, "The Long-Wavelength Edge of Photographic Sensitivity and of the Electronic Absorption of Solids," *Physical Review,* vol. 92, pp. 1324-1324, 1953.

[110] A. T. Pedersen, L. Grüner-Nielsen and K. Rottwitt, "Measurement and Modeling of Low-Wavelength Losses in Silica Fibers and Their Impact at Communication Wavelengths," *Journal of Lightwave Technology,* vol. 27, pp. 1296-1300, 2009.

[111] L. Skuja, K. Kajihara, Y. Ikuta, M. Hirano and H. Hosono, "Urbach absorption edge of silica: reduction of glassy disorder by fluorine doping," *Journal of Non-Crystalline Solids,* vol. 345&346, pp. 328-331, 2004.

[112] J. Zhou, K. Tajima, K. Nakajima, K. Kurokawa, C. Fukai, T. Matsui and I. Sankawa, "Progress on low loss photonic crystal fibers," *Optical Fiber Technology,* vol. 11, pp. 101-110, 2005.

[113] K. Tajima, "Low loss PCF by reduction of hole surface imperfection," presented at the European Conference on Optical Communication - Post-Deadline Papers, Berlin, Germany, 2007.

[114] M. Ohashi, M. Tateda, K. Shiraki and K. Tajima, "Imperfection loss reduction in viscosity-matched optical fibers," *IEEE Photonics Technology Letters,* vol. 5, pp. 812-814, 1993.

[115] K. Imamura, K. Mukasa and T. Yagi, "The study on loss reduction of holey fiber by viscosity profile control," presented at the OptoElectronics and Communications Conference, Vienna, Austria, 2009.

[116] J. Stone and G. E. Walrafen, "Overtone vibrations of OH groups in fused silica optical fibers," *The Journal of Chemical Physics,* vol. 76, pp. 1712-1722, 1982.

[117] R. W. Hepburn and M. Tomozawa, "Diffusion of water in silica glasses containing different amounts of chlorine," *Journal of Non-Crystalline Solids,* vol. 281, pp. 162-170, 2001.

[118] I. Gris-Sánchez, B. J. Mangan and J. C. Knight, "Reducing Spectral Attenuation in Solid-Core Photonic Crystal Fibers," presented at the Optical Fiber Communication Conference, San Diego, California, United States, 2010.

[119] P. Kaiser, "Drawing-induced coloration in vitreous silica fibers," *Journal of the Optical Society of America,* vol. 64, pp. 475-481, 1974.

[120] K. Kurokawa, K. Nakajima, K. Tsujikawa, T. Yamamoto and K. Tajima, "Ultra-Wideband Transmission Over Low Loss PCF," *Journal of Lightwave Technology,* vol. 27, pp. 1653-1662, 2009.

[121] J. Stone, "Interactions of hydrogen and deuterium with silica optical fibers: A review," *Journal of Lightwave Technology,* vol. 5, pp. 712-733, 1987.

[122] K. Saitoh and M. Koshiba, "Confinement losses in air-guiding photonic bandgap fibers," *IEEE Photonics Technology Letters,* vol. 15, pp. 236-238, 2003.

[123] K. Saitoh and M. Koshiba, "Leakage loss and group velocity dispersion in air-core photonic bandgap fibers," *Optics Express,* vol. 11, pp. 3100-3109, 2003.

[124] J. Jackle and K. Kawasaki, "Intrinsic roughness of glass surfaces," *Journal of Physics: Condensed Matter,* vol. 7, pp. 4351-4358, 1995.

[125] N. P. Bansal and R. H. Doremus, "Chapter 5 - Surface Tension," in *Handbook of Glass Properties*, ed San Diego: Academic Press, 1986, pp. 101-124.

[126] A. Kucuk, A. G. Clare and L. E. Jones, "Influence of various atmospheres on the surface properties of silicate melts," *Glass science and technology,* vol. 73, pp. 123-129, 2000.

[127] M.-C. Phan-Huy, J.-M. Moison, J. A. Levenson, S. Richard, G. Mélin, M. Douay and Y. Quiquempois, "Surface Roughness and Light Scattering in a Small Effective Area Microstructured Fiber," *Journal of Lightwave Technology,* vol. 27, pp. 1597-1604, 2009.

[128] X. Buet, C. Brun, J. Gâteau, B. Bresson, S. R. Sandoghchi, E. R. Numkam Fokoua, M. N. Petrovich, F. Poletti, D. J. Richardson, D. Vandembroucq and G. Tessier, "Nondestructive measurement of the roughness of the inner surface of hollow core-photonic bandgap fibers," *Optics Letters,* vol. 41, pp. 5086-5089, 2016.

[129] F. Couny, H. Sabert, P. J. Roberts, D. P. Williams, A. Tomlinson, B. J. Mangan, L. Farr, J. C. Knight, T. A. Birks and P. S. J. Russell, "Visualizing the photonic band gap in hollow core photonic crystal fibers," *Optics Express,* vol. 13, pp. 558-563, 2005.

[130] F. Benabid, "Hollow-core photonic bandgap fibre: new light guidance for new science and technology," *Philosophical Transactions of the Royal Society A: Mathematical, Physical and Engineering Sciences,* vol. 364, pp. 3439-3462, 2006.

[131] X. Feng, T. Monro, P. Petropoulos, V. Finazzi and D. Hewak, "Solid microstructured optical fiber," *Optics Express,* vol. 11, pp. 2225-2230, 2003.

[132] T. P. Hansen, J. Broeng, C. Jakobsen, G. Vienne, H. R. Simonsen, M. D. Nielsen, P. M. W. Skovgaard, J. R. Folkenberg and A. Bjarklev, "Air-guiding photonic bandgap fibers: spectral properties, macrobending loss, and practical handling," *Journal of Lightwave Technology,* vol. 22, pp. 11-15, 2004.

[133] Fujikura Ltd., "Advanced optical fiber cleaver - ARCMaster CT-100," 3rd ed, 2011.

[134] J. K. Lyngsø, C. Jakobsen, J. S. Gretlund and H. R. Simonsen, "Optical fiber with improvements relating to loss and its use, method of its production and use thereof," United States Patent US 2010/0266251 A1, Oct. 21, 2010.

[135] S. R. Sandoghchi, T. Zhang, J. P. Wooler, N. K. Baddela, N. V. Wheeler, Y. Chen, G. T. Jasion, D. R. Gray, E. R. Numkam Fokoua, J. R. Hayes, M. N. Petrovich, F. Poletti and D. J. Richardson, "First Investigation of Longitudinal Defects in Hollow Core Photonic Bandgap Fibers," presented at the Optical Fiber Communication Conference, San Francisco, California, United States, 2014.

[136] J. C. Jasapara, "Non-invasive characterization of microstructured optical fibers using Fourier domain optical coherence tomography," *Optics Express,* vol. 13, pp. 1228-1233, 2005.

[137] A. Stefani, M. H. Frosz, T. G. Euser, G. K. L. Wong and P. S. J. Russell, "Real-time Doppler-assisted tomography of microstructured fibers by side-scattering," *Optics Express,* vol. 22, pp. 25570-25579, 2014.

[138] A. D. Yablon, "Multifocus tomographic algorithm for measuring optically thick specimens," *Optics Letters,* vol. 38, pp. 4393-4396, 2013.

[139] L. L. Lavery, J. Gelb, A. P. Merkle and A. Steinbach, "X-Ray Microscopy for Hierarchical Multi-Scale Materials," *Microscopy Today,* vol. 22, pp. 16-21, 2014.

[140] S. R. Sandoghchi, G. T. Jasion, N. V. Wheeler, J. P. Wooler, R. P. Boardman, N. K. Baddela, Y. Chen, J. R. Hayes, E. R. Numkam Fokoua, T. D. Bradley, D. R. Gray, S. A. Mousavi, M. N. Petrovich, F. Poletti and D. J. Richardson, "X-ray tomography for structural analysis of

microstructured optical fibres and preforms," presented at the European Conference on Optical Communication, Cannes, France, 2014.

[141] S. R. Sandoghchi, G. T. Jasion, N. V. Wheeler, S. Jain, Z. Lian, J. P. Wooler, R. P. Boardman, N. K. Baddela, Y. Chen, J. R. Hayes, E. R. Numkam Fokoua, T. D. Bradley, D. R. Gray, S. A. Mousavi, M. N. Petrovich, F. Poletti and D. J. Richardson, "X-ray tomography for structural analysis of microstructured and multimaterial optical fibers and preforms," *Optics Express,* vol. 22, pp. 26181-26192, 2014.

[142] J. Ballato. (2014, Oct.). *Spotlight on Optics: X-ray tomography for structural analysis of microstructured and multimaterial optical fibers and preforms* [Article]. Available: https://www.osapublishing.org/spotlight/summary.cfm?id=303123

[143] W. J. Stewart, "Optical fiber and preform profiling technology," *IEEE Journal of Quantum Electronics,* vol. 18, pp. 1451-1466, 1982.

[144] P. R. Shearing, D. J. L. Brett and N. P. Brandon, "Towards intelligent engineering of SOFC electrodes: a review of advanced microstructural characterisation techniques," *International Materials Reviews,* vol. 55, pp. 347-363, 2010.

[145] UTCT. (2015, Jul. 18). *About CT* [Article]. Available: http://www.ctlab.geo.utexas.edu/about-ct/

[146] A. C. Kak and M. Slaney, *Principles of computerized tomographic imaging*. Philadelphia: Society for Industrial and Applied Mathematics, 2001.

[147] R. Hanke, T. Fuchs and N. Uhlmann, "X-ray based methods for non-destructive testing and material characterization," *Nuclear Instruments and Methods in Physics Research Section A: Accelerators, Spectrometers, Detectors and Associated Equipment,* vol. 591, pp. 14-18, 2008.

[148] Carl Zeiss Microscopy GmbH, "ZEISS Xradia 810 Ultra: Nanoscale X-ray Imaging at the Speed of Science," 1st ed. Czech Republic, 2013.

[149] J. Hsieh, *Computed tomography : principles, design, artifacts, and recent advances*, 2nd ed. New Jersey: Wiley Interscience, 2009.

[150] A. E. Scott, M. Mavrogordato, P. Wright, I. Sinclair and S. M. Spearing, "In situ fibre fracture measurement in carbon–epoxy laminates using high resolution computed tomography," *Composites Science and Technology,* vol. 71, pp. 1471-1477, 2011.

[151] J. Dinley, L. Hawkins, G. Paterson, A. D. Ball, I. Sinclair, P. Sinnett-Jones and S. Lanham, "Micro-computed X-ray tomography: a new non-destructive method of assessing sectional, fly-through and 3D imaging of a soft-bodied marine worm," *Journal of Microscopy,* vol. 238, pp. 123-133, 2010.

[152] Southampton Imaging. (2014, Aug. 15). *microCT* [Web page]. Available: http://www.southampton.ac.uk/muvis/about/index.page

[153] Nikon. (2016, Dec. 15). *XT H 225 Industrial CT Scanning* [Specification Sheet]. Available: http://www.nikonmetrology.com/en_EU/Products/X-ray-and-CT-Inspection/Computed-Tomography/XT-H-225-Industrial-CT-Scanning/(brochure)

[154] M. E. Phelps, M. H. Gado and E. J. Hoffman, "Correlation of Effective Atomic Number and Electron Density with Attenuation Coefficients Measured with Polychromatic X Rays," *Radiology,* vol. 117, pp. 585-588, 1975.

[155] Z. Lian, M. Segura, N. Podoliak, X. Feng, N. White, P. Horak and W. H. Loh, "Electrical current-driven dual-core optical fiber with embedded metal electrodes," presented at the Optical Fiber Communication Conference, San Francisco, California, United States, 2014.

[156] M. Fokine, L. E. Nilsson, Ã. Claesson, D. Berlemont, L. Kjellberg, L. Krummenacher and W. Margulis, "Integrated fiber Mach-Zehnder interferometer for electro-optic switching," *Optics Letters,* vol. 27, pp. 1643-1645, 2002.

[157] H. W. Lee, M. A. Schmidt, H. K. Tyagi, L. P. Sempere and P. S. J. Russell, "Polarization-dependent coupling to plasmon modes on submicron gold wire in photonic crystal fiber," *Applied Physics Letters,* vol. 93, pp. 111103-111105, 2008.

[158] H. W. Lee, M. A. Schmidt and P. S. J. Russell, "Excitation of a nanowire molecule in gold-filled photonic crystal fiber," *Optics Letters,* vol. 37, pp. 2946-2948, 2012.

[159] N. Podoliak, Z. Lian, W. H. Loh and P. Horak, "Design of dual-core optical fibers with NEMS functionality," *Optics Express,* vol. 22, pp. 1065-1076, 2014.

[160] S. Jain, V. J. F. Rancaño, T. C. May-Smith, P. Petropoulos, J. K. Sahu and D. J. Richardson, "Multi-Element Fiber Technology for Space-Division Multiplexing Applications," *Optics Express,* vol. 22, pp. 3787-3796, 2014.

[161] C. Ding, W. Xiong, T. Fan, D. D. Hickstein, T. Popmintchev, X. Zhang, M. Walls, M. M. Murnane and H. C. Kapteyn, "High flux coherent super-continuum soft X-ray source driven by a single-stage, 10mJ, Ti:sapphire amplifier-pumped OPA," *Optics Express,* vol. 22, pp. 6194-6202, 2014.

[162] J. Becker, M. W. Tate, K. S. Shanks, H. T. Philipp, J. T. Weiss, P. Purohit, D. Chamberlain and S. M. Gruner, "Sub-microsecond x-ray imaging using hole-collecting Schottky type CdTe with charge-integrating pixel array detectors," *Journal of Instrumentation,* vol. 12, p. 6022, 2017.

[163] G. T. Jasion, S. R. Sandoghchi, Y. Chen, N. V. Wheeler, T. D. Bradley, N. K. Baddela, J. R. Hayes, M. N. Petrovich, D. J. Richardson, J. S. Shrimpton and F. Poletti, "Novel fluid dynamics model to predict draw of hollow core photonic band-gap fibres," presented at the European Conference on Optical Communication, Cannes, France, 2014.

[164] J. P. Wooler, D. R. Gray, F. Poletti, M. N. Petrovich, N. V. Wheeler, F. R. Parmigiani and D. J. Richardson, "Robust Low Loss Splicing of Hollow Core Photonic Bandgap Fiber to Itself," presented at the Optical Fiber Communication Conference, Anaheim, California, United States, 2013.

[165] F. Couny, F. Benabid and P. S. Light, "Reduction of Fresnel Back-Reflection at Splice Interface Between Hollow Core PCF and Single-Mode Fiber," *IEEE Photonics Technology Letters,* vol. 19, pp. 1020-1022, 2007.

[166] J. P. Wooler, S. R. Sandoghchi, D. R. Gray, F. Poletti, M. N. Petrovich, N. V. Wheeler, N. K. Baddela and D. J. Richardson, "Overcoming the Challenges of Splicing Dissimilar Diameter Solid-Core and Hollow-Core Photonic Band Gap Fibers," presented at the Workshop on Specialty Optical Fibers and their Applications, Sigtuna, Sweden, 2013.

[167] J. P. Wooler, F. R. Parmigiani, S. R. Sandoghchi, N. V. Wheeler, D. R. Gray, F. Poletti, M. N. Petrovich and D. J. Richardson, "Data transmission over 1km HC-PBGF arranged with microstructured fiber spliced to both itself and SMF," presented at the European Conference on Optical Communication, London, United Kingdom, 2013.

[168] J. D. Shephard, F. Couny, P. S. J. Russell, J. D. C. Jones, J. C. Knight and D. P. Hand, "Improved hollow-core photonic crystal fiber design for delivery of nanosecond pulses in laser micromachining applications," *Applied Optics,* vol. 44, pp. 4582-4588, 2005.

[169] B. Debord, M. Alharbi, L. Vincetti, A. Husakou, C. Fourcade-Dutin, C. Hoenninger, E. Mottay, F. Gérôme and F. Benabid, "Multi-meter fiber-delivery and pulse self-compression of milli-Joule femtosecond laser and fiber-aided laser-micromachining," *Optics Express,* vol. 22, pp. 10735-10746, 2014.

[170] M. Michieletto, J. K. Lyngsø, C. Jakobsen, J. Lægsgaard, O. Bang and T. T. Alkeskjold, "Hollow-core fibers for high power pulse delivery," *Optics Express,* vol. 24, pp. 7103-7119, 2016.

[171] N. V. Wheeler, T. D. Bradley, J. R. Hayes, M. A. Gouveia, Y. Chen, S. R. Sandohgchi, F. Poletti, M. N. Petrovich and D. J. Richardson, "Low Loss Kagome Fiber in the 1 µm Wavelength Region," presented at the Advanced Photonics Congress, Vancouver, Canada, 2016.

[172] M. N. Petrovich, F. Poletti, J. P. Wooler, A. M. Heidt, N. K. Baddela, Z. Li, D. R. Gray, R. Slavik, F. R. Parmigiani, N. V. Wheeler, J. R. Hayes, E. R. Numkam Fokoua, L. Grűner-Nielsen, B. Pálsdóttir, R. Phelan, B. Kelly, J. O'Carroll, M. Becker, N. MacSuibhne, J. Zhao, F. C. G. Gunning, A. D. Ellis, P. Petropoulos, S. U. Alam and D. J. Richardson, "Demonstration of amplified data transmission at 2µm in a low-loss wide bandwidth hollow core photonic bandgap fiber," *Optics Express,* vol. 21, pp. 28559-28569, 2013.

[173] H. Zhang, N. Kavanagh, Z. Li, J. Zhao, N. Ye, Y. Chen, N. V. Wheeler, J. P. Wooler, J. R. Hayes, S. R. Sandoghchi, F. Poletti, M. N. Petrovich, S. U. Alam, R. Phelan, J. O'Carroll, B. Kelly, L. Grüner-Nielsen, D. J. Richardson, B. Corbett and F. C. Garcia Gunning, "100Gbit/s WDM transmission at 2µm: transmission studies in both low-loss hollow core photonic bandgap fiber and solid core fiber," *Optics Express,* vol. 23, pp. 4946-4951, 2015.

[174] A. R. Tynes, A. D. Pearson and D. L. Bisbee, "Loss mechanisms and measurements in clad glass fibers and bulk glass," *Journal of the Optical Society of America,* vol. 61, pp. 143-153, 1971.

[175] Princetel Inc. (2009, Nov. 15). *Tutorial: Fiber optic rotary joints* [Article]. Available: http://www.princetel.com/tutorial_forj.asp

[176] J. P. Dakin, "A simplified photometer for rapid measurement of total scattering attenuation of fibre optical waveguides," *Optics Communications,* vol. 12, pp. 83-88, 1974.

[177] B. L. Danielson, "Optical time-domain reflectometer specifications and performance testing," *Applied Optics,* vol. 24, pp. 2313-2322, 1985.

[178] N. H. L. Wong, S. R. Sandoghchi, Y. Jung, T. D. Bradley, N. V. Wheeler, N. K. Baddela, J. R. Hayes, F. Poletti, M. N. Petrovich, S. U. Alam, P. Petropoulos and D. J. Richardson, "Inspection of defect-induced mode coupling in hollow-core photonic bandgap fibers using time-of-flight," presented at the Conference on Lasers and Electro-Optics, San Jose, California, United States, 2015.

[179] R. Phelan, J. O'Carroll, D. Byrne, C. Herbert, J. Somers and B. Kelly, "$In_{0.75}Ga_{0.25}As$/InP multiple quantum-well discrete-mode laser diode emitting at 2µm," *IEEE Photonics Technology Letters,* vol. 24, pp. 652-654, 2012.

[180] C. Markos, "Photonic-crystal fibre: mapping the structure," *Nature Photonics,* vol. 9, pp. 9-11, 2015.

[181] Carl Zeiss Microscopy GmbH, "Your Guide to Electron Microscopy Techniques from ZEISS," in *Electron Microscopes for Life Sciences*, EN_41_010_021 ed, 2013.

[182] V. N. E. Robinson, "Imaging with backscattered electrons in a scanning electron microscope," *Scanning,* vol. 3, pp. 15-26, 1980.

[183] E. R. Numkam Fokoua, S. R. Sandoghchi, Y. Chen, G. T. Jasion, N. V. Wheeler, N. K. Baddela, J. R. Hayes, M. N. Petrovich, D. J. Richardson and F. Poletti, "Accurate modelling of fabricated hollow-core photonic bandgap fibers," *Optics Express,* vol. 23, pp. 23117-23132, 2015.

[184] T. D. Bradley, N. V. Wheeler, G. T. Jasion, D. R. Gray, J. R. Hayes, M. A. Gouveia, S. R. Sandoghchi, Y. Chen, F. Poletti, D. J. Richardson and M. N. Petrovich, "Modal content in hypocycloid Kagomé; hollow core photonic crystal fibers," *Optics Express,* vol. 24, pp. 15798-15812, 2016.

[185] T. D. Bradley, N. V. Wheeler, M. N. Petrovich, G. T. Jasion, D. R. Gray, J. R. Hayes, S. R. Sandoghchi, Y. Chen, F. Poletti, D. J. Richardson and M. A. Gouveia, "S^2 Measurement of Higher Order Mode Content in Low Loss Hypocycloid Kagomé Hollow Core Photonic Crystal Fiber," presented at the Conference on Lasers and Electro-Optics, San Jose, California, United States, 2016.

[186] J. R. Hayes, S. R. Sandoghchi, T. D. Bradley, Z. Liu, R. Slavik, M. A. Gouveia, N. V. Wheeler, G. T. Jasion, Y. Chen, E. R. Numkam Fokoua, M. N. Petrovich, D. J. Richardson and F. Poletti, "Antiresonant Hollow Core Fiber with Octave Spanning Bandwidth for Short Haul Data Communications," presented at the Optical Fiber Communication Conference - Post-Deadline Papers, Anaheim, California, United States, 2016.

[187] J. R. Hayes, S. R. Sandoghchi, T. D. Bradley, Z. Liu, R. Slavik, M. A. Gouveia, N. V. Wheeler, G. T. Jasion, Y. Chen, E. R. Numkam Fokoua, M. N. Petrovich, D. J. Richardson and F. Poletti, "Antiresonant Hollow Core Fiber with an Octave Spanning Bandwidth for Short Haul Data Communications," *Journal of Lightwave Technology,* vol. 35, pp. 437-442, 2016.